Photo- and Electro-Induced Hadron Production from Nuclei at Jefferson Laboratory

Rhidian Williams

Doctor of Philosophy

University of York

Department of Physics, Engineering and Technology

May 2024

Abstract

Understanding many-body knockout processes is crucial for nuclear physics, particularly in photo- and electro-induced reactions. In turn, understanding two- and three-body forces, including higher-order forces, is vital for a complete understanding of atoms. We present photo-induced many-proton knockout processes, with multiplicities from 1 to 6, using ^{12}C, CH_2, and C_4H_9OH targets in the g9a FROST dataset. Our analysis covers photon energies from 600 to 4500 MeV, significantly expanding current world data. Comparing our experimental data to the state-of-the-art GiBUU model offers a new challenge in the model's theoretical description of many-body processes. GiBUU reasonably describes the data at lower photon energies but struggles at higher energies and missing masses, likely due to missing processes, such as initial 3-pion photoproduction. Our results will inform future developments in describing proton knockout processes, indicating GiBUU's overall reasonable description of many-proton knockout data up to around 2.2 GeV.

We also assess various electro-induced reactions using ^{2}D, ^{12}C, and ^{40}Ar targets in the RGM dataset. Our results, obtained at electron beam energies of 2, 4, and 6 GeV, are compared in detail to GENIE and GiBUU, two widely used theory models in neutrino oscillation experiments. Discrepancies between model predictions and experimental data underscore the need for refining the two theoretical models. Despite discrepancies, GiBUU provides a more accurate modelling of electro-induced reactions, especially for ^{40}Ar - crucial for future neutrino oscillation facilities such as DUNE. Understanding the fundamental nuclear physics involved in neutrino-nuclei interactions is essential for reducing the systematic uncertainties in extracting neutrino oscillation parameters. Many-body processes significantly contribute to the background processes observed in neutrino-nuclei interactions, hence the results from both analyses are crucial for developing the theoretical framework for the underlying nuclear physics.

Dedication

I dad-cu Garnswllt, pryd mae popeth yn gwyllt ac mae cefen fi erbyn y wal, gyda'r pwysau y byd arno fi, fi'n cofio eistedd arno eich glin. Wedyn, mae popeth yn dawel ac mae'r ateb yn glyr. Hefyd, i mam-gu Garnswllt, pwy sy'n ffigwr o gryfder, cred a gwaith caled, diolch. Diolch i mam a dad hefyd, wrth gwrs, am eu cefnogaeth gyson. Diolch yn fawr i pawb yn fy teulu.

Declaration

The data was collected from the g9a and RGM experiments as part of the CLAS collaboration at the Thomas Jefferson National Accelerator Facility, Virginia, USA, and the Nuclear Physics Group at the University of York. I declare that this thesis is a presentation of original work and I am the sole author. This work has not previously been presented for an award at this, or any other, University. All sources are acknowledged as references. The analysis presented in Chap. 8 has undergone a full review from an internal three-person review from the CLAS collaboration.

Rhidian Williams

April 2024

Acknowledgements

"Friendship is a priceless gift that cannot be bought nor sold, but its value is far greater than a mountain made of gold. For gold is cold and lifeless. It can neither see nor hear, and in times of trouble, it is powerless to cheer. Gold it has no ears to listen, no heart to understand. It cannot bring you comfort or reach out a helping hand. So when you ask God for a gift, be thankful if he sends not diamonds, pearls, or riches but the love of real, true friends. Friends are very rare." - Muhammad Ali

I must start by thanking the biggest professional figure of support during my time at York, Professor Daniel Watts. A truly extraordinary man, who has taught me so much since I started. Dan has taught me to follow my heart, to not take life too seriously and to enjoy the journey. The most important lesson; how to be a true scientist. To be a great scientist, you cannot be afraid of the unknown, you must only be excited by it and be willing to take risks. Dan leads by example in this regard, and I only hope I become 10% of the man he is, without all the smoking and vaping, of course.

I have to thank Dr. Nick Zachariou for his constant support throughout my PhD. I would have attempted all my calculations through pen and paper if it wasn't for Nick. His unparalleled patience to teach me the basics of programming is superhuman. My unofficial third supervisor, Dr. Stuart Fegan has been an immense figure to look up to during my PhD. Stuart has been extremely patient with me over the years, regularly sacrificing his time for my benefit. Thank you both! I must also thank the members of staff in the department for many useful discussions and for providing a friendly environment. Particularly, Professor David Jenkins, a fellow Welshman and head of the nuclear physics group. David has been a wonderful head of group during my time at York and offers a platform for the students to be heard. A remarkable scientist and an even better man.

"Be loyal to what matters." - Arthur Morgan

Other members of the department have been exceptional during my time in York. Dr. Mikhail Bashkanov has been a positive figure over the years, always providing great ideas, discussions and solutions. I could almost call Mikhail a fourth supervisor, to enunciate how lucky I am. A big thanks to the top lads in, and regularly seen at, the hadron (coffee) office; Dr. Adam Featherstone, Dr. Pietro Caradonna, Dr. Ryo Taniuchi, Dr. Sidong

Chen, Dr. Wei zhang, Dr. Stephen Kay and especially Dr. Julien Bordes for regularly prescribing pints at the pharmaceutical Phoenix. A big thank you to Dr. James Cubiss is in order, for interesting regular discussions regarding physics, or general life and career advice. Thank you to everyone in this paragraph for regular visits to the cheeky Charles, which is now a staple tradition of the York Nuclear Physics Group.

A big thank you must be given to the members of the department that provided an instrumental level of support during the early years of, and throughout, the PhD, especially during the pandemic. The Discord Lads, Dr. Luke Tetley, Paolo Sassarini, Luke Rose and Alex-Hall Smith, among others, and the older hadron generation Dr. Matt Nicol, Dr. Geraint Glash and Mihai Mocanu. Matt and Geraint were especially helpful in the first few months when I couldn't code for Toffee. After the pandemic, many nights out were enjoyed with these folks, and many quotes were invented by Geraint, in which I had the pleasure of experiencing their invention. I will always remember that 45 minutes is the shortest long amount of time possible for a walk.

"Lack of something to feel important about is almost the greatest tragedy a man may have." - Arthur Morgan

It would be unfair for me not to mention the great people from other departments who have played an instrumental role in this PhD. A huge thank you to the staff at JLab Dr. Raffaella De Vita, Dr. Patrick Achenbach, Dr. Nathan Baltzell, Dr. Maurizio Ungaro, Dr. Eugene Pasyuk, Dr. Pierre Chatagnon, Dr. Carlos Ayerbe Gayoso and Dr. Gerry Gilfoyle. Whenever I have needed something, these people have always offered their full support. I would like to thank Dr. Kai Gallmeister and Professor Ulrich Mosel for their help with the GiBUU model and the great theory discussions we have had over the years. Together with their help, we have produced some very exciting results! I must thank a great mentor for me, especially during my three months at Jefferson Lab, Professor Larry Weinstein. Larry is like a father figure. If it were not for Larry, I would still be very poor at communicating science, have a weaker understanding of fundamental physics and have no experience using firearms. The "group therapy" sessions spent at the firing range were a great time, where ironically, many great physics discussions were had, and something Larry did not need to do for a student not his own. A big thank you to all the students that I have met along the way as part of the CLAS collaboration and through attending conferences. I have to thank the Glasgow folks, in particular Gary Penman. I will always remember Gary's touching words - "Every experience with you is an experience." Dr. Paul Naidoo requires a special mention for bringing me Chik-Fil-A during one of my very first shifts. Finally, I must thank Andrew William Denniston and Dr. Justin Brian Estee who are fantastic physicists and amazing people. Regular discussions with these two, including Larry, about physics, but mostly random nonsense made all my JLab trips very enjoyable. Also, a huge thank you to the g9a and RGM groups. All the folks involved with these groups are the reason the results I have produced during my PhD were possible.

Cheerz to The Dayz Christian and James Osborne, especially The Day Matthew Morse. No matter how far I travelled during my PhD, and no matter where life takes me, Saturday night is for the boys. I can't thank Matthew enough, his constant support through terrible (good) dad jokes, always believing in me and inciting confidence when I have the deepest level of imposter syndrome, is something I can never repay. His time and friendship are more valuable than the materialistic objects in my life. I would also like to thank Brandon Jones for always being there for me. Putting a smile on people's faces just comes naturally to such a positive individual.

"Vengeance is an idiot's game." - Arthur Morgan

My housemates during my time at York have been unbelievable, particularly Sebastian, Dom, David and Lucy. My actions speak louder than words, and since I have remained in the same house during my tenure at York, this exemplifies that I have lived with great people. Sebastian, Dom and Lucy have also been great at doing activities (if you can call going to the pub an activity). They are all great people who are willing to give up time to talk about utter nonsense, which is typically what you need after spending a day discussing mind-bending particle physics. Thank you to you all.

My PhD would have been extremely tough if not for my love of football and the many friends I have met through playing it during my time at York. I would like to thank Baz Bala for being such a wonderful person and a figure of great advice, always with a smile on his face, no matter the situation. Baz has introduced me to many new groups, making plenty of friends along the way. Particularly, granddad (sorreh) Shaun Elsbury, Big Jon Turps, Jordan Timeney, John (Glass) K, Robin, Luke, Stew and Marianne. These folks have given me such great nights out and have been lovely people to play football with over the past few years. Always offering advice and support along the way. A special thank you is in order for Stew and Marianne, for their hospitality and generosity over the years. They have hosted many events and many parties at their house that have been a joy to be a part of (except the times we watched England and they won, and we watched Wales and they lost). Their generosity and kindness are an example for all, and the people I have met in York are truly exceptional. Thank you for the support!

"We'll make it." - Master Chief

Yn olaf, byddain eisiau diolch fy teulu. Mae mam and dad fi wedi cefnogi i trwy'r PhD, galw pob wythnos i checko sut ma i. Diolch I fy chwaer Elizabeth am dangoso fi sut i byw, i mwynhau pob dydd sut mae en dydd olaf chi. Diolch i fy mam-gu a fy ewythrod, Winston a Royston, am fod yno bob amser. Diolch i fy nghi Ella, y doberman, sy'n ddireidus ac yn wych ar yr un pryd a diolch yn fawr i fy nheulu i gyd!

"It isn't the mountains ahead to climb that wear you out; it's the pebble in your shoe." - Muhammad Ali

Contents

List of Figures

List of Tables

Fundamental Constants

- Speed of Light, $c = 3 \times 10^8$ ms^{-1}
- Speed of Light (in cm/ns), $c = 29.98$ cm/ns
- Planck's Constant, $h = 6.626 \times 10^{-34}$ Js
- Reduced Planck's Constant, $\hbar = \frac{h}{2\pi} = 1.055 \times 10^{-34}$ js
- Elementary Charge, $e = 1.6 \times 10^{-19}$ C
- Vacuum Electric Permeability, $\epsilon_0 = 8.854 \times 10^{-12}$ Fm
- Fine Structure Constant, $\alpha = \frac{e^2}{4\pi\hbar c\epsilon_0} = 0.007297 \approx 1/137$
- Gravitational Constant, $G = 6.673 \times 10^{-11}$ Nm^{2}kg^{-2}
- Avogadro's Number, $N_A = 6.022 \times 10^{23}$ mol^{-1}
- Dalton (Unified Atomic Mass unit), $u = 0.931494$ MeV/c^2
- Proton Mass, $m_p = 0.938272$ MeV/c^2
- Electron Mass, $m_e = 0.000511$ MeV/c^2
- Neutron Mass, $m_n = 0.939565$ MeV/c^2
- Positively and Negatively Charged Pion Mass, $m_{\pi^{+/-}} = 0.139570$ MeV/c^2
- Neutrally Charged Pion Mass, $m_{\pi^0} = 0.134977$ MeV/c^2
- Positively and Negatively Charged Kaon Mass, $m_{K^{+/-}} = 0.493677$ MeV/c^2
- Neutrally Charged Kaon Mass, $m_{K^0} = 0.497611$ MeV/c^2
- Deuteron Mass, $m_D = 2.014u = 1.876029$ MeV/c^2
- Carbon Mass, $m_C = 12u = 11.177928$ MeV/c^2
- Argon Mass, $m_{Ar} = 39.962u = 37.224363$ MeV/c^2
- Lead Mass, $m_{Pb} = 207.977u = 193.729328$ MeV/c^2
- Uranium Mass, $m_U = 238.051u = 221.743078$ MeV/c^2

Chapter 1

Introduction

> *"I do not know what I may appear to the world, but to myself I seem to have been only like a boy playing on the sea-shore, and diverting myself in now and then finding a smoother pebble or a prettier shell than ordinary, whilst the great ocean of truth lay all undiscovered before me."*
>
> - Isaac Newton

The universe began with a massive explosion known as the Big Bang, at a period where all the available energy in the universe was concentrated in a very small area. At the very early stages of the universe (before $\approx 10^{-43}$ s after the Big Bang), the universe reached unfathomably high temperatures and the fundamental forces of nature were unified, since the very concept of a particle breaks down under such conditions. The four fundamental forces of nature - the strong nuclear force, the electromagnetic force, the weak nuclear force and the gravitational force - are well known in modern physics, though many of their properties are still not well understood. These forces operate through particles called gauge bosons, which act as "force carriers", and are summarised in Fig. 1.1.

The gravitational force is responsible for the attractive force experienced between all bodies with non-zero energy, while the electromagnetic force is responsible for the interactions of charged particles through electromagnetic fields. The strong nuclear force binds particles together, and the weak nuclear force mitigates radiative interactions (e.g. β-decay) between particles, which allows particles to change species (e.g. proton to neutron). The forces are presented as the strongest to the weakest force, in relative strength. The strong nuclear force is 10s of orders of magnitude stronger than the gravitational force, and a few orders of magnitude stronger than the electromagnetic and weak force, respectively. The electromagnetic force is stronger than the weak force at the energies of the present study, hence the dominant interactions seen at subatomic levels are strong- and electromagnetic-induced reactions. The understanding of these fundamental forces has not only deepened our knowledge of the universe but has also led to the discovery of many technologies that

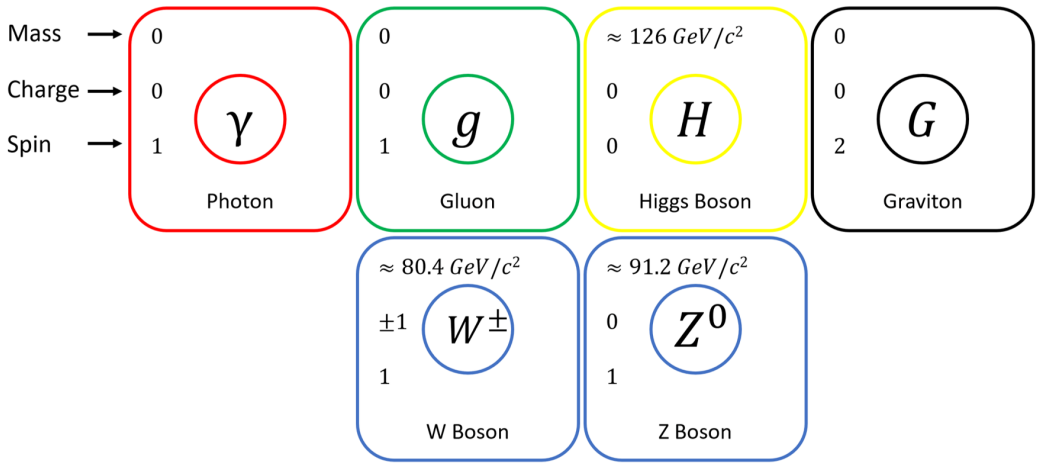

Figure 1.1: The fundamental forces of nature and their respective gauge bosons, with a collection of their properties. Data is taken from [1].

impact our daily lives. For example, our understanding of electromagnetism has been crucial in the development of communication technologies, including the smartphones we use today.

At a time around $\sim 10^{-36}$ s after the Big Bang, the gravitational force separated from the others as the universe was continually cooling and expanding [2]. Figure 1.2 presents a summary of the history of the universe.

At around $< 10^{-32}$ s after the Big Bang, a phase transition occurred, triggering a cosmic inflation during which the universe underwent a rapid expansion at an exponential rate. The temperatures of the universe dropped significantly by many orders of magnitude, and, a little later, the strong nuclear force became distinguishable from the others.

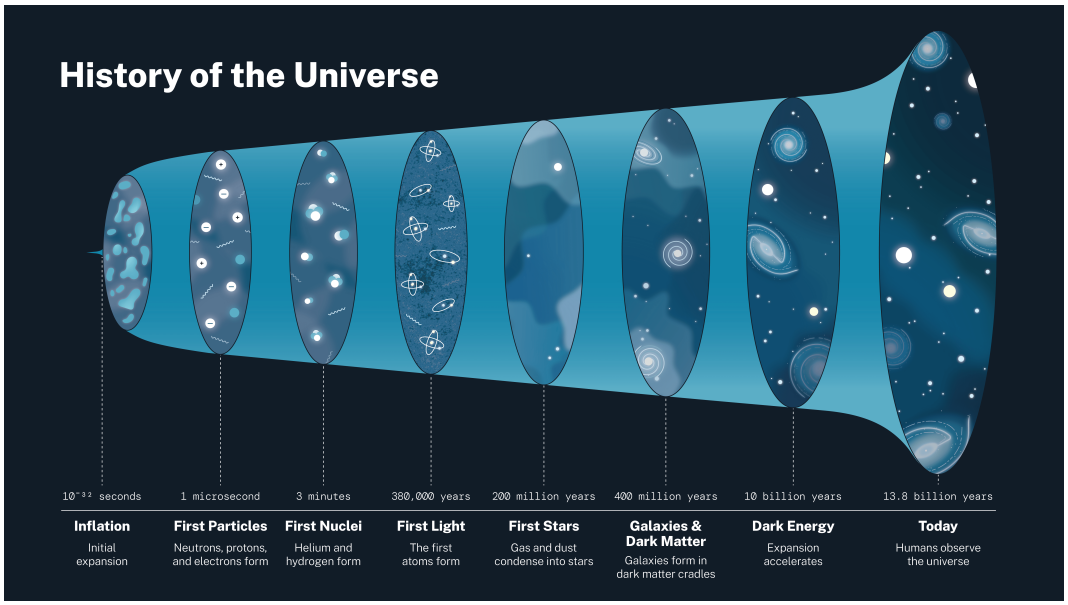

Figure 1.2: A pictorial depiction of the history of the universe, taken from Ref. [3].

This is when the electroweak epoch began, where only the weak nuclear force and electromagnetic force remained unified. Between this time and just before 10^{-12} s after the Big Bang, the electroweak epoch ended and all four fundamental forces of nature were uniquely identifiable. The Higgs mechanism began to take shape, and the conditions of the universe were then appropriate for the production of the Higgs boson. This boson allows the fundamental forces of nature to manifest their energy into physical matter. Before a fraction of a nanosecond after the Big Bang, matter and anti-matter existed with equal proportions and matter-antimatter creation and annihilation occurred continuously. However, briefly afterwards, matter gained the upper hand, resulting in what we now experience as the matter-dominated universe.

After this time, the universe experienced many different stages of evolution, and it continued to gradually expand and cool. Under the correct conditions (after the universe sufficiently cooled down), the first quarks, which are the most fundamental constituents of matter, formed under the influence of the Higgs boson. Afterwards, the first particles, called hadrons, such as the proton, which are composed of quarks, were formed as the quarks were "glued" together by the strong nuclear force. Around the same time the first quarks were produced, the first leptons emerged, which are fundamental particles with no internal structure, such as the electron. A summary of the leptons and the quarks, which compose all hadrons, is provided in Fig. 1.3.

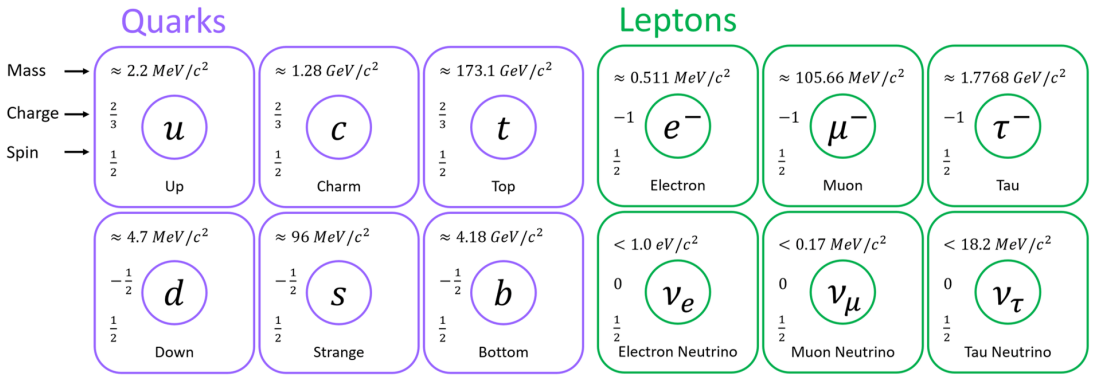

Figure 1.3: The fundamental building blocks of nature; quarks (left table) and leptons (right table), with a collection of their properties. Data is taken from [1].

1.1 Classification of Particles

The hadrons are divided into two groups: baryons and mesons. Baryons are composed of either three quarks (qqq) or anti-quarks ($\bar{q}\bar{q}\bar{q}$), and mesons are formed from a quark and anti-quark pair ($q\bar{q}$). An example of a meson is the positive pion, π^+, composed of an up and anti-down quark pair, and the proton, composed of two up quarks and a down quark is an example of a baryon. A pictorial depiction of a proton, along with the quarks that compose it, is presented in Fig. 1.4. Since these particles are formed under the influence of

the strong nuclear force, they possess an additional property called colour charge, which is unique for each hadron. Colour charge is a theoretical construct and is not analogous to the visible colours. Leptons, on the other hand, such as the electron, do not interact via the strong nuclear force and thus possess a colour charge of 0. However, all particles can be categorized into two groups: fermions and bosons. Fermions have half-integer spin, while bosons have integer spin. Each particle depicted in Fig. 1.3 has its own antiparticle, with particles representing matter and antiparticles representing antimatter. Antiparticles have the same mass as their particle counterparts, but a few of their quantum numbers have opposing magnitudes. For example, the electron and positron have the same mass but opposite charges (-1 and +1, respectively).

There are various quantum numbers associated with particles, and here we provide a brief description of a few. Starting with the aforementioned quantum number spin, denoted as S, it is a fundamental property of each particle that lacks an analogy in classical physics (particles are not actually spinning). Instead, one can envision an arrow, symbolising the electron, fired by a knight, in which the knight's action of tightening the arrow represents the influence of the field, specifically the electromagnetic field in this analogy. If the arrowhead points forward (spin 1/2, or "up"), it interacts differently upon collision compared to when it points backwards (spin -1/2, or "down"). Gauge bosons, like the photon, have spin 1, allowing for various orientations; for instance, the arrowhead can point vertically upwards. The spin of a particle reflects its behaviour under the influence of electromagnetic forces. Angular momentum, denoted as L, is defined similarly to its classical counterpart; it describes the rotation of an object. However, quantum angular momentum can only take on discrete values determined by Planck's constant, h, and the particle's spin. Isospin, denoted as I, is analogous to spin but is related to the symmetry properties of the strong nuclear force rather than the electromagnetic force. Nucleons are assigned an isospin value, which can be an integer or half-integer, like spin, based on how they interact via the strong nuclear force and their quark composition. The arrow analogy

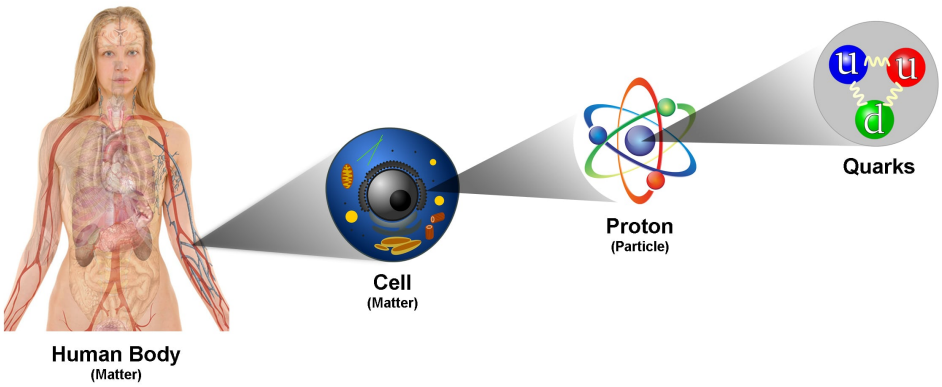

Figure 1.4: A pictorial depiction of the fundamental building blocks of nature, taken from Ref. [4].

can be applied to isospin for protons and neutrons, indicating that the same particles can interact differently depending on their quantum numbers.

Expanding on the idea of isospin, nucleon pairs, such as neutron-neutron, proton-proton, or proton-neutron, can possess specific isospin values. Isospin pairs, denoted by T, can have either integer or half-integer values. The isospin z-projection of neutrons and protons is +1/2 and -1/2, respectively. For $T = 0$ pairs, the total isospin is zero (as the sum of 1/2 and -1/2 is 0), meaning the pair of nucleons is in an isospin singlet state. A $T = 0$ pair refers to a proton-neutron pair, while a $T = 1$ pair could involve two neutrons, two protons or a neutron-proton pair in an isospin triplet state. A triplet state refers to a particle that possesses a quantum number with three allowed values along the projection of a given axis, for example, $S = 1$ has $m_S = -1, 0, 1$. For a quantum number l (angular momentum), the number of allowed states (of angular momentum) is given by $-l \leq m_l \leq l$, in steps of 1.

1.2 The Many-Body Problem

Approximately $380,000$ years after the Big Bang, the first neutral atoms were produced. Atoms are objects composed of a variety of particles, with a particular structure, which possess unique properties. Atoms have a nucleus, which is composed of protons and neutrons held together by the strong nuclear force, and electrons, which orbit the nucleus due to the electromagnetic attraction experienced between the protons and electrons. The first atoms were produced when the universe cooled to a sufficient temperature that the nucleus could capture the electrons.

Atoms have a rich history, but until the late 19^{th} to early 20^{th} century, atoms were believed to be the most fundamental objects in the universe. In 1911, Rutherford, Geiger and Marsden famously discovered the structure of the atomic nucleus when they scattered alpha particles off a thin gold film and observed backwards scattered alpha particles, in keeping with the existence of heavy point-like structures [5]. In 1932, J. Chadwick discovered the neutrally charged objects inside the atom called neutrons [6], and with that came the birth of nuclear physics. The highest priority of nuclear physics is to understand the nature of the interactions between nucleons and how these interactions influence the structure and properties of the atomic nucleus.

This can be achieved theoretically by solving the many-body problem, which aims to understand the interactions of subatomic particles within the nucleus of atoms. The problem is defined by the Hamiltonian, H, which describes the total energy (kinetic and potential) of the particles in the system and accounts for interactions between the particles. For instance, the Hamiltonian includes terms describing the potential energy of interactions between pairs and groups of nucleons. The potential energy of a particle represents its stored energy, which is determined by its position, properties and the forces

acting upon it. Neglecting non-nucleonic interactions, the many-body physics problem offers a comprehensive description of atomic nuclei, as defined by the Hamiltonian:

$$H = T + \sum_{i<j}^{A} \nu_{\text{2body}}(i,j) + \sum_{i<j<k}^{A} \nu_{\text{3body}}(i,j,k) + \cdots, \tag{1.1}$$

where T is the kinetic energy term, A is the mass number of the atom (or nucleus), which is equal to the sum of the protons and neutrons in the atom's nucleus, and ν_{2body} and ν_{3body} are the two- and three-nucleon potentials. These potentials are typically extracted from fits that, in the case of the ν_{3body} potential, replicate the experimentally measured binding energies. Ab initio (from the beginning) methods have proven effective at calculating properties of many nuclei, up to ^{208}Pb [7]. The ab initio method begins by solving the many-body Schrodinger equation for all constituent nucleons (protons and neutrons) and resolving the forces acting between them (for example, two- and three-body forces) [8]. Typically, approximations are employed (especially for heavier nuclei) to solve such calculations, as exact solutions are hindered by the computational resources required. These calculations are simpler for closed-shell nuclei as further approximations can be made. Nuclear physicists are developing ab initio calculations to provide exact solutions for heavier nuclei, by reducing the computational load required for these calculations. For more reasons than those already mentioned, nuclear theory models are constantly in development.

The shell model, formulated in 1949 by M. Mayer and J. Jensen [9], was the first successful effective description of atomic nuclei. The shell model accurately predicts various low-energy properties of nuclei, such as spin, parity, ground-state energy, and more. The model uses the Pauli Exclusion Principle, to model the nucleus as a collection of independent nucleons moving under the influence of an attractive mean-field potential produced by all other nucleons. Hence, within the shell model framework, the neutrons and protons are assumed to have independently defined shell-model states. For the shell-model approximation, the Hamiltonian is modified for the protons and neutrons and can be written as:

$$\begin{aligned} H &= \underbrace{T + \sum_{i=1}^{A} V_{\text{mean-field}}(i)}_{H_{\text{Shell-Model}}} \\ &\quad + \underbrace{\left[\sum_{i<j}^{A} \nu_{\text{2body}}(i,j) + \sum_{i<j<k}^{A} \nu_{\text{3body}}(i,j,k) + \cdots\right] - \sum_{i=1}^{A} V_{\text{mean-field}}(i)}_{H_{\text{Residual}}}, \\ &= H_{\text{Shell-model}} + H_{\text{Residual}}, \end{aligned} \tag{1.2}$$

where $V_{\text{mean-field}}$ is the effective mean-field term. H_{Residual} is neglected when applying the mean-field approximation, which significantly simplifies the problem allowing, in some cases, analytical solutions.

The shell model has been highly successful in predicting the bulk properties of nuclei. However, Ref. [10], which investigated proton knockout measurements through electron scattering ($A(e, e'p)$), revealed that while the shell model accurately predicts the cross-sections for deeply bound protons, it underestimates the cross-sections for valence protons (those in the outermost shells). Specifically, valence proton cross-sections are observed to be approximately $60 - 70\%$ of those for bound protons. Given that the mean-field approximation is a single-body approximation, it is natural to believe the missing piece of the puzzle originates from higher-order configurations. In recent years, there has been a strong effort focused on short-range correlations (SRCs), see Refs. [11, 12, 13]. These correlations are short-range fluctuations occurring within the ground state of the nucleus between two nucleons, where the two nucleons have overlapping wavefunctions, i.e. the NN (nucleon-nucleon) interaction is energetic enough that the nucleons can access free states above the fermi level or in the continuum, bypassing the Pauli blocking that applies for typical NN interactions. Higher-order SRCs are postulated, but not yet observed. SRCs make up approximately 20% of the missing cross section and are difficult to model due to the complexity of the NN interactions, and they strongly suggest that around 20% of nucleons within the nucleus have overlapping wavefunctions.

1.3 Quantum Electrodynamics and Quantum Chromodynamics

Particle interactions occur when particles come within close proximity of one another. A gauge boson may be produced at the interaction point of the particles. The probability of the interaction occurring is proportional to the coupling constant, which represents the strength of the force involved. Quantum electrodynamics (QED) describes the interactions between light and non-zero electrically charged matter via the exchange of photons. Given it is a quantum theory, it accurately determines the probability that a particle (including massless particles such as photons) will be at a given position and the quantity that influences the position of the particle (the field). To explain this more clearly, the idea of quantum mechanics in a simple explanation is that if we put an electron inside a box at some position, and close the box. If we open the box after a time, t, quantum mechanics provides a probability that the electron will be at any given position inside this box. The coupling constant for QED interactions is proportional to $\sqrt{\alpha}$, where $\alpha = \frac{e^2}{4\pi} = 1/137^*$ is the fine-structure constant. It should be noted that the coupling

*We denote that natural units are used here (where $\hbar$, c and ϵ_0 are set to 1) and throughout this thesis unless stated otherwise.

constants are not constant; the QED coupling constant becomes slightly larger (1/128) at energies of $\sqrt{s} > 100$ GeV/c^2, where $\sqrt{s}$ is the total energy available in a particle interaction. The blue line in Fig. 1.5 depicts the QED potential energy ($V(r) = \frac{-\alpha}{r}$), which converges towards zero for largely separated particles, while drastically increasing in magnitude for closely spaced particles. The potential can be attractive (negative) or repulsive (positive) depending on whether the particles involved in the interaction are unlike- or like-charged particles.

Quantum chromodynamics (QCD) describes the strong nuclear force experienced during interactions between quarks, which is mediated by gluons. Analogous to QED, QCD has a colour charge, where there are three colours (red, green and blue) and three anti-colours. Every quark possesses a colour charge and the gluons carry a colour-anticolour pairing (e.g. red and anti-green). A significant piece of evidence for the existence of colour charge came in the 1960s, when the Δ^{++} baryon was discovered. It is a baryon composed of three up quarks. Particles can have either integer or half-integer spin, and since we know fermions have half-integer spin, one of the up quarks would have spin z-projection +1/2, while another would have -1/2. The third up quark would be forbidden by the Pauli-exclusion principle (as it would have the same spin as one of the other up quarks) if not for the existence of colour charge to differentiate states. Similarly to QED, the strength of strong interactions is proportional to $\sqrt{\alpha_s}$, where $\alpha_s = \frac{g_s^2}{4\pi} \sim 1$ is the

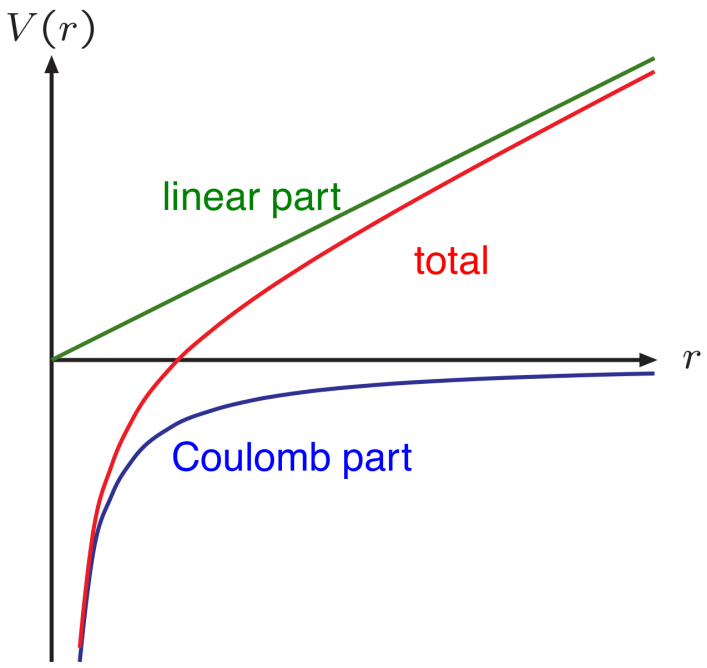

Figure 1.5: Graphical representation of the QED (blue line) and QCD (red line) potential energy, $V(r)$, as a function of the separation between the particles, r, where the two regions (Coulomb and linear part) represent the two contributions to the QCD potential. Note that the QED potential can be positive for like-charged particles. The plot is taken from Ref. [14].

strong (QCD) coupling constant. For intermediate reaction energies ($\sqrt{s} \sim 1$ GeV/c^2), the QCD coupling constant is $\alpha_s \sim 1$, whereas for the higher energy of $\sqrt{s} \sim 100$ GeV/c^2, the QCD coupling constant is $\alpha_s \sim 0.12$. α_s continually becomes weaker for higher energies, similar to the QED coupling constant. The red line in Fig. 1.5 depicts the QCD potential energy, which has a Coulomb-like potential for short distances ($V(r) = -C\frac{\alpha_s}{r}$) and an additional linear term for long distances ($V_s(r) = -C\frac{\alpha_s}{r} + kr$). The constant C has different values depending on the nature of the reaction, for example, $C = 4/3$ for quark-antiquark interactions in a colourless (net zero colour charge) mesonic state.

QED can be solved theoretically, given the small coupling constant ($<< 1$). It is solved through perturbation theory ($A = A_0 + \epsilon A_1 + \epsilon^2 A_2 + \epsilon^3 A_3 + \cdots$) as the higher order terms (known as loop corrections), which are interactions involving the exchange of more than one gauge boson, can be ignored and the solution boils down to $A = A_0 + \epsilon A_1 + \epsilon^2 A_2$ as $\epsilon \to 0$ (here ϵ depicts the coupling constant). However, many-body physics reactions are influenced by QCD, which poses a significant theoretical challenge, as QCD cannot be solved through perturbation theory (other than in specific extremely high energy cases) given the QCD coupling constant is larger than 1. In the past few decades, lattice QCD has proven to be a powerful theoretical technique to solve QCD problems, but some limitations need to be overcome. No review of lattice QCD will be provided here, but see Ref. [15] for details of confinement studies in lattice QCD. A few notable observations of QCD have been made in recent decades, which include colour confinement (well described by lattice QCD) and asymptotic freedom. Particles which carry a non-zero colour charge, e.g. quarks, cannot be isolated in nature. As the quarks are continually separated to larger distances, their potential energy increases linearly (as seen in Fig. 1.5). Typically, the energy grows such that a quark-antiquark pair is produced, transforming the initial single hadron state into a pair of hadrons. This is known as colour confinement. Quarks interacting at very short separation distances almost behave like free particles and interact weakly with one another, whereas at long distances the quarks are confined and do not behave like free particles. In these rare, short-distance instances, QCD can become solvable through perturbation theory. This is referred to as the asymptotic freedom of QCD. It is important to note that in the work presented here, we focus solely on intermediate energies of orders of magnitude around $\sqrt{s} \sim 1$ GeV/c^2, where QCD is not analytically solvable with the current techniques available.

1.4 Motivation

Our discussion here outlines the complexity of many-body physics problems and the necessity of experimental facilities to probe the nucleus. Understanding the fundamental reactions experienced by particles in dense nuclear mediums is crucial to understanding the nature of nuclei. Circling back to Eq. (1.1), determining well-defined potentials for all possible forces (e.g. two- and three-nucleon forces) would allow us to solve the many-body

Hamiltonian. In solving this Hamiltonian, all properties of every atomic state would be determined, which would provide an insight into the formation of the universe (atoms, planets, stars and galaxies). These potentials, along with cross sections (probabilities) for many-body reactions are complicated observables to determine. Particle accelerators, which provide an experimental avenue for circumventing complicated theoretical calculations (which are still necessary for a full understanding), play a big role in determining these observables. Photons and electrons are excellent probes for stationary nuclear target experiments, and with the assistance of state-of-the-art theoretical models, they can provide insight into the fundamental reactions at play which drive the many-body knockout reactions observed.

1.5 Outline

In this thesis, results from two major analyses are presented. The first focuses on the use of photon beams as a spallation source to measure many-proton knockout reactions, with proton multiplicities one through to six. The introductory material for this analysis is presented in Sec. 2.1. The analysis focuses on providing a comparison with the state-of-the-art model, GiBUU, presented in Sec. 3.1. The experimental facility, where both data sets were collected, is presented in Chap. 4, and specific details on the experiment conducted for the many-proton knockout analysis are described in Subsec. 4.5.7. The full analysis for the many-proton knockout is presented in Chap. 8. The results focus on discussing the accuracy of the GiBUU model, with a first look at using photon beams as a spallation source to access exotic neutron-rich nuclei. A full analysis note has been written for this work, which has undergone full approval from a three-person review committee.

The second analysis looks to benchmark the accuracy of electron scattering interactions of two state-of-the-art theory models, GiBUU and GENIE. The background material for this analysis is presented in Secs. 2.2 to 2.4, with a brief review of GENIE given in Sec. 3.2. Experimental details for the data used for this analysis are presented in Subsec. 4.6.8. The full analysis for benchmarking the two theoretical models for many different electron scattering reactions is presented in Chap. 9. The analysis presented has undergone approval from members of the collaboration, with an analysis note being prepared for full review.

Chapter 5 presents the simulation details for the analyses. Since both analyses aim to benchmark the performance of theoretical models, the geometry of the experiment must be implemented into the simulated data (see Chap. 5 for full details). Chapter 6 provides an overview for selecting 'good quality' particles in the two analyses, where a 'good quality' particle refers to measured particles that have successfully passed our event reconstruction requirements. An overview for analysing the residual system after a particle interaction is presented in Chap. 7. The final summary, presented in Chap. 10, brings the conclusions

of the two analyses together and discusses their implications for next-generation neutrino facilities, with a brief outlook on future work.

The author notes that throughout this thesis, unless explicitly stated otherwise (e.g., in certain equations like the wavelength of a particle or wave, as presented in Sec. 2.1), natural units are used where $c = \hbar = 1$. This simplification, for example, reduces the energy-momentum-mass relationship $E^2 = p^2c^2 + m^2c^4$ to $E^2 = p^2 + m^2$. All theoretical, experimental and simulation details are stated in natural units where possible, particularly in the analysis and conclusion sections, where all figures and results are expressed in natural units.

Chapter 2

Photon-, Electron- and Neutrino-Nuclei Interactions

> *"An alleged scientific discovery has no merit unless it can be explained to a barmaid."*
>
> - Ernest Rutherford

This chapter summarises the basic physics of how photons, electrons and neutrinos interact with nuclear targets. Firstly, an overview of photonuclear reactions is presented with a brief discussion of the fundamental reactions, with a focus on those which contribute to reactions where one, or more protons are ejected from the target nucleus (the central topic of the analysis of photo-reactions using the CLAS detector in this thesis).

Subsequently, the fundamental reactions involved in electronuclear interactions are provided. For the current thesis, analysis of electronuclear scattering data with CLAS12 involves the detection of a range of mesonic and nucleonic final states and assessment of the quality of the beam energy reconstruction from the final state particles alone. The fundamental interactions producing such particles in electronuclear reactions are discussed. The similarities between electron and neutrino interactions, along with their differences, are also outlined.

Both the CLAS and CLAS12 analyses aim to improve our understanding of many-body physics and subsequently the description of neutrino interactions and detection. An introduction to neutrino oscillations, particularly the limitations in determining neutrino oscillation parameters due to current uncertainties in the many-body nuclear processes, is provided. The underlying methodology as to how electronuclear data can be used to benchmark neutrino-nucleus processes is described.

2.1 Photonuclear Interactions

An important result in the last century was the discovery of the photoelectric effect by A. Einstein in 1905 [16], who postulated that light consisted of packets of energy called photons, with each behaving like a particle with discrete energy and momentum. This idea was expanded upon by L. de Broglie, who in 1924 postulated the wave-particle duality [17], that is to say, all matter in the universe has wave-like properties. The wavelength of a particle, or wave, is given by $\lambda = \frac{hc}{E}$.

Subsequent technological advances enabled intense beams of high-energy photons or electrons in the MeV and GeV ranges, where the dominant interaction processes are with the nuclear, nucleonic or quark degrees of freedom in the nucleus. An overview of the interaction processes for photon and electron beams with nuclei is outlined in the following sections.

The photon is well suited for studying nuclear structure, as its relatively weak electromagnetic interaction with the bound nucleons allows for a deeper penetration through the volume of the nucleus. This is a direct advantage over strongly interacting probes such as protons or pions, for which surface absorption is dominant and the incident probe suffers from initial state interactions, which complicate the interpretation of the data. The electromagnetic nature of the photon means it sees the nucleus as a collection of charges, currents and magnetisation densities that it can couple to. In the following sections, the main reaction processes are discussed, starting with the isolated nucleon and then outlining the additional processes, which can occur in heavier nuclei.

- **Reaction mechanisms for a single nucleon**

  The simplest reaction to understand the interactions of photons with nucleonic matter is with the hydrogen nucleus, i.e. a free proton. The world data for the total photon-proton cross-section as a function of photon energy, as well as a breakdown into the different reaction channels (up to meson multiplicity two), is presented in Fig. 2.1. The total cross section from $0.2 - 3.0$ GeV is of the order of 200 μb. The photon cross-section shows structures which are energy-dependent. These are associated with excited resonant states of the proton. The large peak forming around incident photon energies of 300 MeV, visible in Fig. 2.1, is due to the $P_{33}(1232)(\Delta)$ nucleon resonance, which occurs when the wavelength of the photon is comparable with the size of a nucleon. A particle resonance occurs when sufficient energy from a probing particle (e.g. photon) is provided to a nucleon (e.g. proton), which excites the particle to a higher energy state. The Δ resonance is the lowest-lying excited state of the proton and corresponds to a spin flip of one of the quarks in the proton. Resonances have characteristic widths that are directly related to their lifetimes as $\Gamma = \frac{\hbar}{\tau}$, where Γ is the decay width and τ is the mean lifetime of the resonant state. The bump structures above the Δ up to around 1.7 GeV reflect the

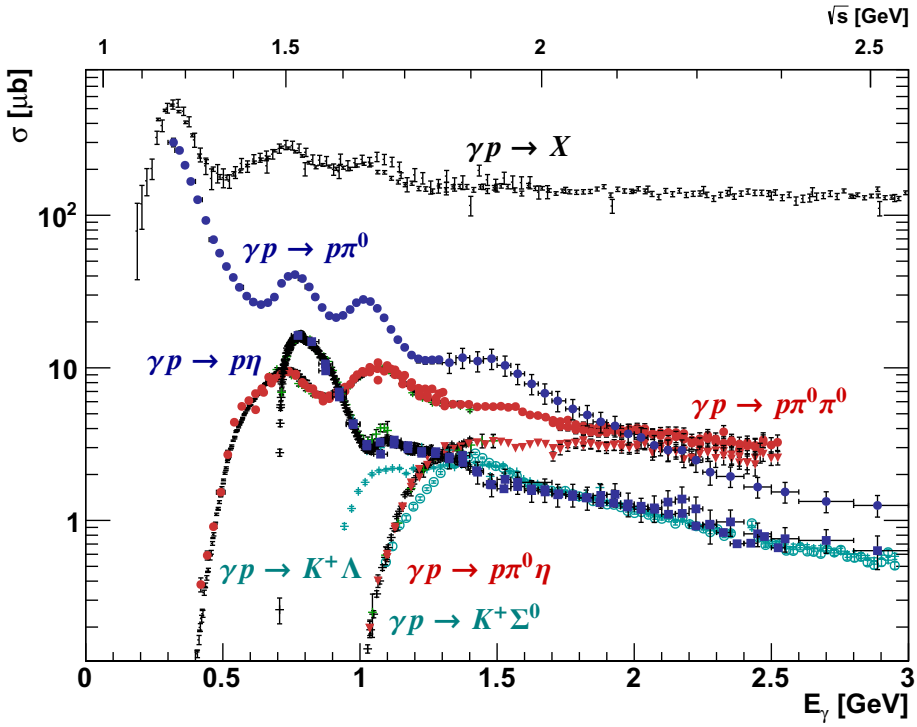

Figure 2.1: The fully integrated exclusive meson photoproduction cross sections in the resonance region as a function of the incident photon energy, taken from Ref. [18].

contribution from combinations of higher mass excited proton states (N^* and higher Δ states). At higher energies, the high density of excited nucleon states means their contributions are not resolvable in a cross-section alone.

The total cross-section, broken down into different particles detected in the final state, is shown by the coloured data points in the figure. At any given photon energy the total photoabsorption cross section represents the coherent sum of all possible final states. The nucleon resonances excited in the absorption process will decay to different reaction products (note also that such final states have background contributions from non-resonant reaction processes which interfere with the resonance mechanisms). Typical resonance lifetimes are of the order of 10^{-24} s producing typical widths of 100's of MeV. The decays are mainly via the strong interaction (e.g. with the emission of single or multiple mesons). Up to 2 GeV, the dominant reaction is the production of a π meson. Above 2 GeV the photoproduction mechanisms and resonances involved lead to the strength of two-pion final states being comparable to the single-pion component. Three-pion final states are less well-studied but are comparable to the two-pion strength at about 2.5 GeV [19].

As well as comparisons of photonuclear cross sections with theory, polarisation observables for specific final states (e.g. single-pion photoproduction) are crucial to disentangle specific reaction mechanisms and to extract contributions to the nucleon resonance spectrum via Partial Wave Analysis (PWA) [20]. Single polarisation ob-

servables from polarised targets, photon beams or recoil nucleon polarisation, and combinations thereof, are necessary to provide sufficient PWA constraints and deconvolute the spectrum. Recent studies in the last two decades, particularly at the Thomas Jefferson National Laboratory (JLab), have investigated higher-order resonances and aimed to elucidate the excitation spectrum of the nucleon in detail [21]. This is illustrated in Fig. 2.1 which shows our current knowledge of the excitation spectrum of the nucleon. The density of excited states greatly increases with photon energy.

For photon interactions with nuclei heavier than a single proton, there are additional degrees of freedom, which enable more reaction mechanisms and final states. In Fig. 2.2 the total photoabsorption cross section from the nucleon is compared to the total photoabsorption cross sections measured in a range of heavier nuclei. Although some general features from the nucleon cross section are evident in heavier targets, indicating reactions on the moving nucleons in the nucleus are an important contribution, there are important additional mechanisms. Below we discuss the typical processes occurring in photonuclear reactions with heavier nuclei.

- **Dipole Resonance**

  There is a broad structure typically centred around photon energies of 30 MeV, in

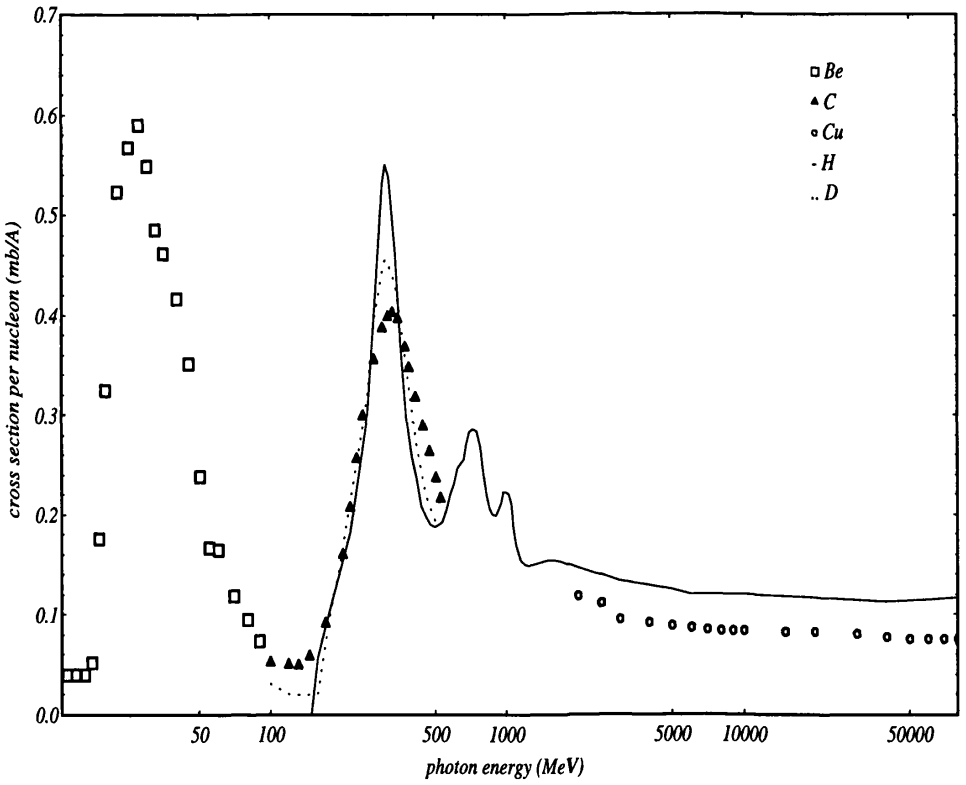

Figure 2.2: Total cross section for photoabsorption reactions, for various nuclear targets, taken from Ref. [22].

the 10s of MeV range, which corresponds to a photon with a wavelength of the order of a nuclear radius. This is visible in Fig. 2.2. At these energies, the photon couples to the whole nucleus, as it is viewed as an electric dipole by the photon, produced by the relative motion of the nucleons. During this process, the nucleus absorbs the energy of the photon and forms an excited state. These excited states decay with the emission of nucleons, where in-medium and heavy-nuclei neutrons are typically emitted, as they do not need to overcome the Coulomb barrier to escape the nucleus since they are uncharged. The photon energies used in the current analysis are higher than this region, therefore such processes will not contribute to the current data.

- **Resonance Production through interaction with nucleons**

  The processes discussed for the proton above also play a key role in interactions with heavier nuclei. Photons with appropriate energies can interact with single nucleons in the nucleus and produce reaction products, such as those described in Fig. 2.1. When these resonances are produced in nuclei, effects such as Fermi motion, nuclear binding, and Pauli blocking can affect the widths and masses of these resonances within the medium. Resonances in a nuclear medium are generally broader due to increased interactions with surrounding nucleons. In a free proton target, a resonance is less likely to interact with other particles, similar to how a person in an empty store is less likely to bump into others. In a nuclear medium, however, the resonance frequently interacts with the surrounding nucleons, analogous to a person navigating a crowded store, which causes the resonance to decay more quickly and thus broadens its width ($\Gamma = \hbar/\tau$). It has been shown that the Δ resonance exhibits an almost linear increase in mass and width with the size of the nucleus [23]. Although the Δ resonance is clearly seen in photonuclear cross sections, the higher-order resonances, such as N^* and Δ^* that are visible in Fig. 2.2, are washed out in heavier nuclei given the in-medium effects at play, which typically broaden the resonance and can shift its in-medium mass.

  An important difference when such reactions occur on nucleons in the nucleus is that the final-state particles must travel through the nuclear medium. Final-state nucleons, such as pions and other mesons, have a high probability of interacting through subsequent absorption or scattering reactions (e.g., $(\pi, \pi' N)$, $(\pi, 2N)$, $(\pi, 3N)$, (N, NN')). The initial production of pions in the nucleus, via the Δ (or higher-mass resonances, or from non-resonant background processes), is, therefore, a key seed reaction for subsequent nucleon knockout processes. Such high-multiplicity proton knockout processes can arise from initial single-, double-, or triple-meson (M) photoproduction on a nucleon with subsequent in-medium reabsorption (e.g., via $(M, 2N)$, $(M, 3N)$). Final-state interactions of produced nucleons can also knock out additional nucleons from the nucleus.

- **Direct nucleon Knockout Mechanisms**

  As well as nucleon knockout seeded by initial (on-shell) pion production from nucleons in the nucleus, the absorption of a photon in the nuclear medium can proceed by mechanisms involving more than one nucleon, which can lead to the direct knockout of nucleons. Figure 2.3 presents a selection of reaction mechanisms involving (off-shell) pion and nucleon resonance currents. The seagull term (a) refers to reactions where the nucleon (proton or neutron) absorbs the incoming photon beam and a virtual pion (mediating the strong nuclear force) is produced, which results in the emission of two nucleons. The pion-in-flight term (b) can arise through meson exchange currents (MECs), which are processes where nucleons interact with each other by exchanging a virtual pion. This occurs due to the strong interaction between nucleons, which can modify the nuclear dynamics observed. Lastly, the excitation term (c) occurs when a nucleon that has undergone a resonance process emits a virtual pion which is absorbed by another nucleon, which, like in the case of real pions, can induce additional nucleon knockouts or absorption of the pions for further resonances. The seagull term is suppressed at higher energies but is prevalent around photon energies of 80 MeV. Due to the rise of pion-in-flight terms, at photon energies around 140 MeV, the seagull term begins to deteriorate in strength. Typically, the photon is absorbed by $T = 0$ (pn) pairs, as the cross-section for $T = 1$ (pp, nn) pairs is an order of magnitude less due to the suppression of MECs.

  At the photon energies of the current work, the mechanisms of direct knockout are not well understood. At higher energies, as the inter-nucleon separation reduces, other short-range MECs may give increased contributions such as ρ- and ω-in-flight terms. As the photon energy increases beyond the Δ, higher-order resonances may contribute to the isobar-current mechanisms (Fig. 2.3 (c)). Observing direct knockout in these regions, and comparisons with theoretical models, has the potential to provide constraints on the interactions of the higher-order resonances in the nuclear medium.

  Despite this, the strength and role of direct 2N knockout from nuclei above approximately 0.6 GeV are not well constrained by experimental data. A key aim of the current work is to establish whether such processes can be identified and isolated at higher energies. As well as different (non-Δ) resonance mechanisms, the higher photon energies may be expected to produce an increased role for short-range correlations in the mechanisms. It is important to try and quantify such direct processes and compare them with theoretical predictions.

  As well as the direct 2N knockout processes, direct 3N knockout mechanisms (involving the exchange of two off-shell pions between three nucleons with or without additional resonance currents) are predicted. This channel is weaker than that of the 2N due to the lower probability of finding three nucleons within a tight enough

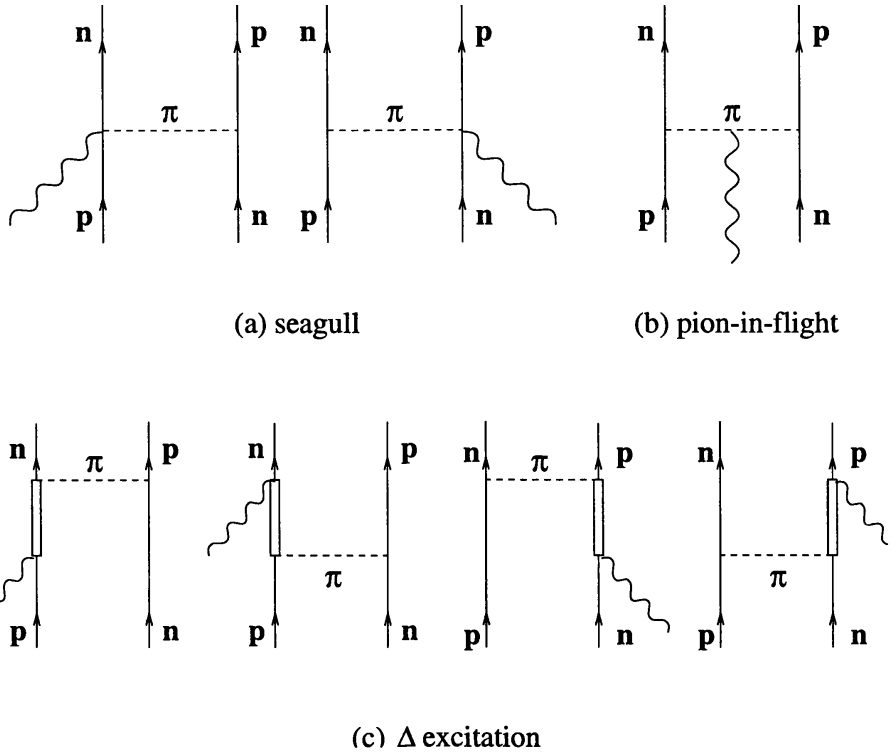

Figure 2.3: A selection of absorption terms for the (γ, pn) reaction, where a virtual pion is emitted from the reaction vertex of a nucleon and then absorbed by the second nucleon. The figure is taken from Ref. [22].

space in the nucleus to interact, but detailed studies may give constraints on the nature of three-body forces. Higher-order processes such as direct 4N knockout, if quantifiable, have the potential to constrain 4-body currents and forces.

- **Shadowing Region**

  Photons with energies above 2 GeV have a relatively flat and reduced cross-section, which can be seen in Fig. 2.1. This may reflect the flattening of the absorption cross section on the nucleon due to a large number of contributing resonances (Fig. 2.1), but also the hadronic components of the photon (where the photon fluctuates into a vector meson in the interaction process) are predicted to be significant in these regions and create a shadowing effect. Establishing exclusive reaction processes in this region and comparing them with theoretical models would give more information on the nature of the interactions in this region.

Results in this thesis present the first measurements of several photoinduced many-proton knockout channels for photon energies in the range $600-4500$ MeV. This new dataset will provide a challenge to our understanding of the contributing mechanisms and many-body medium effects.

2.2 Electronuclear Interactions

The electron was discovered in 1897 by J.J. Thomson [24]. Electrons are leptonic in nature and are fundamental, point-like particles with no internal structure. They are spin 1/2 particles that do not interact via the strong nuclear force. The electron interacts via the electromagnetic (EM) force by exchanging a single vector boson. The current for electromagnetic interactions is given by:

$$j_{\mu}^{\text{em}} = ig_e \bar{u} \gamma_{\mu} u, \tag{2.1}$$

where u and $\bar{u}$ are Dirac spinors, γ_{μ} are the Dirac matricies, $\mu = 0, 1, 2, 3$ are the four spacetime coordinates and $g_e = \sqrt{4\pi\alpha}$ is the electromagnetic coupling constant. The current, j_{μ}^{em}, describes the motion of charged particles (electrons) moving under the influence of an electromagnetic field and encapsulates the charge density and flow of charge associated with the aforementioned movement. The Dirac spinors are simply mathematical constructs that describe the quantum numbers of the electron, such as spin and angular momentum. The Dirac matrices are mathematical tools used to describe the behaviour of particles. Figure 2.4 presents the cross-section as a function of the energy transferred from the electron to the nucleus, ω, in electron scattering, with key mechanisms labelled appropriately, for a fixed four-momentum transfer $Q^2 = \bar{q}^2 - \omega^2$, where $\bar{q}^2$ is the three-momentum transferred.

The structures in electron scattering are analogous to those seen in photon absorption, although some structures correspond to different mechanisms. Below is a brief discussion of the fundamental mechanisms at play in electron-nuclei scattering interactions (as discussed earlier, these processes have a close analogy with neutrino-nucleus interactions, see

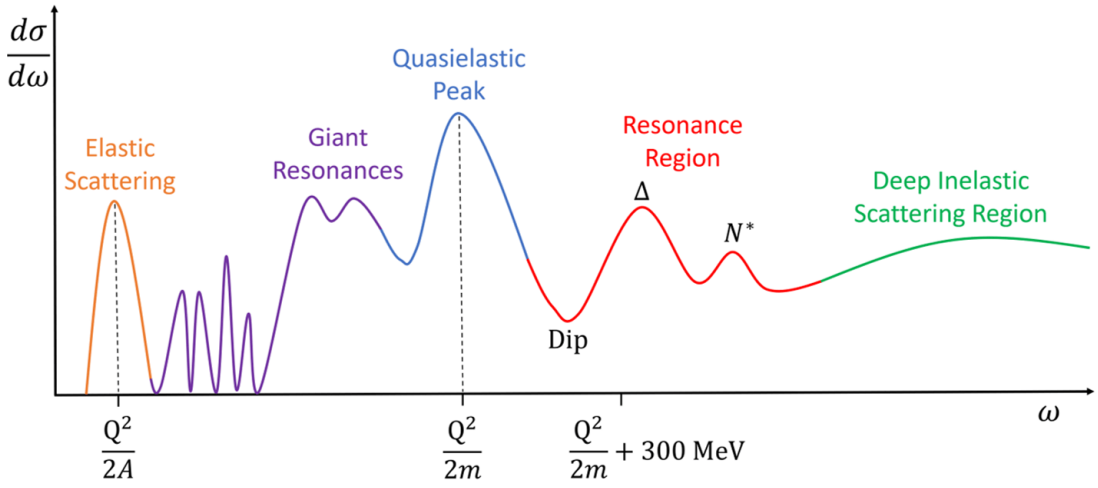

Figure 2.4: Schematic diagram showing the cross-section as a function of electron transfer energy, ω, highlighting the different fundamental regions of interest. The figure is adapted from Ref. [25]

Sec. 2.3).

- **Elastic Scattering**

  The orange peak refers to interactions where the electron and nucleus scatter from one another and do not change identities in the final state. It occurs when the size of the electron wavelength is comparable to the size of the nucleus at $\omega = Q^2/2A$. The electron probes the charge distribution of the nucleus and scatters electromagnetically. This process becomes highly suppressed at high electron energies for several reasons, including decreased wavelength size and an increase in cross-section for inelastic processes, to name a few.

- **Giant Resonances**

  Giant resonances (purple) are collective excitations of nucleons within the nuclear medium with sharp peaks at specific excitation energies. They arise due to the coherent motion of nucleons with the nucleus and require electrons with energies of a few hundred MeVs to several GeVs to probe. Note that, unlike the photon case where the energy and momentum of the photon are identical, in electron scattering processes, a given beam energy can produce a range of energy and momentum transfers in the virtual photon, meaning that resonances can be excited when the beam energy is above the excitation energy of the resonance.

- **Quasi-Elastic Peak**

  The large broader blue peak at $\omega = Q^2/2m$, where m is the mass of a nucleon, is quasielastic scattering, which occurs when the size of the electron wavelength is comparable to the inter-nucleon distance. The position of the peak is determined by the kinetic energy transferred to the nucleon, that was initially at rest, in the centre-of-mass frame. The width of the peak is influenced by the Fermi motion of the nucleus, therefore it increases with nuclear mass.

- **Interaction with single nucleons**

  At energy transfers of around $\omega = Q^2/2m + 300$ MeV, the electron scatters from a nucleon and, in the process, excites the struck nucleon to a Δ. This region is the resonance region (labelled red), which, at larger energy transfers than $\omega = Q^2/2m + 300$ MeV, produce higher-order resonances such as N^* and heavier Δ resonances. The peaks for these resonances are broader for bound nucleons, as discussed in the photon-nucleon case.

- **Direct multiple nucleon knockout mechanisms**

  At energy transfers (distance scales) between the quasielastic peak and resonance region, meson exchange currents (MECs) become more prevalent. For electron scattering, they are predicted to be highly suppressed in the DIS region [13]. As dis-

cussed in the photon-nucleus case, these mechanisms involve the exchange of virtual mesons (such as pions, rho mesons, etc.). At higher electron energies approaching the DIS region, MECs become less dominant as the probe becomes small and is not sensitive to long-range interactions [12]. Additional kinematic cuts, such as those applied to Bjorken x ($x_B = Q^2/2m_p\omega$), which represents the fraction of the momentum of the proton carried by the struck quark, can further suppress their contribution.

As discussed in the photon-nucleus case, excited nucleon resonance currents can contribute to direct knockout mechanisms. Recent work indicates that, with kinematic restrictions, their contributions can also be suppressed. An important distinction for electro- and photo-knockout reactions is that the virtual photon for electron scattering has a longitudinal component, which enhances direct coupling to the proton and is predicted to provide an enhanced role for SRCs in the mechanisms.

- **Deep Inelastic Scattering Region**

  At very high energy transfers, the deep inelastic scattering (DIS) process dominates, as the size of the electron wavelength is small enough to resolve the individual constituents of the nucleon, namely the quarks and gluons. The cross-section for this reaction scales with $1/Q^4$ at the leading order, hence, at high Q^2, the DIS cross-section rapidly decreases. Higher electron beam energies are preferentially selected for studying DIS reactions. DIS reactions are largely determined by the parton distribution functions (PDFs), which describe the momentum distribution of the quarks and gluons which compose the nucleon. DIS is particularly important for understanding SRC contributions within nuclei, as it has been shown that high Bjorken x refers to regions with high-momentum nucleons and SRCs.

2.3 Discussion of the Corollary Between Electron and Neutrino Scattering From Nuclei

A key part of the current CLAS12 analysis of electronuclear reactions is the constraining of the analogous neutrino scattering processes. In the following sections, we describe the coupling of electrons and neutrinos to nucleons and draw analogies between the two reaction processes.

2.3.1 Theoretical Description of Electron-Nucleon Interactions

The strength of the coupling of an electron (via virtual photon exchange) to a nucleon depends on the nucleonic form factors $F_1(Q^2)$ and $F_2(Q^2)$, referred to as the Dirac, or charge, and Pauli, or magnetic, form factors, respectively. In the context of DIS reactions, the modified structure functions $F_1(x_B, Q^2)$ and $F_2(x_B, Q^2)$ are denoted as they encode

the probability distributions of partons (quarks and gluons) and the distribution of charge and magnetic momenta in the nucleons. The inclusive electron scattering cross section can be written as:

$$\frac{d^2\sigma}{d\Omega dE'} = \left(\frac{d\sigma}{d\Omega}\right)_{\text{Mott}} \left[v_L F_1(x_B, Q^2) + v_T F_2(x_B, Q^2)\right], \tag{2.2}$$

where E is the incident electron energy, θ_e is the scattered electron angle, $v_L = 1/\nu^2$ and $v_T = \tan^2\left(\frac{\theta_e}{2}\right)$ are the longitudinal and transverse components of the electron four-vector and $\left(\frac{d\sigma}{d\Omega}\right)_{\text{Mott}}$ is the Mott cross-section, which describes the elastic scattering cross section of point-like particles ignoring the internal structure of the target nucleus, given by the following equation:

$$\left(\frac{d\sigma}{d\Omega}\right)_{\text{Mott}} = \left(\frac{\alpha^2 \cos^2\left(\frac{\theta_e}{2}\right)}{4E^2 \sin^4\left(\frac{\theta_e}{2}\right)}\right). \tag{2.3}$$

Reactions which include more particles in the final state and are more complex in nature, such as DIS, will consequently have more complicated cross-sections.

2.3.2 Neutrino-Nuclei Interactions

The neutrino was discovered in 1956 by F. Reines and C. Cowan [26], a few decades after the electron. Its discovery was challenging due to its light mass, neutral charge, and the fact that it interacts only via the weak nuclear force, which is about 10^6 times weaker than the electromagnetic force, the primary force driving electron scattering interactions. Neutrinos are also leptons and fundamental, point-like particles with no internal structure. The neutrino possesses similar attributes to the electron, e.g. spin 1/2. While the electron has a significantly larger mass than the neutrino, both particles interact by exchanging a single vector boson. The initial interaction vertices of electrons and neutrinos are different, but following this, the transport of particles through the nucleus should be common. Neutrinos interact via the weak nuclear force and the current for the charged-current (CC) weak interaction is split into its vector (similar to the electron) and axial components given by:

$$j^{\mu}_{\pm} = \bar{u}\frac{-ig_w}{2\sqrt{2}}(\gamma^{\mu} - \gamma^{\mu}\gamma^5)u, \tag{2.4}$$

where $g_W = 0.66$ is the weak coupling constant. The weak current, $j^{\mu}_{\pm}$, is analogous to the EM current, except it now describes the motion of particles moving under the influence of the weak nuclear force. Vector and axial currents are defined by their parity non-violating and violating interactions, respectively. When humans look in mirrors, their left hand appears as their right hand, so after a "mirror flip" human hands appear differently,

whereas a perfectly round ball appears the same. Therefore, parity typically refers to the symmetry of an object and is analogous to a "mirror flip". A system has even parity if it remains the same after a spatial inversion, just like a perfectly round ball under a "mirror flip", and has odd parity if it alters after a spatial inversion. Electrons do not change under spatial inversion ("mirror flip") and therefore have even parity, but neutrinos have odd parity as they violate parity conservation. For Dirac spinors, the parity operator is given by $\hat{P} = \gamma^0$, and the vector and axial components transform under the influence of the parity operator by:

$$\begin{aligned} \hat{P}(\bar{u}\gamma_\mu u) &= (\bar{u}\gamma_0)\gamma_\mu(\gamma_0 u), \\ \hat{P}(\bar{u}\gamma_\mu\gamma_5 u) &= (\bar{u}\gamma_0)\gamma_\mu\gamma_5(\gamma_0 u). \end{aligned} \tag{2.5}$$

The space and time coordinates transform under the parity operator for the vector current as:

$$\begin{aligned} \hat{P}(\bar{u}\gamma_0 u) &= (\bar{u}\gamma_0)\gamma_0(\gamma_0 u) = \bar{u}\gamma_0 u, \\ \hat{P}(\bar{u}\gamma_\mu u) &= (\bar{u}\gamma_0)\gamma_\mu(\gamma_0 u) = -\bar{u}\gamma_\mu u. \end{aligned} \tag{2.6}$$

For the axial current, the time and space coordinates transform as:

$$\begin{aligned} \hat{P}(\bar{u}\gamma_0\gamma_5 u) &= (\bar{u}\gamma_0)\gamma_0\gamma_5(\gamma_0 u) = -\bar{u}\gamma_0\gamma_5 u, \\ \hat{P}(\bar{u}\gamma_\mu\gamma_5 u) &= (\bar{u}\gamma_0)\gamma_\mu\gamma_5(\gamma_0 u) = \bar{u}\gamma_\mu\gamma_5 u, \end{aligned} \tag{2.7}$$

which means parity is violated in the weak interaction, i.e. predominantly neutrino interactions, as the signs flip for both the time and spatial coordinates (time is denoted by 0). Given that these two species interact identically with matter, electron scattering data can be used to test the nuclear physics and reaction mechanisms implemented in state-of-the-art theory models used in neutrino scattering facilities, by removing the axial response and running the models in electron scattering mode.

The neutrino physics community take a deep interest in the CC QE Weak interaction of neutrino-nucleon scattering inside the nucleus, which results in a charged lepton and nucleon in the final state. An analogous reaction in electron scattering is the quasielastic scattering of an electron-nucleon inside the nucleus, where the resulting final state consists of the scattered electron and the knocked-out nucleon. This reaction is advantageous for studying, as the nucleon scatters elastically and remains unexcited. Feynman diagrams showing the CC QE Weak interaction of neutrino-nucleon scattering (left) and

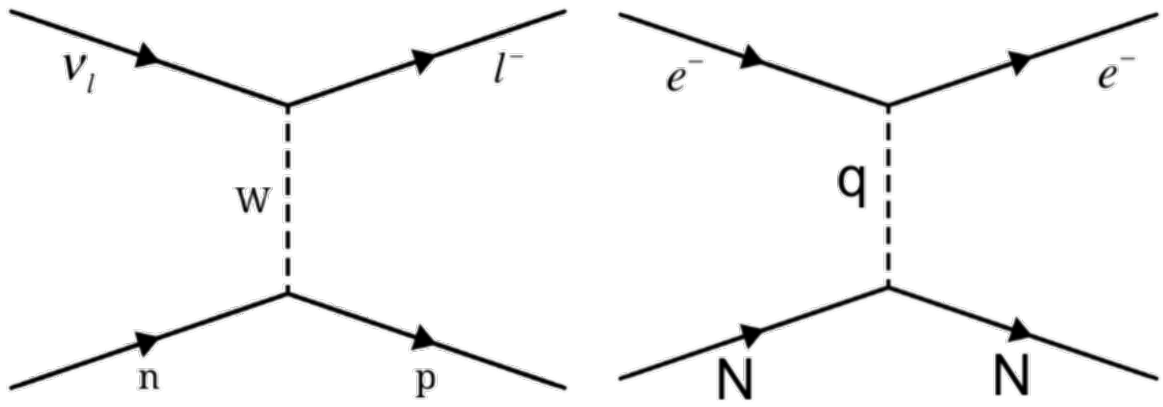

Figure 2.5: Feynman diagrams for the CC QE Weak interaction of neutrino-nucleon scattering (left) and the quasielastic scattering of an electron-nucleon (right) inside the nucleus.

the quasielastic scattering of an electron-nucleon (right) inside the nucleus are presented in Fig. 2.5.

Other reactions are fundamental for constraining neutrino- and electron-nucleus interactions. Direct 2N and 3N processes, including higher-order multiplicities, are driven by pion production and nucleon-nucleon scattering, among other processes. These mechanisms describe the nuclear physics influencing neutrino scattering reactions. Kaon channels are also important for neutrino physics, as they play a crucial role in understanding the Charge-Parity (CP) violation in particle interactions.

For both neutrinos and electrons the propagator behaves like $\frac{1}{Q^2+M^2}$, where M is the mass of the exchanged boson. Therefore, for neutrino scattering, the propagator has a $1/M^2$ dependence, since the masses of the bosons are usually much greater than the four-momentum transfer. This implies that in neutrino scattering the cross section goes as $1/M^4$ and in electron scattering it goes as $1/Q^4$, since the photon is massless. Therefore, scaling electron scattering data by $1/Q^4$ makes electron scattering cross sections more similar to neutrino scattering cross sections.

2.4 Neutrino Oscillations

Neutrinos appear in three flavour eigenstates: electron, muon or tau. These flavour states, ν_α, where $\alpha = e, \mu, \tau$, have poorly defined masses and appear as superpositions of mass eigenstates (m_1, m_2, m_3). Typically, their interaction with matter is described by the flavour states and their propagation through space is described using the mass eigenstates. Neutrinos do not have a fixed mass like electrons, or rocks. To explain this, we can think of the three generations (flavours) of neutrinos as three variations of lemonade, each with a distinguishable taste. The mass eigenstates can be thought of as the ingredients for each flavour, with m_1, m_2, and m_3 corresponding to sugar, water and

lemon juice. Differing amounts of these ingredients will produce a specific taste, very much like for neutrinos. These flavour states are related through the "Pontecorvo-Maki-Nakagawa-Sakata" (PMNS) mixing matrix by $\nu_\alpha = \sum_{m_i} U_{\alpha m_i} \nu_{m_i}$. The PMNS matrix depends on the neutrino mixing angles, $\theta_{12}, \theta_{13}, \theta_{23}$, which determine how much the mass and flavour eigenstates mix, and the δ_{CP} phase is the source of leptonic-CP violation, if found to be non-zero. We can think of the PMNS matrix as a set of instructions, or recipe, to tell us how much sugar, water and lemon juice we require for a specific neutrino flavour.

If we consider the simpler case of two neutrino flavours, then the probability that neutrino flavour ν_μ oscillates to flavour ν_e is given by:

$$P_{\nu_\mu \to \nu_e}(E, L) \approx \sin^2(2\theta) \sin^2 \left(\frac{\Delta m^2 L}{4E} \right), \tag{2.8}$$

where $\Delta m^2 = m^2_{\nu_1} - m^2_{\nu_2}$ is the square of the neutrino mass difference that determines the oscillation wavelength as a function of the distance travelled by the neutrino, L, and its initial energy, E, and θ is the neutrino mixing angle which defines the oscillation amplitude. Neutrino oscillation experimental facilities mainly produce ν_μ or $\bar{\nu}_\mu$ by bombarding heavy nuclei, such as graphite, with high-energy protons. The interactions of the protons with the nuclear targets produce secondary particles such as π^+ and π^- which decay via weak interactions to produce muons and muon neutrinos, or their antiparticles. Some ν_μ will oscillate and change flavour to ν_e at a distance L from the origin of the neutrinos. This oscillation results in neutrino fluxes of approximately:

$$\Phi_e(E, L) \propto P_{\mu_\nu \to \mu_e}(E, L) \Phi_\mu(E, 0), \tag{2.9}$$

where the constant of proportionality depends on the geometry of the experimental setup. The electron neutrino flux, $\Phi_e(E, L)$, represents the number of electron neutrinos passing a given area per second at the far detector (at a length L from the near detector) and the muon neutrino flux, $\Phi_\mu(E, 0)$, corresponds to the number of muon neutrinos passing a given area per second at the near detector.

Therefore, $\nu_\mu \to \nu_e$ oscillations are observed by measuring the fluxes of the electron and muon neutrinos as a function of the distance or energy. Solving the three-oscillation equations is similar to the two-flavour case, but includes additional terms. Experimentally, the interaction rate is given by the following equation:

$$\underbrace{N_\alpha(E_{\text{Rec}}, L)}_{\text{Measure Particles (1)}} \propto \sum_i \int \underbrace{\sigma_i(E) f_{\sigma_i}(E, E_{\text{Rec}})}_{\text{Apply Theory Model (2)}} \times \underbrace{\Phi_\alpha(E, L)}_{\text{Infer Flux (3)}} \, dE, \tag{2.10}$$

where E_{Rec} is the reconstructed neutrino energy from all the detected particles, $\alpha = e, \mu, \tau$ is the three neutrino flavours, σ_i is the cross section (probability) for the process i (for example direct 2p knockout) and $f_{\sigma_i}(E, E_{\text{Rec}})$ is a smearing matrix, or migration matrix, which is a mathematical construct that connects the real energy E and the reconstructed energy E_{Rec}, and the labels (with their numbers) in Eq. (2.10) refer to different parts of Fig. 2.6. Figure 2.6 presents a schematic diagram for determining the initial neutrino flux in neutrino oscillation experiments. The particles are measured, $N_\alpha(E_{\text{Rec}}, L)$ (this refers to part (1) of Eq. (2.10)), the interaction (theory) model is applied, $\sigma_i(E) f_{\sigma_i}(E, E_{\text{Rec}})$ (this refers to part (2) of Eq. (2.10)), and then the flux is inferred, $\Phi_\alpha(E, L)$ (this refers to part (3) of Eq. (2.10)).

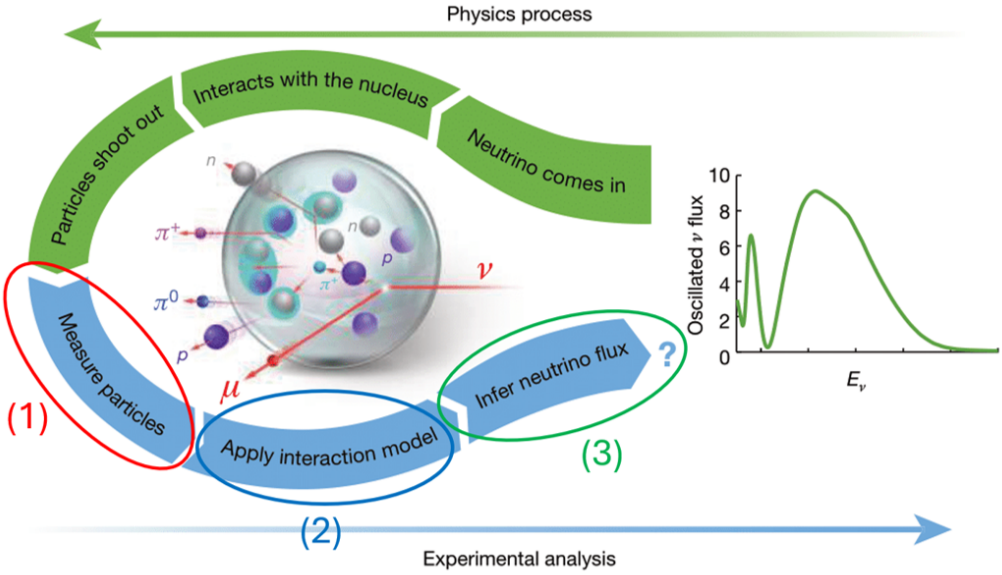

Figure 2.6: Schematic diagram presenting the methodology for extracting the initial neutrino flux in neutrino oscillation experiments, taken from Ref. [27].

The reconstructed energy differs from the true beam energy, due to experimental effects such as resolution, background, inefficiency and the role of nuclear processes other than direct single nucleon knockout without significant final state interactions. Experimental effects are generally well understood, but nuclear effects are ever-present and require theory models to deconvolute their contributions. Therefore, the accuracy of the determination of the initial neutrino flux heavily depends on the modelling of the nuclear physics by the theory model used [28], which is illustrated by Fig. 2.7.

Using migration matrices, the theoretical models allow us to connect the reconstructed energy to the true energy, in which different models have different migration matrices. Figure 2.7 presents the difference in using the two leading models of nuclear reaction processes, GENIE and GiBUU to extract the oscillation parameters (for more details of these models see Secs. 3.1 and 3.2). In this figure, the data was generated using GiBUU in both cases, but the different generators were used to extract the oscillation parameters.

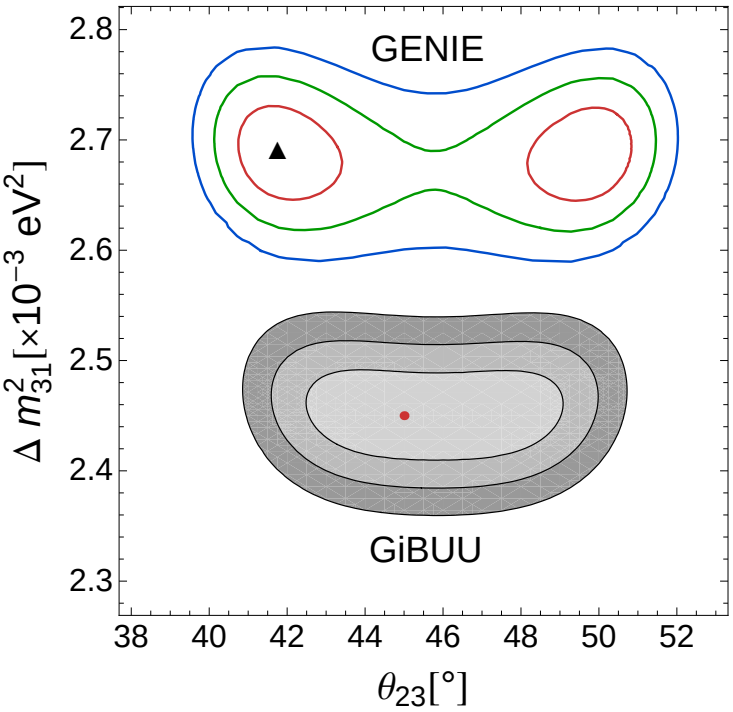

Figure 2.7: Impact on extracted neutrino oscillation parameters if the neutrino event generator does not describe the underlying physics accurately. The grey regions show the 1, 2 and 3σ confidence regions for the case when the data was generated and analyzed with the same event generator GIBUU, and red, green and blue lines show the same confidence regions for the case when oscillation parameters were obtained by generating data with GIBUU and analyzing with the GENIE event generator. The red dot indicates the true input value while the the black triangle shows the location of the best-fit point. The figure is taken from Ref. [28].

The results of the oscillation parameters show a clear reliance on the model used, and it is not clear which generator is more accurate. Additionally, the poor modelling of the fundamental nuclear physics at play leads to large systematic uncertainties when extracting oscillation parameters, reported in many oscillation experiments [29, 30, 31, 32]. A poor reconstruction of the initial energy leads to large biases in extracting δ_{CP} at the Deep Underground Neutrino Experiment (DUNE) [33].

The biggest challenge of neutrino oscillation experiments is that there are no mono-energetic high-energy neutrino beams. Therefore, the models used to extract the fluxes cannot be tested for individual neutrino beam energies. Neutrino oscillation experiments tune models of σ_i and $f_{\sigma_i}(E, E_{\mathrm{Rec}})$ to reproduce the initial unoscillated flux, $\Phi(E, 0)$, found at the near-detector, from hadronic reaction rates; see Refs. [34] and [35]. These constraints are insufficient to verify that the theoretical models are precise for each value of E. Therefore, when dealing with precision measurements from broad-energy neutrino beams, how well the near-detector data can constrain the models is unclear, given that

far-detector fluxes can be vastly different due to neutrino oscillations.

Many electron beam facilities can precisely tune the electron energy; hence, electron scattering facilities such as JLab can test the theory models used in neutrino oscillations by reconstructing the initial electron beam energy using an identical method to that used in such experiments. The energy is reconstructed using a calorimetric method, which sums the energy of the detected particles. The following equation describes the reconstructed energy:

$$E_{\text{Rec}} = E_{e'} + \sum_i \epsilon_i + \sum_i T_i + \sum_j E_j, \tag{2.11}$$

where $E_{e'}$ is the energy of the scattered electron, $\sum_i \epsilon_i$ is the average separation energy per nucleon (≈ 20 MeV), $\sum_i T_i$ is the sum of the kinetic energies of each detected nucleon and $\sum_j E_j$ is the sum of the energies of each detected meson. Electron beam facilities can therefore test the models used in neutrino oscillation experiments and their ability to reconstruct the initial electron beam energy with the same method used at neutrino facilities. Advantageously, with a mono-energetic beam the fundamental nuclear physics at play can be constrained to improve the accuracy of the models, thereby reducing the systematic uncertainties of extracting neutrino oscillation parameters.

Chapter 3

The GiBUU and GENIE Theoretical Models for Photo- and Electro-Nuclear Reactions

> *"The supreme task of the physicist is to arrive at those universal elementary laws from which the cosmos can be built up by pure deduction. There is no logical path to these laws; only intuition, resting on sympathetic understanding of experience, can reach them."*
>
> - Albert Einstein

The development of theoretical models is crucial for our understanding of the fundamental nuclear physics responsible for the reactions we observe. Here, we review two state-of-the-art theoretical models, crucial for future neutrino oscillation facilities. Afterwards, a summary of previous results of two- and three-nucleon photonuclear knockout reactions is presented. A brief review of recent results for electron scattering reactions from JLab, with comparisons to a state-of-the-art theoretical model GENIE, is provided.

3.1 GiBUU

The GiBUU (Giessen Boltzmann-Uehling-Uhlenbeck) model [36] provides for us a unified theory and transport framework within the MeV/GeV energy domain. The model applies to many types of beam particles on nuclei, including real photon beams (the code also models electron, neutrino, pion and heavy ion reactions). The code provides a full dynamical description of the initial interactions, as well as a treatment of the interactions of the interacting particles with the residual nuclear system. For all types of interactions within this model, the flow of particles is modelled within a BUU (Boltzmann-Uehling-Uhlenbeck) framework [37], and it is essentially a semi-classical statistical model. For

details on the theoretical aspects and the physics input of the model, in addition to many practical details, see the review paper [37].

The relevant degrees of freedom in the simulation are particles, specifically baryons, mesons, leptons, their respective anti-particles and the gauge bosons. For the non-exotic hadrons (built up of up and down quarks), the πN scattering phase shift by Manley and Saleski is utilised as an input for the parameters, and parameters documented by the particle data group are used for the exotic hadrons. In total, there are 61 resonant states with 31 composed of up and down quarks and 30 non-zero strangeness and/or charm content resonances. Additionally, there are 21 mesonic states in the model, where both resonant and mesonic particles whose lifetimes are considered long (e.g. π meson) are treated as stable particles. The leptons and gauge bosons are not propagated in the model; they are assumed to decouple given the small coupling strength to the hadrons after production (e.g. $\pi^0 \to \gamma\gamma$) or after the first reaction vertex (e.g in $eA \to eX$). Pre-hadrons or strings carry information related to gluonic excitations, but the gluons themselves are also not propagated.

The GiBUU model allows baryon resonances to decay to two-body final states only and follows the analysis by Manley to model the vacuum decay widths of the resonance poles. In the context of mesonic resonances, there are a number of different two-body decay channels and a limited number of distinct three-body channels. There are several different two- and three-body reaction mechanisms implemented in GiBUU, but higher correlations are neglected, as it is assumed the nuclear density remains at appropriate values and does not reach values too high for the assumption to break down during the reactions.

The simulation implements baryon-meson, baryon-baryon and meson-meson scattering into the two-body processes. For baryon-meson processes, the implemented resonance model by [38], which implements resonance production cross sections for $ab \to R$, is reliable from pion-threshold to energies of 2.3 GeV. The background processes implemented for single vertex reactions are point-like, whereas two vertex reactions are separated in spacetime. Many non-resonant backgrounds are added to the baryon-meson processes to improve comparisons with experimental data. The matrix elements for baryon-baryon cross sections have been fitted for several particles such as π and ρ and, up to CM-energy of 2.6 GeV, for strangeness production. Processes such as $NN \leftrightarrow NN$ and $NN \leftrightarrow NR$ are implemented and the background contribution is the point-like $NN \to NN\pi$ process. Meson-meson scattering is implemented and resonance production channels (e.g. $\pi\pi \to \rho$) are implemented along with non-resonant background channels (e.g. $\pi\pi \to X$). Details of this are described in detail by the works of Larionov and Wagner [39, 40]. Limited three-body channels are implemented into GiBUU, though it does contain $NN\pi \to NN$ and $NN\Delta \to NNN$ processes.

GiBUU splits the production mechanisms into low- and high-energy processes. The low-energy processes are implemented from the works we have briefly discussed, while the

high-energy processes are modelled from the implemented PYTHIA model [41] (above 2 GeV for baryon-meson and 2.6 GeV for baryon-baryon collisions). In this high-energy region, the total and elastic cross sections are fitted to the available data. The modern version of GiBUU implements modifications to PYTHIA by K. Gallmeister [37] that forbid the creation of diffractive events when kinematics and parameters conflict. In previous versions, FRITIOF [37] was used to connect the high-energy and resonance-model regions.

Medium modifications such as Pauli-blocking, Fermi-motion of the nucleons, Coulomb forces and hadronic potentials are critical for generating events in GiBUU. A short overview of these concepts is provided below. Starting with the electromagnetic forces, the EM potential is incorporated in the propagation of test particles, but it does not fluctuate heavily in typical reaction volumes and is a smooth, long-range potential. Therefore, it is omitted from the collision term, as it is assumed it does not influence particle reaction rates. The algorithm used in GiBUU, which speeds up calculations, is cross-checked against the integral representation of the EM potential, $\Phi_{\vec{r}}$, which slows down the processing and is given by:

$$\Phi_{\vec{r}} = \int d^3\vec{r}\,' \frac{\rho\,(\vec{r}\,')}{|\vec{r} - \vec{r}\,'|}, \tag{3.1}$$

where $\rho\,(\,\vec{r}\,'\,)$ is the charge density at the source position, $\vec{r}\,'$, $\vec{r}$ is the position of the particle where the potential is being calculated and $|\,\vec{r} - \vec{r}\,'\,|$ is the distance between the particle position and the source position where the charge density is located.

The hadronic potentials are introduced as time-like components of vector potentials in the local rest frame. The parameterisation for the nucleon mean-field potential is provided by Welke [42], and is a sum of a Skyrme term [43], which depends solely on the density, and a momentum-dependent contribution, given by:

$$A_N^0 = a\frac{\rho\,(\,\vec{r}\,)}{\rho_0} + b\left(\frac{\rho\,(\,\vec{r}\,)}{\rho_0}\right)^{\tau} + \frac{2c}{\rho_0} g \int \frac{d^3\vec{p}\,'}{(2\pi)^3} \frac{f\,(\,\vec{r},\vec{p}\,'\,)}{1 + \left(\frac{\vec{p}\,' - \vec{p}}{\Lambda}\right)^2}, \tag{3.2}$$

where $\rho_0 = 0.168$ fm^{-3} and $g = 4$ is the nucleon degeneracy. Here, $\vec{p}$ represents the momentum of the nucleon under consideration, $\vec{p}\,'$ represents the momentum of other nucleons and $f\,(\,\vec{r},\vec{p}\,'\,)$ is the phase-space distribution function. The coefficients a, b, c, τ and Λ are parameters that determine how nucleons (protons and neutrons) interact within the nuclear medium. Different parameters can be chosen, but by default, the medium momentum-dependent (EQS 5) parameters are used, and details on those can be found in the GiBUU manual [44].

The approximation for the Pauli blocking is that each state is Pauli blocked if it is below the Fermi momentum and the implementation is summarised here. A sum of δ functions

composes the phase-space density of particles, where for Pauli Blocking these δ functions are smeared by a Gaussian of width $\sigma = 1$ fm*. Then the following integral is defined:

$$I\left(\vec{r},\vec{p}\right) = \sum_{i\in\{1,\ldots,N(t)\} \text{ with } \vec{p}_i\in V_p} \frac{1}{\sqrt{2\pi\sigma}^3} \int_{V_r} d^3\vec{r} e^{-\frac{(\vec{r}-\vec{r}_i')^2}{\sigma^2}}, \tag{3.3}$$

which essentially measures the number of test particles occupying the momentum space within the volume V_p around $\vec{p}$, that are close to the volume V_r around $\vec{r}$. Finally, due to spin statistics, only two fermions may occupy a phase space cell of size $1/(2\pi)^3$. Therefore, the probability that a particle is Pauli blocked, $P\left(\vec{r},\vec{p}\right)$, is given by:

$$P\left(\vec{r},\vec{p}\right) = \frac{I\left(\vec{r},\vec{p}\right)}{\Delta V_r \Delta V_p \frac{2}{(2\pi)^3} \times \text{Number of Ensembles}}. \tag{3.4}$$

ΔV_r and ΔV_p are chosen with radii $r_r = 1.86$ fm and $r_p = 0.08$ fm. Reactions in the medium then modify the cross sections determined by GiBUU, which is a long and complicated process of detailed theoretical physics work. The fine details of these calculations for modifying the in-medium cross sections are presented in [43]. As a summary of the GiBUU model's implementation, the model simulates several reactions from many different implementations and each reaction is provided with a weight, which is the cross-section per nucleon determined by GiBUU. To determine the total cross-section of a particular reaction in GiBUU, we must sum over all weights (not just the pure number of events measured) and multiply this weight by the nucleon mass, A, to obtain the total cross-section for the target nucleus rather than the cross-section per nucleon. The total reaction cross-section in GiBUU is determined by the following equation:

$$\sigma_{\text{tot}} = \frac{A}{N} \sum_{i=1}^{i=N} \sigma^i, \tag{3.5}$$

where N is the total number of events generated, A is the atomic mass number, σ_{tot} is the total reaction cross section and σ^i is the cross section (weight) of each reaction. Therefore, the number of reactions in GiBUU is not the true cross-section; instead, it is the sum of all weights. These weights can be negative due to interference terms (further explained and shown in Subsec. 8.4.1). The GiBUU model can be used to simulate many weak reactions to remove statistical sensitivity, while the weight puts the cross-section on scale for the given reaction. For a photon, electron and neutrino beam the weight is in units of 10^{-30} cm^2, 10^{-33} cm^2 and 10^{-38} cm^2, respectively.

As an indication of the simulating power of GiBUU and its remarkable potential to de-

*As GiBUU is a statistical model, which depends on the number of ensembles used to generate the data, this value is tuned to a number of ensembles N > 200. The width could be reduced for larger N [43].

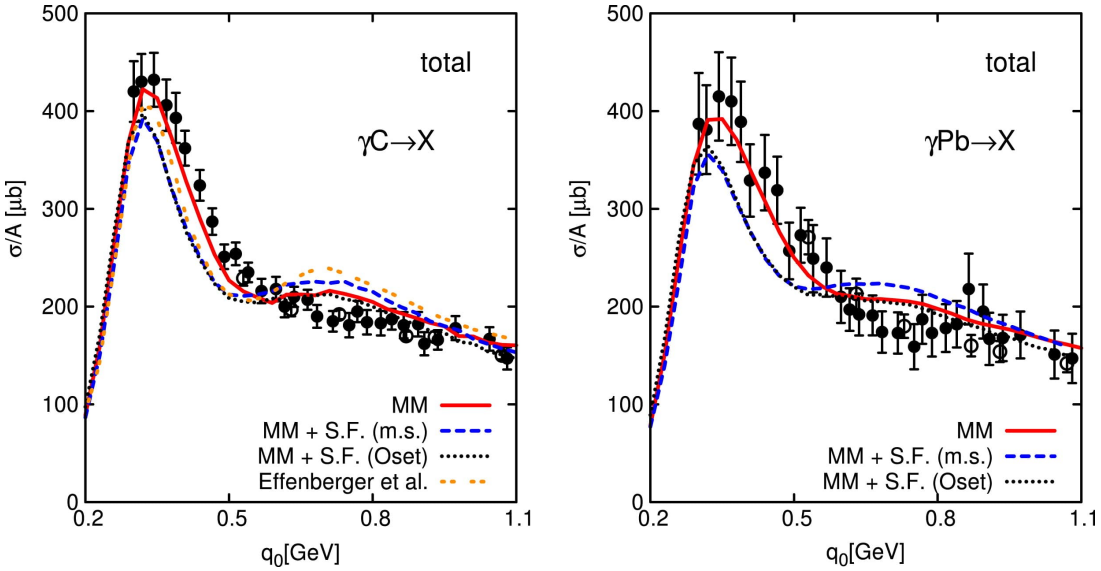

Figure 3.1: The total photoabsorption cross section per nucleon as a function of the photon beam energy (here denoted by q_0). The black dots present the experimental data taken from [23] where the error bars represent the full statistical and systematic uncertainty. The solid red line presents the GiBUU predictions with an MM potential, with two further modifications to the in-medium self-energy shown; mass shift (m.s) option (blue line) and the Oset option (black dashed line) [37]. The figure is originally taken from [43].

scribe the fundamental processes of nature, Figs. 3.1 and 3.2 present comparisons of the GiBUU model to experimental data. Figure 3.1 shows good agreement between the total photoabsorption cross section predicted by GiBUU for both ^{12}C (left) and ^{208}Pb (right) and the experimental data taken from [23]. The total cross-section per nucleon for the experimental data (black line) is shown and the red line shows the agreement in using only a momentum-dependent (MM) potential, which is the most widely used potential in GiBUU simulations. The additional lines present improvements to the resonance spectral function, which represents the probability of finding a nucleon with a certain binding energy and momentum in the nuclear wave function, which worsens the results due to how these improvements were calculated. For example, the increased in-medium width obtained from [45] (Oset) has contributions from 2-body mechanisms, but the calculation depends on an impulse approximation that does not contain such contributions [37].

Figure 3.2 presents the inclusive electron scattering cross section, $d^2\sigma/d\omega d\Omega_{k'}$, on ^{16}O as a function of the energy transfer, ω, for the experimental data (black dots), taken from [46], and the GiBUU predictions (red line). The distribution is for a fixed electron beam energy $E_{e'} = 0.737$ GeV and a fixed scattering angle $\theta_{k'} = 37.1°$. The calculation uses the spectral function, which gives rise to the good agreement observed. This good agreement between the experimental data and the prediction of the GiBUU model for electron scattering data cements the remarkable ability of the GiBUU model to accurately simulate a beam (of many different species) impinged on many nuclei from light to heavy. We remark that the results presented in this thesis utilise the GiBUU 2021 release [44].

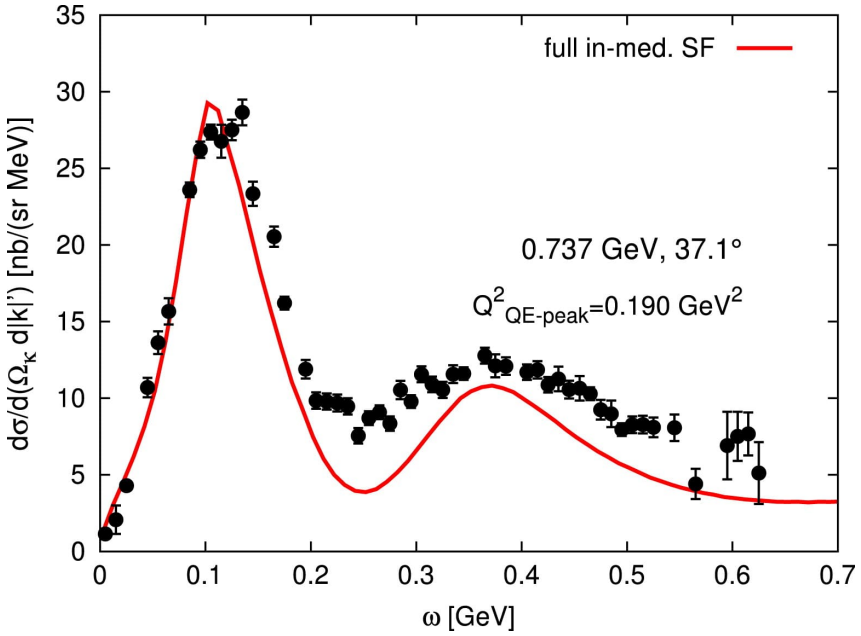

Figure 3.2: Inclusive electron scattering cross section as a function of the energy transfer for an electron beam energy of 0.737 GeV and a scattering angle of 37.1° predicted by GiBUU (red line) and compared to the experimental data measured by [46]. The parameter Q^2 denotes the square of the four-momentum transfer at the quasi-elastic peak, where excellent agreements with GiBUU are observed [37]. The figure is originally taken from [47].

3.2 GENIE

The GENIE (Generate Events for Neutrino Interaction Experiments) model is a comprehensive suite of products which utilises many different theoretical models and software for use within the neutrino physics community [48]. GENIE generates events using the combination of theoretical models and empirical data to predict the probability that a probe (e.g. electron, neutrino), with a given energy, interacts with a specified target. There are over 100 adjustable parameters in GENIE, see Ref. [49], which are adjusted through "tunes." These tune files can be selected and used when producing GENIE simulations, where each tune is characterised using electron, neutrino and hadron scattering data.

The GENIE model generates events with equal weight (= 1.0), and provides a total cross-section of all reactions for the primary electron beam energy of interest. This is illustrated in Fig. 3.3, which shows the total cross-section predicted by GENIE at each incident electron beam energy, up to the maximum generated for the present analysis (5.986 GeV), but not the maximum GENIE is capable of.

After determining the total cross-section at the incident electron beam energy of interest, the following equation determines the reaction cross-section in GENIE:

$$\sigma = \frac{N \times \sigma_{\text{tot}}}{N_{\text{tot}}}, \tag{3.6}$$

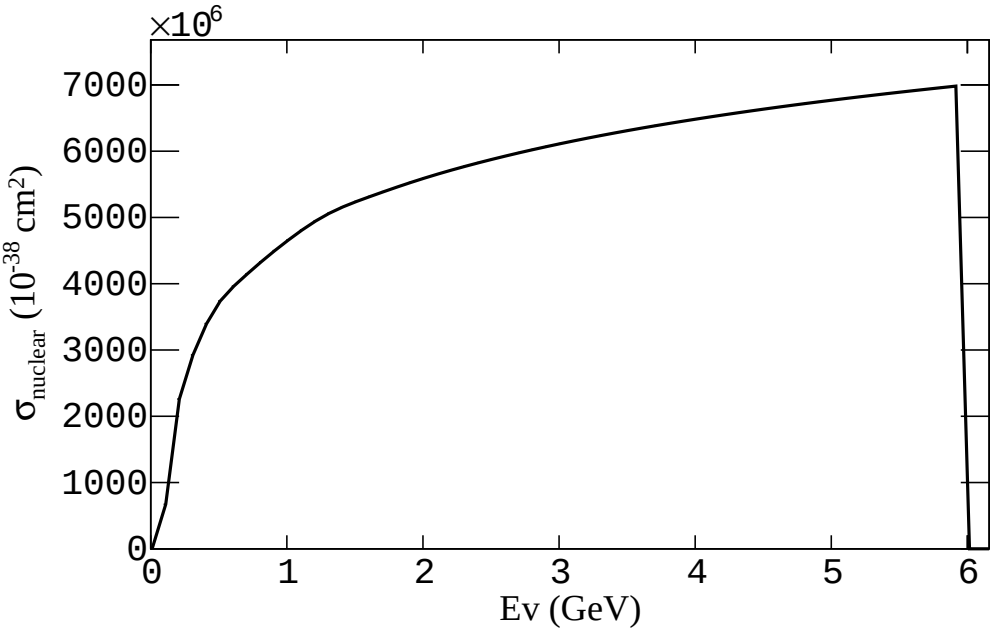

Figure 3.3: The total cross section predicted by Genie as a function of the incident electron beam energy for the G18 tune.

where N is the number of events measured for the reaction of interest, N_{tot} is the total number of events generated, σ is the reaction cross-section and σ_{tot} is the total cross-section predicted by the GENIE model. The units of σ_{tot} is 10^{-38} cm^2, in which if we multiply the y-axis of Fig. 3.3 by 10^{-38} cm^2, then the units are on the order of tens of μb (10^{-30} cm^2). The GENIE model uses a single scaling factor for a given cross-section at a given beam energy, rather than assigning weights (cross-sections) to each reaction. Therefore, when we simulated our GENIE events they did not oversample weak reactions as GENIE does not have this functionality.

For energies on the order of a few GeVs, GENIE utilises the Relativistic Fermi Gas (RFG) model [49] for all processes. The version adopted by GENIE is from Bodek and Ritchie [50], which has modifications implemented to include short rage NN correlations [51]. At high energies, due to shadowing, and other effects, the model requires broad features to fully describe the particle interactions. However, at lower energies, the impulse approximation [52] works well, and the RFG model is often successful [48]. The impulse approximation simplifies the situation by assuming that the incoming particle interacts with just one proton or neutron inside the nucleus, rather than the entire nucleus. Struck nucleons are given momentum and an average binding energy by the nuclear medium model, which have been determined from electron scattering experiments. For light nuclei ($A < 20$), the modified Gaussian density parameterisation is used, while for heavier nuclei, the Woods-Saxon density function is used [48]. Therefore, GENIE can model all target nuclei. Nuclear modifications and Pauli blocking are incorporated into many interactions, particularly those involving nuclear targets. Many features of the fundamental theoretical

physics behind GENIE's modelling are similar to those previously discussed for GiBUU. Further details, including the modelling of cross sections, can be viewed in Refs. [48] and [49].

3.3 Previous Results

3.3.1 Tests of Many-Body Theories with Photoinduced Nucleon Knockout

In the 1980s and 1990s, there was a programme of measurements of 2N and 3N knockout from nuclei at the tagged photon facility in Mainz. For an overview, see Ref. [53]. Of most direct relevance to the current work on two-nucleon knockout is the publication [54], where $^{12}\mathrm{C}(\gamma, np)X$ and $^{12}\mathrm{C}(\gamma, pp)X$ reactions were studied in restricted kinematics for photon energies $E_\gamma = 150 - 700$ MeV. The previous work predates the more recent GiBUU and GENIE developments and compared the data to an earlier photonuclear reaction theory based on the self-energy of the photon in nuclear matter, referred to as the Valencia model. Details on the Valencia model can be found in [55] (we do not compare to this model in our work). The visible cross sections for different nucleon knockout reactions were determined as a function of missing energy, recoil angle and recoil momentum and the results were further separated into bins of photon energy.

The $^{12}\mathrm{C}(\gamma, np)X$ reactions showed evidence for direct knockout up to approximately 700 MeV in the sampled kinematic range (polar angles 36.7° to 71.2°). Backgrounds from Final State Interactions (FSI) between particles after the initial reaction has occurred and initial pion-production mechanisms became significant around $E_\gamma = 400 - 500$ MeV. For $^{12}\mathrm{C}(\gamma, pp)X$ reactions, direct knockout processes were not well identified beyond $E_\gamma \sim$ 300 MeV, and clean separation was not achieved. The Valencia model captured the general features of the distributions for both reactions to a reasonable level, although the cross sections were generally overpredicted, attributed to an overestimate of the pion-production processes in the medium.

Three-nucleon mechanisms were studied in [56] by investigating the $^{12}\mathrm{C}(\gamma, ppn)X$ reaction in restricted kinematics and comparing the results of the experimental data with the Valencia model. The visible cross-section as a function of the missing energy for different photon energy bins is presented in Fig. 3.4, with a breakdown of contributions from the Valencia model. As can be seen from the figure, despite a reasonable replication of the experimental data by the Valencia model, the existence of a direct 3N knockout process is only suggestive as the process is not observed without large FSI and initial pion-production backgrounds.

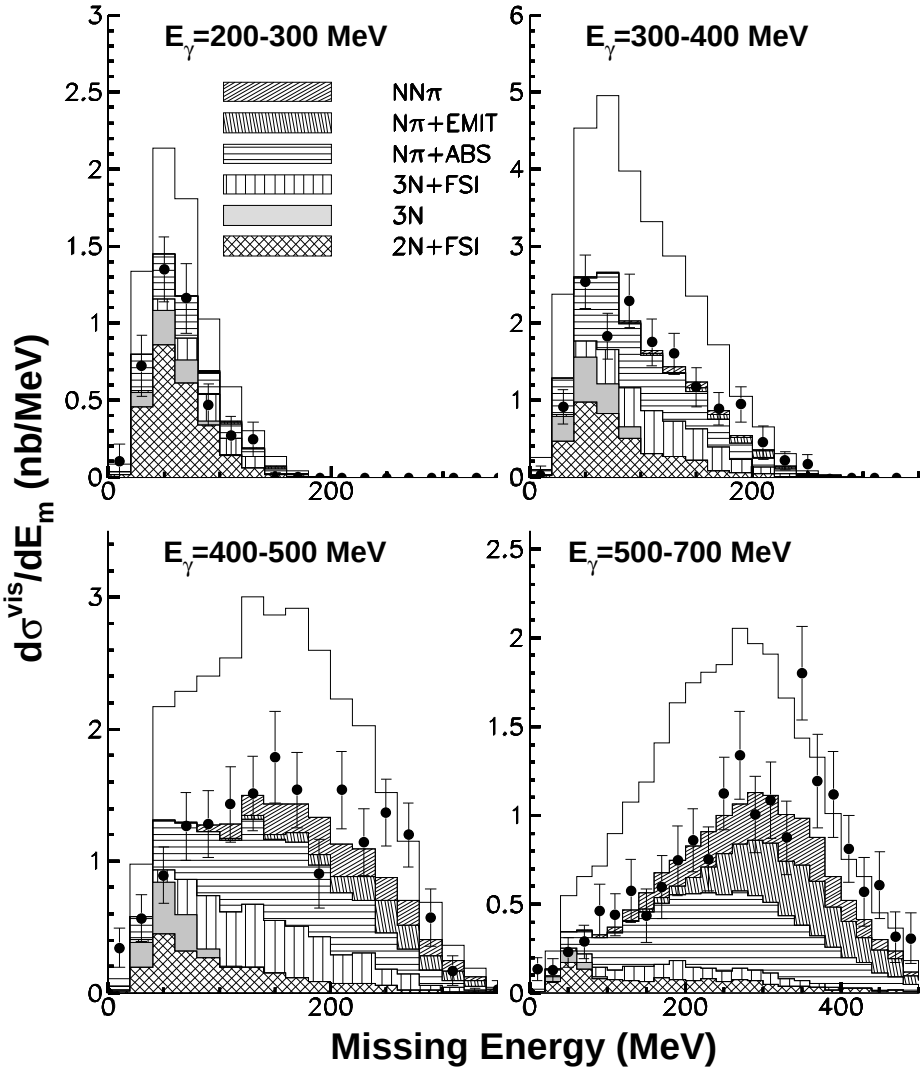

Figure 3.4: The visible cross section for the reaction $^{12}\mathrm{C}(\gamma, ppn)X$ as a function of the missing energy, where the shaded regions present the Valencia model predictions for different mechanisms. The solid line presents the total cross section without the reduction of the $N\pi$ + ABS prediction [56].

3.3.2 Electron Beam Energy Reconstruction

The first electrons for neutrinos (e4ν) analysis was obtained with CLAS using nuclear targets ^{12}C and ^{56}Fe and studying the $A(e, e'p)$ reaction to reconstruct the incoming electron beam energy. The recent publication [27] provided a detailed comparison of mono-energetic electron-nucleus scattering with the leading theory model (GENIE) used for beam reconstruction in neutrino experiments. The authors investigated the model's ability to reproduce the cross section for the reaction $A(e, e'1p0\pi)X$ (i.e. detection of a proton with no detection of any associated pions). Data was obtained for multiple beam energy settings (1.1, 2.2 and 4.4 GeV) and multiple nuclear targets (^{12}C and ^{56}Fe). The reaction studied is expected to be dominated by the well-understood quasielastic

scattering process (which allows kinematic reconstruction of the beam energy), and the results are presented in Fig. 3.5. The results present the cross-section as a function of the reconstructed beam energy using the calorimetric method, presented in Eq. (2.11).

The findings of their investigation were surprising. The results indicate that GENIE, one of the leading theory models used in neutrino oscillation parameter extraction, reconstructed the correct electron beam energy less than 50% of the time, even for such simple reactions. The background (mis-reconstructed) events were overstated by the model for non-quasielastic reactions at the higher incident electron energies. These results highlighted the shortcomings of our current understanding of neutrino interactions. If the models are not corrected, it could limit the potential of next-generation neutrino oscillation facilities, such as DUNE, by introducing large systematic uncertainties.

In this work, we carry out an e4ν analysis with CLAS12 and beam energies of 2.1, 4.0 and 6.0 GeV, which means the beam reconstruction can be obtained in the specific reaction kinematics of DUNE. The larger beam intensity also enables the beam reconstruction quality to be established for a much wider range of final states. The measurements are an important new challenge to many-body theory in electron-nucleus scattering. Once benchmarked such reactions may be implemented in the analysis methodologies for DUNE and other future facilities.

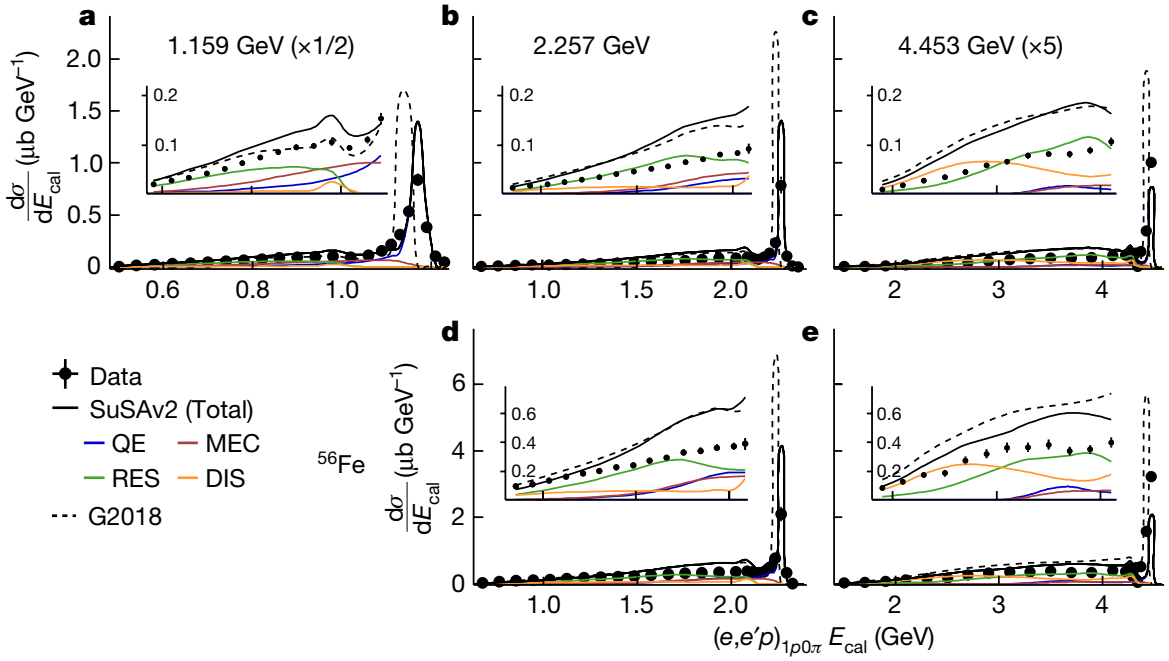

Figure 3.5: e2a data presenting quasielastic $A(e, e'1p0\pi)$ scattering for different beam energy settings for ^{12}C and ^{56}Fe targets with comparisons to the GENIE model. The GENIE model is broken down to the contributions of fundamental processes and for two different tuning settings G2018 and the newer SuSAv2 parameterisation. Panels (a) through (e) present the electron beam energy reconstruction for different beam energies for the ^{12}C (top) and ^{56}Fe (bottom) targets [27].

Chapter 4

Experimental Details

> *"The first thing to realize about physics is its extraordinary indirectness... For physics is not about the real world, it is about 'abstractions' from the real world, and this is what makes it so scientific... Theoretical physics runs merrily along with these unreal abstractions, but its conclusions are checked, at every possible point, by experiments."*
>
> - Anthony Standen

The research discussed in this thesis relies on data collected at Hall B within the Thomas Jefferson National Accelerator Facility (JLab), situated in Newport News, Virginia. An aerial shot of the accelerator facility is presented in Fig. 4.1. JLab has been in operation since 1984, offering a unique environment for experiments involving electron and photon beams. It celebrated its inaugural beam on July 1st, 1994. Presently, the facility can generate electron beams with energies reaching up to 12 GeV, with plans underway to potentially increase this to 24 GeV, or introduce positron beams reaching up to 12 GeV. JLab specializes in investigating the intricacies of hadronic and nuclear physics at these intermediate energy levels (few GeVs), across various target materials. These endeavours play a crucial role in advancing our understanding of the standard model of particle physics.

4.1 Continuous Electron Beam Accelerator Facility

The Continuous Electron Beam Accelerator Facility (CEBAF) [58] at JLab provides a high-luminosity electron beam with up to 12 GeV of energy. The electrons are produced using radio-frequency-gain switch lasers, which direct their intensity towards a gallium-arsenide photo-cathode at 100 keV, providing sufficient energy for the ionisation of the electrons to occur. Using a single cryounit and two cryomodules, the ionised electrons are accelerated to 67 MeV before they are further separated into 2 ns beam bunches

Figure 4.1: A bird's eye view of JLab taken from Ref. [57], showing all four experimental halls, with Hall B marked where the experiments discussed in this thesis were conducted.

and injected into the accelerator. The electron beams produced can have a longitudinal polarisation of up to $\approx 85\%$ [59].

After their production, the electrons venture into the accelerator, via the injector, to begin their first circulation of the CEBAF with velocities close to the speed of light. The configuration of the accelerator is analogous to a racetrack, with a circumference of 7/8 of a mile. The two straight sections are covered by a series of liquid-helium-cooled niobium cavities, which constitute a superconducting radio-frequency (SRF) linear accelerator (linacs). The curved sections are fitted with re-circulation arcs which direct the electron beam between the two linacs; hence, the electrons gain energy by travelling through the linacs only. With each pass of one of these linacs, the electron gains 1.2 GeV in energy. The first complete circulation of CEBAF (one pass) provides 2.4 GeV in energy, with the maximum of five passes providing a 12 GeV electron beam. Remarkably, these electrons travel with a tightly constrained beam with widths similar to human hair thanks to the electromagnet technology at JLab. Note, in the old CLAS era, before the upgrades [60], each linac provided 600 MeV of energy and one pass provided 1.2 GeV of energy, providing a maximum of 6 GeV after all five passes were complete. The Overview of CEBAF, from the old CLAS and current CLAS12 era, is presented in Fig. 4.2

Once the desired energy has been attained, the electron beam can be split into four

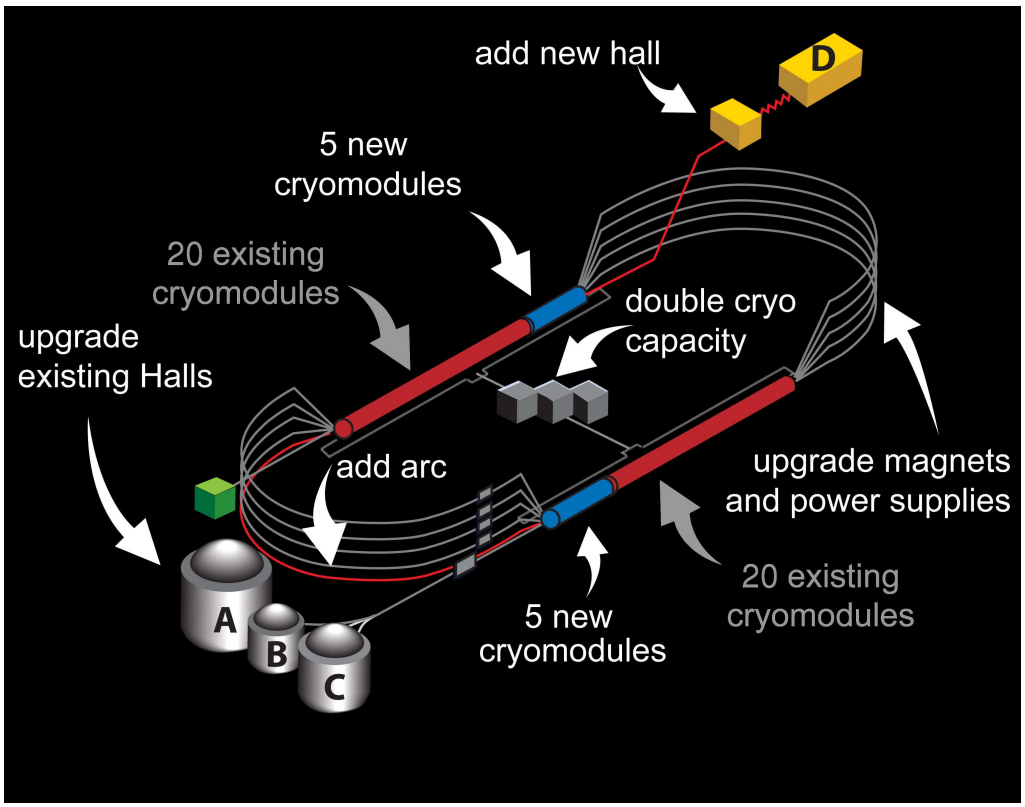

Figure 4.2: An overview of CEBAF, including the old CLAS era and the upgrades made to the current CLAS12 era. Figure taken from Ref. [60].

independent beams and simultaneously delivered to four experimental halls. Each experimental Hall, named Halls A, B, C and D, has its own experimental program with different apparatus and goals. Halls A and C focus on high-precision electron scattering experiments, and the reaction products in both halls are detected via high-resolution spectrometers. This limits the acceptance of the spectrometers to approximately 1 steradian. Hall D focuses on the usage of real photon beams, described in detail in Sec. 4.4, and utilises the full 12 GeV electron beam energy capabilities of CEBAF. Hall B houses a large acceptance spectrometer, with a nearly 4π steradian coverage, called CLAS12 (formerly CLAS). Halls A, B and C complete a maximum of 4 and a half passes, providing a maximum beam energy of approximately 11 GeV due to their positioning with respect to the injector for CEBAF.

4.2 Hall B

Hall B, home of the CLAS12 spectrometer and formerly CLAS spectrometer, is one of four experimental halls in JLab and it uses an electron beam with the lowest amperage current of all halls. The experimental setup at Hall B (marked on Fig. 4.1) varies between experiments. In the old CLAS era, Hall B could conduct primary electron beam and secondary photon beam experiments [61] by making use of the tagging spectrometer

detailed in Subsec. 4.4.3. In its current configuration, Hall B provides only electron scattering experiments, with an increased luminosity.

4.3 Beamline

Additional equipment is placed along the beamline, including 3 Beam Position Monitors (BPM) composed of 3 resonant (RF) cavities each, which are placed at different positions to monitor the beam's quality. Two BPMs, 2C21A and 2C24A, are placed 36 m and 24.6 m upstream of the CLAS12 target and upstream of the tagger magnet. However, 2H01A is placed downstream of the tagger and 8.2 m upstream of the CLAS12 target, hence 2H01A is not operational during real photon beam experiments. As the electron beam passes through these cavities, it induces an electromagnetic field, which depends on the position and intensity of the electron beam and is used to determine the (x, y) coordinates. During photon beam experiments this information is used to centre the electron beam on the tagger radiator, and the CLAS12 target during electron beam experiments.

The Hall B beam profile is determined by three devices called harps, which consist of a set of wires (20 μm and 50 μm tungsten, and 100 μm iron) oriented along two orthogonal directions perpendicular to the beam. During beam-profile monitoring, the harps are moved into the beamline with a direction of motion of 45° with respect to the horizontal axis, taking measurements at regular intervals. Typically, the harp scan is performed before collecting data, since it can affect the beam quality [58].

4.4 Real Photon Beams at JLab

Photon experiments in Hall B were conducted by scattering a primary electron beam, of known energy, from a suitably chosen radiator to produce secondary photon beams via the bremsstrahlung radiation process. The bremsstrahlung process occurs when an electron is decelerated or deflected by a charged particle or a nucleus. The energy lost during this process is released as electromagnetic radiation (photons).

When the electron interacts with a crystal lattice, which is a well-ordered lattice, at high energies ($>$ 100 MeV), then coherent bremsstrahlung production occurs. This happens because the wavelength of the emitted photons are comparable to the lattice spacing, leading to constructive interference, which produces intense peaks in the photon energy distribution at specific momentum transfers due to the periodic arrangement of the atomic structure, typically referred to as coherent peaks.

In contrast, amorphous materials, which lack a regular atomic arrangement, produce photons through incoherent bremsstrahlung production, resulting in a broad spectrum without sharp peaks. At lower energies, bremsstrahlung in both crystalline and amorphous materials is dominated by incoherent processes, as the electron's wavelength is

larger than the lattice spacing, preventing coherent interactions.

The resulting photon energy spectrum from bremsstrahlung typically exhibits a characteristic $1/E_\gamma$ shape, with coherent peaks appearing if a suitable radiator is used. The orientation of the radiator is crucial for maximising coherent bremsstrahlung production. When the electron beam is aligned with a specific crystallographic direction of the lattice, the emitted photons undergo constructive interference, leading to coherent peaks. Additionally, a properly oriented radiator can produce photons with a high degree of linear polarisation. If the radiator is misaligned, the electron beam interacts incoherently with the lattice, resulting in fewer coherent bremsstrahlung photons and more incoherent radiation.

The g9a experiment utilised linearly and circularly polarised photon beams impinged on nuclear targets. An overview of the experimental apparatus used in producing real photon beams is presented in Fig. 4.3

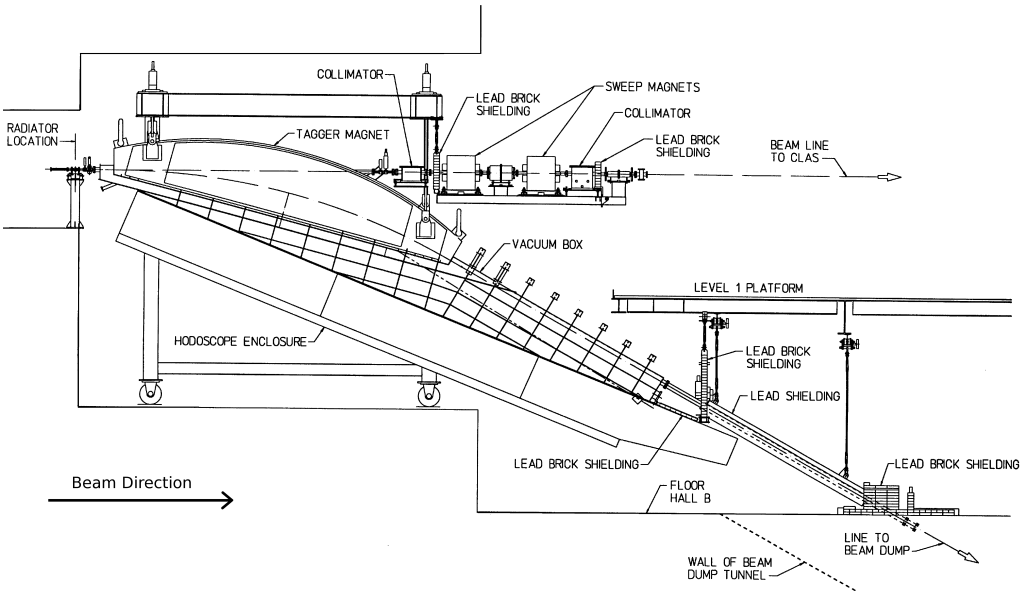

Figure 4.3: A schematic overview of the experimental apparatus used to produce real photon beams in CLAS, showing the positioning of key apparatus, such as the radiator, tagger and collimator (discussed later). The figure is taken from Ref. [62].

4.4.1 Radiator

The purpose of a radiator is to deflect the incoming electron beam and produce bremsstrahlung radiation. Diamond is a suitable choice because its excellent thermal properties reduce thermal effects in bremsstrahlung production, and its small lattice constant offers additional advantages. The thickness of the radiator is an important quantity, as the thickness affects the angular divergence of the secondary photon beam due to multiple scattering effects of the primary electron beam. Crystal defects within the radiator are

also problematic. In the g9a experiment, a diamond radiator with a thickness of 50 μm was used. It was cut in the [100] orientation and photons were produced when the electrons scattered from the [022] reciprocal lattice vector.

4.4.2 Goniometer

To produce a photon beam with a high degree of linear polarisation the diamond must be well aligned, such that the electrons can scatter from precise reciprocal lattice vectors of the crystal. To suitably align the diamond with the incoming electron beam with the required level of precision, the diamond is mounted to a goniometer [63]. This device allows for precise movement of the diamond about all three axes (and it can also be rotated) with a precision of around 10 μrad, which translates to a precision of the placement of the coherent peak energy of ≤ 1 MeV. The goniometer is kept under vacuum conditions, is positioned upstream of the tagger by several meters and can hold several radiators of different materials. The goniometer is kept under vacuum conditions to maintain beam quality and focus, and to prevent unnecessary energy losses before the electrons interact with the radiator. The goniometer used in the g9a experiment is presented in Fig. 4.4 in its test condition.

Figure 4.4: The George Washington University goniometer [63] used in the g9a experiment, presented here in its test condition.

4.4.3 Photon Tagging Spectrometer

The tagging spectrometer is used to detect the electrons that scatter from the radiator and subsequently determine the secondary photon beam energy. It consists of a dipole

magnet and a hodoscope to provide energy and timing information from two planar arrays of plastic scintillators. The system is positioned vertically as the electron is deflected vertically downwards from the beamline by the dipole magnet onto the tagger hodoscope. The energy transferred to the scattering nucleus is negligible, hence the energy of the photon beam is determined through the relation $E_\gamma = E_0 - E_e$, where E_0 is the primary electron beam energy and E_e is the scattered electron energy determined by the tagger. The scattered electron energy is determined from the position it is detected in the tagger hodoscope, since lower energy electrons have larger deflections within magnetic fields, thereby producing higher energy photons and vice versa. If an electron does not produce a photon it is deflected into the tagger beam dump.

The two planes of scintillators in the hodoscope, shown in Fig. 4.5, are referred to as the E- and T-plane. They each contain many overlapping scintillators with their surfaces perpendicular to the beam. The E-plane provides the scattered electron momentum information with an energy resolution of $0.001E_0$ (GeV). In this plane, there are 384 scintillators, each with PMTs sub-divided into 767 energy bins. The scintillators are 20 cm long, 4 mm thick and 6 - 18 mm wide, providing momenta distinguishable by $0.003E_0$ (GeV/c). As for the T-plane, its occupation is to correctly distinguish beam buckets. It has a similar structure to the E-plane, but there are 61 overlapping scintillators further subdivided into 121 time bins. The scintillators are 2 cm thick, and achieve the required timing resolution ($\approx$ 300 ps) to associate photons with individual beam buckets every 2 ns. The total photon energy coverage of the photon tagging spectrometer is 20 - 95% of the primary electron beam energy.

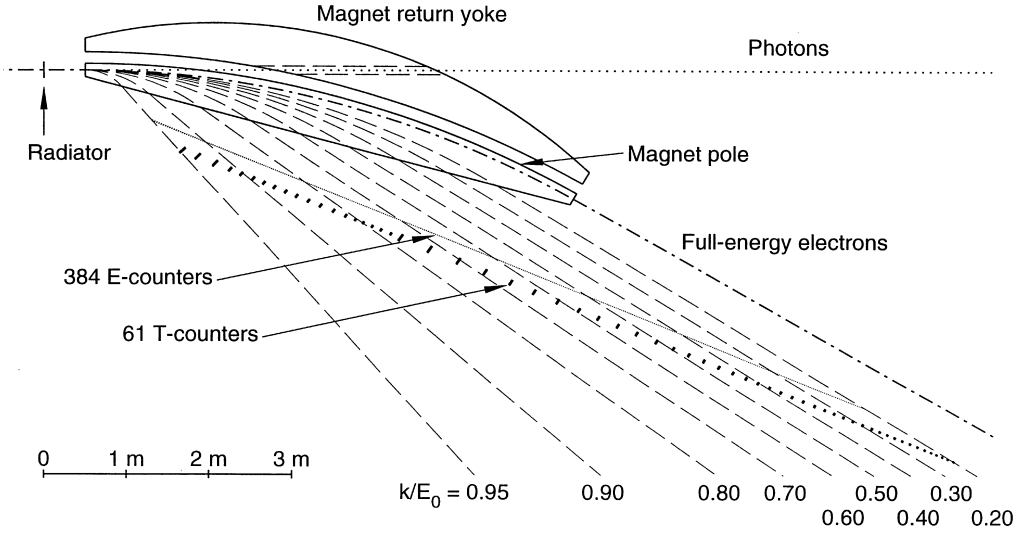

Figure 4.5: A diagram of the tagging spectrometer utilised in CLAS photon beam experiments, showing the positions of the E- and T-counters. The image is taken from Ref. [62].

4.4.4 Collimator

The collimator is used to increase the degree of linear polarisation, as the angular spread of incoherent bremsstrahlung radiation is greater than the coherent spread in the regions of the coherent peaks. The collimator used in the g9a experiment has a diameter of 2 mm. It is located downstream of the tagger and is composed of a series of nickel disks with a small 2 mm diameter hole in the centre. These disks are stacked inside a cylindrical stainless steel structure with four 4 mm cubic-shaped scintillators situated between them. The design of the collimator enables monitoring of the count rates within the scintillators by measuring the number of e^+e^- pairs produced by the incoming photons outside of the first nickel disk. This improves the monitoring of shifts in the beam position.

4.5 CEBAF Large Acceptance Spectrometer

A total of 178 experiments were completed with the original CEBAF with a large proportion of those undertaken in Hall B using the CEBAF Large Acceptance Spectrometer (CLAS) detector [64]. It was the main detector in Hall B and was used to conduct many electron and photon beam experiments. The detector itself was composed of a multitude of different detectors, situated in a ball-like structure with a diameter of approximately 10 m that surrounded a cylindrical target cell. It provided excellent charged particle identification and momentum tracking over a large region of the full solid angle ($\approx 2.8\pi$). A schematic of the detector is presented in Fig. 4.6.

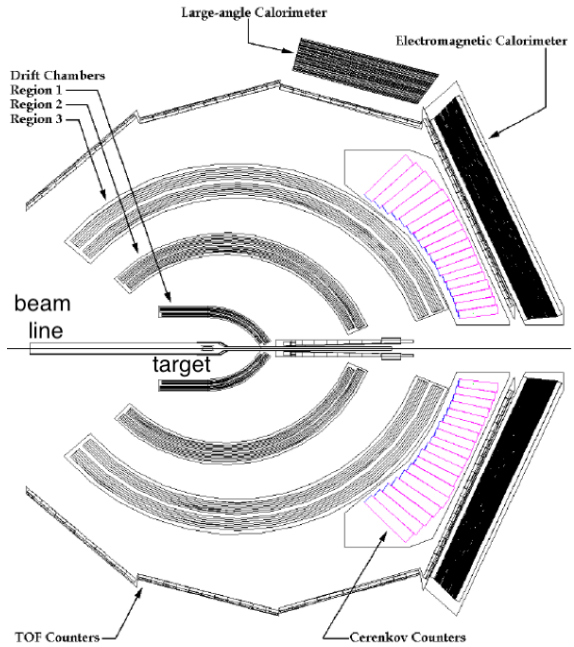

Figure 4.6: A computer-generated image of the CLAS detector [64], with important detector sub-systems for particle identification labelled.

The torus magnet produces a magnetic field predominantly in the azimuthal direction, thereby allowing for momentum spectrometry. Charged particles bend due to the presence of the magnetic field and the momentum of the particle is determined directly from the curvature of its trajectory through CLAS. The particle's trajectory is determined by the drift chambers and the time-of-flight information is provided by scintillators located outside of the drift chambers. Low, forward angle particles are supplemented by the Cherenkov Counters and Electromagnetic Calorimeters, which provide additional information, such as energy deposition and number of photoelectrons produced, which improve electron identification and neutral particle detection. The trigger and data acquisition system is responsible for the reading and collection of events, securely storing them for future calibrations and use.

4.5.1 Torus Magnet

The CLAS experiments utilised a toroidal magnetic field generated by the torus magnet, with an arrangement of six superconducting coils surrounding the beamline. The torus magnet is the reason for the characteristic six-sector structure of the CLAS detector, where the coils produce the low-acceptance boundaries between the six sectors, reducing the overall acceptance to $\approx 2.8\pi$ steradians. The coils consist of four layers of 54 turns of NbTi/Cu and are roughly 5 m in diameter and during operation are cooled to 4.5 K using super-critical helium. The toroidal (doughnut-shaped) configuration of the magnet's inner coils ensures that the magnetic field lines are directed primarily in the azimuthal (ϕ) direction, wrapping around the beamline. Despite the decrease in acceptance due to the placement of the magnet, the product of the efficiency and acceptance is much larger, as the torus field allows for the detection of charged particles and the determination of their momentum by tracking their trajectories within the field. During the CLAS era, there was no magnet surrounding the target cell, allowing for polarized target experiments.

4.5.2 Start Counter

In electron scattering experiments, mini torus coils were placed around the target, as the detection of the scattered electron would trigger an event for data collection. This was not possible in photon beam experiments, so the start counter (SC) [65, 66] was deployed. The SC detected charged particles, such as protons, as they ionised the material within the SC. This detection initiated the start time for time-of-flight (TOF) measurements of charged particles. The SC consisted of a ring of plastic scintillators that provided precise timing signals, which were used to determine the time of the interaction by searching for a timing coincidence between the SC and the photon tagger.

The start counter is shown in Fig. 4.7. It was designed to cover the full acceptance of CLAS and in each of the six sectors, there were four straight scintillator paddles which were 502 mm long. The minimum hit multiplicity requirement in the paddles was 2 to

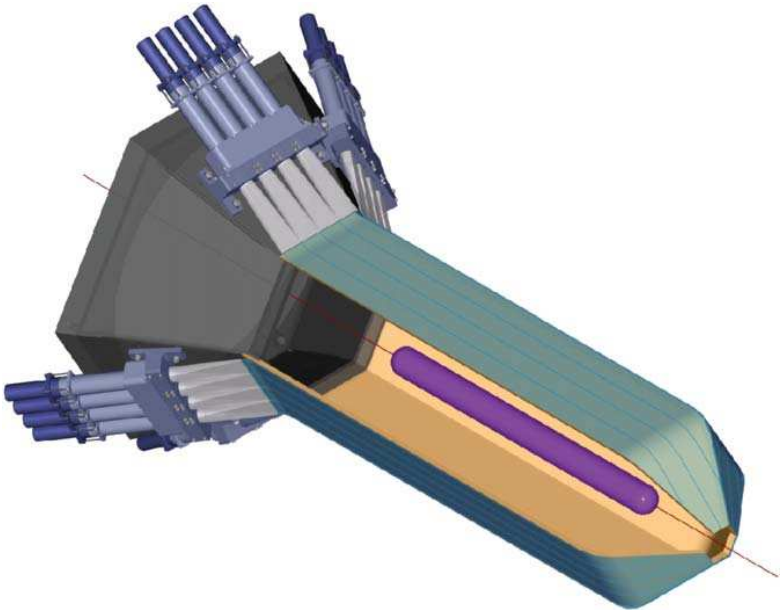

Figure 4.7: A computer-generated image of the start counter in CLAS, with a single sector removed to demonstrate its configuration around the 40 cm long target cell.

maintain acceptable electromagnetic background levels in final states involving multiple particles. Light guides and photomultiplier tubes were used to enable the readout of signals in the SC. The beam buckets in CEBAF occur every 2 ns, so a sub-nanosecond timing resolution was required in the SC. The timing resolution of the SC was < 388 ps.

4.5.3 Drift Chambers

The Drift Chambers (DC) track the trajectories of charged particles that bend under the influence of the toroidal magnetic field. The DC modules are filled with gas which is a mixture of argon (Ar) and carbon dioxide (CO_2) with a mixing ratio of 90:10. As charged particles traverse the DC, they ionise the gas, producing electrical signals in the form of drift times from the wires to the point where the particle passed. These signals are collected and used to calculate the drift distance, which is the shortest distance from the wires to the particle's trajectory. By measuring the time it takes for the ionisation electrons to drift from the point of ionisation to the wires, and using the known drift velocity of the electrons in the gas, the precise position of the particle's trajectory relative to the wires can be determined. Electrons travelling close to the anode wires generate a stronger electric field around the anode. This intensified electric field enhances electron-atom collisions, leading to ionisation and a process known as an avalanche. The CO_2 present in the detector helps to suppress secondary avalanches by quenching excess ionisation.

The DC consists of three regions; Regions 1 and 3 are situated in low magnetic field regions, while Region 2 is contained within a region of high magnetic field strength. The three regions each consist of two superlayers, each consisting of six layers of honeycomb-

shaped drift cells presented in Fig. 4.8. The two superlayers are referred to as the axial and stereo superlayers. The stereo superlayer is tilted at a 6° stereo angle and the axial superlayer is positioned axially to the magnetic field to provide azimuthal information for the tracked particles. The axial superlayer is the innermost layer for Regions 2 and 3, positioned at a radial distance closer to the centre of the CLAS spectrometer than the stereo superlayer. Contrariwise, the order is flipped in Region 1 and there are only four layers of wire (due to space constraints). The position resolution of the DC is ≈ 400 μm, which corresponds to an angular resolution of a few mrad and $\leq 1\%$ for the reconstructed momentum [67].

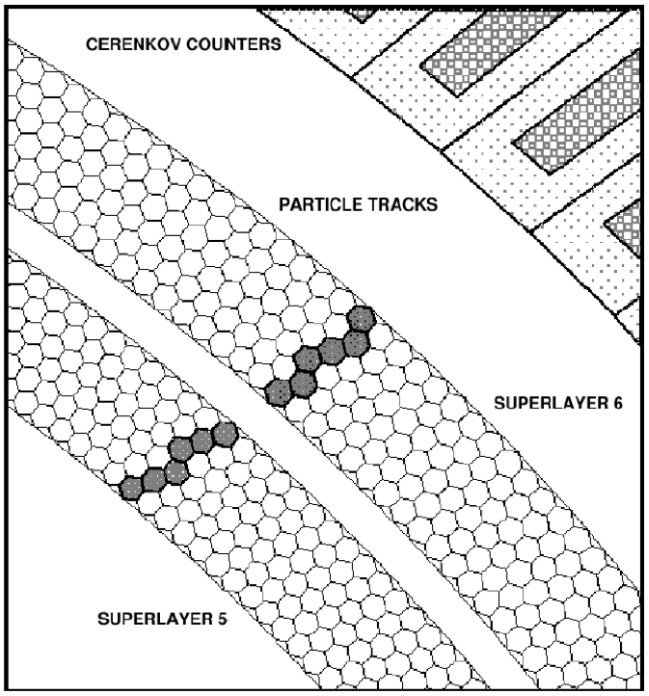

Figure 4.8: A schematic view of two DC superlayers. The drift cells have a honeycomb-like shape with sense wires at the centre of each hexagon and the field wires at the vertices. The shaded cells indicate a charged particle track has traversed the DC. The image is taken from Ref. [67].

4.5.4 Cherenkov Counters

The Cherenkov Counters have a dual purpose of contributing to the triggering of electron scattering experiments and separating electrons from pions. Each sector of CLAS contains six counters, with each of the six counters further divided into 18 regions in the polar angle (θ) from $8° \leq \theta \leq 45°$ (see Fig. 4.9). Each region is subdivided into two separate modules called segments, which are symmetric around the mid-plane of the sector. Therefore, there are 36 Cherenkov Counters in each CLAS sector. The Cherenkov Counters utilise a perfluorobutane (C_4F_{10}) gas with a refractive index of $n = 1.00153$, where the threshold for detecting particles is influenced by the refractive index of the medium. The detection

threshold is governed by the Cherenkov radiation condition, given by:

$$\cos(\theta_C) = \frac{1}{\beta n}, \tag{4.1}$$

where θ_C is the Cherenkov angle that light is emitted at, β is the velocity of the particle relative to the speed of light in vacuum and n is the refractive index of the medium.

Cherenkov light is emitted when the particle velocity exceeds the modified speed of light in the detector medium (c/n). Since electrons are much lighter than pions, they require less energy to achieve a velocity that exceeds the speed of light in the medium. Therefore, the refractive index of the C_4F_{10} gas corresponds to an energy detection threshold of 9.24 MeV for electrons and 2.51 GeV for pions. The Cherenkov light produced is then re-directed by several mirrors within each module towards the light-collecting Winston cone and focused into the PMT. The Cherenkov Counter produces an average signal of 7 photoelectrons and its inefficiency is on the order of 10^{-3} [68]. This means there is a 0.1% chance (1 in 1,000) that the Cherenkov Counter will fail to produce a signal when it should.

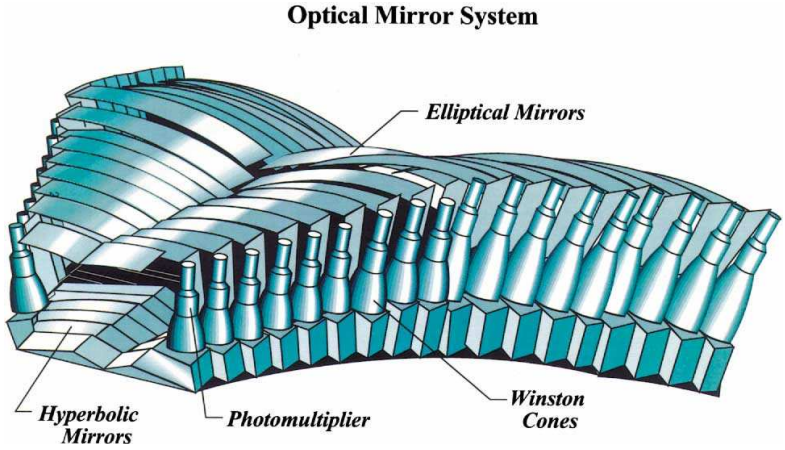

Figure 4.9: A 3D view of the CLAS Cherenkov Detector, taken from Ref. [68].

4.5.5 Time-of-Flight Scintillators

The Time-of-Flight (ToF) detectors are a set of scintillator paddles in a single array for measuring the time of flight of particles. By measuring the time of flight, t, from TOF and the distance travelled, d, from DC tracking information, the speed of charged particles is determined by $\beta = d/t$, i.e. the simple speed, distance and time relation. Utilised in conjunction with the momentum, p, measured from the DC*, the particle's mass can be determined as:

*It is important to note that p in this context is the magnitude of the measured momentum, $|\vec{p}|$.

$$m = \frac{p\sqrt{1-\beta^2}}{\beta}. \tag{4.2}$$

In each sector of CLAS, there are 57 BC-408 TOF paddles, which are situated perpendicular to the beam and each covers around 2° of the polar angle. These paddles are split into 4 arrays and mounted together to cover a polar angle of 8° to 142°, as shown in Fig. 4.10. The "forward paddles" refers to the first 23 TOF paddles that cover polar angles of 8° to 45°, with each paddle increasing in length and width from 30 cm to 450 cm and 15 cm to 22 cm, respectively, with the polar angle. The thickness of each paddle is 5.08 cm and they have a PMT mounted on each end. The final 18 paddles, designed for large scattering angles, were combined in pairs. Each of the two scintillators had the same output on each side, resulting in a total of 48 logical counters per sector. The average time resolution of the TOF paddles for electrons was found to be 163 ps [69].

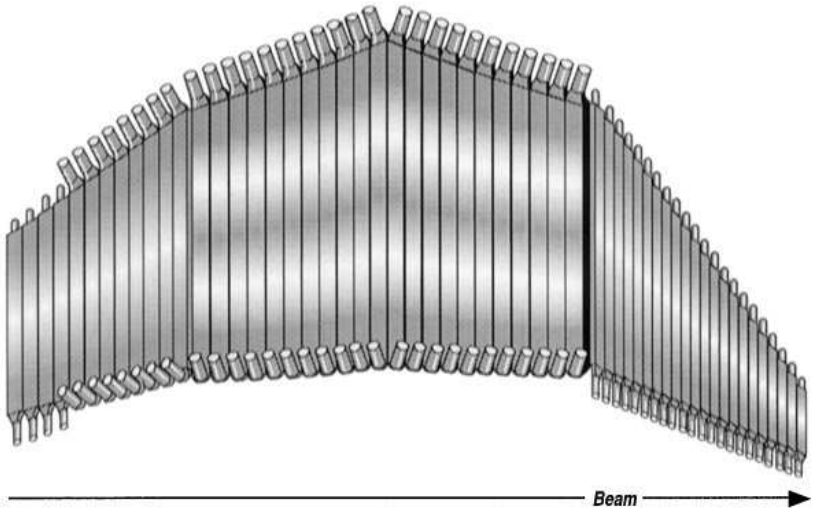

Figure 4.10: A schematic view of the time-of-flight bars where each sector of CLAS houses four arrays of scintillators called panels. The schematic diagram is taken from Ref. [69].

4.5.6 Electromagnetic Calorimeter

The forward Electromagnetic Calorimeter (EC) is a multi-purpose detector system used for electron identification and serves as part of the triggering for electron scattering events, with the additional task of detecting neutral particles with an efficiency of up to 60%. Each sector in CLAS has an EC module, which has a triangular pizza slice shape and is placed about 5 m from the CLAS target cell. The design of the structure minimises the leakage at the edges of the active volume. Each module contains 39 layers of 10 mm thick BC-412 scintillator strips followed by a 2.2 m thick layer of lead to stop the particles. Overall, each module is around 16 radiation lengths long and all layers within the EC are triangular. Each layer of the scintillator is parallel to one side of the triangle, with each

subsequent layer being rotated by 120°.

This formation produces the three different views, U, V and W (see Fig. 4.11), typically referred to as coordinates, that provide information relating to the energy deposited in the EC. In total, there are 13 layers for each coordinate, with the first 5 grouped as "E_{IN}" and the last 8 grouped as "E_{OUT}" to improve particle identification using longitudinal sampling. Longitudinal sampling involves measuring the energy deposited across different layers along the particle's path, which enhances resolution and accuracy. Each layer captures a portion of the total energy deposited by the particle at that specific depth inside the calorimeter. The signals from these layers are then combined to reconstruct the particle's total energy and spatial distribution, thereby improving the energy resolution of the EC. Overall, the lead is 8.4 cm thick and the total scintillator material is 39 cm thick, which results in around a third of the energy being deposited in the scintillators [70]. The timing resolution of the EC for electrons is 200 ps and 600 ps for neutrons, with an energy resolution of:

$$\frac{\Delta E}{E} = 0.003 + \frac{0.093}{\sqrt{E[\mathrm{GeV}]}}. \tag{4.3}$$

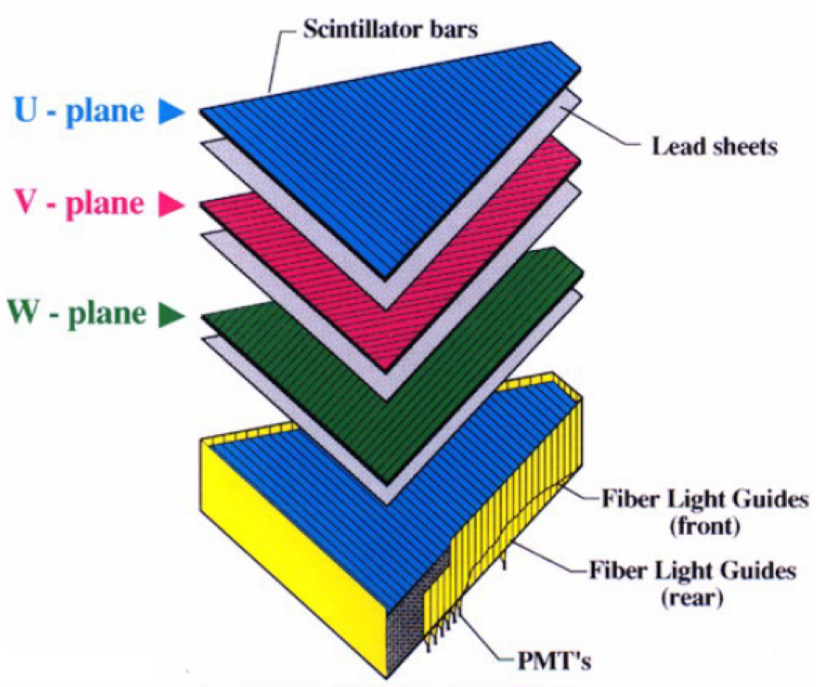

Figure 4.11: A schematic view of the Electromagnetic Calorimeter and the layers inside a single EC module, taken from Ref. [70].

4.5.7 The g9a (FROST) Experiment

The data used for the analysis presented in Chap. 8 was collected during the g9 experimental run that took place between 2007 and 2008, as well as 2010, in experimental Hall B. Specifically, 26 billion triggers were produced utilizing both circularly and linearly polarized photon beams on the frozen-spin butanol target [71] located at the centre of the CLAS spectrometer [64], with spin polarization aligned either longitudinally or transversely to the direction of the photon beam. In addition to the butanol target, additional carbon (^{12}C) and polythene (CH_2) targets were placed downstream of the butanol (C_4H_9OH) target. The purpose of the additional targets was to study the background contributions from bound nucleons present in the carbon and oxygen nuclei of the butanol target. The carbon and polythene targets were 1.5 mm- and 3.5 mm-thick solid disks. The butanol target was a 50 mm-thick liquid target cell. The analysis from this data set utilises data on photoreactions from all targets (butanol, carbon and polythene), with their contributions separated through selections on the reaction vertex (see Fig. 8.7 for the full reaction vertex). For more details of the experimental setup and conditions see Ref. [72]. Table 1 summarizes the experimental conditions for the runs used in our analyses.

Run Period: g9a Target: Frozen-spin butanol CLAS Torus Field: +1918.6 A		
E_e **(GeV)**	**Nominal coherent edges (GeV)**	**Run range**
2.751	0.73 0.93 1.10	55854 - 55938
3.539	1.10 1.30 1.50 1.70	55678 - 55844
4.599	1.90 2.10 2.30	55945 - 56152

Table 4.1: Experimental conditions of the runs used in the g9a analysis presented in Chap. 8. The table provides information for the primary electron beam energies, E_e, used, the coherent edge positions for each primary electron beam energy setting (see Sec. 8.3) and the run numbers used.

4.6 CLAS12

Since the CEBAF was upgraded in 2012, Hall B upgraded its equipment to handle the more intense, higher energy and luminosity electron beam. Since 2017, the CLAS12 detector [73] has been operational and at the forefront of many experiments to date. The detector system largely consists of the old CLAS equipment ($\approx 40\%$), with upgrades to their resolution and design, in conjunction with new detector systems and hardware. Its operation is identical to CLAS, only now with additional detectors to provide more information for physics analyses. Due to the upgrades to CEBAF, the tagging spectrometer was retired, so photon beam experiments are no longer conducted in Hall B, although they remain feasible.

The design of CLAS12 allows the system to be split up into 3 sections; the Forward Tagger (FT) which focuses on very small angles ($\approx 2.5°$), Forward Detector (FD) with θ coverage of $5° < \theta < 40°$ and the Central Detector (CD) with a coverage of $40° < \theta < 140°$. The FT and CD are composed of new detectors, whereas the FD is primarily composed of recycled designs from CLAS with upgrades. A schematic view of the detector system is shown in Fig. 4.12.

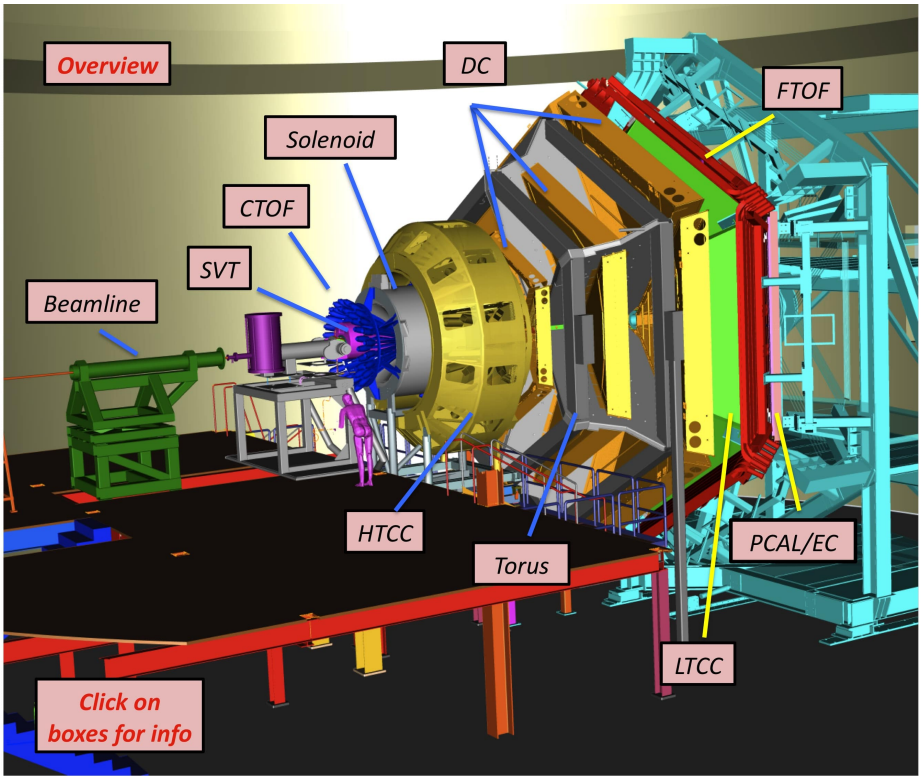

Figure 4.12: A computer-generated image of the CLAS12 detector, with important detector sub-systems for particle identification labelled. The image is taken from Ref. [74].

4.6.1 Upgraded Equipment

- **Drift Chambers**

  There are minor differences between the CLAS12 DC and the DC that operated successfully for 15 years in the old CLAS era. The single major difference in design is the positioning of the DC. In CLAS12, the DC is located further downstream from the target cell, reducing the solid angle coverage of the DC, and providing efficient tracking at higher luminosities, as the accidental occupancy (particles not associated with the event) is lower [75]. The CLAS12 DC has a polar angle resolution of $d\theta <$ 1 mrad and momentum resolution of $dp/p < 1\%$.

- **Forward Time-of-Flight System**

  The CLAS12 Forward Time-of-Flight (FTOF) system replaces the TOF forward paddles from the previous era, with an upgraded design for improved particle de-

tection. There are 6 FTOF systems (1 in each sector) and 3 layers, with each layer consisting of an array of scintillators, with PMTs at both ends, that are positioned just upstream of the CLAS12 EC. The panel-1a arrays are first mounted with the panel-1b arrays mounted just upstream of panel-1a. These two panels have a polar angle coverage of 5° to 35°. The panel-1a array consists of 23 refurbished panel-1 TOF counters from the CLAS spectrometer, while the panel-1b array is a new design, where counters $1-31$ and $32-62$ are BC-404 and BC-408 scintillators, respectively. Panel-2 has an angular coverage of $35° \leq \theta \leq 45°$ and the array consists of 5 refurbished panel-2 TOF BC-408 counters [76]. The three layers are depicted in Fig. 4.13. The size and dimensions (length, width and height) of the scintillators in each array is 32.3 to 376.1 cm, 15 cm and 5 cm (panel-1a), 17.3 to 407.9 cm, 6 cm and 6 cm (panel-1b) and 371.3 to 426.2 cm, 22 cm, 5 cm (panel-2). Panel-1a, 1b and 2 have timing resolutions of $90-180$ ps, $60-110$ ps and $170-180$ ps, respectively. The FTOF system has a 4σ differentiation of pions and kaons up to momenta of 2.8 GeV/c, protons and kaons up to 4.8 GeV/c and protons and pions up to 5.4 GeV/c.

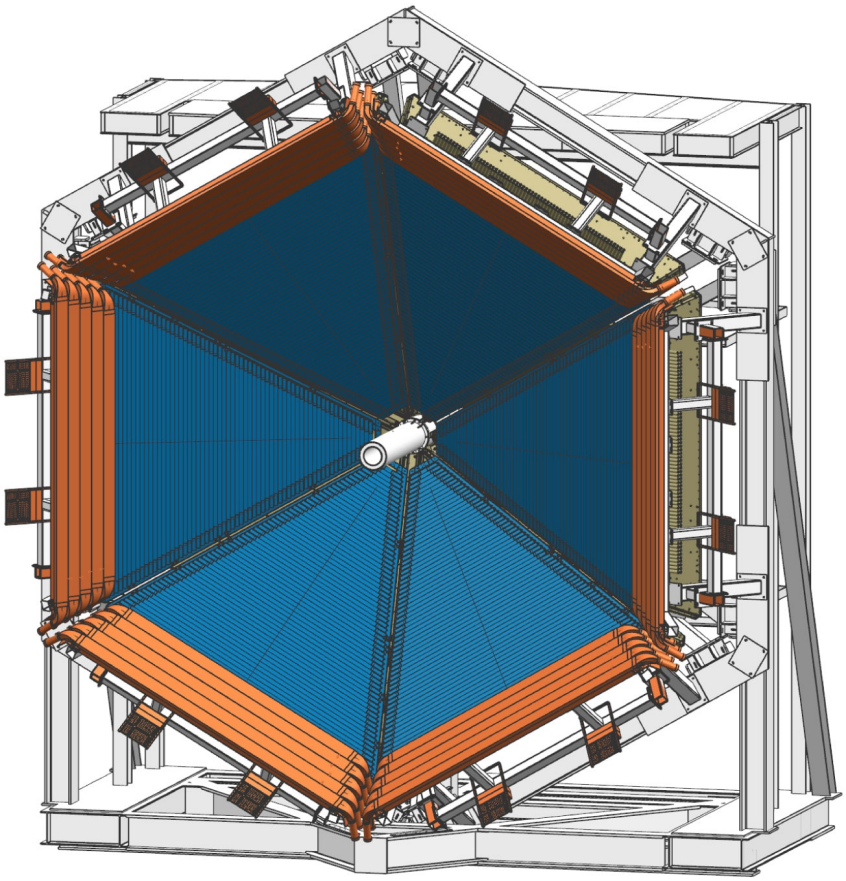

Figure 4.13: A schematic of the FTOF system, where panel-1b is shown in blue and panel-2 is shown in orange. Panel-1a is not visible as it is mounted directly behind panel-1b. This image is taken from Ref. [76]

- **Central Time-of-Flight System**

The CLAS12 Central Time-of-Flight (CTOF) system aims to determine the time-of-flight of charged particles moving under the influence of the solenoid field with polar angles 35° to 125°. The system is a hermetic barrel of 48 scintillator counters positioned at a radius of 25 cm from the beamline. The counters are 3.4 cm wide, 3.0 cm thick and 90 cm long. The counters are housed within the solenoid magnet with light guides mounted to each end of the scintillators to move the light into fringe-field regions. The upstream light guides are 1 m long, while the downstream light guides are 1.6 m long, which are carefully chosen to direct the light to the field-sensitive PMTs (shown in Fig. 4.14) [77]. The operation of these PMTs is only possible through multi-layer magnetic shielding. The CTOF system has a time resolution of 80 ps and has a 3σ differentiation of pions and kaons up to momenta of 0.58 GeV/c, protons and kaons up to 0.93 GeV/c and protons and pions up to 1.14 GeV/c. The minimum momentum threshold for the system is around 300 MeV/c as lower momenta tracks are curled by the solenoid field.

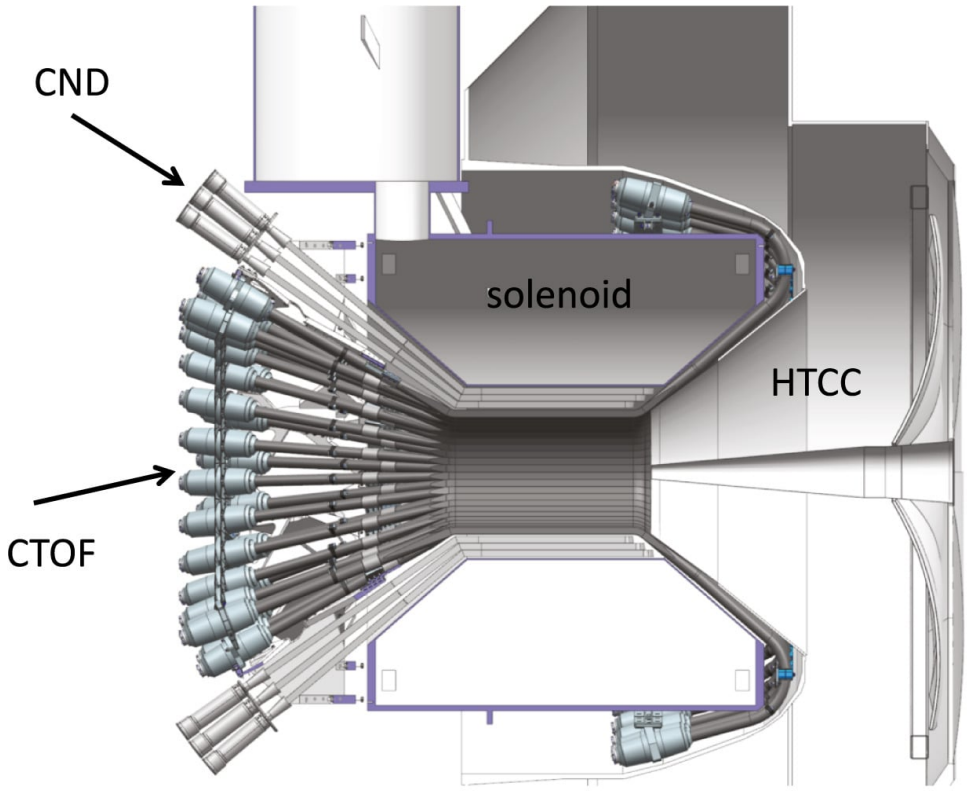

Figure 4.14: A cut view of the CTOF system where it is mounted within the solenoid magnet, where the electron beam travels from left to right and its axis runs along the barrel symmetry axis. This image is taken from Ref. [77]

- **Electromagnetic Calorimeter**

  Each sector of the CLAS12 detector contains a calorimeter package consisting of two modules, the legacy EC from CLAS and a new pre-shower calorimeter (PCAL) located directly upstream of the EC, to extend the coverage of electron detection

up to 12 GeV by introducing a longer total detector radiation length. Together they form the ECAL. The PCAL component is composed of 15 layers of 1 cm-thick scintillators with 14 layers of 0.22 cm-thick lead sandwiched between each layer, which is a similar design to E_{IN} from CLAS [78]. The acceptance of the PCAL is slightly larger than the EC, and it uses a novel triangular hodoscope design (shown in Fig. 4.15) to accommodate CLAS12's hexagonal layout. In the U, V and W layers, there are 84 and 77 strips, respectively, for a total of 1190 scintillator strips installed in each PCAL module. Each scintillator has four WLS fibres to accumulate a total of 4760 fibres per module. To optimise the total number of readout channels, strips are combined into a single readout channel (single PMT). There are 68 PMT readout channels for the U coordinate and 62 for the V and W coordinates [78]. The position, energy and time-of-flight resolution for the ECAL are $\delta r \approx 1$ cm for showers, $\sigma/E \leq 0.1/\sqrt{E(\text{GeV})}$ and ≈ 0.5 ns, respectively.

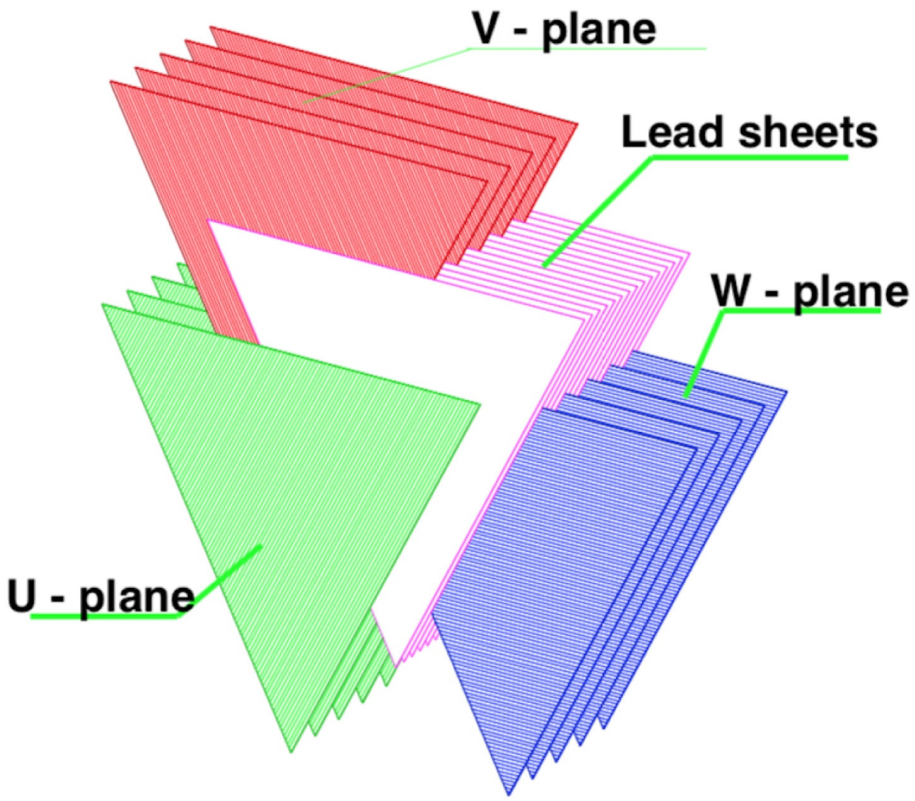

Figure 4.15: A schematic displaying the scintillator layers and the lead sheets for the ECAL, taken from Ref. [78].

- **High Threshold Cherenkov Counters**

  The High Threshold Cherenkov Counter (HTCC) is used to generate quick trigger signals for electron scattering experiments with scattering angles from 5° to 35°. The HTCC is positioned directly in front of the DC and consists of 60 ellipsoidal mirrors. The working gas for the HTCC was CO_2 at 1 atm and 25 °C. To provide efficient coverage of the forward acceptance in CLAS12, in each sector, the HTCC is

Figure 4.16: The fully assembled High Threshold Cherenkov Counter, taken from Ref. [79].

covered by two identical half-sector mirrors that focus the Cherenkov light produced onto 8 PMTs. In total, the HTCC contains 48 channels, each equipped with an 8923QKB PMT, which has a 5-inch quartz faceplate for detecting Cherenkov light [79]. The HTCC provides reliable rejection of negatively charged pions travelling with momenta below 4.8 GeV/c for improved electron identification. The HTCC timing resolution is about 0.6 ns and the fully assembled HTCC is presented in Fig. 4.16.

- **Low Threshold Cherenkov Counters**

  The Low Threshold Cherenkov Counter (LTCC) operates identically to the old CC in CLAS. It utilises the same gas as previously used (C_4F_{10}) and the minor changes to the LTCC aimed to address gas leaks and hardware issues. The LTCC supports pion and kaon separation with momenta from 3.5 to 9.0 GeV/c with a timing resolution of 0.6 ns [80].

4.6.2 Forward Tagger

For experiments discussed here, the Forward Tagger (FT) was turned off, so only a brief discussion will be provided. The FT consists of an electromagnetic calorimeter composed of an array of lead-tungstate ($PbWO_4$) crystals. The crystals measure the energy shower

deposited by particles interacting with the detector and can identify electrons in the energy range $0.5 - 4.5$ GeV. A Micromegas tracker (FT-Trk) is used to measure the scattering angles of the particles (both polar and azimuthal) and a scintillator counter (FT-Hodo) provides e/γ separation. The FT-Cal and FT-Hodo provide rapid responses which can trigger the data acquisition by comparing signals in coincidence from CLAS12 [81]. The polar angle coverage of the FT is 2.5° to 4.5°, with an energy deposition range from $0.5 - 8.0$ GeV, both with resolutions on the few percent level, and a timing resolution of ≤ 300 ps.

4.6.3 Backwards Angle Neutron Detector

The Backwards Angle Neutron Detector (BAND) is designed to measure neutrons emerging from the target at large backward angles of 155° to 175°, with momenta between 0.2 and 0.6 GeV/c. BAND is situated about 3 m upstream of the CLAS12 target cell and consists of 18 rows × 5 layers of 7.2 cm by 7.2 cm scintillator material. There are PMTs at both ends of each scintillator bar that measure the time and energy deposition in the scintillator. There are two layers between the target cell and BAND; first, a 2 cm thick lead wall, followed by a 2 cm veto layer to reject charged particles and minimise photons [82]. BAND has a momentum resolution of $< 1.5\%$ for neutron momenta 200 MeV/c $\leq p \leq$ 600 MeV/c and a timing resolution < 250 ps. The BAND is not used in our analyses.

4.6.4 Central Neutron Detector

Another detector not utilised in our analyses is the CLAS12 Central Neutron Detector (CND), which is a barrel of three layers of scintillators with PMTs connected to 1 m-long bent light guides at the upstream ends and U-turn light guides at the downstream ends. Neutron detection in plastic scintillators involves an indirect process. Neutrons interact with special materials within the scintillator, which undergo nuclear reactions and produce secondary charged particles. These secondary particles ionise the scintillator material, causing it to emit visible light. This scintillation light is then detected by photodetectors, which convert it into an electrical signal for analysis. The design of the CND is such that the light guides and PMTs position themselves away from the CLAS12 solenoid into a fringe-field region. The CND is designed to detect neutrons moving with momenta $0.2 - 1.0$ GeV/c and a polar angle of 40° to 120°. The neutron momentum resolution for the CND is within 10% [83].

4.6.5 CLAS12 Solenoid and Torus Magnet

For the physics program at CLAS12 two superconducting ion-free magnets were required, namely the torus and solenoid magnets [84]. The torus had similar designs to that of the

CLAS configuration since it was NbTi coils connected in series with an operating current of 3770 A. The torus magnet delivers a bending magnetic field for high energy ($0.5 - 10$ GeV) charged particles, along with its structural support for other detectors such as the DC. The torus mainly operates to provide a field for forward scattering particles with polar angles from 2.5° to 45°.

The solenoid magnet was a new edition to the CLAS12 program and it is an actively shielded 5 T barrel-shaped magnet consisting of 5 NbTi coils connected in series at an operating current of 2416 A. The solenoid is positioned upstream from the torus and primarily serves to provide a bending field for low-energy ($0.3-1.5$ GeV) charged particles. It provides important tracking information for centrally scattering particles with polar angles of 35° to 125°. The solenoid has additional purposes which include providing a homogeneous field at the centre of the magnet for the operation of polarised targets, and providing shielding from Moller electrons [84] that allows the CLAS12 system to operate at higher data rates.

4.6.6 Silicon Vertex Tracker

The Silicon Vertex Tracker (SVT) is a solid-state sector comprised of silicon semiconductors, making it affordable for large complex arrays. Semiconductor devices work by having an excess of electrons or holes in the outer shells of the atoms, which are classified as negative (n-type) and positive (p-type). Electrons can travel from the n-type to the p-type material and combine with the holes when the two materials come into close contact with one another. The depletion region, defined as the junction between the two materials, contains neutralised charge carriers. Once radiation enters the depletion region, it produces electron-hole pairs, identical to ionization chamber functionality. Electrons flow towards the p-type semiconductor (due to charge attraction) and holes travel towards the n-type and the total number of electrons accumulated form an electrical pulse which is proportional to the radiation energy.

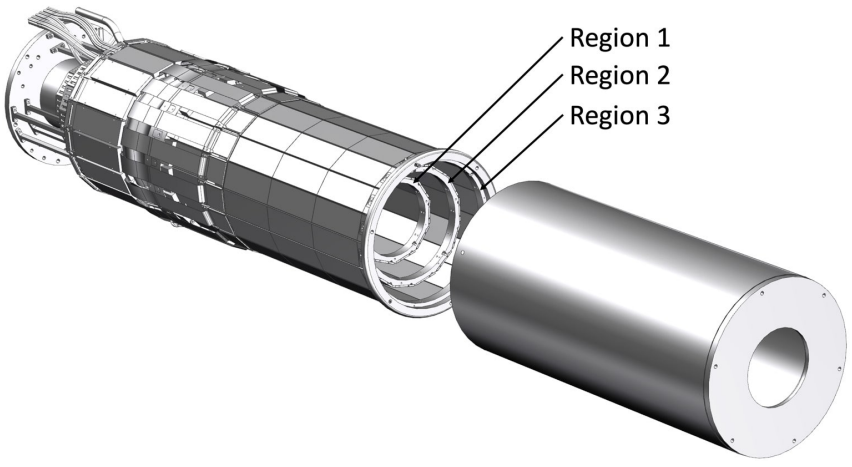

Figure 4.17: An overview of the SVT barrel, taken from Ref. [85].

The SVT is set up similarly to the CTOF: it has 3 sectors and tracks particles with polar angles from 35° to 125°. The SVT has 3 regions (shown in Fig. 4.17), much like the DC, where region 1 (the innermost layer) contains 10 double-sided SVT modules positioned at a radius 65 mm from the beamline. Regions 2 and 3 are positioned at radii 93 mm and 120 mm from the beamline with 14 and 18 SVT modules, respectively. The dimensions of each SVT module are 41.9 cm × 4.2 cm × 0.39 cm. At both ends of the modules are single-sided 320 μm microstrip sensors and three 112 mm × 42 mm sensors (making up 256 strips) that make up each of the two layers [85]. The SVT's momentum resolution is 6% compared to the DC's 1%, hence particles travelling through the central detector have lower quality momentum resolutions than forward travelling particles.

4.6.7 Faraday Cup

Placed further downstream of the CLAS12 spectrometer at the beam dump is the Faraday cup, which is a device used to measure the electron-beam current, shown in Fig. 4.18. The Faraday cup consists of a 4000 kg block of lead, which is placed on ceramic supports inside a vacuum seal [58]. This translates to roughly 75 radiation lengths, which will stop the electrons. A radiation length is a measure of the thickness of a material required to reduce the energy of high-energy particles by a factor of $e \approx 2.718$ (approximately 37%). For lead, with a radiation length of about 0.56 cm, a block with 75 radiation lengths corresponds to a physical thickness of approximately 42 cm.

As the electrons are stopped, their energy is deposited into the Faraday cup and an electrical feed-through determines the total charge deposited into the device. The total charge can be used to determine the incident electron flux on the target, using the following relation:

$$N_{e^-} = \frac{Q_{\text{tot}}}{q}, \tag{4.4}$$

where N_{e^-} is the electron flux, Q_{tot} is the total charge accumulated in the Faraday cup and q is the charge of a single electron ($q = 1.6 \times 10^{-19}$ C). Knowing the electron flux is crucial for cross-section determination in any electron scattering experiment.

4.6.8 The Run Group M Experiment

The Run Group M (RGM) experiment, which collected data between November 2021 and October 2022 in experimental Hall B, utilised many different targets and beam energies, and the target properties are summarised in Tabs. 4.2 and 4.3. It was the first experiment in the CLAS12 era to utilise a target heavier than deuterium, with the aim of studying nuclear reactions. Electron beams of energies 2.071, 4.030 and 5.986 GeV were impinged on the various nuclear targets, where four unique target cells were used: the standard

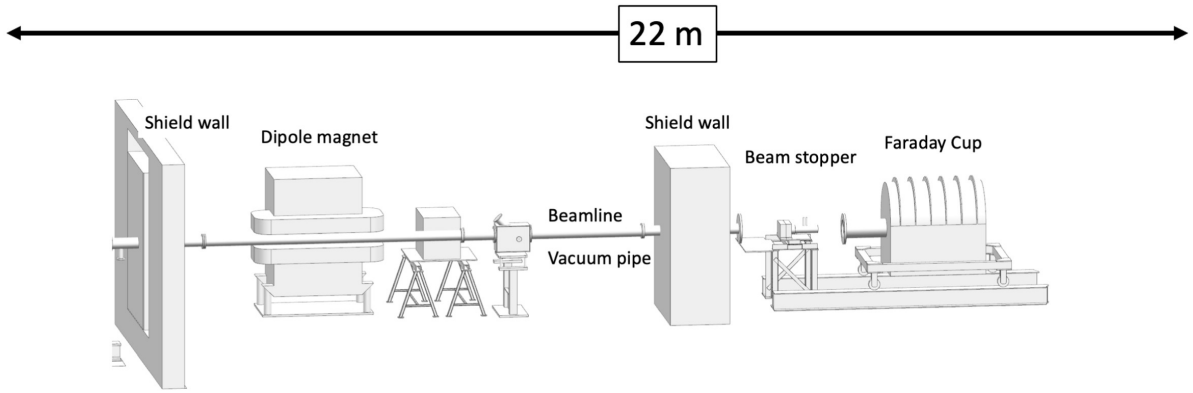

Figure 4.18: An overview of the beamline beyond the CLAS12 spectrometer, showing the positioning of the Faraday cup, taken from Ref. [73].

CLAS12 liquid target cell (5 cm thick), calcium, 4-foil targets (^{120}Sn/^{12}C) and a liquid argon cell (0.5 cm thick, which included single-foil targets for ^{120}Sn/^{12}C). Figure 4.19 presents the design drawings of each target cell with the coordinates given in units of mm from the Hall centre. The materials used to construct the cells and support the target operation are also provided.

Target	**Total Areal Density (mg/cm^2)**	**Thickness (cm)**	**State**
^{1}H	354.25	5.0	Liquid
^{2}D	819.00	5.0	Liquid
^{4}He	625.00	5.0	Liquid
^{40}Ca	148.10	0.2	Solid, 1 Foil
^{40}Ca	304.90	0.2	Solid, 1 Foil
^{48}Ca	288.50	0.2	Solid, 1 Foil
^{12}C	450.00	0.2	Solid, 4 Foil
^{12}C	440.00	0.2	Solid, 1 Foil
^{120}Sn	202.86	0.028	Solid, 1 Foil
$^{\text{Natural}}$Sn	182.00	0.025	Solid, 4 Foil
^{40}Ar	698.00	0.5	Liquid

Table 4.2: Target properties and dimensions for the RGM experiment.

4.7 Data Acquisition

The detector systems used in Hall B, and in other physics experiments, experience a massive flux of signals in which only a small proportion of these signals can be used for data collecting. Therefore, for accelerator-based experiments, these signals must be filtered rapidly (orders of kHz) to ensure the data collection of useful events. The CLAS12 Data Acquisition (DAQ) operates on such scales, recording data at speeds reaching a few hundred MB/s, equating to a livetime (this is the measure of how sensitive the experiment is to the events of interest) of 95% [87]. The conditions for storing an event are broad and

Target	Beam Energy (GeV)	Integrated Luminosity (fb^{-1})	Total Charge (mC)
^{1}H	5.986	3.68	2.92
^{1}H	2.071	0.39	0.31
^{2}D	5.986	52.00	16.87
^{2}D	2.071	1.81	0.59
^{4}He	5.986	57.24	24.37
^{12}C	5.986	80.31	48.56
^{12}C	4.030	10.46	6.33
^{12}C	2.071	1.00	0.60
^{40}Ar	5.986	4.91	1.87
^{40}Ar	4.030	6.67	2.54
^{40}Ar	2.071	1.35	0.51
^{40}Ca	5.986	51.59	44.28
^{48}Ca	5.986	20.75	17.81
^{120}Sn	5.986	9.29	12.06

Table 4.3: Target and beam energy information for the RGM experiment.

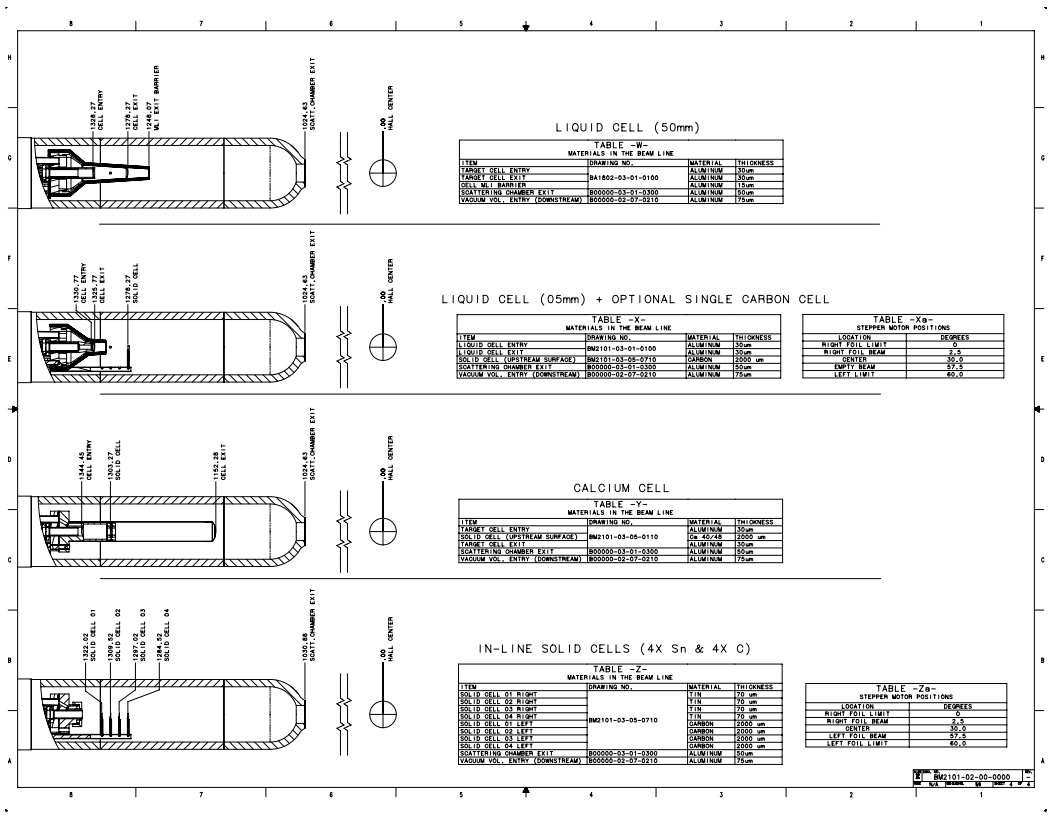

Figure 4.19: The design drawings of the different RGM target cells used in the experiment. Drawings provided by [86].

specific to the experiment but typically depend on hardware responses and the physics requirements of the experiment. The RGM experiment required a particle (of any charge) in the FD and was a broad requirement, as the RGM group are interested in inclusive cross-sections for electron scattering.

4.8 Data Processing

Once the data has been collected from the experiment it undergoes a few post-experiment processes to translate the detector information to real physical values (momentum, energy, velocity).

4.8.1 Data Cooking

The raw data in most particle physics experiments, particularly in Hall B experiments, is stored in files containing all the relevant detector information collected from the numerous detector systems used that measure channel IDs and values for the Charge-to-Digital Converters (QDCs), which measure the total charge or energy deposited in a detector and convert this analogue signal to a digital value, and Time-to-Digital Converters (TDCs), which measure the time at which a signal is detected and converts the information measured into a digital value. These quantities must be converted into physical values (e.g. particle momentum) through a lengthy process referred to as "cooking". The data is stored on an event-by-event basis, with each detector system having its own 'bank' for the storage of data. Each bank contains all the relevant information collected by the detector system for each event. Each bank can be accessed as required for calibration and analysis purposes. The data must be calibrated after the cooking process before it can be fully analysed. The new CLAS12 data utilises an 'online' calibration, with the assistance of artificial intelligence, to filter bad events more efficiently. These are calibrations which are performed while continuing to collect data from the experiment. Further calibrations are still required for a full analysis of the data set.

4.8.2 Data Calibrations

Calibrations are critical to the fine-tuning of experimental data to reproduce well-established results and remove offsets present in the data. For example, proton tracks are well understood and the time-of-flight of protons should be reproduced by the data. Careful calibrations ensure this is the case. Both data sets analysed in this thesis from the two eras of Hall B's experimental program utilise several detectors, which are carefully calibrated on a collaboration-wide scale. Once the detector subsystems are calibrated and reproduce well-known physical observables, the experimental data is ready for re-cooking. Re-cooking involves cooking the data from the raw data files with the addition of calibration constants to provide a calibrated data set. This data is then stored in the relevant file types for the analysis - Bank Operating System (BOS) for CLAS and High-Performance Input/Output (HIPO) for CLAS12.

4.8.3 Data Skimming

The data sets collected at JLab are typically several terabytes in size, especially the g9a and RGM data sets which employed loose trigger conditions. The large data size results in a longer run time of the analysis code, as the events of interest must be extracted from millions of events not containing the particles of interest. The processing time of the analysis is reduced by "skimming" the data, which is a process that reduces the file size of the data*.

For the g9a analyses performed in this thesis, we reduce the file size by selecting candidate proton tracks with measured speeds, $\beta = \frac{p}{E}$, between

$$\begin{aligned} \beta_{\text{min}} =& \frac{p}{\sqrt{p^2 + (1.1\ \text{GeV/c})^2}} - 0.06, \quad \text{and} \\ \beta_{\text{max}} =& \frac{p}{\sqrt{p^2 + (0.8\ \text{GeV/c})^2}} + 0.06, \end{aligned} \tag{4.5}$$

where the equation above is derived using the energy-momentum-mass relation ($E = \sqrt{p^2 + m^2}$). The β cuts are deduced to significantly reduce the file size whilst retaining data with a minimum of 4.5σ around zero in the $\Delta\beta$ distribution (shown in Fig. 8.2), where $\Delta\beta$ is the difference between the velocity measured by the time-of-flight system and the calculated velocity by assuming the particle's mass and using the particle's momentum measured by the drift chambers. These cuts do not affect the final analysis since the particle identification cuts for the many-proton knockout analysis, discussed in Chap. 8 and shown in Fig. 8.2, provide a tighter restriction on the events of interest.

Figure 4.20 presents β as a function of momentum for positively charged tracks (data from 4 random unskimmed runs) from the g9a data. The loci of protons and pions are clearly seen and the loose skim cuts applied are shown by the red lines (upper region are pions, lower region are protons).

In addition to the cuts discussed above, we also count the number of positive, N_{pos}, negative, N_{neg}, and neutral, N_{neu}, particles and we check that no negative particles are detected in the event. We require that the number of positives is equal to the number of protons in the event, i.e. there are no other positive particle species in the event. Since the efficiency of neutral particles was notoriously low in CLAS experiments, we do not reject the small fraction of events with uncharged particles in our analysis†.

*The skim selection cuts are not the final cuts applied to the analysis performed. Their purpose is to preserve all events of interest, while removing problematic events to significantly reduce the data file size, allowing for a more efficient detailed analysis

†Comparisons were performed with and without the inclusion of neutral particles which showed no significant effect on the reactions of interest.

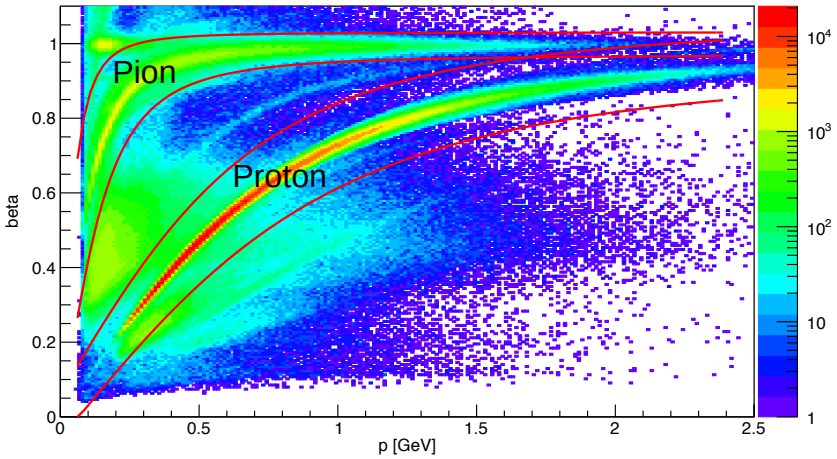

Figure 4.20: β as a function of momentum of positively charged tracks before any skim cuts. The red lines show the skim cuts applied to select pions (top two red lines) and protons (bottom two red lines) (data from 4 random runs is shown). The pair of red lines show the cuts imposed for pions and protons, respectively.

The analysis performed with the RGM experiment poses a significant challenge for skimming. Since the work aims to benchmark the methodology employed at neutrino facilities (who do not know the initial beam energy) for many different reactions (including inclusive scattering), there are only a limited number of skim cuts that can be applied. Events with candidate electron triggers (i.e. a scattered electron) are retained, while events not including a scattered electron are removed. No additional cuts are applied to the final state particles due to the wide demographic of reaction channels investigated.

Chapter 5

Simulation Details

"In theory, theory and practice are the same. In practice, they are not."

- Albert Einstein

Many analyses in particle and nuclear physics aim to compare the results of experimental data with the predictions of a theoretical model. The data generated by the theoretical model, typically referred to as simulated data, is usually produced for the full phase space, for instance, the full polar angle coverage (0° to 180°). Experimental setups, as we have seen from Chap. 4, almost certainly have gaps in the physical acceptance of the detector systems used, and the efficiency of the detectors is not perfect. It is important to consider these effects as the measured (visible) cross-section is proportional to the following observables:

$$\sigma^{\text{vis}} \propto \frac{N \times \epsilon \times A}{L}, \tag{5.1}$$

where N is the yield (observed number of events), ϵ is the efficiency of the detector system, A is the acceptance, and L is the luminosity.

As an example, the CLAS TOF paddles can only detect particles with polar angles ranging from 8° to 142°; therefore, if a theoretical model had perfectly modelled a reaction observed in CLAS (with perfectly efficient TOF paddles) the cross-section predicted by the model would differ from that observed in the experiment due to acceptance effects. Hence, to produce meaningful comparisons with the experimental data, the geometry of the experimental data must be implemented into the simulated data. In the context of comparing GiBUU and GENIE to the CLAS and CLAS12 detectors, they must be simulated through a virtual CLAS and CLAS12 detector that captures the full properties of each respective detector system.

The measured cross-sections are visible cross-sections within the acceptance of the detector system used. The simulated data is crucial in obtaining the total cross-section as the

acceptance effects must be removed from the visible cross-section to obtain a total cross-section. This is done by analysing the total number of events observed in the theory data before and after applying the detector geometry into the theory data. The acceptance correction is given by the following equation:

$$A = \frac{\text{Processed MC}}{\text{Pure MC}}, \tag{5.2}$$

where Processed MC refers to theory data that has undergone detector simulations and Pure MC is the theory data as generated by the theoretical model. Visible cross-sections, σ^{vis}, which are the measured cross-sections within the detector acceptance and efficiency (geometry), are powerful observables that are simpler to obtain, as (typically) more steps, other than acceptance corrections, must be implemented to obtain a total cross-section. It should be noted that if the theory model correctly models the cross-section in all phase spaces, then both the visible and total cross-sections between the experimental and simulated data will match. However, if the total cross-section agrees, the visible cross-section may not agree (and vice versa), as visible cross-sections limit observables such as momentum and angle to specific ranges. Throughout our analyses, we measure visible cross-sections as fewer steps are required to measure them.

5.1 GSIM

The GSIM framework for simulating the theoretically generated data through the CLAS detector utilizes the GEANT routines from CERN libraries to produce a Monte Carlo-based simulation of the CLAS detector. The GSIM framework is based on GEANT3, which was written in Fortran-77 (F-77) and was not upgraded to the more modern GEANT4, which is based on C++. It implements key variables to the theoretical data, such as the timing information for the particles, the detector geometry, and measured particle velocities, to name a few. Importantly, GSIM implements the CLAS detector acceptance and efficiency into the theoretical data we have generated and allows us to implement identical analysis conditions to those in the experimental data. This allows for a direct comparison of the visible cross-sections measured in the experiment with those predicted by the theoretical model. Further details of the GSIM framework can be found in [88]. The GSIM framework was used for the analysis presented in Chap. 8.

Figure 5.1 presents the virtual CLAS detector in GSIM, where all detector components in CLAS (TOF, EC, DC, etc.) are visible (as in Fig. 4.6), and the red lines present simulated particles traversing the detector medium. As an example, TOF paddles that were dead during a particular run period are turned off in GSIM, and the efficiencies of paddles (especially low-efficiency paddles) are matched for the simulation. This is to ensure the efficiency of the simulated data matches the experimental data. Different experiments

conducted during the CLAS era can be simulated by feeding the GSIM package with an Ffread card as a command-line argument when executing the GSIM software, which simulates particles through the virtual CLAS detector. The Ffread card is a geometry file that specifies crucial experimental parameters such as target position, type, composition, experiment number, and magnetic field strength, among others. This information is passed to GSIM, enabling a simulation that accurately reflects the specific experimental conditions. The Ffread card is essentially a simple text file containing variable names and corresponding values that define the conditions of the experiment. Before running GSIM, the software implements these features and appropriately matches the efficiencies of detector systems and simulates particles emerging from the specified target position, where the trajectory of charged particles is influenced by the given magnetic field strength. It is also important to note that GSIM implements detector resolution and smearing into the simulated data. This is important, as resolution and smearing effects contribute to the widths of observed distributions. Detector resolution refers to how accurately a quantity can be measured and provides an uncertainty on the measurement. For example, a momentum resolution of 0.1 GeV/c will exhibit a broader distribution for observables calculated using the momentum than an experimental setup with a momentum resolution of 0.01 GeV/c.

The half-life of particles and resonant states is also implemented into GSIM. For example, in CLAS experiments, due to the distance of the EC from the target position, neutral pions are not directly measured, as the neutral pion has a half-life of around 10^{-17} s. The two photons that decay from the neutral pion are detected and the neutral pion is reconstructed from the two measured photons. This is also the case in GSIM, as neutral pions in the final state in GiBUU and GENIE will decay into two photons in GSIM. This also causes some resonant states with sufficiently long half-lives to travel some distance through the detector medium before decaying, and this decay can be simulated in GSIM by turning on the appropriate flags.

The GSIM package is run by first converting the generated theory data format into Bank Operating System (BOS) files. The appropriate Ffread card for the experimental data used is fed to the GSIM framework with the theory data in the BOS format as the input data, and the theory data is then simulated through the virtual CLAS detector. A package called gpp is implemented to then smear the simulated data to match the effects seen in the experimental data (also experiment dependent). Finally, the reconstruction software (user_ana) is used to reconstruct all the particles and their information for each event. This requires a tcl file, which contains information related to the reconstruction algorithm (also experiment dependent). The tcl file is used to "cook" the data and translate detector information (TDC and ADC values) to physical information (energies and momenta). The reconstructed data is given in the BOS format, and using rootbeer [90] it can be transformed into ROOT trees for ease of use.

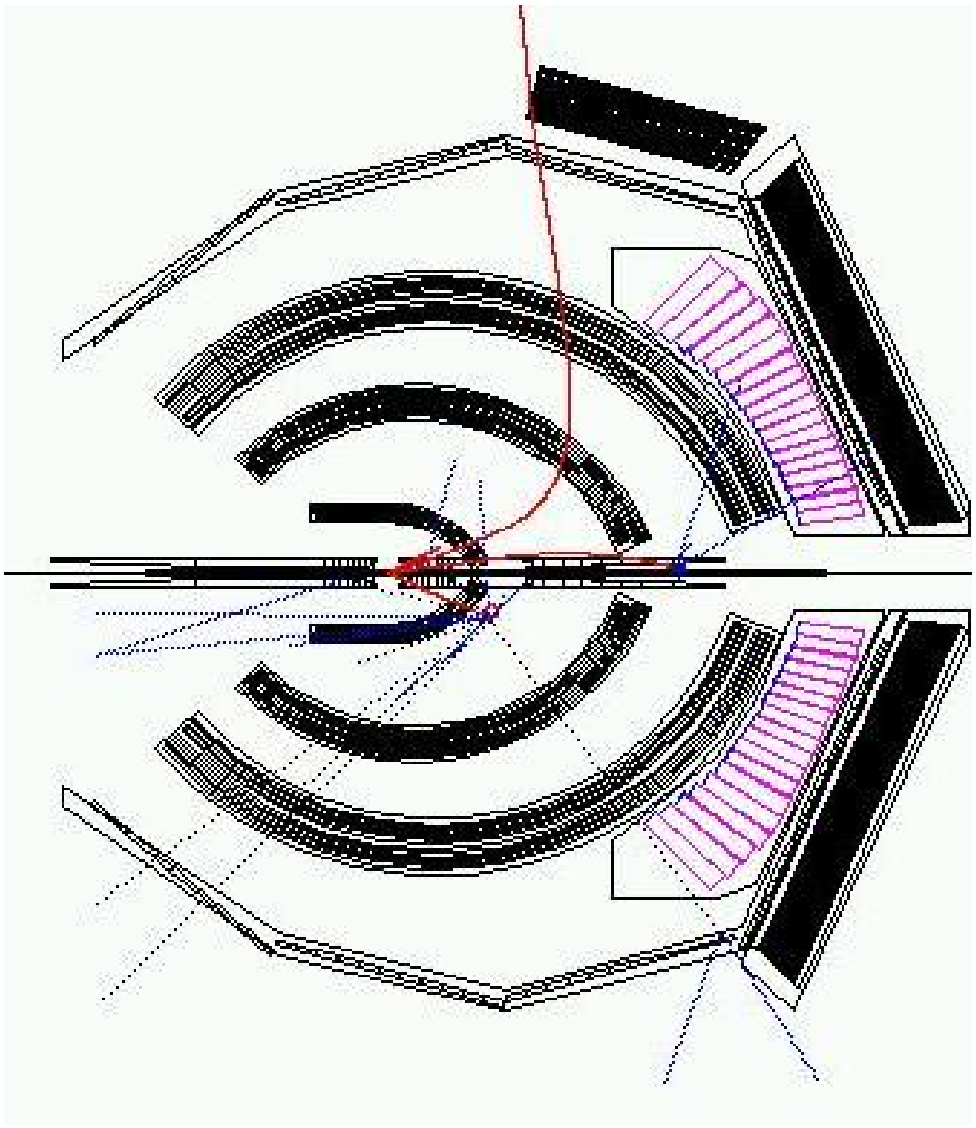

Figure 5.1: A Computer computer-generated image of the virtual CLAS detector used in the GSIM package to simulate theoretical data through the CLAS geometry. The straight dashed blue lines present neutral particles traversing through the detector (since they are straight lines) and the curved solid red lines depict charged particles traversing the detector medium under the influence of the magnetic field, hence their curved trajectory. The image is taken from Ref. [89].

5.2 GEMC

GEMC has similar principles to the GSIM framework, but it is a C++ framework that utilises the newer GEANT4 packages to simulate particles passing through a virtual CLAS12 detector. Figure 5.2 outlines the general procedure of GEMC which is similar to the GSIM framework. All important features such as acceptance, efficiency and resolution matching are consistently implemented in the two simulation packages, with smearing also implemented in GEMC. The major difference between the two, apart from the two different detector systems modelled, is that the GEMC framework reads in the theory data in the LUND file format [91] and reconstructs the data simulated through

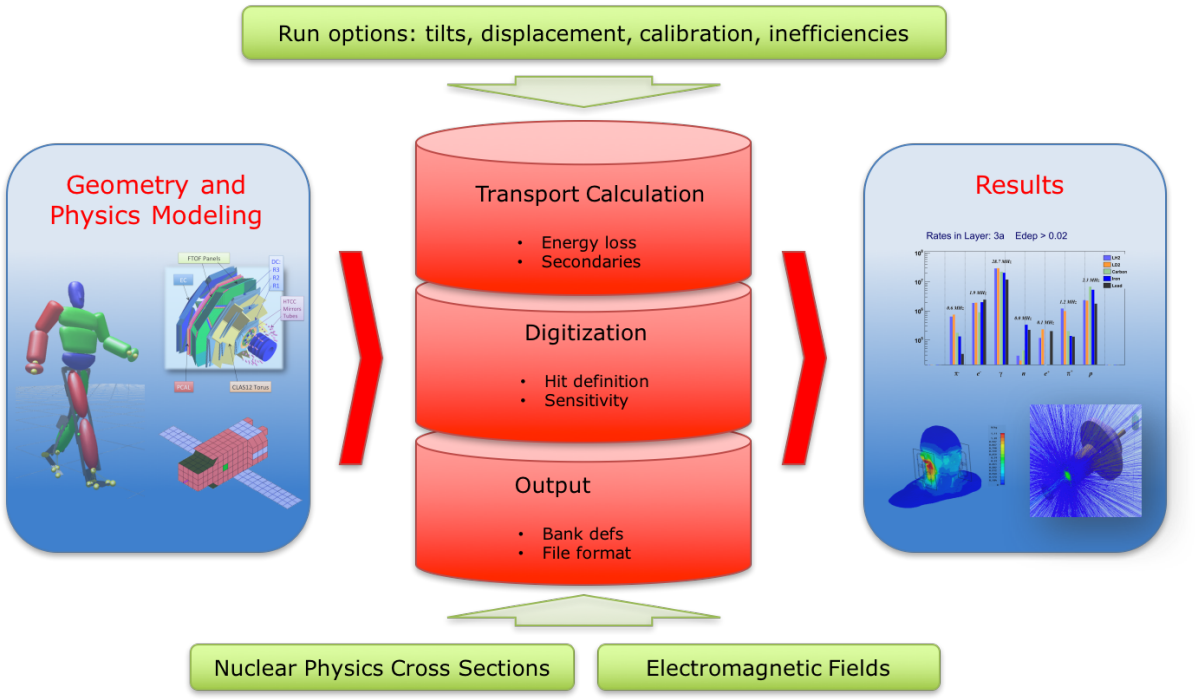

Figure 5.2: A flow chart for the simulating procedures of GEMC, taken from Ref. [92].

the virtual CLAS12 detector into HIPO files. This change is due to how the data in the new CLAS12 experiments are stored and that the reconstruction algorithm is written in JAVA. More details on the GEMC package can be found in [92]. The GEMC framework was used for the analysis presented in Chap. 9.

Chapter 6

Particle Selection

"The art of simplicity is a puzzle of complexity."

- Douglas Horton

This chapter provides a general overview for selecting a charged track as a "good" candidate for the particle of interest from a data set, be it experimental or simulated. The concepts explained here are common to both the many-proton knockout and the e4nu analyses, which despite differences in detector geometry, both obtain particle identification (PID) from combined measurements of track curvature and time-of-flight. As well as these, general principles for obtaining tagged real photon beams, as used in the many-proton knockout analysis are outlined.

Specific details of the bespoke PID procedures for each analysis are presented in later chapters (Chap. 8 and Chap. 9, respectively).

6.1 Particle Charge and Momentum

A charged particle with charge, q, travelling through a magnetic field, $\vec{B}$, with velocity, $\vec{v}$, will experience a force, $\vec{F}$, called the Lorentz Force. The Lorentz force is given by:

$$\vec{F} = q\vec{v} \times \vec{B}. \tag{6.1}$$

For a body moving in circular motion, the centripetal force required to keep the particle in its circular path is given by:

$$\vec{F_c} = \frac{mv^2}{r}\hat{r}, \tag{6.2}$$

where $\hat{r}$ is the unit vector pointing from the particle towards the centre of the circular

path, m is the mass of the particle, v is the speed and r is the radius of the circular trajectory.

In a magnetic field, the Lorentz force acts as the centripetal force. By equating the magnitude of the Lorentz force to the magnitude of the centripetal force, and considering that the magnetic field $\vec{B}$ is predominantly perpendicular to the velocity $\vec{v}$, the momentum of the particle is determined by:

$$p = qBr. \tag{6.3}$$

The particle's charge is determined based on its curvature since Eq. (6.3) shows that negative and positive particles will bend in opposite directions under the influence of a magnetic field. A schematic diagram presenting the influence that magnetic fields hold over charged particles, alongside a real experimentally observed electron travelling through a magnetic field, is shown in Fig. 6.1.

From detector information, the particle's four-vector, p^{μ}, is then determined and defined

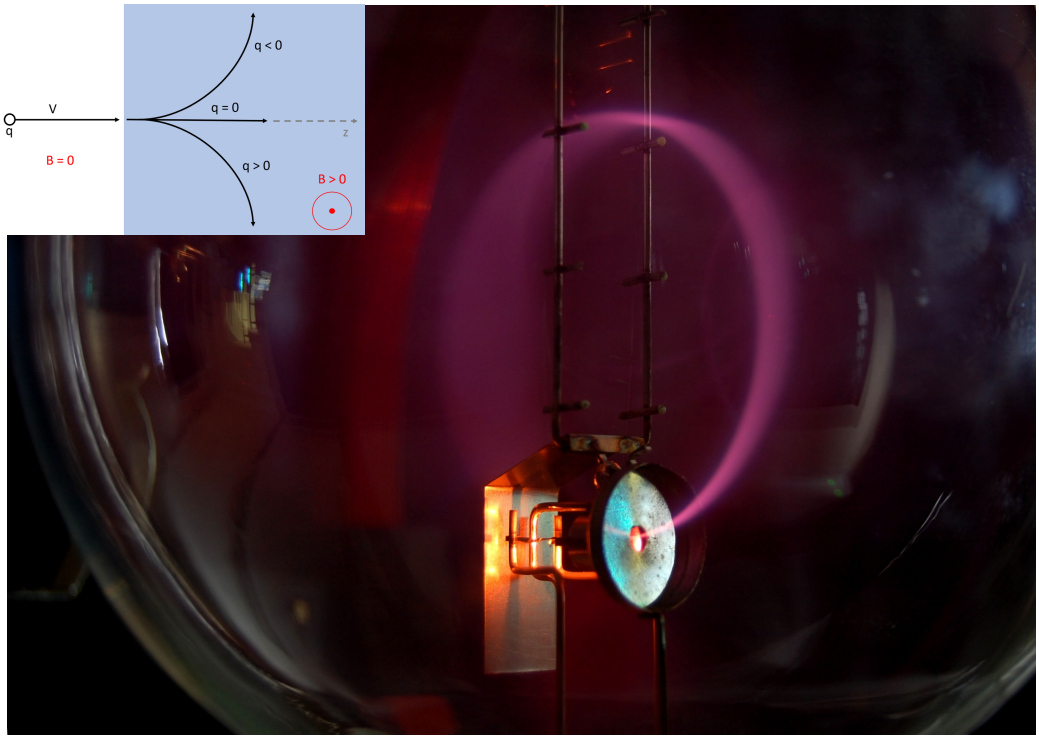

Figure 6.1: An overlayed diagram and photograph showing the effect of magnetic fields on charged particle trajectories. The smaller overlayed picture presents a schematic of charged particles influenced by a magnetic field, with the blue-filled zone indicating a region where the magnetic field is perpendicular and coming out of the paper. The main image, taken from Ref. [93], presents experimentally observed electrons traversing through a magnetic field, leaving a pink mist due to fluorescence as the fast-moving electrons interact with air molecules. The electrons travel vertically upwards as their charge is negative, in line with the smaller overlayed image.

as:

$$p^{\mu} = (\vec{p}_x, \vec{p}_y, \vec{p}_z, E), \tag{6.4}$$

where $\vec{p}_x$, $\vec{p}_y$ and $\vec{p}_z$ are the x, y and z components of the particle's three-momentum and E is the sum of the kinetic and rest energy of the particle. The angular components (namely the polar (θ) and azimuthal (ϕ) angle) of the four-vectors can be determined by the following equations:

$$\theta = \cos^{-1}\left(\frac{\vec{p}_z}{|\,\vec{p}\,|}\right) \qquad \text{and} \qquad \phi = \arctan 2\left(\vec{p}_y, \vec{p}_x\right), \tag{6.5}$$

and the function $\arctan 2(\vec{p}_y, \vec{p}_x)$ is defined as:

$$\phi = \arctan 2(\vec{p}_y, \vec{p}_x) = \begin{cases} \arctan\left(\frac{\vec{p}_y}{\vec{p}_x}\right) & \text{if } \vec{p}_x > 0, \\ \arctan\left(\frac{\vec{p}_y}{\vec{p}_x}\right) + \pi & \text{if } \vec{p}_x < 0 \text{ and } \vec{p}_y \geq 0, \\ \arctan\left(\frac{\vec{p}_y}{\vec{p}_x}\right) - \pi & \text{if } \vec{p}_x < 0 \text{ and } \vec{p}_y < 0, \\ +\frac{\pi}{2} & \text{if } \vec{p}_x = 0 \text{ and } \vec{p}_y > 0, \\ -\frac{\pi}{2} & \text{if } \vec{p}_x = 0 \text{ and } \vec{p}_y < 0, \\ \text{undefined} & \text{if } \vec{p}_x = 0 \text{ and } \vec{p}_y = 0, \end{cases} \tag{6.6}$$

where $|\,\vec{p}\,|$ is the magnitude of the three-momentum and $\arctan 2\left(\vec{p}_y, \vec{p}_x\right)$ is a function that returns the angle whose tangent is the quotient of the arguments. This two-dimensional function ensures the correct sign is assigned, regardless of the signs of the momentum components, and is defined between $(-\pi, \pi)$ radians.

6.2 Particle Speed

The time-of-flight system determines the particle's timing information, namely the time-of-flight, t_f. This quantity corresponds to the time difference between the particle's ejection from the target (i.e. the event start time) and its detection in the time-of-flight system. The event start time is determined by the reconstruction software by comparing the hit times in the start counter to the RF electron beam bunch times. In traversing from the target to the time-of-flight system, the particle covers a distance, d, which is determined from the reconstructed track length in the drift chambers. Therefore, the particle's speed as a fraction of the speed of light, c, is given by:

$$\beta = \frac{d}{c \times t_f}. \tag{6.7}$$

6.3 Scattered Electron Selection

Electron scattering experiments (such as the e4ν analysis presented in Chap. 9) rely on the detection of the scattered electron to initiate the data collection for the event, which is referred to as the trigger electron. CLAS12 experiments in Hall B put the trigger particle through a collection of particle selection cuts. For the electron to be considered a trigger particle in CLAS12 and successfully initiate data collection for the event, it must register at least one hit in the FTOF, HTCC and ECAL. The charge of the particle must also be identified as negative in magnitude. The electron trigger selection criteria for the e4ν project will be outlined in Chap. 9.

6.4 Photon Selection

In photon beam experiments (such as the many-proton knockout analyses presented here), it is important to identify the incident photon interacting with the target. Photons that pose as candidates have a correlated time between the calculated arrival time of the photon at the target, t_γ (from the tagger), and the vertex time of the fastest particle ejected from the target, t_v, calculated using information from CLAS. The vertex time of the fastest particle is given by:

$$t_v = \left(t_{SC} - \frac{l_{SC}}{\beta_{\text{calc}} c} \right), \tag{6.8}$$

where t_{SC} is the time-of-flight of the charged track, l_{SC} is the path-length of the charged track, determined from the time-of-flight system, β_{calc} is defined by Eq. (6.11) and c is defined as before. The vertex time of the photon was calculated using the photon time deduced from the tagger and propagated to the event vertex:

$$t_{v,\gamma} = \left(t_\gamma + \frac{z}{c} \right), \tag{6.9}$$

where t_γ is the photon time and z is the z-vertex position of the charged track (typically at the position of the physical target during the experiment). Hence the coincidence time, Δt_γ, is calculated as the difference between the two variables:

$$\Delta t_\gamma = t_{v,\gamma} - t_v. \tag{6.10}$$

If the time-of-flight system and tagger are well calibrated, then the times will be identical, hence the coincidence time will be minimal. The cut defined for the coincidence time is typically determined by fitting a Gaussian to the Δt_γ distribution.

Additionally, there may be more than one photon that results in a minimum coincidence

time between the selected windows. It is important to identify which photon initiated the interaction, but it can complicate the analysis. Therefore, removing all events with more than one photon consistent with the vertex time is a well-established technique. Events with no photons consistent with the vertex time correspond to accidental events, and these are also removed from further analysis.

6.5 Particle Identification

Particle Identification is determined by directly comparing two separate and independent determinations of the particle's velocity. Namely, β_{meas}, which is the velocity as measured using the time-of-flight system, is compared to β_{calc}, the particle's velocity calculated using information from the drift chambers and assuming the particle's mass:

$$\beta_{\text{calc}} = \frac{p}{\sqrt{p^2 + m^2_{\text{PDG}}}}, \tag{6.11}$$

where $m_{\text{PDG}} = 0.9383$ GeV/c^2 is, for example, the proton mass from the particle data group [1]. The two quantities are heavily correlated and particles whose β_{meas} varies from β_{calc} are discarded. A further distribution of $\Delta\beta$ is studied to determine the strictness of the cut employed*, where $\Delta\beta$ is given by the following equation:

$$\Delta\beta = \beta_{\text{meas}} - \beta_{\text{calc}}. \tag{6.12}$$

This cut is employed in the g9a experimental data analysis, but for the RGM experiment a different particle identification technique (identical to $\Delta\beta$) was employed.

The coincidence time, for events with many particles in the final state, can constrain the timing information between each subsequent particle in order of descending momentum. The time between subsequent particles, or ΔTOF, is calculated as:

$$\Delta TOF = t_{v,p_i} - t_{v,p_j} = \left(t_{p_i,SC} - \frac{l_{p_i,SC}}{\beta_{p_i,\text{calc}}c}\right) - \left(t_{p_j,SC} - \frac{l_{p_j,SC}}{\beta_{p_j,\text{calc}}c}\right), \tag{6.13}$$

where $i = 2, ..., n$ and $j = i - 1$, with n being the total number of particles in the final state, and the other variables are defined as before, but now for specific particles. The particle with the fastest momentum can be taken as the reference particle since it will have the largest momentum translating to the best resolution, which will result in fixing $j = 1$. Likewise to Δt_γ, subsequent particles with consistent timing information between the given timing windows, deduced from a Gaussian fit to the timing distribution, will be

*$\Delta\beta$ is also typically studied as a function of momentum, given the momentum plays a role in its determination.

kept for further analysis. This method applies to charged hadrons and leptons, where (at JLab) electrons are assumed to have the speed of light given their low mass and the high minimum momentum threshold (300 MeV/c).

6.6 Energy and Momentum Corrections

Charged particles travelling through the physical matter of the detector mediums will lose energy by interacting with the electrons in the matter, leading to the excitation or ionization of the atoms. The Bethe-Bloch formula [1] describes the mean rate of energy loss (also referred to as stopping power) of a charged particle travelling through matter due to ionization and excitation of the atoms in the medium:

$$-\frac{dE}{dx} = \kappa z^2 \frac{Z}{A\beta^2}\left[\frac{1}{2}\ln\frac{2m_e c^2\beta^2\gamma^2 T_{\max}}{I^2} - \beta^2 - \frac{\delta(\beta\gamma)}{2}\right], \tag{6.14}$$

where A and Z are the atomic mass and atomic number of the absorbing material, respectively, I is the mean excitation energy of the atoms in the absorbing material (which is material dependent), z is the charge of the incident particle in units of elementary charge e, β is the velocity of the particle relative to the speed of light, $\gamma = 1/\sqrt{1-\beta^2}$ is the Lorentz factor $T_{\max}$ is the maximum kinetic energy which can be imparted to a free electron in a single collision, and κ is a constant which depends on the classical electron radius, Avogadro's number and the mass of the electron. $\delta(\beta\gamma)$ is the density correction that accounts for particles moving with high velocities, where the electric field of the charged particle becomes flattened due to Lorentz contraction, thereby reducing the energy loss.

The energy dissipated by the charged particles needs to be modelled and corrected. In the example of CLAS and CLAS12, a software package called eloss was developed to correct for the energy lost. As previously stated, the momentum of charged particles is determined by the drift chambers, as the drift chamber reconstruction software returns a momentum value (without eloss) between Region-1 and Region-3 of the drift chambers. Along this track, the eloss package determines the path length in each material and corrects for the energy lost through each material, depending on the particle's measured momentum and angular position. Additional momentum corrections may be required, depending on the detector system and the experimental stipulations.

6.7 Physical Acceptance Cuts

There are regions where the detector system is not physically present, which depends on the system used for collecting data. In the example of the CLAS and CLAS12 detectors, there are physical gaps where the toroidal magnetic field is placed and regions close to

the field which have poor reconstruction due to the magnetic field strength. Also, near the edges of the drift chambers, the acceptance changes rapidly due to charged particles escaping detection or failing reconstruction, due to their curved trajectory influenced by the magnetic field. There are also limits to the angular coverage of the detectors. These regions can be removed by cutting on the θ and ϕ distributions of the particles detected, but more complicated geometries may require more carefully considered acceptance cuts.

Vertex Selection

Each experiment will have its own vertex position and target cell. In CLAS and CLAS12 experiments, the vertex position of each charged particle is determined by reversing its trajectory from the TOF paddles back through the DC and extrapolating its trajectory back to the target in a straight line from the DC (since the region between the DC and target has no magnetic field). Neutral particles are given the same vertex position as the trigger particle. It is important to select events which emerge from the target cell to reduce background and enhance the signal of interest. This is because particles can interact along the beamline with materials surrounding the target cell and those used to concentrate the beam to a central position (i.e. no x and y component). The beam typically travels in the z-direction with little to no x and y components. The physical targets used in the g9a and RGM experiments were placed at some position along the z-axis with no (x, y) components. In addition to constraining the z-vertex, the (x, y) vertex, which ensures the beamline was directed at the target, can be limited to select events with an appropriate (x, y) vertex position that further reduces background contributions.

Malfunctioning Hardware

It is important to identify hardware that is not adequately performing during the collection of the data since efficiency is a factor in yield and cross-section determination. For example, malfunctioning scintillators, or paddles, in CLAS and CLAS12 experiments can be identified by comparing the paddles with very low counts to the average value of the paddles in a given sector. These paddles can then be omitted from the analysis or corrected.

Chapter 7

Description of Kinematic Observables Employed in Analysis of the Photo- and Electro-Nuclear Data

"In the end, it's not the years in your life that count. It's the life in your years."

- Abraham Lincoln

Event selection is an important step in the physics analysis, as there are different event selection criteria for all analyses. Typically, event selection in particle physics analyses is broken down into four categories: inclusive, semi-inclusive, semi-exclusive and exclusive event selection. Inclusive event selections mainly aim to determine total cross sections and global properties of the interaction as there is little to no restriction on the final state. Semi-inclusive and semi-exclusive are similar in that both require the detection of a specific set of particles; however, in semi-inclusive event selection, the analysis allows for additional undetected particles in the final state, without specifying what those particles are. In contrast, semi-exclusive event selection involves detecting a specific set of particles while explicitly excluding certain other particles, thereby restricting the final state more than semi-inclusive selection. Exclusive event selection refers to a strict event selection where certain particles detected are required in the final state and strict requirements on particle multiplicity and types are imposed on the remaining particles in the final state. The analyses in this thesis focus on semi-exclusive event selection, where strict selection criteria are applied to charged particles, while neutral particles are ignored due to the low efficiency in detecting them. Therefore, we will highlight the key ingredients for a semi-exclusive event selection.

7.1 Particle Multiplicity

Particle multiplicity, often referred to as event topology, is the requirement of a certain number of particles in the final state. It is usually the first step in a semi-exclusive event selection after determining the full topology of the final state through particle selection cuts, discussed in the previous chapter (Chap. 6). In our analyses, we have many different topologies, as we are investigating many-body particle reactions from nuclear targets, although efficiency for neutral particle detection is notoriously lower than charged particle detection in CLAS and CLAS12 experiments. Therefore, we do not place any restrictions on neutral particles unless it is explicitly stated we are studying neutral pion channels.

7.2 Analysis of the Recoiling System

In particle interactions, especially those involving nuclear targets, analysing the recoiling system can be informative. The momentum and direction of the recoiling system can correspond to direct reactions, especially signatures of direct processes, which may reveal themselves in the momentum distributions. Other quantities, such as invariant mass, can be informative for studying the intermediate reactions at play. An overview of analysing the recoiling system for a semi-exclusive analysis is provided in this section.

7.2.1 Missing Mass

In every particle interaction, momentum and energy must be conserved. The missing mass is a Lorentz invariant quantity (meaning it retains the same magnitude in all frames of reference) defined as the total mass available to the residual system, assuming no other product particles are present in the final state. In the rest frame of the system (where the total momentum is zero), the missing mass represents the total available energy corresponding to the undetected particles, often referred to as "X". A simple example is quasielastic electron scattering $A(e, e'p)X$, where A is the target nucleon mass and X is the missing mass, from a free proton target (^{1}H) and a bound proton target (^{12}C). For this reaction, the missing mass is defined as:

$$\begin{aligned} p^{\mu}_{\text{miss}} &= p^{\mu}_{\text{Beam}} + p^{\mu}_{T} - p^{\mu}_{e'} - p^{\mu}_{p}, \\ m_{\text{miss}} &= \sqrt{E^2_{\text{miss}} - |\vec{p}_{\text{miss}}|^2}, \end{aligned} \tag{7.1}$$

where p^{μ}_{miss}, E_{miss}, $\vec{p}_{\text{miss}}$ and m_{miss} are the missing 4-momentum, energy, 3-momentum and mass, respectively, and p^{μ}_{Beam}, p^{μ}_{T}, $p^{\mu}_{e'}$ and p^{μ}_{p} are the beam (in this case initial electron), target (at rest), scattered electron and detected proton 4-momentum, respectively. In the case of ^{1}H, if the reaction were indeed quasielastic, we would expect a missing mass

of 0 GeV/c^2, as there is no residual nucleus left. Contrariwise, in the case of ^{12}C, the expected residual target left after a quasielastic reaction is ^{11}B and we would expect the missing mass to correspond to the mass of $M_{^{11}\mathrm{B}} = 10.2551$ GeV/c^2. If the reactions were not quasielastic and instead the reaction $e + {}^1\mathrm{H} \rightarrow e' + p + \pi^+ + \pi^-$ occurred then our missing mass would be shifted from the expected residual mass. Figure 7.1 presents a schematic diagram for quasielastic electron scattering off a stationary target nucleus of mass number A and presents the recoiling nucleus of mass number $A-1$. For ^{1}H in this picture $\theta_{\mathrm{Recoil}} = 0°$ and the $A-1$ nucleus does not exist. The diagram is a useful sketch for presenting the quantities of interest. The residual nucleus $(A-1)$ is the missing mass in our definition, which will be distorted if additional undetected particles are present as per our previous discussions above.

A useful adaptation of the missing mass is the shifted missing mass which is defined by taking the difference between the calculated missing mass and the expected residual nucleus mass. It is given by the following equation:

$$m_{\mathrm{miss}}^{\mathrm{shift}} = m_{\mathrm{miss}} - m_{\mathrm{expected}}, \tag{7.2}$$

where m_{expected} is the expected residual nucleus mass. In the example of quasielastic electron scattering from ^{12}C, we expect the residual nucleus to be ^{11}B. Therefore, if we shift the missing mass by the mass of ^{11}B then our shifted missing mass would be 0

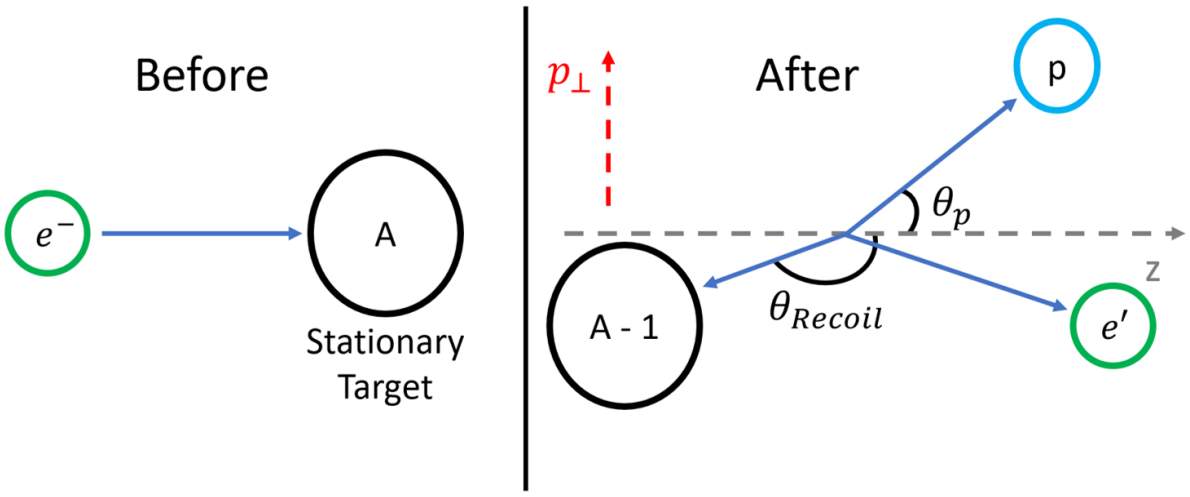

Figure 7.1: A schematic diagram representing quasielastic electron scattering off a nucleus of mass number A, where the before picture shows the electron impinged on a nucleus of mass number A. The after picture represents the final state after the quasielastic particle interaction has occurred, where the proton (blue circle), scattered electron (green circle) and the recoiling $A-1$ system (black circle) are marked. The angular directions of the proton (θ_p) and the recoiling nucleus (θ_{Recoil}) are shown. The direction of the transverse momentum is marked (red line) and the z-direction (direction of the beam) is marked (grey line).

GeV/c^2, if the reaction were quasielastic and no energy losses were experienced.

The general definition of the missing four-momentum, applicable to all reactions and all beam types, is given by the following equation:

$$p^{\mu}_{\text{miss}} = p^{\mu}_{\text{Beam}} + p^{\mu}_{T} - \sum_{i=1}^{n} p^{\mu}_{i}, \tag{7.3}$$

where p^{μ}_{miss}, p^{μ}_{Beam} and p^{μ}_{T} are defined as before, and $\sum_{i=1}^{n} p^{\mu}_{i}$ is the sum of the four-momentum of all detected particles in the final state.

7.2.2 Invariant Mass

Another Lorentz invariant quantity is the invariant mass which is the sum of a subset of product particles in an interaction. It is especially useful for determining resonant states such as the Δ since the Δ particle is not detected due to its finite lifetime. Instead, the product particles from its decay are detected and are used to determine whether resonance production occurred as the mass of the sum of the product particles should equate to the Δ mass. The invariant mass is defined as:

$$W^2 = \left(\sum_{i=1}^{N} E_i\right)^2 - \left|\sum_{i=1}^{N} \vec{p}_i\right|^2, \tag{7.4}$$

where $i = 1, 2, \cdots, N$ is the i^{th} particle and N is the total number of particles. The Invariant mass can be used to determine the total mass available before and after an interaction and can play a useful role in determining the kinematics of the system.

7.2.3 Centre of Mass Frame Analysis

The Centre of Mass (CM) frame refers to a frame of reference where the total momentum of the system is exactly 0 GeV/c. To demonstrate this methodology, we will use the example of a real photon beam, travelling with momentum E_γ in the z-direction, impinged on a ^{12}C target at rest with two protons detected in the final state ($^{12}\text{C}(\gamma, pp)X$). We will boost into the CM frame of the photon and target. The four-momentum of the system is given by $p^{\mu}_{\gamma} + p^{\mu}_{T} = (0, 0, E_\gamma, E_\gamma + M_{^{12}\text{C}})$ (where the invariant mass of the system is then calculated as the magnitude of this four-momentum, which corresponds to the total mass of the system in the rest frame) and the detected proton four-vectors are defined as $p^{\mu}_{1} = (\vec{p}_{1x}, \vec{p}_{1y}, \vec{p}_{1z}, E_1)$ and $p^{\mu}_{2} = (\vec{p}_{2x}, \vec{p}_{2y}, \vec{p}_{2z}, E_2)$. Therefore the boost vector is defined as:

$$\beta = \frac{p}{E} = \left(0, 0, \frac{E_\gamma}{E_\gamma + M_{^{12}\text{C}}}\right), \tag{7.5}$$

and the corresponding Lorentz boost transformation is defined as:

$$\Lambda_{\mu}{}^{\nu} = \begin{bmatrix} \gamma & 0 & 0 & -\beta\gamma \\ 0 & 1 & 0 & 0 \\ 0 & 0 & 1 & 0 \\ -\beta\gamma & 0 & 0 & \gamma \end{bmatrix}, \tag{7.6}$$

where $\gamma = 1/\sqrt{1-\beta^2}$ is the Lorentz factor. The relationship between the lab frame and the CM frame is given by $p'_{\mu} = \Lambda_{\mu}{}^{\nu} p_{\nu}$, where p_{ν} and p'_{μ} are the four-vectors of the particles in the lab and CM frame, respectively, and μ and $\nu = 0, 1, 2, 3$. The well-established coordinate transformations from the rest frame to a frame moving with velocity β in the z-axis are given by:

$$\begin{aligned} x' &= x \\ y' &= y \\ z' &= \gamma(z - \beta t) \\ t' &= \gamma(t - \beta z). \end{aligned} \tag{7.7}$$

We know the photon beam is moving with momentum E_{γ} in the z-direction only and that the target is at rest. Therefore, contracting our matrices provides the following four-vectors for the photon and target in the CM frame:

$$\begin{aligned} p'^{\mu}_{\gamma} &= (0, 0, \gamma\beta M_{^{12}\mathrm{C}}, \gamma\beta M_{^{12}\mathrm{C}}) \\ p'^{\mu}_{T} &= (0, 0, -\gamma\beta M_{^{12}\mathrm{C}}, \gamma M_{^{12}\mathrm{C}}). \end{aligned} \tag{7.8}$$

These equations are consistent with a few observations; the total momentum is 0 GeV/c, the photon energy and momentum are equal (it still has mass zero in all frames of reference) and the energy of the target is always greater than the photon since their momenta are the same magnitude. This process can then be repeated for the detected protons, and a good observable to identify is the opening angle between the two protons in the CM frame, which should (for a direct knockout process) be near back-to-back (it will be slightly lower than 180° since the target is a nuclear target and has a residual nucleus left following the $A(\gamma, pp)X$ reaction). The opening angle of two particles with two four-vectors p_1^{μ} and p_2^{μ} is defined as:

$$\cos(\theta_{\mathrm{open}}) = \frac{p_1^{\mu} . p_2^{\mu}}{|\vec{p}_1|\,|\vec{p}_2|}, \tag{7.9}$$

where $|\vec{p}_1|$ and $|\vec{p}_2|$ are the magnitude of the three-momentum of the two four-vectors and $p_1^\mu.p_2^\mu$ is the dot product of the four-vectors. The process of boosting into the CM frame of the photon and target is a specific example, and other boosts are applied depending on the kinematics of the reaction.

7.2.4 Missing Momentum

The momentum of the recoiling system, reconstructed from the known beam momentum and the momentum of the detected particles for each topology, ("missing momentum") also provides valuable physics variables to gain information on the underlying mechanisms. Particularly for direct knockout processes, this momentum would be expected to reflect the momentum of the participating nucleons in the initial state. As discussed for missing mass, other energetic undetected particles emitted with the detected particles will tend to increase the recoil momentum. The missing momentum is defined as the momentum component of the missing mass four-vector given by:

$$\vec{p}_{\text{miss}} = \sqrt{E_{\text{miss}}^2 - m_{\text{miss}}^2}. \tag{7.10}$$

7.2.5 Missing Transverse Momentum

Of particular interest for studying direct processes and suppressing background (non-direct) contributions are the missing transverse momentum, $p_\perp^{\text{miss}}$, which is just the transverse component of $\vec{p}_{\text{miss}}$. As the beam only brings in momentum in the z-direction, the perpendicular components of momentum can provide a cleaner signature of such events. Of course, for reactions where there are additional (undetected) particles in the final state, $p_\perp^{\text{miss}}$ can take on a much wider range of values, larger than the momentum of the nucleons in the target. The missing transverse momentum is defined as:

$$p_\perp^{\text{miss}} = \sqrt{|\,\vec{p}_x^{\,\text{miss}}\,|^2 + |\,\vec{p}_y^{\,\text{miss}}\,|^2}, \tag{7.11}$$

since the stationary target and z-plane orientated beam provide no x and y component of momentum. Alternatively, it can be defined as the transverse component of the sum of all detected final state particles. The direction of the transverse momentum is presented in Fig. 7.1.

7.2.6 Recoiling Theta

The residual system will have an overall direction of travel, which can be defined by its momentum and recoiling angle, θ_{Recoil} (see Fig. 7.1). Additional undetected particles in the final state will produce a θ_{Recoil} with no clear relationship. Contrariwise, particularly in the case of $^{12}\text{C}(\gamma, pp)X$ reactions, a direct process will produce an isotropic θ_{Recoil}

distribution. Advancing on this idea, the distribution for $\cos(\theta_{\text{Recoil}})$ will exhibit a flat behaviour if the reaction produces an isotropic recoiling system. Certain kinematics can have an expected θ_{Recoil} where the strength of a particular reaction is strongest, hence selecting regions of θ_{Recoil} can increase and decrease particular reactions. In the context of background processes for the present analyses, since both the CLAS and CLAS12 detectors are unable to detect far backwards ($> 140°$) and forwards travelling particles ($< 5°$), a θ_{Recoil} with very far forward angles ($\theta_{\text{Recoil}} \rightarrow 0°$) and far backwards angles ($\theta_{\text{Recoil}} \rightarrow 180°$) can be strongly correlated with background processes, especially for nuclear targets with a mass number A > 6, as nuclear recoiling systems are expected to have lower momenta, given their high mass, and scatter isotropically (especially for direct multi nucleon knockout reactions). θ_{Recoil} and $\cos(\theta_{\text{Recoil}})$ are defined by the following equation:

$$\theta_{\text{Recoil}} = \cos^{-1}\left(\frac{\vec{p}_z^{\,\text{miss}}}{\vec{p}_{\text{miss}}}\right). \tag{7.12}$$

Chapter 8

Many-Proton Knockout Using Real Photon Beams

> *"The most beautiful experience we can have is the mysterious. It is the fundamental emotion that stands at the cradle of true art and true science. Whoever does not know it and can no longer wonder, no longer marvel, is as good as dead, and his eyes are dimmed."*
>
> - Albert Einstein

This chapter presents our results on photoinduced many-proton knockout reactions from nuclear targets (butanol, carbon and polythene), with proton multiplicities from one through to six. The photon beam energies utilised in this data range from $600-4500$ MeV. The particle selection requirements for determining a good proton are described in detail, for both the experimental and simulated data. Afterwards, the methodology for placing the experimental and simulated data on a common cross-section scale is presented. The analysis of the recoiling system, which will improve the direct knockout signal observed, is presented. Then, the full statistical and systematic uncertainties are discussed. Finally, the results for the many-proton knockout reactions are summarised and presented. The potential for using real photon beams as a spallation source to reach exotic neutron-rich nuclei is also explored using the (benchmarked) GiBUU theoretical model.

8.1 Introduction

In this work, we measure photoinduced many-proton (multiplicity $1-6$) knockout from ^{12}C nuclei. The data is obtained from the ^{12}C containing solid targets present in the g9a FROST experiment (carbon (^{12}C), polythene (CH_2) and butanol (C_4H_9OH)), using photon beams with energies $600-4500$ MeV. The data provides an important challenge to our understanding of many-body physics processes in theoretical models. The different

processes can show sensitivities to the incident photon energy and reaction observables - offering some opportunities to deconvolute and assess their contributions.

This first experimental study of such high-multiplicity many-proton knockout processes challenges the theoretical descriptions of this range of feeding processes in theoretical models - providing a real challenge to the detailed descriptions of many-body nuclear physics processes in theoretical models. A better understanding of such processes has impacts on nuclear reaction theory and reaction theories for neutrino detection via neutrino-nucleus interactions (due to the common nuclear processes at play following the interaction of the incident beam). In addition, it also underpins a benchmarking of the possibilities for a future photon-driven spallation source, which may have benefits due to the reduced beam heating from the use of a photon beam compared to traditional methods (e.g. proton, ion spallation). The possibilities to use future intense (e.g. Compact Photon Source (CPS) [94]) photon beams to generate long-lived isotopes from vapour targets and employ subsequent mass, charge separation and implantation will be explored in future work.

In this study, the many proton knockout experimental data are compared to predictions from the GiBUU model, which is currently the most comprehensive transport model including a broad range of initial interaction processes and a detailed model of subsequent interactions of the produced particles in the medium. To compare with GiBUU predictions, pseudo-events generated from the model are passed through the CLAS acceptance (with each event having an associated weight relating to the cross-section for the reaction process). The modelling of the CLAS acceptance uses the GSIM framework, a simulation package based on GEANT3, which implements detector efficiency, acceptance and experimental resolutions on Monte Carlo events. The sum of the GiBUU weights in a given bin provides the visible cross section (within the CLAS acceptance) in that bin.

This work provides a first benchmarking of the GiBUU model for predicting the many-proton knockout processes for ^{12}C. carbon is one of the lightest nuclei amenable to the model. Having a relatively low mass and nucleon number also offers more clarity in investigating the mechanisms than possible with heavy nuclei. For light nuclei such many-proton knockout processes may produce very exotic residual systems with asymmetric N, Z ratios - having compositions up to a recoiling system comprised of 6-neutrons (^{6}n) or 6-protons (^{6}p). Although light residual exotic states are typically unstable on short timescales (and therefore not feasible for subsequent recoil spectrometry), the benchmarking of the description of the many-proton knockout processes in GiBUU for light nuclei would give more confidence in the modelling of the seed knockout reaction processes across the nuclear chart. A lighter system offers a cleaner environment to study their contributions. The knockout mechanisms will have common ground with those in heavier nuclear targets, where relatively long-lived recoil nuclei could be produced.

Photoinduced many-proton knockout may provide a new way to access nuclei out of reach of current methods. Figure 8.1 illustrates the sparsity of observed nuclei going down the

$N = 126$ line, below ^{208}Pb. These nuclei are key waiting points in the r-process but their key properties, e.g. half-life, are unmeasured. The r-process is a set of rapid neutron capture events for elements heavier than ^{56}Fe, where neutron capture reactions describe processes where a neutron and a nucleus collide to form a heavier isotope. The processes must be rapid, such that the nucleus does not undergo radioactive decay before another neutron is captured (the neutron-rich nuclei are short-lived). Eventually, these isotopes undergo reactions such as β-decay, which converts neutrons to protons, thereby increasing the atomic number of the nucleus. The result is the creation of stable, or near-stable, elements much heavier than Iron (^{56}Fe), such as gold, platinum and uranium (^{195}Pt, ^{197}Au and ^{238}U), among many others. The r-process is important for understanding the synthesis of heavy elements in the universe, and the formation of planets, stars and galaxies. See the recent review by [95] for an overview of current progress relating to the r-process.

Previous experiments, where the data for known nuclei in the chart were obtained, used facilities where two lighter nuclei were fused together. Due to the N/Z ratio of nuclei heavier than ^{56}Fe, near-stable or proton-rich nuclei are preferentially produced (as evidenced on the chart where the proton-rich side is well established). For the heaviest nuclei in the lead-to-uranium region, rather modest numbers of knocked-out protons would reach terra-incognita. A side aim of the current project is to provide a benchmark for the GiBUU model, such that the accuracy of its predictions for the operation of a photon spallation source could be obtained.

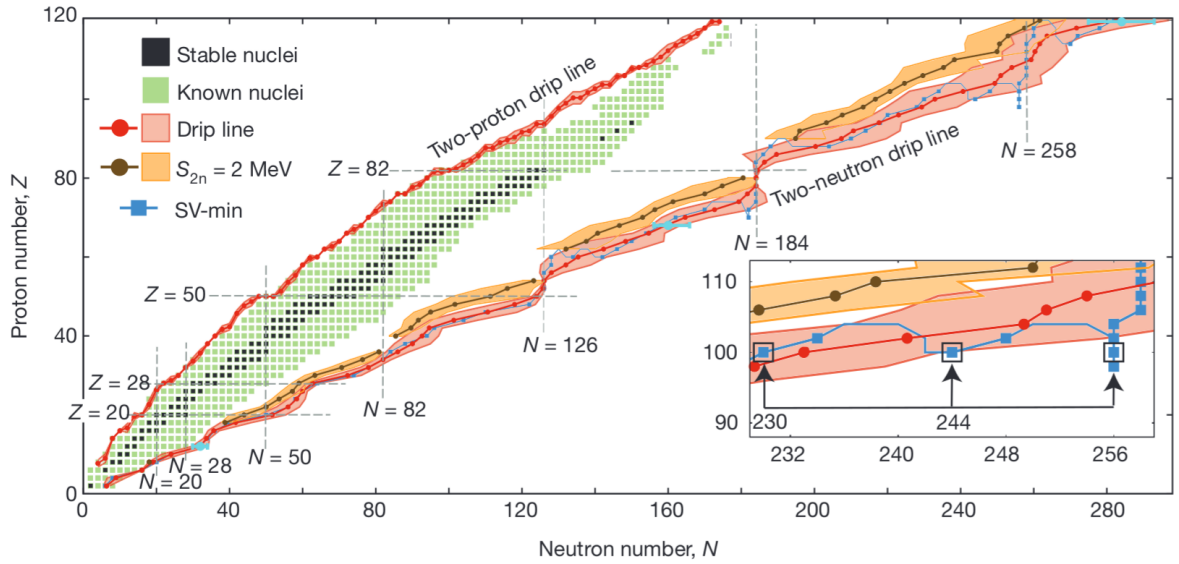

Figure 8.1: A map of the nuclear chart, adapted from [96], showing both the stable (black squares) and radioactive (green squares) nuclei. The two-proton and two-neutron drip line (red dots) are also shown.

8.2 Particle Selection

The standard CLAS software for data reconstruction (user_ana) was used to "cook" data and translate detector information (TDC and ADC values) to physical information (energies and momenta). The reconstructed particle information was stored in BOS banks and ROOT trees (using rootbeer ntuples [90]). This analysis focuses on a semi-exclusive event selection for many proton knockout reactions. The protons are selected with a series of requirements and all events containing a different detected charged hadron species are removed. Neutral particles are ignored due to the sensitivity of GiBUU's modelling of neutral particles and the poor detection of neutrals in CLAS experiments. Below is a list of the particle identification cuts used in this analysis to select the protons. The protons are listed in descending momentum i.e. the fastest proton is denoted as the first proton.

8.2.1 Particle Identification

The selection criteria for the protons begins by correctly identifying them from their expected and measured velocities, namely $\Delta\beta$, which is calculated using Eq. (6.12). The measured velocity is determined by the TOF paddles, while the calculated velocity is determined by using information from the drift chambers, by measuring the curvature of the particle induced by the magnetic field, and by assuming the particle's mass. The $\Delta\beta$ distribution for the protons in this data set exhibits a momentum-dependent behaviour (shown in Fig. 8.2) for both the experimental data and the simulated GiBUU events passed through GSIM. Therefore, to determine the position of our cuts we fit a polynomial (of order 7) to the extracted $\mu \pm 3\sigma$ (mean $\pm$ 3 sigma) from a Gaussian fitted in a limited range of $\Delta\beta$ (-0.03, 0.03), in slices of momentum.

Exemplar fits are shown for particular slices of momentum in Fig. 8.3. The $\mu \pm 3\sigma$ (red) and 2.5σ (black) positions are shown as the systematic uncertainty arising from the PID cut involves varying the cut between the two cut positions and studying its effect on the final results. The parameters for the fits are provided in App. A.

8.2.2 Photon Identification

The secondary real photon beams are produced via the bremsstrahlung process and determined using the tagging spectrometer and hits in the start counter, as discussed in Chap. 4. Photon identification was undertaken by selecting the photons with timing information at the event vertex consistent with the vertex time of the first proton knocked out and detected. The timing distribution of the tagger focal plane hits (the coincidence time between the photon and the fastest proton) is determined from Eq. (6.10) and shown in Fig. 8.4 for the experimental (left) and simulated (right) data. Photons whose coincidence time $|\Delta t_\gamma| < 1$ ns are selected as "good" photons that mediated the reaction, which is consistent with previous FROST analyses.

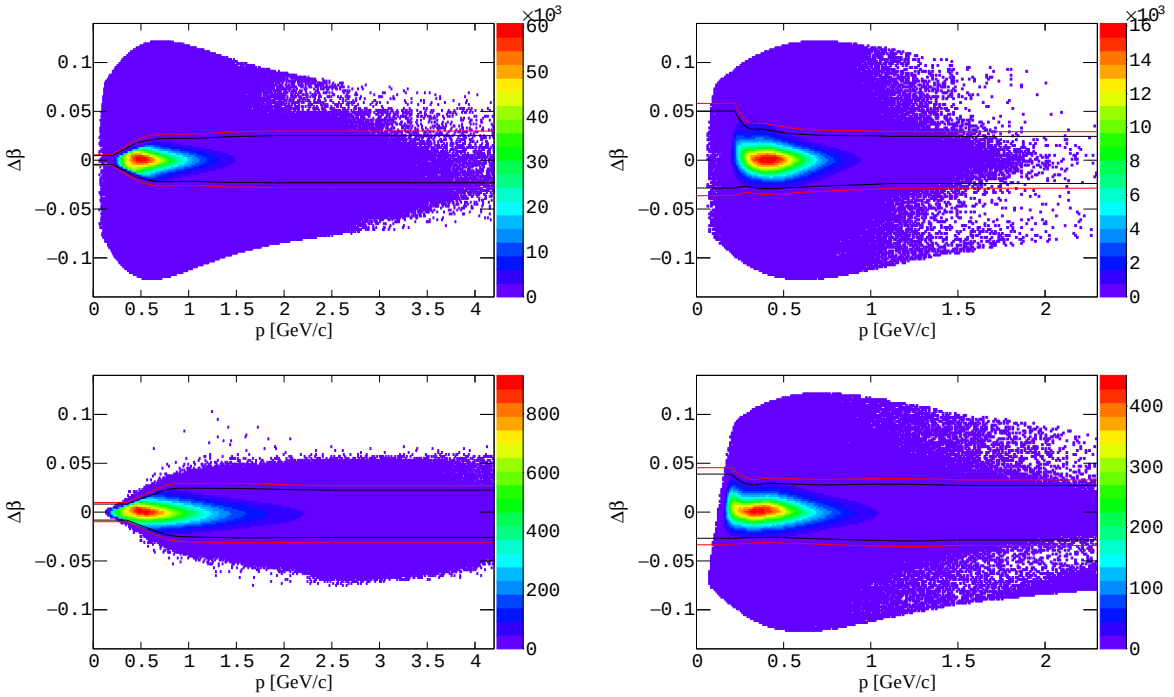

Figure 8.2: $\Delta\beta$ as a function of the measured momentum for protons detected in CLAS, where the red and black lines show the 3σ and 2.5σ momentum-dependent $\Delta\beta$ cuts applied to the distributions. The left distribution presents $\Delta\beta$ as a function of momentum for proton 1 and the right distribution presents $\Delta\beta$ as a function of momentum for all other protons > 1. The top row shows the experimental distributions the bottom row presents the simulated distributions.

The tagger focal plane event multiplicity (for events within this ± 1 ns coincidence timing window) is shown in Fig. 8.5 (on a logarithmic scale). For completeness the simulated data are also shown in Fig. 8.5 - but by construction there is only 1 photon generated in the simulated interactions. The peaks at every 2 ns for the experimental determination of Δt_γ represent the beam bunching phenomena*. Events where multiple photons lie between

*As expected this structure is not evident in the simulated data

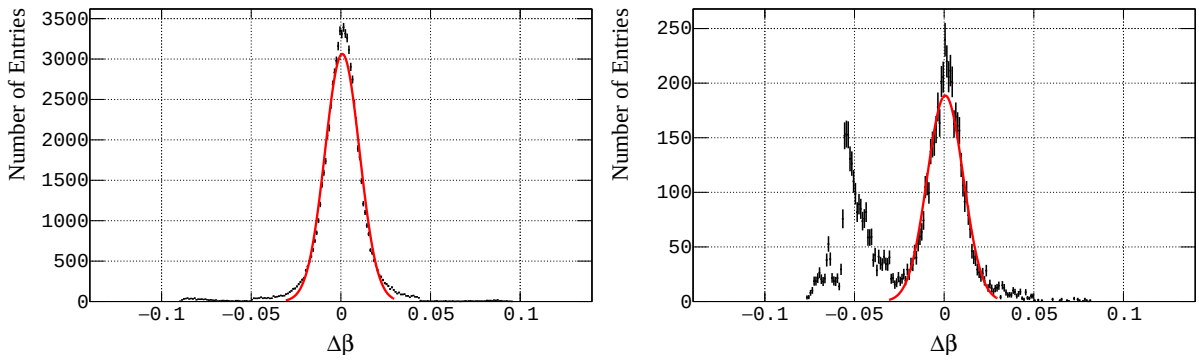

Figure 8.3: Example fits of $\Delta\beta$ for different slices of momentum; $1.69 - 1.74$ GeV/c (left) and $2.52 - 2.57$ GeV/c (right). The distributions were fitted using a Gaussian function in a limited range of $\Delta\beta = (-0.03, 0.03)$. The distributions are for the experimental data.

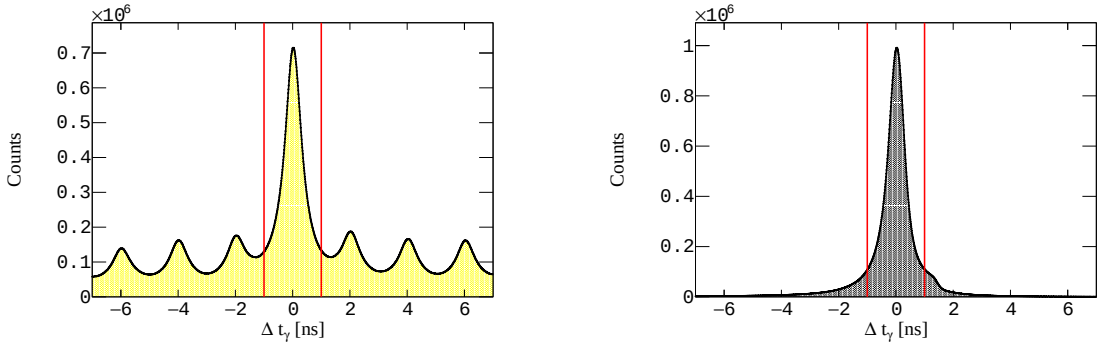

Figure 8.4: Coincidence time at the event vertex between the photon and the first proton, p_1, after PID cuts, used to identify the photon which initiated the interaction in CLAS. The left plot presents the experimental distribution and the right plot presents the simulated distribution. The red lines indicate where we cut on the distributions.

$|\Delta t_\gamma| < 1$ ns are discarded from further analysis, as determining the true mediator of the reaction greatly complicates the analysis and systematic uncertainties.

8.2.3 Energy and Momentum Corrections

As discussed in Sec. 6.6, particles that traverse the detector mediums exhibit energy losses. The standard CLAS eloss package [97] was used to correct the three-momentum of all protons in both the experimental and simulated data by accounting for energy losses in the target material, target wall, carbon cylinder and start counter. Additional momentum corrections (due to slight misalignments of the drift chambers [98]) were not applied to the experimental data, as their contribution is minimal (orders of MeVs) and much smaller than the eloss corrections[†].

[†]The momentum corrections available from the g9a run period were employed for fine-tuning of the narrow missing mass peak from pion photoproduction on hydrogen. The current analysis is not sensitive to effects at this scale as all structures are smeared by the nuclear Fermi momentum. Also, as the corrections are derived from the hydrogen in the butanol their accuracy for other targets in different positions on the beamline is not established.

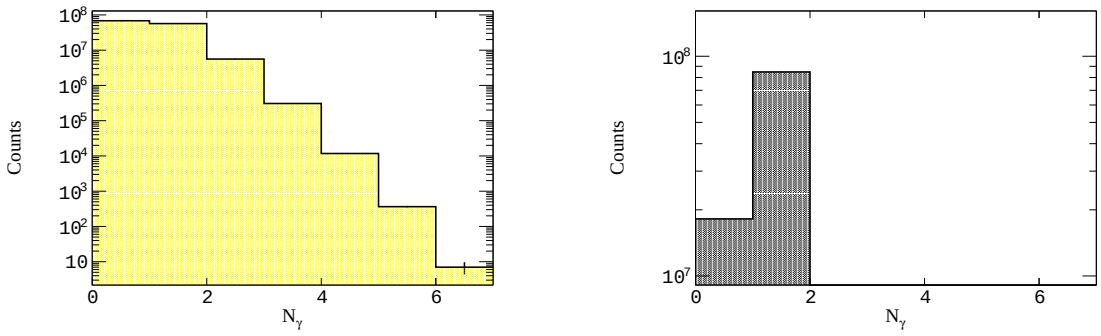

Figure 8.5: The photon multiplicity showing how many photons survive our $|\Delta t_\gamma| < 1.0$ ns cut between the photon and the first proton for the experimental data (left) and simulated data (right).

The influence of the eloss corrections on a typical observable is presented in Fig. 8.6. The top row presents the missing mass of $^{12}\mathrm{C}(\gamma, pp)X$ reactions before (red line) and after (solid fill) applying energy losses (see Subsec. 7.2.1 for a definition of missing mass). The energy loss corrections are noticeable although modest, and they are more prominent at higher missing mass which is correlated with lower momentum protons (the amount of energy lost is largely proportional to the particle's time-of-flight).

The middle row shows the difference in the momentum before and after energy losses were applied, as a function of the momentum measured by CLAS. As expected, the influence of

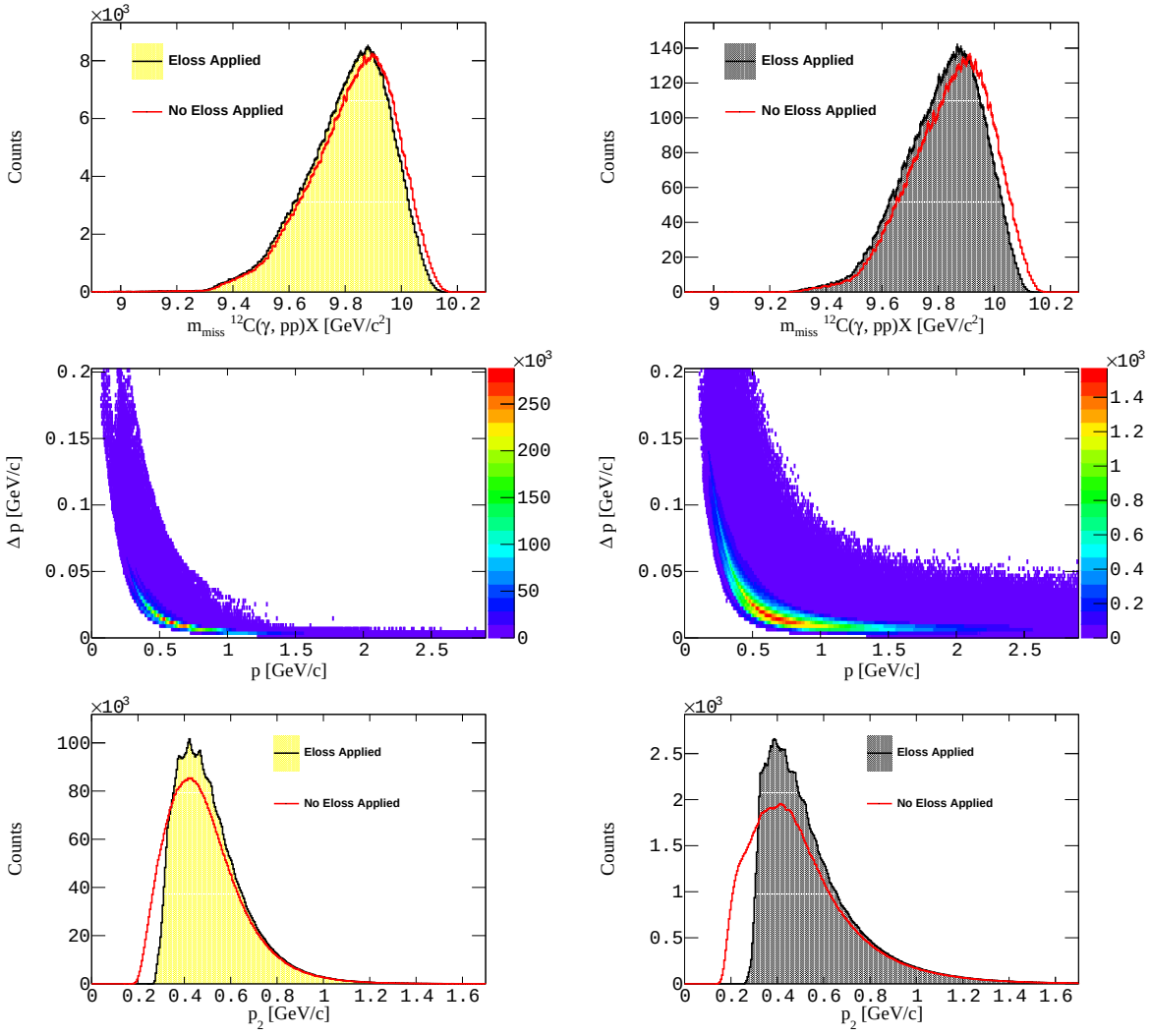

Figure 8.6: Left column shows experimental data. The right column shows simulated data. The top row shows the missing mass for the interaction $^{12}\mathrm{C}(\gamma, p_1 p_2)X$ for photon energies 0.8 GeV $\leq E_\gamma \leq$ 1.0 GeV. Solid fill shows distributions after eloss corrections are applied. The red line before eloss corrections. The middle row shows the change in momentum between the momentum measured in CLAS and that after eloss corrections are applied, as a function of the momentum measured in CLAS (for all photon energies). The bottom row shows the momentum for proton 2 with the same convention as the top row plots (for all photon energies).

the corrections is modest ($\approx 0 - 50$ MeV/c) and largest at the lower momenta (note that the omitted momentum corrections would see only an additional $0 - 5$ MeV/c change). Finally, the bottom row presents the effect of including (solid fill) and omitting (red line) energy loss corrections on the momentum distribution of the second proton in each event. The aforementioned arguments for the missing mass distributions are further highlighted here - the corrections are modest ($\approx 0 - 50$ MeV/c) and affect the lower momentum protons more than higher momentum protons (which see very little change ($\approx 0 - 10$ MeV/c)).

8.2.4 Bad or Malfunctioning Time-of-Flight Paddles

During the g9a experiment, there were a selection of time-of-flight paddles that were not adequately performing during the data collection. These were identified by comparing the counts in these paddles to the average value of the time-of-flight paddles in the given sector, where there are an array of paddles in each of the six sectors as discussed in Subsec. 4.5.5. Our collaborators [99] identified the bad paddles in this experiment which are listed in Tab. 8.1. These paddles were removed from the analysis of both the experimental and simulated data. We remark that results with and without these paddles have only a small effect on the measured yields at different proton multiplicities.

Sector	Paddle
1	17, 24
2	45
3	23, 35
4	23, 49
5	23, 55
6	54

Table 8.1: List of bad time-of-flight paddles, as identified in Ref. [99].

8.2.5 Reaction Vertex

Identifying the reaction vertex, corresponding to the position of the target and the origin of the particles is important for determining accurate yield or cross-section measurements, as the incident beam can interact along the beamline (either further upstream or downstream of the target position). In g9a analyses, there are two different vertex calculations we need to consider: the MVRT and GPID vertex. The MVRT bank is used to determine the position of the origin of the reaction which takes place between the photon and the first proton. The MVRT vertex reconstructs the initial reaction position by taking into account all particles detected in the event and reconstructing their tracks back to the vertex position. It is a distance of closest approach (DOCA) calculation to determine the vertex position, where the MVRT DOCA is done by looking at the DOCA between all

final state vectors. In the case of single proton events, MVRT DOCA is determined using the particle vector and the photon beam vector defined from multi-charge track events (events with more than 1 detected charged particle).

Following the analysis done by S. Strauch [98] a cut on the x and y coordinates was made to remove poorly reconstructed tracks from the analysis. Specifically, in the previous analysis tracks with a distance from the centre of the beam, located at (-0.03 cm, -0.18 cm), larger than 2 cm were removed. We have adopted a radial cut of $\sqrt{x^2 + y^2} < 2.83$ cm, which is commensurate with the previous analysis. The full MVRT vertex position is shown in Fig. 8.7, where the three separate targets are shown between 3 sets of lines; butanol (blue), carbon (red) and polythene (green). The butanol target is located at -3 cm $\leq z \leq 3$ cm, carbon is located downstream at 5 cm $\leq z \leq 8$ cm, and placed further downstream is the polythene target around 13.5 cm $\leq z \leq 18.5$ cm. The asymmetry in the distribution for the carbon target (small bump on the right-hand side of the Gaussian peak) was established in previous FROST analyses to be due to ice buildup on the downstream surface of the carbon target. This was observed in Ref. [20] and [100], for example, and other analyses also observed this behaviour.

Our analysis focuses mainly on the carbon target, with event yields identified according to the standard cut (red lines) as used in other analyses for FROST. Additionally, the x- and y-vertex distributions, for both the simulated and experimental data, are presented in Fig. 8.8, where the red circle depicts the radial cut imposed. Structures associated with the six sectors of CLAS are clearly seen in both distributions. We note that the other carbon-containing targets (polythene and butanol) are additionally analysed for our final results. They adopt the same (x, y) vertex cuts as for the carbon target.

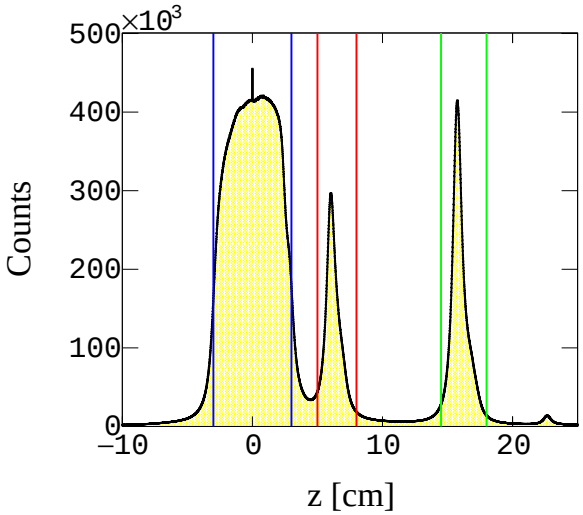

Figure 8.7: The full MVRT z-vertex displaying the geometry of the FROST experiment, where the three targets are displayed between three sets of lines; butanol (blue), carbon (red) and polythene (green).

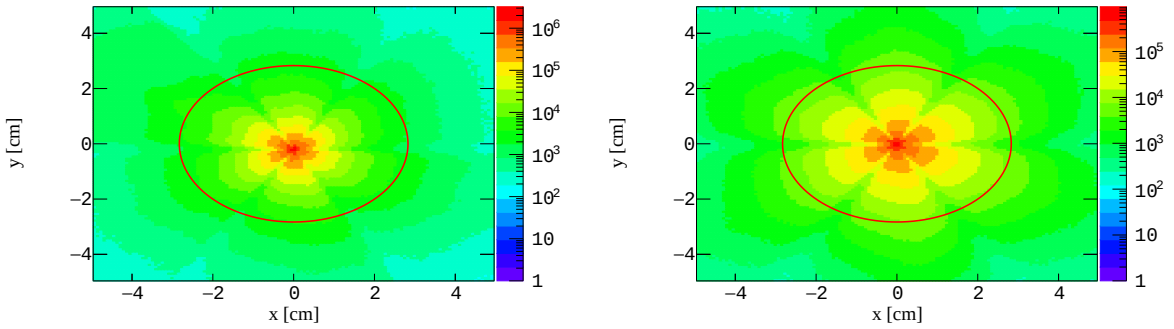

Figure 8.8: the y-vertex as a function of the x-vertex from the MVRT bank for both the experimental (left) and simulated (right) event samples, with a log scale applied. The red circle indicates where we cut on the vertex positions.

The GPID bank stores the information of all particles detected in the event, including the vertex position of each particle. To ensure we perform an accurate determination of the yield, we also impose the same cuts on the vertex position of each individual proton. Figure 8.9 presents the MVRT vertex for the carbon target and the vertex position of the protons from the GPID bank after cutting on the MVRT vertex around the carbon target.

Also shown in Figs. 8.8 and 8.9 are the equivalent vertex distributions for the simulated data. Note the GiBUU simulated events were generated at a vertex (0,0,0) cm to be

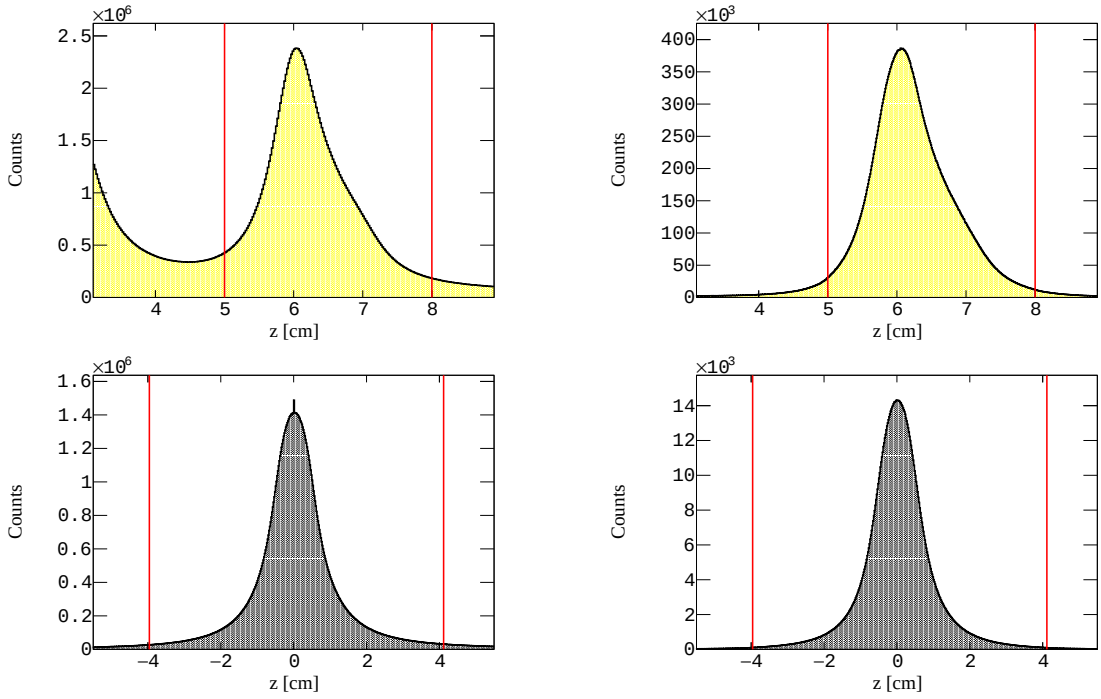

Figure 8.9: z-vertex of the target from the MVRT bank (left) and the GPID/EVNT bank (right) after cutting on the MVRT vertex. The top distributions present the geometry of the experimental data and the bottom distributions present the geometry of the simulated target. The red lines indicate where we cut on the vertex positions.

compatible with the existing GSIM simulation for this run period - centred for events from the butanol target z-position (-3 to 3 cm). The systematic effects of comparing with data having a 6 cm displacement of the carbon target vertex, presented in Sec. 8.7, are quantified by the differences between the butanol and carbon target yields - found to be 2% on average.

The simulated data shows the expected symmetrical vertex distribution centred at (0,0,0) cm (the asymmetry caused by ice in the experimental data is of course not present). The z-vertex cut on simulated data was determined by taking the 3σ position of the Gaussian with the largest σ from a double Gaussian + linear fit (thereby keeping the same large fraction of the yield as for the experimental data). The cuts applied on both the simulated and experimental data are shown by the red lines in Fig. 8.9. See App. A for the fit parameters used to determine the simulated cuts.

8.2.6 Coincidence Time Between the Protons

Since we are (typically) studying a many-body final state, we need to consider the timing difference between each proton in addition to the timing difference between the photon and the first proton. The coincidence time between the protons is calculated using Eq. (6.13). We have opted to determine the timing difference between the first proton and all other subsequent protons as the first proton has the best resolution[‡] (since CLAS orders particles in descending momentum and particles with larger momenta have better resolutions). This implies that in Eq. (6.13) $j = 1$. The coincidence times between the first proton and all higher order protons as a function of the average momentum ($(p_1 + p_n)/2$) of p_1 and p_n, where $n > 1$, are shown in Fig. 8.10. The average momentum is used as higher-order protons will have differing resolutions to the first proton.

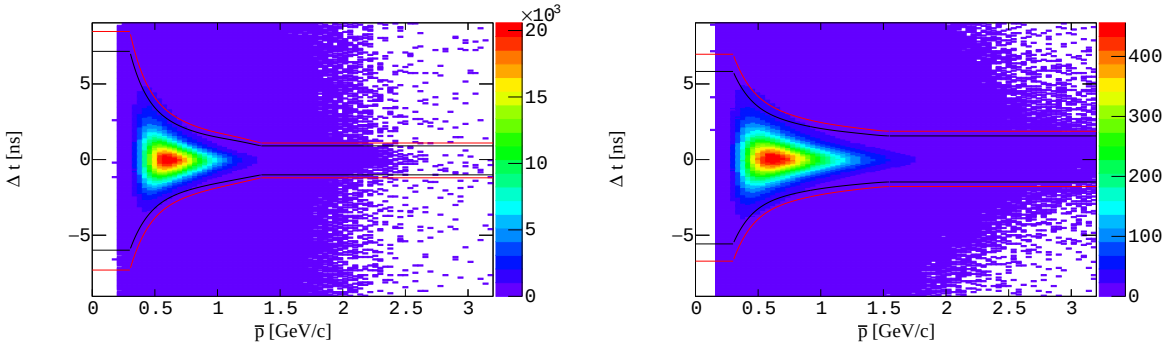

Figure 8.10: Coincidence time between the first and n^{th} proton in the event as a function of the average measured momentum of the first and n^{th} proton, $(p_1 + p_n)/2$, in CLAS, where the red lines show the 3σ momentum-dependent coincidence time cuts applied to the distributions and the black lines present the 2.5σ window. The left plot presents the experimental distribution and the right plot presents the simulated distribution.

[‡]The systematic uncertainty between using the first proton as a reference and using subsequent protons was studied and found to produce a negligible difference.

The red lines on the Δt distributions present the positions of the cuts imposed on the protons. The position of the cuts is determined by fitting a polynomial (of order 6) to the extracted $\mu \pm 3\sigma$ position of a Gaussian fitted in a limited range of Δt (-3 ns, 3 ns), in slices of momentum. Example fits are shown in Fig. 8.11. The fit parameters are provided in App. A.

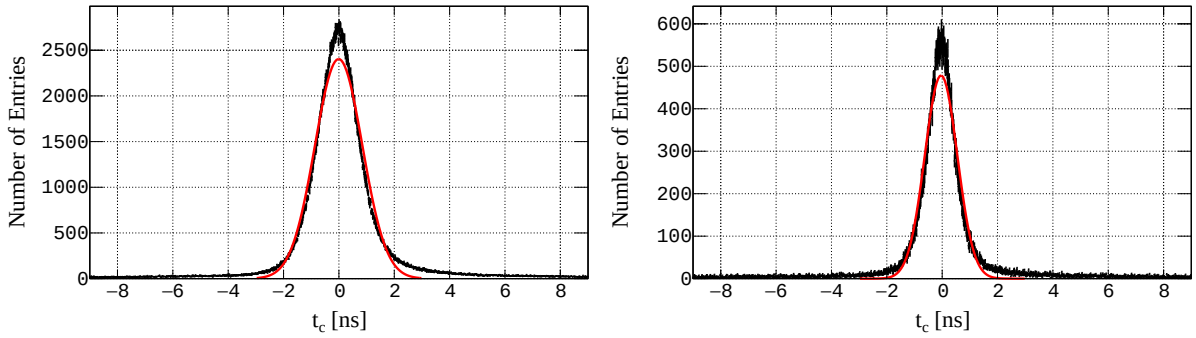

Figure 8.11: Example fits of Δt for different slices of average momentum $(p_1 + p_n)/2$; $0.705 - 0.755$ GeV/c (left) and $1.075 - 1.125$ GeV/c (right). The distributions were fitted using a Gaussian function in a limited range of Δt = (-3 ns, 3 ns).

8.2.7 Fiducial Cuts for CLAS Acceptance

In Chap. 4 we discussed the hardware of the CLAS detector, in particular the placement of the torus magnet, which produces void regions of acceptance where no particles can be detected. Additionally, particles which are detected close to the torus magnet have poor reconstruction due to the non-uniform magnetic field strength, hence we remove these regions from our analysis. These regions are eliminated by limiting the azimuthal (ϕ) angle of the detected protons and the cut regions are shown by the red lines in Fig. 8.12. Any protons detected within the void regions are considered badly defined protons and are removed from the analysis.

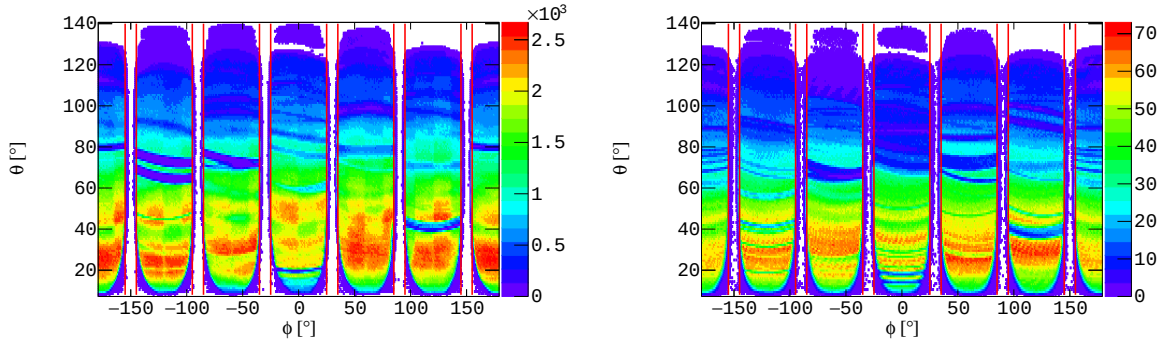

Figure 8.12: Experimental data (left column) and simulated data passed through gsim (right column). Plots show θ as a function of ϕ for all protons detected in CLAS after PID, photon selection and vertex cuts. The vertical red lines show the azimuthal fiducial cuts applied in the analysis.

The systematic uncertainty associated with the effect of including these azimuthal fiducial regions and excluding them is accounted for. The impact is small compared to the overall systematic error budget so fine-tuning the fiducial azimuthal regions (e.g. by using regions which curve at a small polar angle) is not necessary (effects are at the $<<$ 1% level). The polar angle (θ) coverage is also limited to $8^\circ < \theta < 140^\circ$ and any protons detected outside these regions are removed from the event sample. The θ as a function of ϕ, or angular acceptance, distributions for the protons is presented in Fig. 8.12 for both the experimental (left) and simulated (right) data. Discrepancies between the angular acceptance of the two data sets are accounted for in Sec. 8.7.

8.2.8 Momentum Cuts

We apply a uniform threshold for the momenta of the protons detected by CLAS. The minimum momentum threshold varies depending on the distribution and physics we want

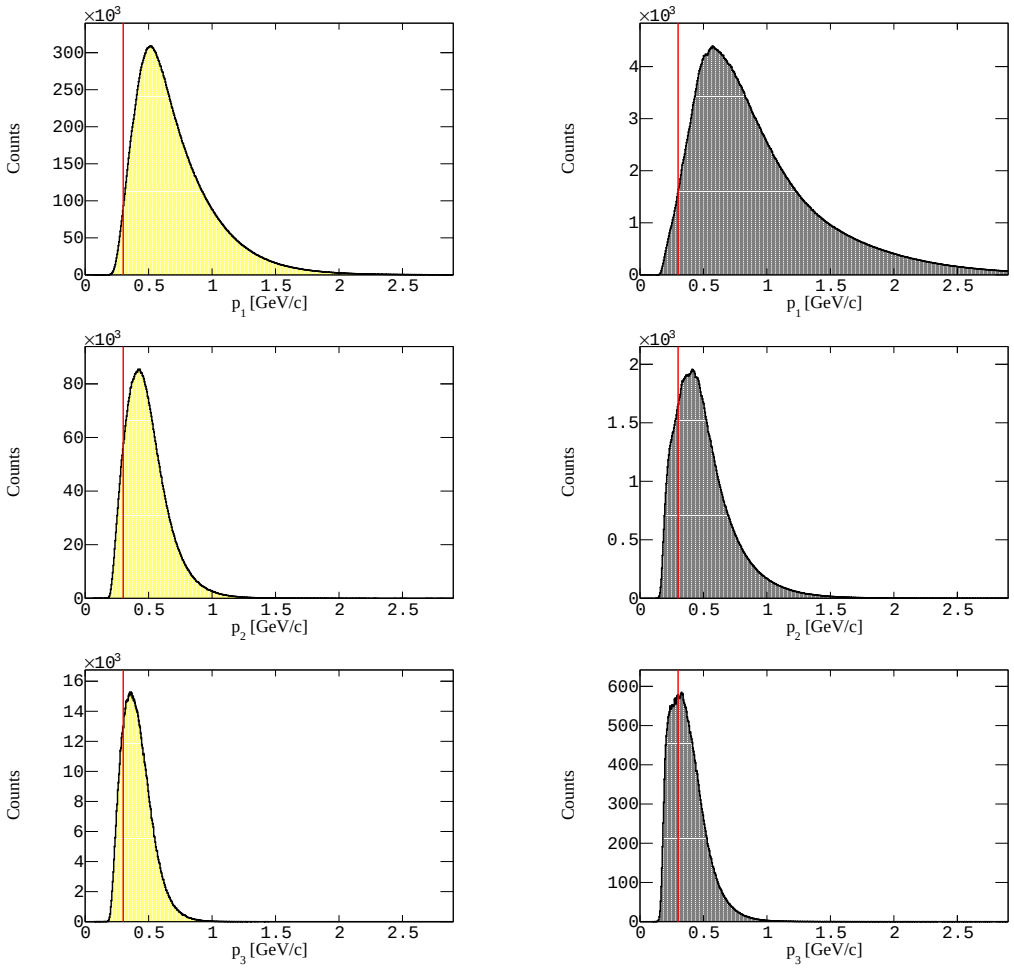

Figure 8.13: The momentum distributions of the 1st (top), 2nd (middle) and 3rd (bottom) proton knocked-out after all cuts are applied. The left plots show the experimental distributions and the right plots show the simulated distributions. The red line indicates the momentum cut imposed on the protons.

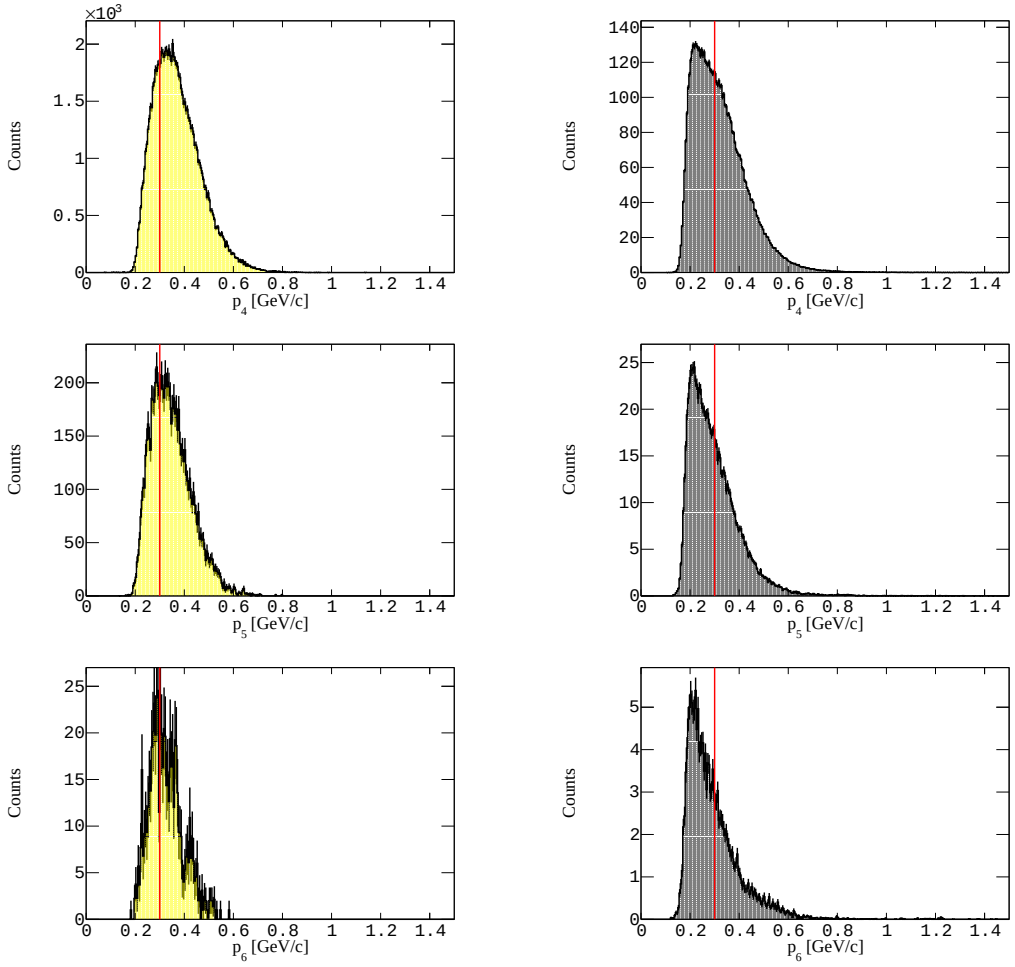

Figure 8.14: The momentum distributions (before applying eloss corrections) of the 4^{th} (top), 5^{th} (middle) and 6^{th} (bottom) proton knocked-out after all cuts are applied. The left plots show the experimental distributions and the right plots show the simulated distributions. The red line indicates the momentum cut imposed on the protons.

to show, but 0.3 GeV/c is our nominal minimum momentum cut. The momentum distributions presented in Fig. 8.13 are for the first (top), second (middle) and third (bottom) proton, and in Fig. 8.14 for the fourth (top), fifth (middle) and sixth (bottom) proton after applying all aforementioned cuts.

In comparing cross-sections from the three targets in FROST (see Subsec. 8.5.4) a higher minimum proton momentum threshold was necessary. The momentum distributions of protons from the 3 targets are shown in Fig. 8.15. Butanol suffers the highest energy losses for protons and polythene has a lower minimum momentum threshold due to its placement further upstream. We therefore choose 500 MeV/c as the minimum threshold to select regions where all targets have acceptance and avoid any regions where the acceptance is changing rapidly with momentum. For the highest multiplicity knockout distributions (> 4), results with the 300 MeV/c momentum threshold are presented in our results section. This expansion of the cut maximises statistics for such higher-order proton multiplicities (where the minimum momentum threshold has a more significant effect).

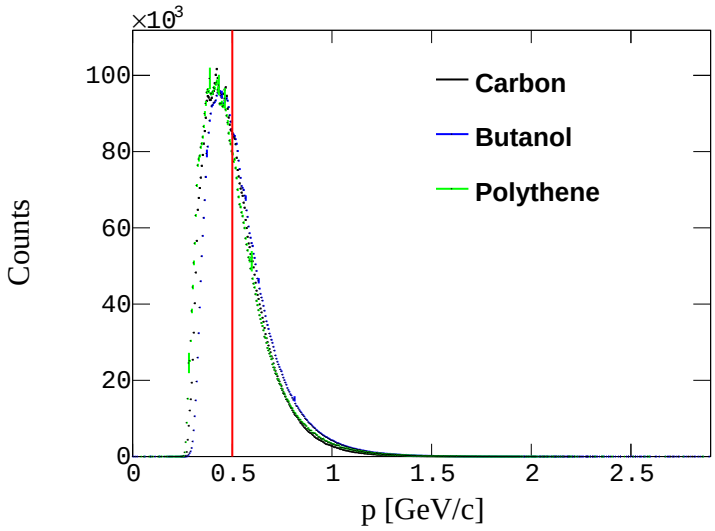

Figure 8.15: Momentum distribution (before applying eloss corrections) for all targets in FROST; carbon (black), butanol (blue) and polythene (green) for all E_γ, after eloss is applied. The scaling for this distribution is arbitrarily selected to put the three targets on scale.

8.2.9 Summary

A summary of the particle identification cuts applied in this analysis is provided in Tab. 8.2 for the multiplicities extracted in the analysis (up to six protons).

Cut	Experimental Data	Simulated Data
$\Delta\beta$	Momentum-dependent (see App. A.1)	
Δt	Momentum-dependent (see App. A.3)	
Δt_γ	$\pm$ 1.0 ns	
p_{min}	0.3 GeV/c	
ϕ	Void Regions	
θ	$8^\circ < \theta < 140^\circ$	
N_γ	1	
$\sqrt{x^2+y^2}$	$\sqrt{x^2+y^2} < 2.83$ cm	
z	5.00 cm $< z <$ 8.00 cm	-3.96 cm $< z <$ 4.12 cm

Table 8.2: Summary of particle identification and reaction reconstruction cuts applied in the determination of the protons for the experimental and simulated data.

8.3 Photon Energy Spectrum

The g9a FROST experiment exploited primary electron beams, with energies of 2780 MeV, 3545 MeV and 4599 MeV, impinged on a diamond and amorphous radiator. The data using the diamond radiator will have coherent bremsstrahlung (CB) peaks, which we remove, using a procedure discussed throughout this section, to create an effective

unpolarised beam from the linearly polarised data.

8.3.1 Deriving the Flux as a Function of Photon Energy in the Experiment

The enhancement fit is given as the ratio between the incoherent and coherent bremsstrahlung photon energy spectra (for photons in timing coincidence with CLAS i.e. which have passed through the collimator), and is presented in Fig. 8.16 as a function of the photon energy for the coherent edge setting 930 MeV. These enhancements have been accurately determined from previous analyses such that we can use them as a weight (W_{enh}) to effectively remove the enhancement of the flux near the coherent edges*. This gives a flux distribution equivalent to that of an unpolarised photon beam (we note that these corrections apply only in the region of the coherent peak i.e. a small energy bite of the overall photon spectra). These structures are removed from the photon spectra (flux) as otherwise photon energy bins in the coherent peak regions would have a biased sampling of yields from across the bin. The experimental data is weighted by $1/W_{\text{enh}}$ to remove the enhancement and photons far from the coherent edges, or photons produced from an amorphous radiator, have an enhancement set to 1 as these photons have zero polarization.

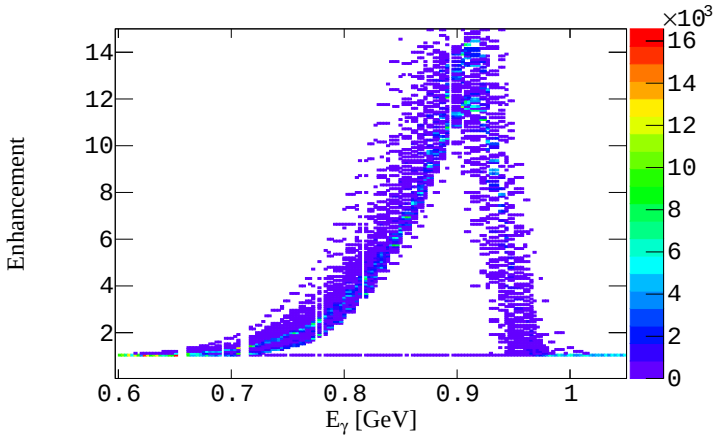

Figure 8.16: The enhancement fit function, as read from the polarisation tables, as a function of photon energy for all primary electron beam energies and coherent edge 930 MeV.

The experimental photon energy spectra with and without this enhancement weighting applied are presented in Fig. 8.17, which shows the coherent and (reconstructed) incoherent bremsstrahlung photon energy spectra for the experimental data (these are for photons passing an additional requirement of at least 1p detected in CLAS - from which the enhancement factors were derived in FROST analyses). It is clear that the method is effective in removing coherent structures from the data.

*The procedure for determining the enhancements is involved, completed by collaborators in advance of the present analysis, and described in detail in [101].

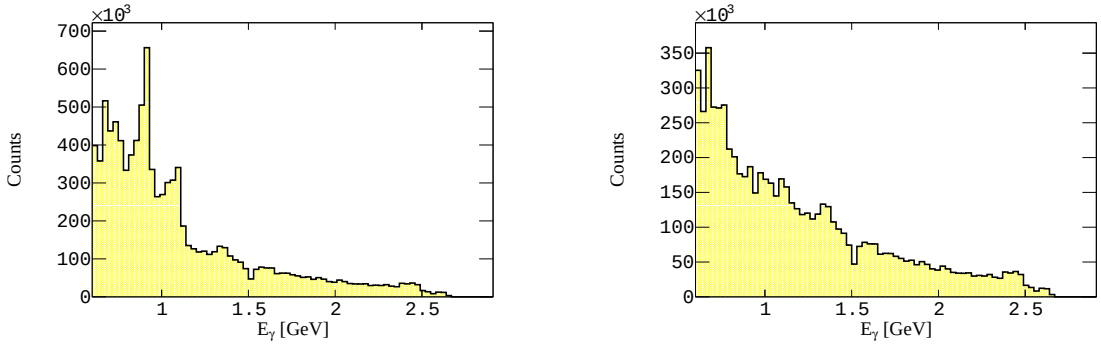

Figure 8.17: The left plot shows the experimental photon energy spectrum before applying the enhancement fit weighting, with coherent peaks evident. The right plot shows the photon energy spectrum after applying the enhancement fit weighting. The data are from the primary electron beam energy of 2780 MeV for the experimental data.

The shape of the photon spectra without trigger conditions (ungated for electrons detected at the tagger focal plane) can be extracted from the energy distribution of "out-of-time" photons. Although this samples the photon spectrum before passing through the collimator, it is informative to compare the distributions and check that this photon flux distribution has a comparable shape to the "in-time" photon flux - that is for photons which passed through the collimator and triggered CLAS (these are photons that pass our $|\Delta t_\gamma| < 1$ ns cut, i.e. our trigger condition). The "out-of-time" photon energy spectra are shown in Fig. 8.18 - derived from regions prior to and after the tagger prompt peak. It is clear that the photon flux before and after the collimator are similar in shape, and the distribution is not strongly affected by the collimation. The small discrepancies in the region of the coherent peaks are expected (as the enhancement factor is calculated for prompt photons passing through the collimator and would not accurately describe the enhancements from uncollimated spectra). It is clear that away from these regions the shape of the collimated and uncollimated photon energy distributions are consistent.

The bottom right distribution in Fig. 8.18 presents the ratio of the "in-time" and "out-of-time" photon energy distributions for all three primary electron beam energy settings, with coarser binning. The mean ratio, $\overline{R\left(\frac{\text{In}}{\text{Out}}\right)}$, and the root mean square (RMS) value of the mean ratio, $\overline{R\left(\frac{\text{In}}{\text{Out}}\right)}_{RMS}$, is determined and we take the systematic error in the flux shape to be $1 - \left[\overline{R\left(\frac{\text{In}}{\text{Out}}\right)} + \overline{R\left(\frac{\text{In}}{\text{Out}}\right)}_{RMS}\right]$. This provides us with an upper limit on the systematic uncertainty arising from the flux shape. This results in a global systematic of 8.3% from the flux shape, which is applied to all observables.

8.3.2 Deriving the Photon Energy Spectra for use with GiBUU

The previous studies indicate the shape of the photon energy spectra can be established with reasonable accuracy. Unfortunately, in the g9a experiment the tagging efficiency was not directly measured, which presents challenges for putting these photon distributions on

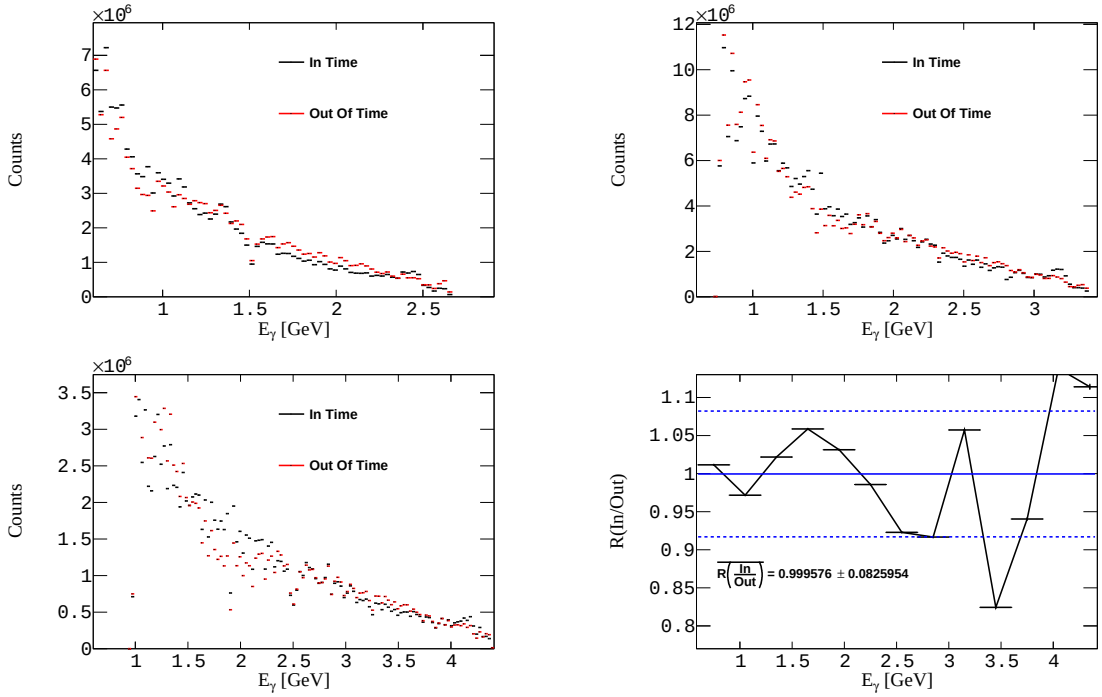

Figure 8.18: The weighted experimental photon energy spectrum for both the "in-time" and "out-of-time" photons, where a single global scale factor was used to scale the two data sets. The distributions are presented for each primary electron beam energy setting: 2780 MeV (top left), 3545 MeV (top right) and 4599 MeV (bottom left). The bottom right distribution presents the ratio of the "in-time" to "out-of-time" photons, for all primary electron beam settings, where the solid blue line represents the average ratio and the dashed blue lines present the $\mu \pm$ RMS value.

an absolute scale as the tagging efficiency is required for cross-section determination. However, as our analysis is aimed at comparing cross-sections to those predicted by GiBUU, we choose to normalise the photon spectra such that the experimental cross-section matches that predicted from GiBUU for a well-established reaction in a well-established photon energy regime ($^{12}\mathrm{C}(\gamma, p\pi)$ for photon energies $600-700$ MeV as discussed later). This normalisation will then put the photon flux on scale for all energies as the energy dependence of the flux is known.

The cross-sections for the experimental data for other photon energies can then be determined by accounting for the number of photons in the photon energy bin of interest. Therefore, we take the ratio of the number of photons (yield) in the bin of interest ($Yield_{\mathrm{bin}}$, typically 200 MeV wide) to the number of photons in the bin we scale the data to GiBUU ($Yield_{\mathrm{scale}}$, in the photon energy bin $E_\gamma = 600 - 700$ MeV). This accounts for the flux dependence of the photon energy distribution as the tagging efficiency is not constant and depends on the photon energy, and the distribution has a characteristic $1/E_\gamma$ incoherent bremsstrahlung shape (since we have removed the coherent peaks), which is also removed using this method. Due to inefficient tagger channels and differing efficiencies between tagger channels, we opted for a 200 MeV photon energy bin-by-bin scaling

method to average the bremsstrahlung and tagging efficiency dependencies across the 200 (500 for high photon energies) MeV wide bins. The systematic uncertainty determined for the flux dependence (8.3%) accounts for discrepancies between our method and a tagger-channel by tagger-channel scaling method. Studies were performed for the two methods and it was found that the yields of the two methods agreed within the flux systematic uncertainty. The GiBUU model predictions are produced with a uniform distribution of photon energies across the range covered by the experimental data. Note as GiBUU predicts a cross-section, the number of photons at each energy is accounted for - more photons just gives better statistical accuracy but does not change the cross-section, see Fig. 8.19 (see Eq. (7.1) for the definition of missing mass).

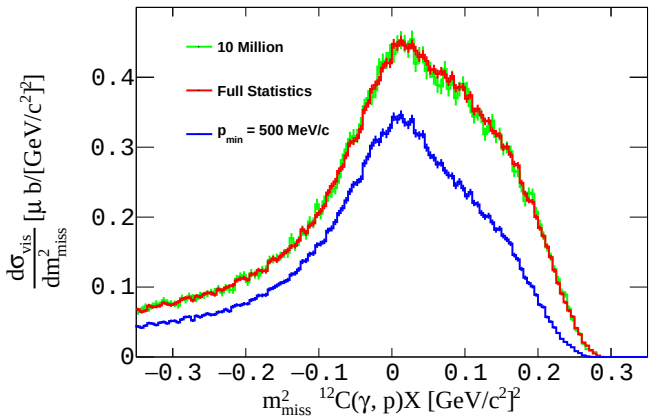

Figure 8.19: The visible cross-section as a function of the missing mass squared (assuming a proton target rather than carbon, note the target is still carbon in reality) for the reaction $^{12}\mathrm{C}(\gamma, p)X$ the GSIM data with 36 (red) and 10 (green) million events analysed in the photon energy bin $600 - 700$ MeV. The cross-section does not change with more statistics. The blue line presents the same observable but with a higher minimum momentum threshold of 500 MeV/c, which reduces the visible cross-section, as expected.

The consistency of the method can be checked by choosing photon energy bins covered by all 3 electron beam energy settings and comparing the shapes and cross sections of the distributions for a key physics observable. Some examples of these studies, the missing mass of the reaction $^{12}\mathrm{C}(\gamma, p)X$ for all 3 beam energy settings, are shown in Fig. 8.20. It is clear that the observed cross-sections for all three primary electron beam energy settings match. Figure 8.21 presents the same observable as in Fig. 8.20 for the simulated data. As expected, these also match.

8.3.3 Deriving the Experimental Cross-Section from the Measured Yields

As discussed in the subsections above, the yields in the experimental data are appropriately weighted by the enhancement fit. The experimental cross sections in each photon energy bin are then calculated by Eq. (8.1):

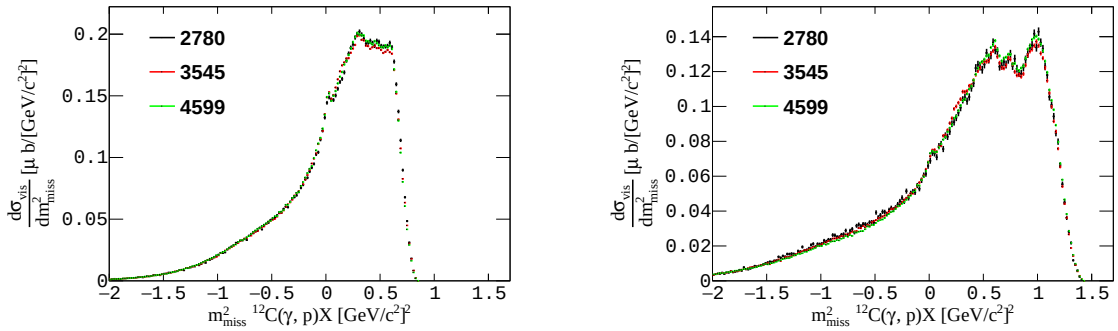

Figure 8.20: The visible cross-section as a function of the missing mass squared (assuming a proton target) for the reaction $^{12}\mathrm{C}(\gamma, p)X$, for each primary electron beam energy setting, for the photon energies $E_\gamma = 1200 - 1400$ MeV (left) and $E_\gamma = 1800 - 2000$ MeV (right). The distributions are for the experimental data.

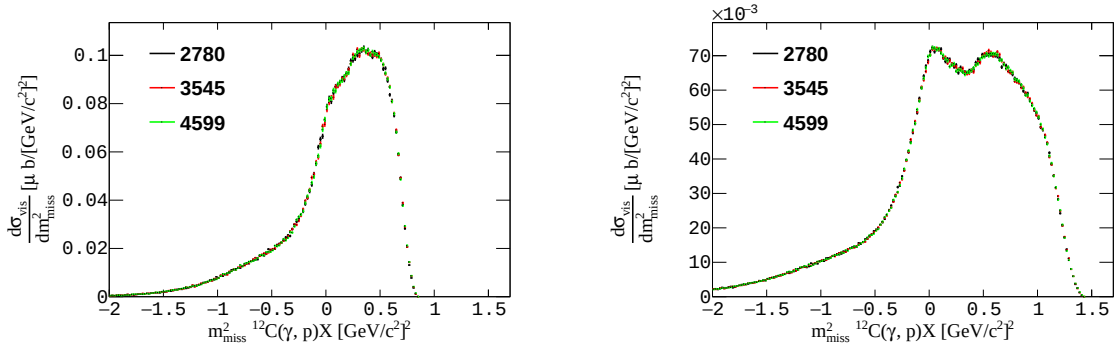

Figure 8.21: As for Fig. 8.20, but for the simulated data.

$$\sigma_{Exp} = \frac{Yield_{\mathrm{bin}} \times SF}{Yield_{\mathrm{scale}} \times W_{\mathrm{enh}}}, \tag{8.1}$$

where $Yield_{\mathrm{scale}}$ and $Yield_{\mathrm{bin}}$ are defined as before. SF is a scale factor to be determined from the normalisation of the experimental data to the GiBUU predicted cross sections for a well-established reaction ($^{12}\mathrm{C}(\gamma, p)X$ where X is near the peak of quasi-free pion photoproduction), in the photon energy bin $E_\gamma = 600 - 700$ MeV. The scale factor is defined as

$$SF = \frac{\sigma_{p\pi}^{\mathrm{tot,\ gibuu}}}{Yield_{p\pi}^{\mathrm{tot,\ data}}}, \tag{8.2}$$

where $\sigma_{p\pi}^{\mathrm{tot,\ gibuu}}$ is the cross section in GiBUU and $Yield_{p\pi}^{\mathrm{tot,\ data}}$ is the yield of the experimental data for 1p reactions with the cuts around the pion mass (see Sec. 8.4), respectively. SF is a constant which is an estimate of the ratio of the yield to luminosity in the photon energy bin $600 - 700$ MeV for the experimental data, that transforms the data from a yield to a cross-section. Since the cross-section is proportional to such a ratio, it is used to predict the cross-section for experimental data in different photon energy bins (by

also taking the ratio of the photons to account for tagging efficiency differences etc. as discussed previously). The normalisation procedure is discussed in Sec. 8.4.

The many proton knockout yields vary with photon energy and typically diminish at the higher energies measured here. Our results therefore use different sized photon energy bins for different regions. For 0.6 GeV $\leq E_\gamma \leq$ 2.2 GeV, the photon energy is segmented into 200 MeV bins, and for 2.2 GeV $\leq E_\gamma \leq$ 3.7 GeV, E_γ is segmented into 500 MeV bins, then the final bin includes all the data where $E_\gamma >$ 3.7 GeV.

8.4 Normalisation

As mentioned in Sec. 8.3, we need to normalise the yields of the experimental data to match the GiBUU cross-sections and put the experimental data on an absolute visible cross-section scale, i.e. extract the scale factor (SF) in Eq. (8.1). We achieve this using $p\pi$ photoproduction in an energy range where GiBUU is known to reproduce the cross section to an accuracy of $5-10\%$ (see Fig. 3.1). This normalisation to GiBUU is obtained from the lowest electron beam energy setting. The photon energy spectra from other beam settings are then matched to this benchmark in common photon energy regions where they overlap. This procedure matches the photon flux from the higher beam energy data to that of the (GiBUU normalised) lowest beam energy setting.

8.4.1 Determination of the Normalisation Factor

To determine the normalisation factor, we study $^{12}\mathrm{C}(\gamma, p)X$ reactions for both the experimental and simulated data in the photon energy range $600-700$ MeV. The missing mass distributions are presented in Fig. 8.22.

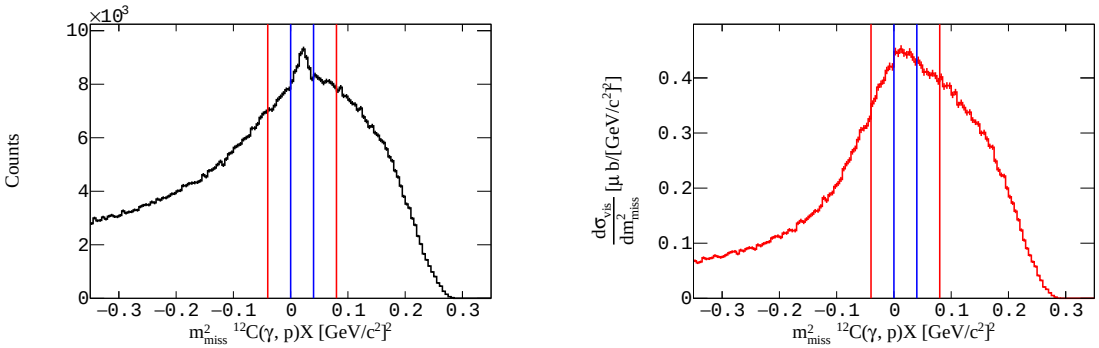

Figure 8.22: The missing mass squared (assuming a proton target) of the reaction $^{12}\mathrm{C}(\gamma, p)X$ for the experimental (left) and simulated (right) data in the photon energy bin $E_\gamma = 600-700$ MeV. The lines present our integral; we integrate between the red and blue lines and exclude the area outside of the red lines and between the two blue lines.

In extracting the $^{12}\mathrm{C}(\gamma, p\pi)$ reaction from the carbon target data, care was taken to exclude the small contributions from ice build-up on the downstream face of the target

(established in previous FROST analyses). For this reason, we normalise to regions around the quasi-free pion production peak in ^{12}C but exclude the narrow peak from the hydrogen in the ice, i.e. reconstructed π mass (-0.04 MeV/c^2 $< m^2_{\text{miss}} <$ 0.0 MeV/c^2 and 0.04 MeV/c^2 $< m^2_{\text{miss}} <$ 0.08 MeV/c^2). The regions are marked in Fig. 8.22; and we compare the yields in the experimental data ($Yield^{\text{tot, data}}_{p\pi}$) to the visible cross-sections in the simulated data ($\sigma^{\text{tot, gibuu}}_{p\pi}$), integrated between the red and blue lines.

The justification for the regions used for determining our scale factor can be seen from Fig. 8.23, which shows the GiBUU prediction for the observable broken down into the contributions from 1π production and 2π production. It is clear the cut region is dominated by 1π production. It is also clear the left- and right-hand regions contain different contributions from 2π, which is used in assessing the systematic uncertainty from this background contribution.

We extract SF from the yields in this mass region for the photon energy bin (0.6 GeV $\leq E_\gamma <$ 0.7 GeV). It has been shown in [37] and in particular [102] that, in this photon energy range, GiBUU accurately describes the cross section for this reaction and the total photoabsorption cross section at the $5-10\%$ level (see Fig. 3.1). The low energy bin also shows minimal contribution from 2π production which, as discussed in the results, is not well modelled in GiBUU. However, to produce a systematic for our normalisation we integrated four regions; between the leftmost red and blue lines, between the rightmost blue and red lines, both sets of lines (taken to be our scale factor) and between the two red lines including the hydrogen peak. The scale factors were determined to be 3.775×10^6, 3.944×10^6, 3.863×10^6 and 3.871×10^6, respectively, which produces a 1.8% systematic

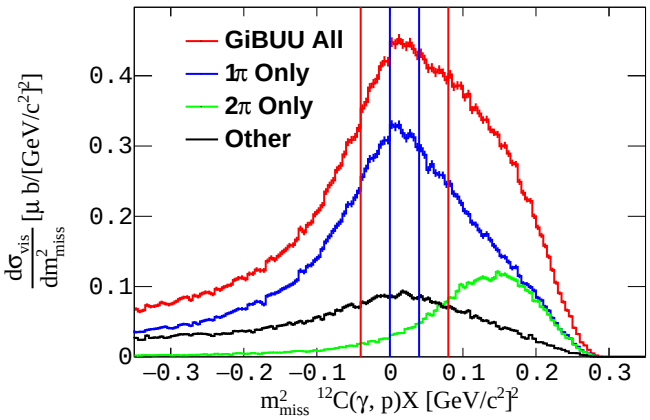

Figure 8.23: The missing mass squared (assuming a proton target) of the reaction $^{12}\text{C}(\gamma, p)X$ for the simulated data in the photon energy bin $E_\gamma = 600 - 700$ MeV, with a breakdown of the different contributions to the distribution. 1π, 2π and other. The breakdown is achieved by checking whether there is 1π (of any species), 2π (of any species) and other (any events not in these categories) in the GiBUU generated event (before passing through GSIM). We integrate between the red and blue lines and exclude the area outside of the red lines and between the two blue lines.

for the deviation of the scaling factor.

It is interesting to compare the ratio of yields between data and simulation (for the specific missing mass regions shown above) at other photon energies. Figure 8.24 presents the ratio of yields between the experimental and simulated data for the aforementioned reaction, along with a comparison of the distributions shown in Fig. 8.22 after applying the scale factor to put the two data sets on scale. The ratios are within 20% of unity apart from photon energies in the $1-1.5$ GeV region. These deviations between data and GiBUU will be discussed in more detail in the results section and arise from significant sensitivity in this ratio from inaccuracies in the modelling of 2π production, which for these photon energy ranges contribute significantly to the visible cross sections in this mass region. The deviations should not be taken implicitly that the GiBUU description of the single π process is inaccurate.

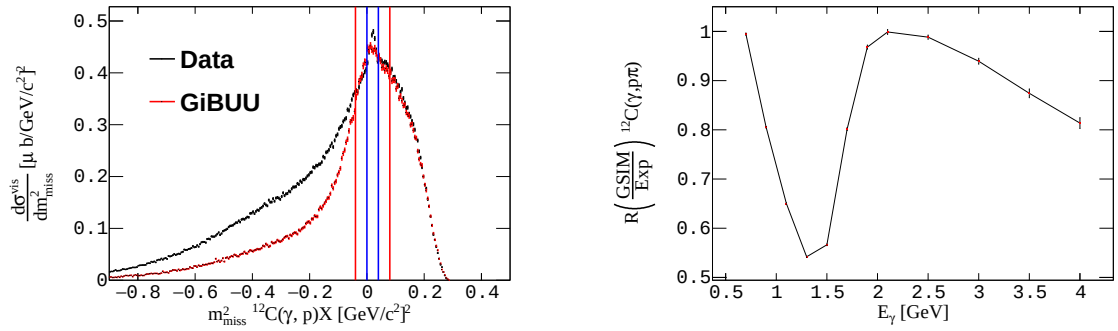

Figure 8.24: The left distribution presents that shown in Fig. 8.22 on an absolute visible cross section scale. The Right plot presents the $^{12}\mathrm{C}(\gamma, p\pi)$ ratio of yields between the experimental and simulated data as a function of E_γ, integrated over all bins of $\cos\theta$, for all primary electron beam settings. The ratio is determined after we have applied the scale factor.

This is illustrated in the GiBUU missing mass distributions for the reaction $^{12}\mathrm{C}(\gamma, p)X$ integrated overall $\cos\theta$ in Fig. 8.25 and Fig. 8.26. As well as the total GiBUU prediction, the contributions from specific processes are also shown*. In and around the bin where we normalise ($E_\gamma = 0.6 - 0.7$ GeV) the selected mass region is dominated by 1π with 2π below 20%. As the photon energy increases, this mass region becomes more dominantly fed by 2π production (e.g. above $E_\gamma = 1.8$ GeV 1π gives negligible contributions to the yield). The ratios in Fig. 8.24 therefore only accurately represent the agreement of the 1π cross-section in the lowest photon energy bin.

*We remark that in particular energy bins, the resonance-only yields are larger than when all processes are turned on since the GiBUU model has negative weights which account for interference between the resonant and non-resonant amplitudes in π production.

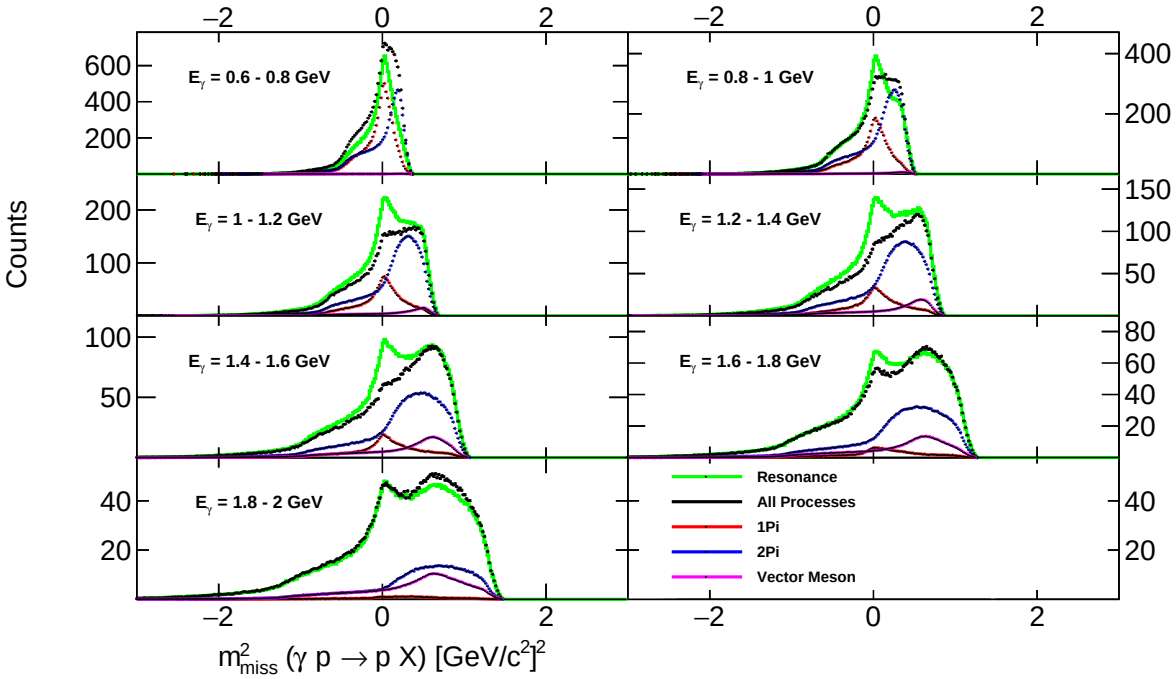

Figure 8.25: The missing mass squared (assuming a proton target) for the reaction $^{12}\mathrm{C}(\gamma, p)X$ for the raw GiBUU model data, with different processes turned on and off to isolate production cross sections for low/medium photon energy bins.

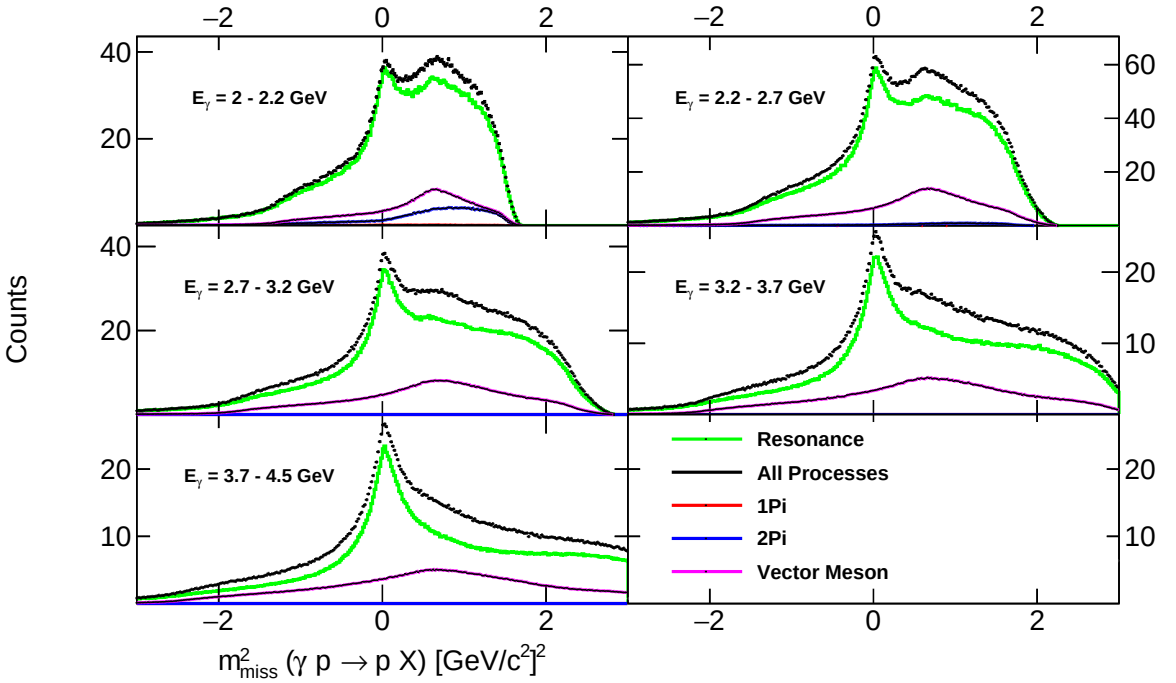

Figure 8.26: The missing mass squared (assuming a proton target) for the reaction $^{12}\mathrm{C}(\gamma, p)X$ for the raw GiBUU model data, with different processes turned on and off to isolate production cross sections for high photon energy bins.

8.4.2 Normalisation of Other Targets to carbon

As previously mentioned, the g9a FROST experiment had 3 targets; butanol, carbon and polythene. Butanol (C_4H_9OH) and polythene (CH_2) have more complex compositions than the pure carbon target, but knowing their target lengths and densities we can calculate the number of molecules in each target and subsequently the number of carbon atoms in each target. Using Eq. (8.3), we can calculate the number density of each target, and knowing the number of atoms per molecule from the compositions of the target we can calculate the number of carbon atoms per unit area.

$$N = \frac{N_A \rho L}{m_{\text{mol}}}, \tag{8.3}$$

where N is the number density, N_A is Avogadro's number, ρ is the target density, L is the length (or thickness) of the target and m_{mol} is the molar mass of the target material. We remark that due to the positions of these targets and their different dimensions and densities to that of carbon, there may be small effects on the acceptance of protons from each of the targets. This will be discussed in future sections and we mitigate these effects from a judicious choice of proton energy thresholds such that a common threshold can be applied across the targets. The butanol target may display additional features to carbon and polythene since it also contains oxygen. Data from the other targets is only analysed for events where 2 or more protons are knocked out, eliminating any contributions from the hydrogen.

Table 8.3 presents the number densities and number of carbon atoms in each target per unit area (in cm). The butanol and polythene distributions are then scaled by the ratio of carbon atoms in the respective targets to the pure carbon target. The ratios are as follows: $N_{^{12}\text{C}}/N_{\text{butanol}} = 0.1687$ and $N_{^{12}\text{C}}/N_{\text{polythene}} = 0.6857$.

Target	butanol	carbon	polythene
Length (cm)	5	0.15	0.35
Density (g/cm^3)	0.538	1.926	1.41
Molar Mass (g/mol)	74.12	12.011	28.05
Number Density (cm^{-2})	2.1855×10^{22}	1.4486×10^{22}	1.0595×10^{22}
Number of ^{12}C (cm^{-2})	8.742×10^{22}	1.4486×10^{22}	2.119×10^{22}
Chemical Composition	C_4H_9OH	C	CH_2

Table 8.3: Summary of information about the three targets in the g9a FROST experiment, including the number of carbon atoms present in each target.

8.5 Analysis of the Recoiling System

The properties of the recoiling system after the many-proton knockout reactions can be used to infer the nature of the reactions that occurred. Here we analyse the nature of the recoiling system for both the experimental and simulated data samples to maximise the signal of direct many-proton knockout reactions. Note we only show a selection of photon energy bins and multiplicities in this section, but the full missing mass plots for all multiplicities and photon energy bins are presented in the results section (see Sec. 8.9).

8.5.1 Missing Mass

An important quantity to consider is the missing mass of the recoiling system. This is calculated using Eq. (7.1) and Fig. 8.27 presents the missing mass for 2 (left) and 3 (right) proton knockout reactions for both experimental and simulated data. In such distributions, a direct knockout process would give a missing mass close to the intact recoil nucleus (with a distribution of yield above this minimum determined by the binding energies of the shells of the knocked-out nucleons), while the associated emission of other undetected particles, e.g. neutrons and pions, would tend to contribute to higher values of missing mass.

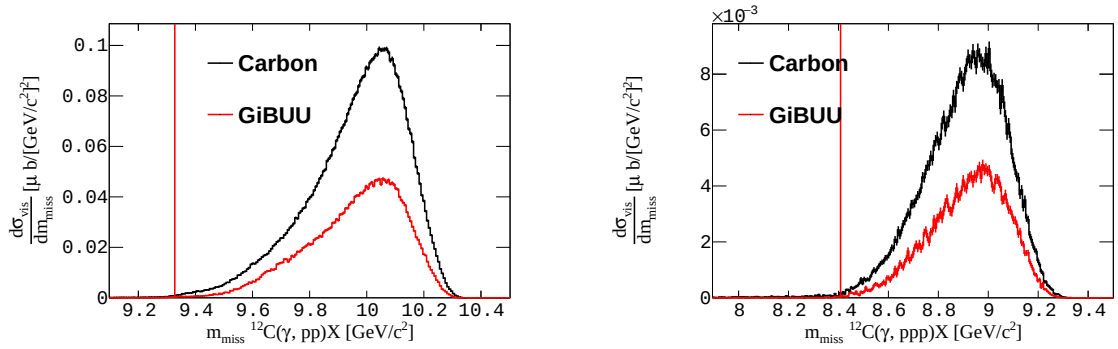

Figure 8.27: The missing mass for $^{12}\mathrm{C}(\gamma, p_1p_2)X$ (left) and $^{12}\mathrm{C}(\gamma, p_1p_2p_3)X$ (right) reactions with 1.0 GeV $< E_\gamma <$ 1.2 GeV. The black (experimental) and red (simulated) curves represent the two data sets. The red lines indicate the expected residual mass location.

The shifted missing mass is calculated using Eq. (7.2) and the $m_{\mathrm{miss}}^{\mathrm{shift}}$ distributions for 2 (left) and 3 (right) proton knockout reactions are presented in Fig. 8.28, for both experimental and simulated data. As discussed in Subsec. 7.2.1, shifted missing mass values near zero are heavily correlated with direct knockout processes. On the contrary, shifted missing mass values that deviate far from zero are attributed to additional undetected particles in the final state, i.e. non-direct knockout processes. A detailed comparison of such spectra for the full range of photon energies and multiplicities is discussed in the results section.

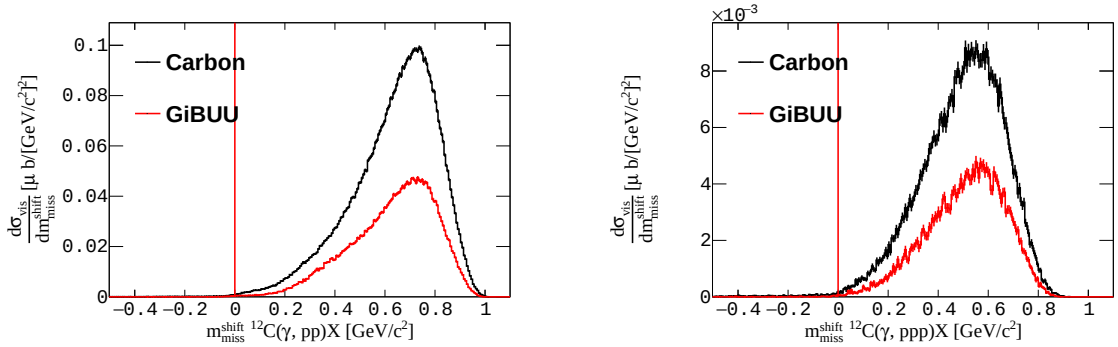

Figure 8.28: The shifted missing mass for $^{12}\mathrm{C}(\gamma, p_1p_2)X$ (left) and $^{12}\mathrm{C}(\gamma, p_1p_2p_3)X$ (right) reactions with 1.0 GeV $< E_\gamma <$ 1.2 GeV, where we have subtracted the expected residual target mass. The black (experimental) and red (simulated) curves represent the two data sets. The red lines are at the zero of shifted missing mass - corresponding to the mass of the respective intact ground state nucleus following 2p or 3p knockout.

8.5.2 Missing Transverse Momentum

The missing transverse momentum, $p_\perp^{\mathrm{miss}}$, is a very important quantity for this research since we are searching for direct knockout signals. $p_\perp^{\mathrm{miss}}$ is calculated using (7.11) and Fig. 8.29 presents the distributions of $p_\perp^{\mathrm{miss}}$ for 1p, 2p, 3p and 4p knockout reactions for all E_γ.

Due to momentum mismatch single proton knockout at these photon energies is very

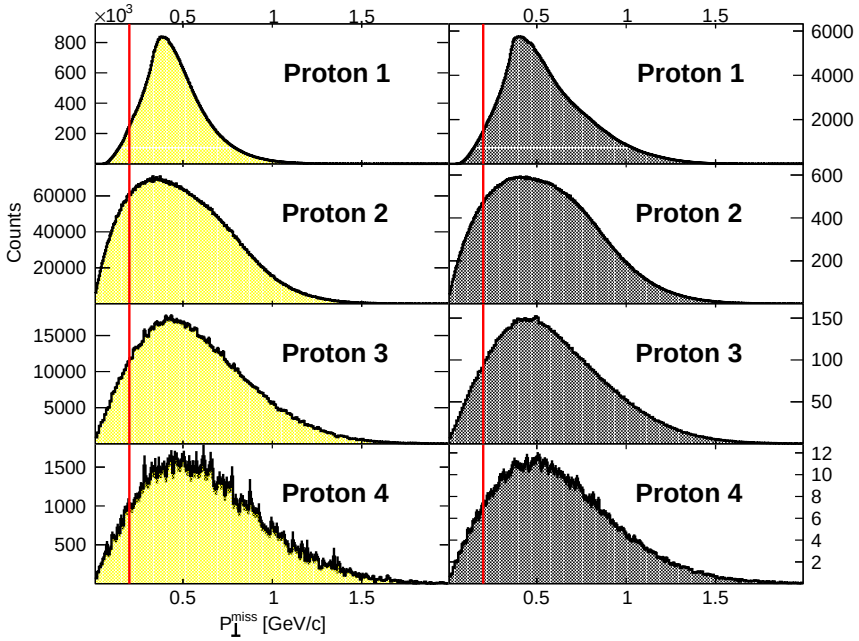

Figure 8.29: $p_\perp^{\mathrm{miss}}$ for the reaction $^{12}\mathrm{C}(\gamma, p_1)X$ (top), $^{12}\mathrm{C}(\gamma, p_1p_2)X$ (top-middle), $^{12}\mathrm{C}(\gamma, p_1p_2p_3)X$ (bottom-middle) and $^{12}\mathrm{C}(\gamma, p_1p_2p_3p_4)X$ (bottom) protons knocked-out. The left plots show the experimental distributions and the right plots show the simulated distributions for all photon energies. The red lines indicate the position of the cuts.

strongly suppressed. These 1p data will therefore arise through meson production or through 2N etc. absorption processes where one of the protons is undetected. For 2p and 3p reactions direct knockout is feasible, either through processes such as 2N, 3N or through initial meson production and reabsorption. GiBUU allows us to explore what $p_\perp^{\text{miss}}$ regions such direct processes would contribute. This is shown in Fig. 8.30 for direct proton knockout processes and Fig. 8.31 for direct + 1 neutron knockout reactions. These distributions are presented with the raw GiBUU data, so there are no undetected particles in these distributions. As expected, the distributions reflect the Fermi momentum for the knocked-out nucleons - peaking around the 0.2 GeV/c mark. Restricting $p_\perp^{\text{miss}}$ to values below 0.2 GeV/c, therefore, would be expected to enhance the contribution from direct knockout processes to the yield, as the introduction of additional final state particles shifts the missing transverse momentum to higher momenta.

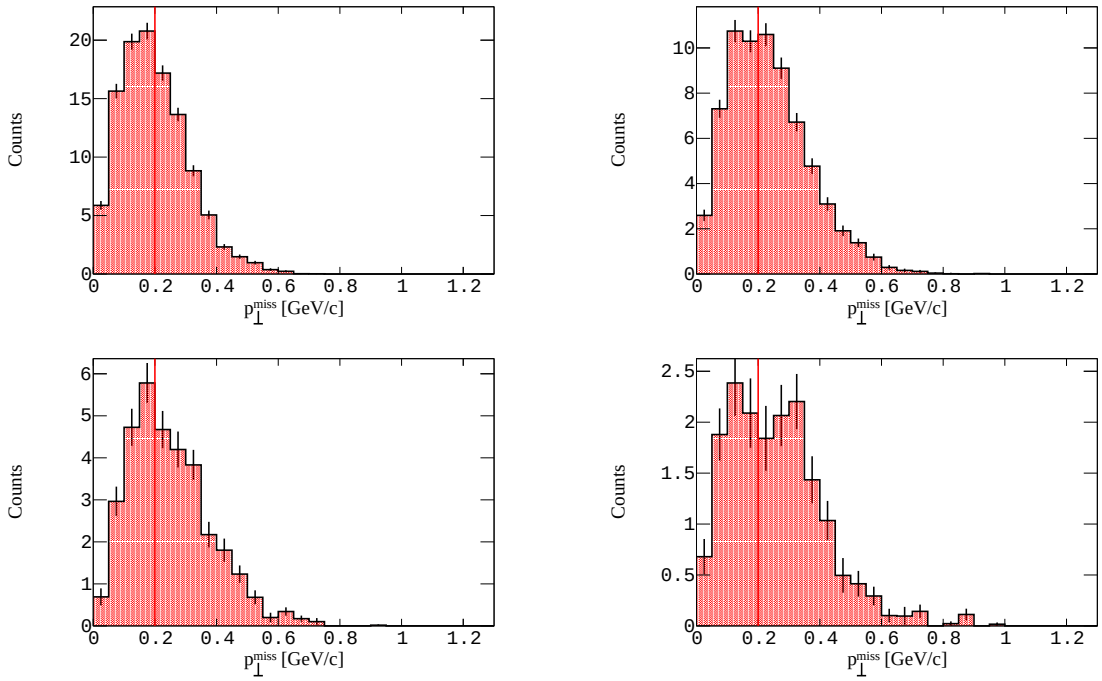

Figure 8.30: $p_\perp^{\text{miss}}$ for the reaction $^{12}\text{C}(\gamma, p_1 p_2)$ (top) and $^{12}\text{C}(\gamma, p_1 p_2 p_3)$ (bottom) from the raw GiBUU data for 0.8 GeV $\leq E_\gamma \leq$ 1.0 GeV (left) and 1.0 GeV $\leq E_\gamma \leq$ 1.2 GeV (right). The red line indicates the position of the 0.2 GeV/c cut applied in the analysis of the experimental and GSIM data.

It is informative to look at the missing mass distributions with this $p_\perp^{\text{miss}} < 0.2$ GeV/c cut applied. The missing mass after cutting on $p_\perp^{\text{miss}} < 0.2$ GeV/c is displayed in Fig. 8.32. The cut clearly emphasizes the strength at low missing mass - even showing a "bump" structure in this region. Similar features are observed in the GiBUU predictions for the direct process. Figure 8.33 presents the missing mass distributions after cutting on $p_\perp^{\text{miss}} <$ 0.2 GeV/c before and after checking for direct knockout contributions from the truth-level data, for 2 and 3 proton knockout reactions. The truth-level data is the raw GiBUU data before passing it through GSIM, hence it retains the full knowledge of the final state.

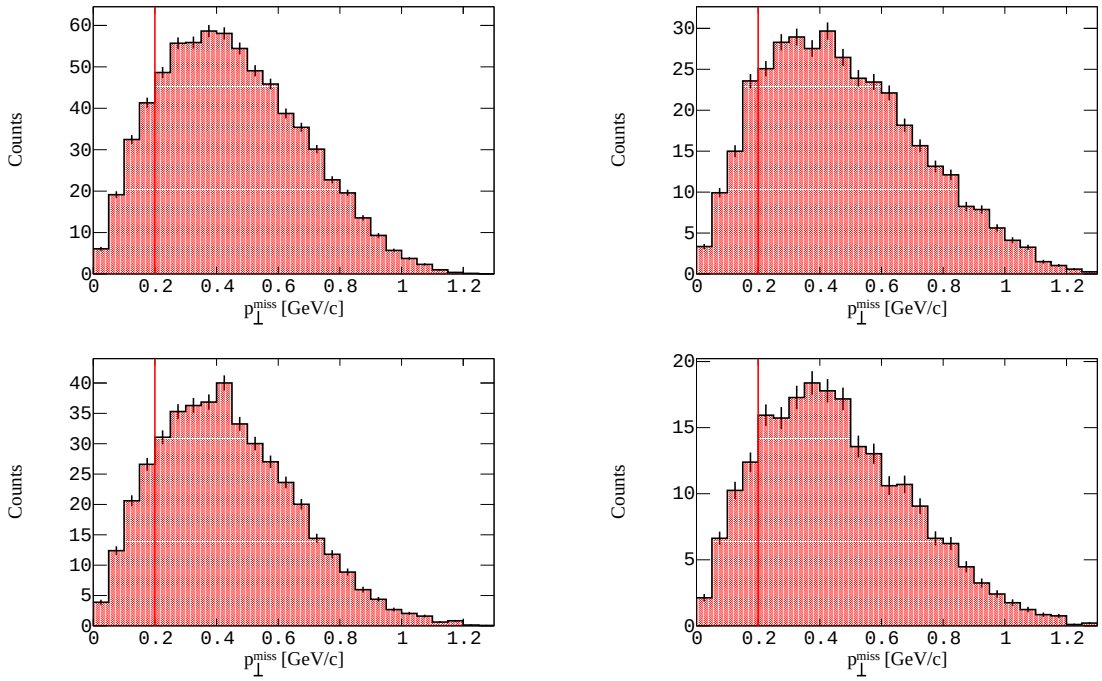

Figure 8.31: $p_\perp^{\text{miss}}$ for the reaction $^{12}\text{C}(\gamma, p_1 p_2 n)$ (top) and $^{12}\text{C}(\gamma, p_1 p_2 p_3 n)$ (bottom) from the raw GiBUU data for 0.8 GeV $\leq E_\gamma \leq$ 1.0 GeV (left) and 1.0 GeV $\leq E_\gamma \leq$ 1.2 GeV (right). The red line indicates the position of the 0.2 GeV/c cut applied in the analysis of the experimental and GSIM data.

All data presented under the blue line are for direct proton knockout reactions, where no additional particles are in the final state, verified by the truth-level data. The low missing mass bump appears to be strongly fed by the direct knockout processes.

8.5.3 Recoiling Theta

The polar angle of the reconstructed recoil momentum, θ_{Recoil}, is also a useful physical observable. For a direct process only involving the detected protons, this would reflect

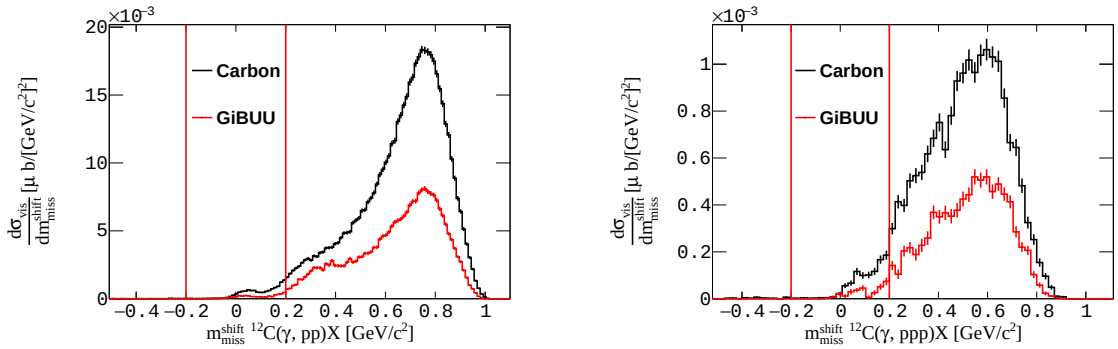

Figure 8.32: $m_{\text{miss}}^{\text{shift}}$ after cutting on $p_\perp^{\text{miss}} < 0.2$ GeV/c for the $^{12}\text{C}(\gamma, p_1 p_2)X$ (left) and $^{12}\text{C}(\gamma, p_1 p_2 p_3)X$ (right) reaction for 1.0 GeV $\leq E_\gamma \leq$ 1.2 GeV. Both the experimental (black) and simulated (red) distributions are shown and the red lines indicate 200 MeV/c^2 around the expected mass for a direct knockout.

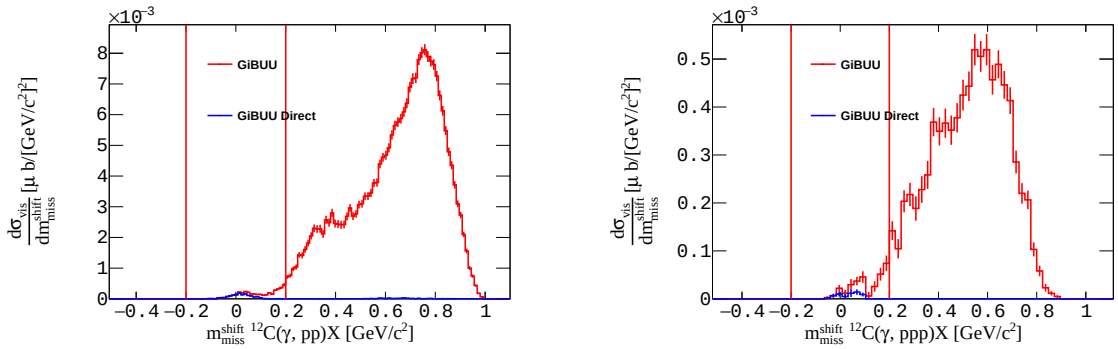

Figure 8.33: $m_{\text{miss}}^{\text{shift}}$ after cutting on $p_{\perp}^{\text{miss}} < 0.2$ GeV/c for the $^{12}\text{C}(\gamma, p_1p_2)X$ (left) and $^{12}\text{C}(\gamma, p_1p_2p_3)X$ (right) reaction for 1.0 GeV $\leq E_{\gamma} \leq$ 1.2 GeV after checking for direct knockout reactions from the truth-level data. Both the simulated (red) and simulated after checking the truth-level data (blue) distributions are shown and the red lines indicate 200 MeV/c^2 around the expected mass for a direct knockout.

the direction of the Fermi momentum of the knocked-out nucleons - i.e. it would be isotropic. Other processes would tend to produce more forward angle recoils due to the

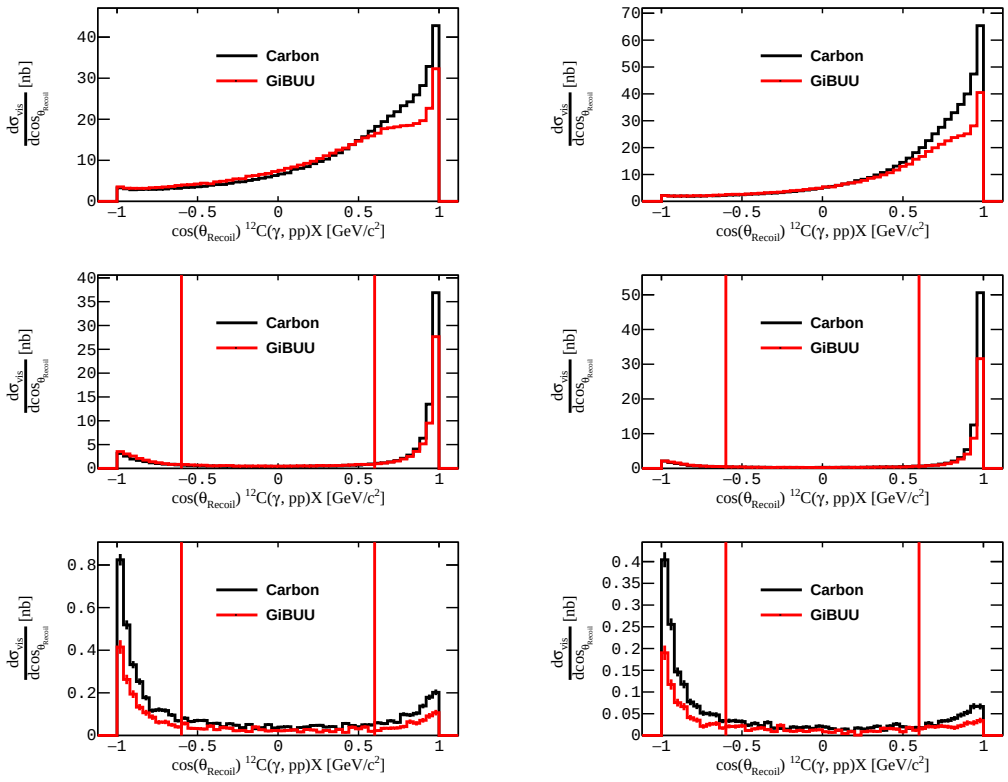

Figure 8.34: Cosine theta of the recoil angle for the reaction $^{12}\text{C}(\gamma, p_1p_2)X$ without residual target cuts (top), a cut on $p_{\perp}^{\text{miss}} < 0.2$ GeV/c (middle) and a cut on $p_{\perp}^{\text{miss}} < 0.2$ GeV/c and 200 MeV/c^2 around the expected mass for a direct knockout (bottom) for two photon energy bins; 0.8 GeV $\leq E_{\gamma} \leq$ 1.0 GeV (left) and 1.0 GeV $\leq E_{\gamma} \leq$ 1.2 GeV (right). The figure presents the isotropic nature of the residual nucleus produced between -0.6 $< \cos\theta_{\text{Recoil}} <$ 0.6. Both the simulated (red) and experimental (black) data are shown and the red lines indicate the cuts imposed to enhance the direct knockout signal.

other undetected particles. Direct nucleon knockout processes would be expected to show a flat dependence with $\cos\theta_{\mathrm{Recoil}}$. Figure 8.34 presents $\cos\theta_{\mathrm{Recoil}}$ before cutting on the residual target (top), after cutting on $p_{\perp}^{\mathrm{miss}} < 0.2$ GeV/c (middle) and after cutting on $p_{\perp}^{\mathrm{miss}} < 0.2$ GeV/c and 200 MeV/c^2 around the expected mass for a direct knockout (bottom), for both the experimental and GSIM data for two photon energy bins; 0.8 GeV $\leq E_{\gamma} \leq$ 1.0 GeV (left) and 1.0 GeV $\leq E_{\gamma} \leq$ 1.2 GeV (right). It is clear that the cuts reveal an isotropic component in the spectra. Figure 8.35 presents the same distributions shown in Fig. 8.34, but zoomed in to illustrate the effect that the residual target cuts applied have on the $\cos\theta_{\mathrm{Recoil}}$ distributions.

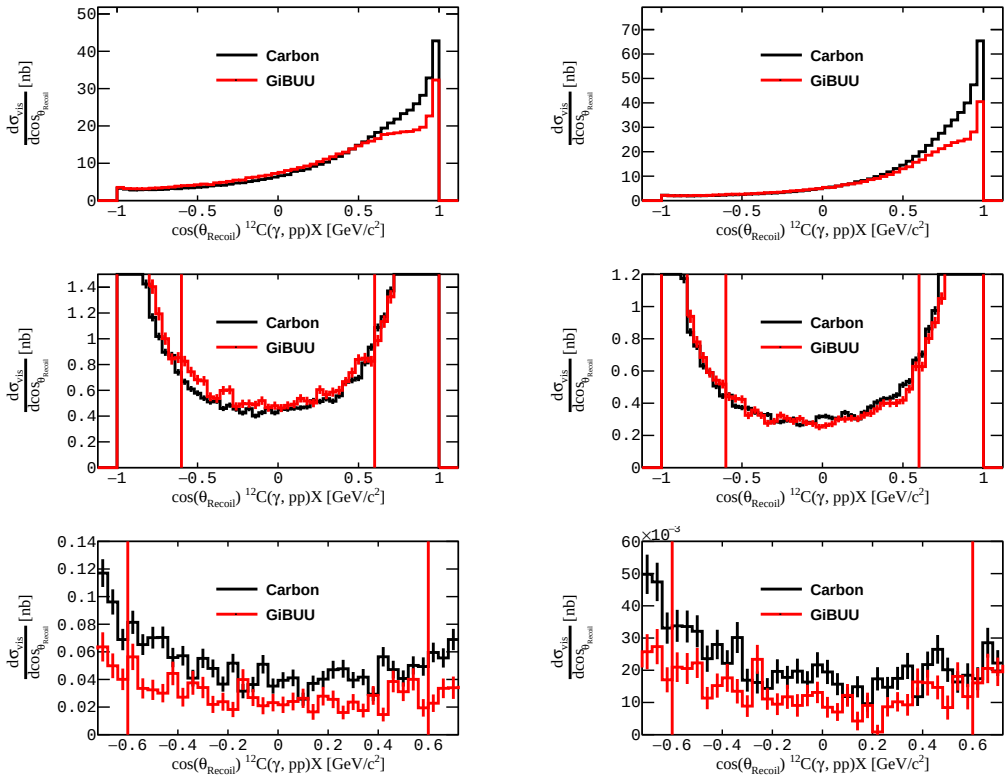

Figure 8.35: As for figure 8.34, but zoomed in on the x-axis.

We adopt a cut -0.6 $< \cos\theta_{\mathrm{Recoil}} <$ 0.6 to select the isotropic region where a flat dependence is seen. At regions outside of this, it is clear there is a background of non-isotropic events arising from processes other than direct knockout. Figure 8.36 presents the missing mass after restricting that $p_{\perp}^{\mathrm{miss}} < 0.2$ GeV/c and -0.6 $< \cos\theta_{\mathrm{Recoil}} <$ 0.6 on the reactions $^{12}\mathrm{C}(\gamma, p_1p_2)X$ and $^{12}\mathrm{C}(\gamma, p_1p_2p_3)X$. The missing mass distributions show enhanced relative contributions from the direct knock-out peak, which is better separated from the processes at higher missing mass.

8.5.4 Missing Mass for Additional Targets

As well as the carbon target, there are other suitable targets in FROST viz. the butanol and polythene targets. Comparing the missing mass cross sections from the different

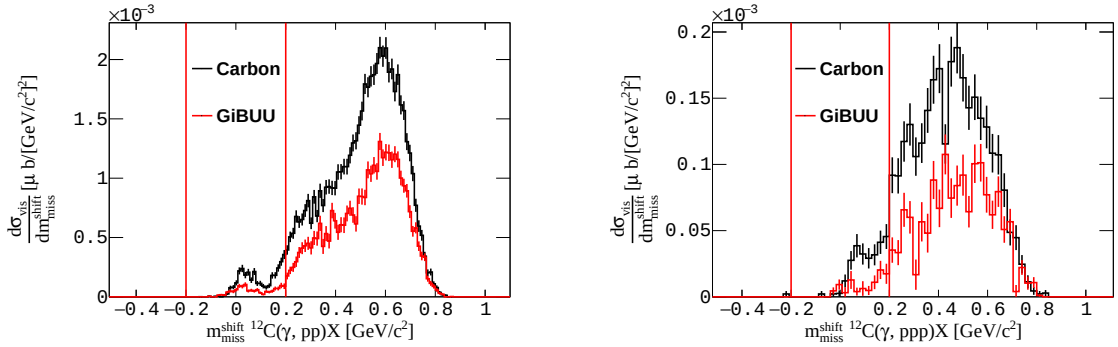

Figure 8.36: Shifted missing mass after selecting the isotropic region of -0.6 < $\cos\theta_{\mathrm{Recoil}}$ < 0.6 and cutting on $p_{\perp}^{\mathrm{miss}}$ < 0.2 GeV/c, for the reaction $^{12}\mathrm{C}(\gamma, p_1p_2)X$ (left) and $^{12}\mathrm{C}(\gamma, p_1p_2p_3)X$ (right) for 1.0 GeV ≤ E_γ ≤ 1.2 GeV. Both the simulated (black) and experimental (red) data are shown and the red lines indicate 200 MeV/c² around the expected mass for a direct knockout.

targets, as well as providing an increase in statistics, provides a further constraint on systematics due to the target placement in CLAS (butanol at the centre and other targets 6 cm and 15 cm downstream.)

In Subsec. 8.4.2 the method for scaling the total number of carbon atoms inside the additional targets present in the FROST experiment to the carbon target was discussed. By scaling the butanol and polythene data by the ratios determined in the previous section, the data for all three targets will be put on scale. We note that we do not expect the three data sets to match in detail due to the ice (oxygen) present in the butanol and carbon targets (by differing amounts - butanol and carbon have approximately 20% and 7% oxygen, these contributions were added to the "carbon" target densities). Polythene has no oxygen build up and provides a further constraint on systematic uncertainties.

Figures 8.37 and 8.38 present the shifted missing mass with an additional cut on $p_{\perp}^{\mathrm{miss}}$ < 0.2 GeV/c, and $p_{\perp}^{\mathrm{miss}}$ < 0.2 GeV/c and -0.6 > $\cos\theta_{\mathrm{Recoil}}$ < 0.6, and Fig. 8.39 presents

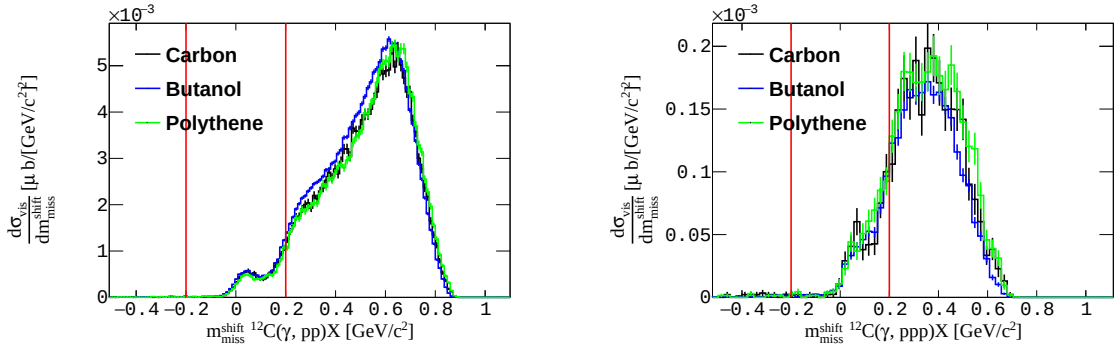

Figure 8.37: $m_{\mathrm{miss}}^{\mathrm{shift}}$ after cutting on $p_{\perp}^{\mathrm{miss}}$ < 0.2 GeV/c for the reaction $^{12}\mathrm{C}(\gamma, p_1p_2)X$ (left) and $^{12}\mathrm{C}(\gamma, p_1p_2p_3)X$ (right) for 1.0 GeV ≤ E_γ ≤ 1.2 GeV. Data is shown for all three targets in FROST and the red lines indicate 200 MeV/c² around the expected mass for a direct knockout.

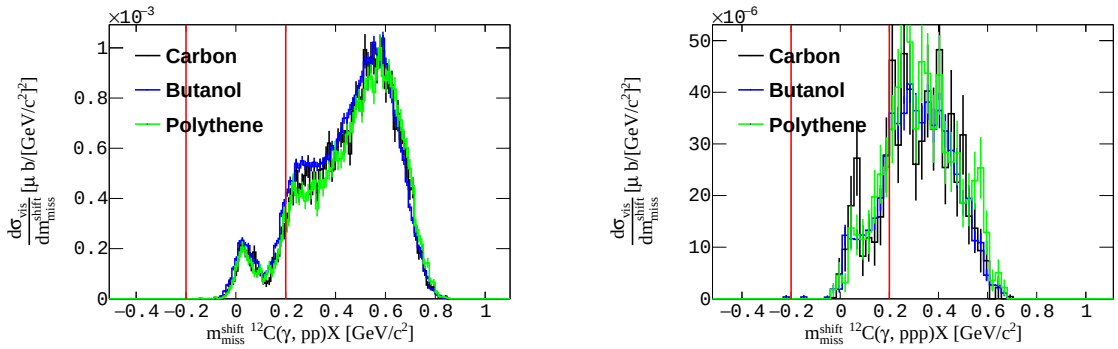

Figure 8.38: Shifted missing mass after selecting the isotropic region of -0.6 $< \cos\theta_{\mathrm{Recoil}} <$ 0.6 and cutting on $p_{\perp}^{\mathrm{miss}} < 0.2$ GeV/c for the reaction $^{12}\mathrm{C}(\gamma, p_1p_2)X$ (left) and $^{12}\mathrm{C}(\gamma, p_1p_2p_3)X$ (right) for 1.0 GeV $\leq E_{\gamma} \leq$ 1.2 GeV (right). Data is shown for all three targets in FROST and the red lines indicate 200 MeV/c^2 around the expected mass for a direct knockout.

$\cos\theta_{\mathrm{Recoil}}$ with the same layout as Fig. 8.34, for all three targets, where all distributions have a minimum momentum threshold of 500 MeV/c.

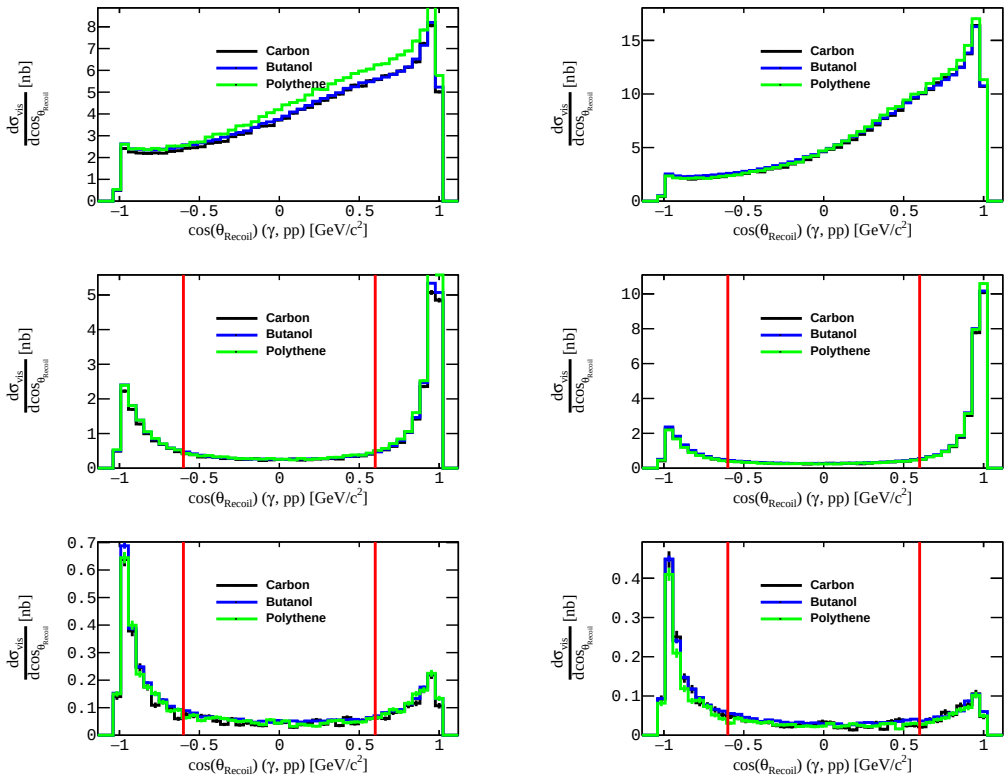

Figure 8.39: Cosine theta of the recoil angle for the reaction $^{12}\mathrm{C}(\gamma, p_1p_2)X$ without residual target cuts (top), cutting on $p_{\perp}^{\mathrm{miss}} < 0.2$ GeV/c (middle) and cutting on $p_{\perp}^{\mathrm{miss}} < 0.2$ GeV/c and 200 MeV/c^2 around the expected mass for a direct knockout (bottom) for two photon energy bins; 0.8 GeV $\leq E_{\gamma} \leq$ 1.0 GeV (left) and 1.0 GeV $\leq E_{\gamma} \leq$ 1.2 GeV (right). The figure presents the isotropic nature of the residual nucleus produced between -0.6 $< \cos\theta_{\mathrm{Recoil}} <$ 0.6. Data is shown for all three targets in FROST and the red lines indicate the cuts imposed to enhance the direct knockout signal.

It is clear that all three targets provide similar missing mass distributions, particularly at the low missing mass regions where the cut on the isotropic region enhances the relative contribution of direct knockout reactions. The small differences in the three targets at higher missing mass (sensitive to low energy proton thresholds) can be attributed to acceptance differences.

The $\cos\theta_{\mathrm{Recoil}}$ distributions for the three targets show similar cross sections when the residual target cuts are applied. Without cuts, there are some indications that carbon shows a somewhat larger strength at backward angles (this region correlates with the small discrepancies already seen at higher missing mass where such events tend to produce backward recoils).

8.6 Statistical Uncertainties

In this analysis, we used different weights for the experimental and simulated data and both sets of histograms must take into account the weights used to scale the bins. The total content of each histogram bin, W, is given by the sum of weights for all events in the bin and not the pure number of events. The bin content is calculated as:

$$W = \sum_{i=1}^{N} w_i^{\mathrm{event}}, \tag{8.4}$$

where w_i^{event} is the weight of each event and N is the total number of events in each bin. The statistical error, σ_{stat}, is therefore given by:

$$\sigma_{\mathrm{stat}} = \sqrt{\sum_{i=1}^{N} (w_i^{\mathrm{event}})^2}. \tag{8.5}$$

If all events in the bin have $w_i^{\mathrm{event}} = 1$, then the statistical error reduces to the $\sqrt{N}$ relation.

8.7 Systematic Studies - Missing Mass Distributions

In this section, we estimate the major sources of systematic error in the measurements. The estimated systematic errors for the key physics quantity, the missing mass, are summarised in Tab. 8.4. Some systematic errors (e.g. flux shape and acceptance) are missing mass and photon energy independent. Others, where systematic errors are being derived from varying the σ of analysis cuts, are derived from studying the difference in agreement between the missing mass distributions from gsim and experimental data, $m_{\mathrm{miss}}^{\mathrm{sim}} - m_{\mathrm{miss}}^{\mathrm{exp}}$, and are missing mass dependent. The change when varying the σ cut

is given as $\Delta\frac{d\sigma^{\text{vis}}}{dm_{\text{miss}}} = \left(m^{\text{sim}}_{\text{miss}} - m^{\text{exp}}_{\text{miss}}\right)_{\text{nom}} - \left(m^{\text{sim}}_{\text{miss}} - m^{\text{exp}}_{\text{miss}}\right)'$, where $\left(m^{\text{sim}}_{\text{miss}} - m^{\text{exp}}_{\text{miss}}\right)_{\text{nom}}$ and $\left(m^{\text{sim}}_{\text{miss}} - m^{\text{exp}}_{\text{miss}}\right)'$ is the difference in missing mass between the two data sets for the nominal and tighter/looser cuts, respectively. The deviations are studied, in photon energy bins across the measured range, as a function of missing mass. The systematics are determined for each bin in missing mass, and each error is discussed in this section.

Error	m_{miss} dependent	Value
Flux Normalisation	N	8.3%
Normalisation Factor	N	1.8%
GiBUU Accuracy	N	10%
$\Delta\beta$	Y	$\sigma\left(m^{\Delta\beta}_{\text{miss}}\right)$
Δt_γ	Y	$\sigma\left(m^{\Delta t_\gamma}_{\text{miss}}\right)$
Bad Paddles	Y	$\sigma\left(m^{\text{Paddles}}_{\text{miss}}\right)$
z-vertex	Y	$\sigma\left(m^{z}_{\text{miss}}\right)$
Δt	Y	$\sigma\left(m^{\Delta t}_{\text{miss}}\right)$
θ	Y	$\sigma\left(m^{\theta}_{\text{miss}}\right)$
ϕ	Y	$\sigma\left(m^{\phi}_{\text{miss}}\right)$
p_{min}	Y	$\sigma\left(m^{p_{\text{min}}}_{\text{miss}}\right)$
Acceptance	N	$\sqrt{N_p \times 5.7^2}\%$
Target Nuclei Normalisation	Y	$\sigma\left(m^{\text{Targets}}_{\text{miss}}\right)$
Statistical Error	Y	$\sigma\left(m^{\text{stat}}_{\text{miss}}\right)$

Table 8.4: A summary of the sources of systematic uncertainty and, where applicable, their estimated values. Where the systematics are quoted in this table they are global and apply to all observables in every bin. Those that are missing mass dependent are denoted by σ with a superscript for the cut.

- **Particle Identification ($\Delta\beta$)**

As an example, the systematic studies arising from the particle identification cut applied are presented for all photon energy bins. The systematic uncertainty associated with the PID cut ($\Delta\beta$), applied to identify the protons in our reactions, was studied by varying the cut from its nominal value to a tighter and looser cut. The nominal value for the $\Delta\beta$ distribution was determined by taking the 3σ position of a fitted Gaussian, in slices of momentum. The cut was varied to the 2.5σ position for the tighter cut and 3.5σ position for the looser cut, then the results of $\Delta\frac{d\sigma^{\text{vis}}}{dm^{\text{shift}}_{\text{miss}}}$ were compared. Moreover, Figs. 8.40 and 8.41 present $\Delta\frac{d\sigma^{\text{vis}}}{dm^{\text{shift}}_{\text{miss}}}$ as a function of missing mass, for different photon energy bins, for the reaction $^{12}\text{C}(\gamma, pp)X$ with no additional cuts applied to the residual system. The largest systematic between the tighter/nominal and looser/nominal cut was taken as $\Delta\frac{d\sigma^{\text{vis}}}{dm^{\text{shift}}_{\text{miss}}}$ on a bin-by-bin basis. We did not combine the variation of the tighter and looser cut in quadrature. The average systematic arising from the particle identification cut was 3%. The average systematic will be stated for all other sources of systematic uncertainty unless stated otherwise but, as previously stated, the systematic uncertainty is determined on a

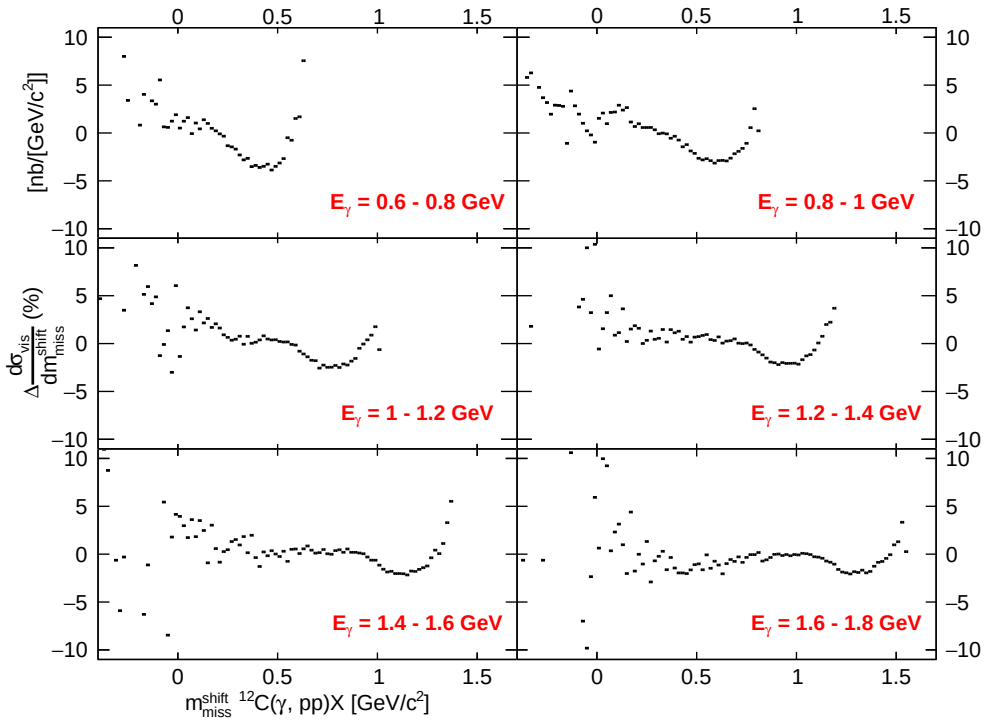

Figure 8.40: PID systematic uncertainty, showing $\Delta\frac{d\sigma^{\text{vis}}}{dm_{\text{miss}}^{\text{shift}}}$ as a function of $m_{\text{miss}}^{\text{shift}}$ for low/medium E_γ bins. The $\Delta\beta$ cuts were varied between the 3σ and 2.5σ tighter and 3.5σ looser cut, respectively. The largest systematic was determined and taken as $\Delta\frac{d\sigma^{\text{vis}}}{dm_{\text{miss}}^{\text{shift}}}$.

bin-by-bin basis.

- **Photon Identification**

The systematic uncertainty associated with the photon identification cut (Δt_γ), applied to identify the first proton and the photon in our reactions, was studied by varying the cut from its nominal value to a tighter and looser cut. The nominal value for the Δt_γ distribution was determined by previous FROST analyses. The cut was varied to the 2.5σ position for the tighter cut and 3.5σ position for the looser cut, then the results of $\Delta\frac{d\sigma^{\text{vis}}}{dm_{\text{miss}}^{\text{shift}}}$ were compared as shown previously, and the larger of the two effects was taken as the systematic uncertainty. The average systematic uncertainty, across all values of $m_{\text{miss}}^{\text{shift}}$ and E_γ, arising from the photon selection cut was 4%.

- **Bad or Malfunctioning Time-of-Flight Paddles**

The systematic uncertainty associated with bad or malfunctioning time-of-flight paddles was studied by determining the difference in including and removing the paddles. The average systematic arising from including and excluding the bad paddles was 2%.

- **Reaction Vertex**

The systematic uncertainty associated with the reaction vertex cut (z), applied to identify the protons in our reactions, was studied by varying the cut from its nominal value to a

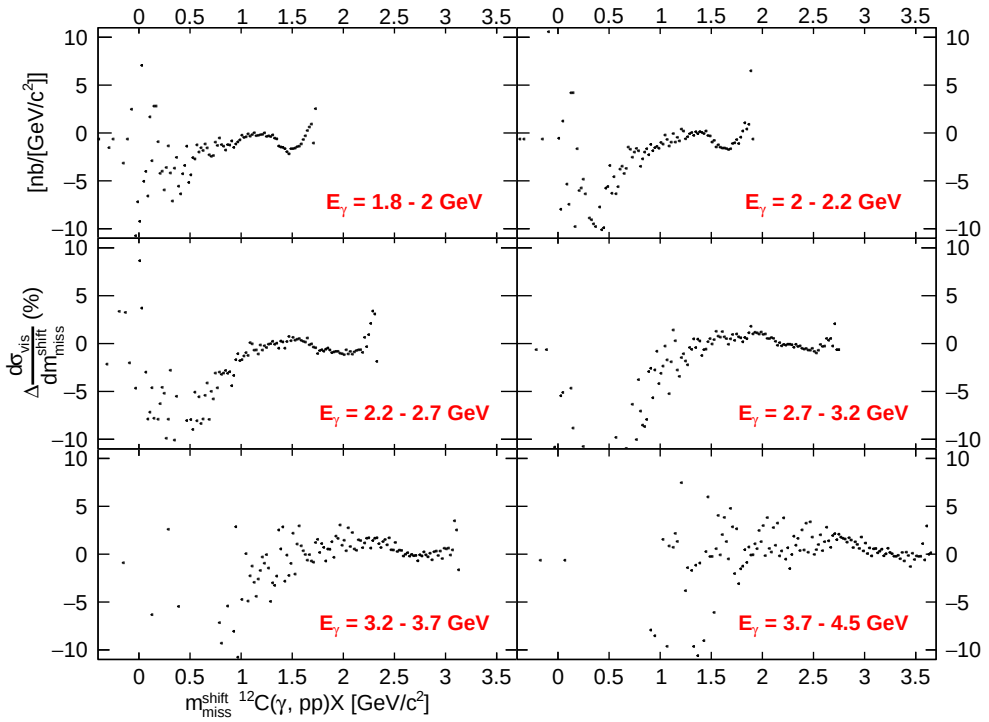

Figure 8.41: Particle ID systematic uncertainty, showing $\Delta\frac{d\sigma^{\rm vis}}{dm^{\rm shift}_{\rm miss}}$ as a function of $m^{\rm shift}_{\rm miss}$ for high E_γ bins. The $\Delta\beta$ cuts were varied between the 3σ and 2.5σ tighter and 3.5σ looser cut, respectively. The largest systematic was determined and taken as $\Delta\frac{d\sigma^{\rm vis}}{dm^{\rm shift}_{\rm miss}}$.

tighter and looser cut. The nominal value for the z-distribution was taken to be the usual z-vertex cut for carbon 5 cm $< z <$ 8 cm, and determined by taking the largest 3σ position of a fitted double Gaussian + linear fit for the simulated data. For the experimental data, we varied the cut by 0.5 cm from the downstream end to understand how the ice build-up affects our results. For the simulated data, the cut was varied to the 2.5σ for the tighter cut and 3.5σ for the looser cut. The average systematic arising from the reaction vertex selection was 4%.

- **Proton Timing Cuts**

The systematic uncertainty associated with the proton timing cut (Δt), applied to identify the protons in our reactions, was studied by varying the cut from its nominal value to a tighter and looser cut. The nominal value for the Δt distribution was determined by taking the 3σ position of a fitted Gaussian in slices of momentum. The cut was varied to the 2.5σ position for the tighter cut and 3.5σ position for the looser cut, then the results of $\Delta\frac{d\sigma^{\rm vis}}{dm^{\rm shift}_{\rm miss}}$ were compared. The average systematic arising from the proton timing cuts was 2%.

- **Fiducial Cuts**

The systematic uncertainties associated with both the θ and ϕ cuts, applied to identify

the proton in our reactions, were studied by determining the difference in including and removing the cuts. The average systematic arising from the fiducial cuts was 3%.

- **Minimum Momentum Cut**

When making comparisons between the carbon target experimental data and the simulated data, the systematic uncertainty associated with the minimum momentum cut (p_{min}), applied to identify the proton in our reactions, was studied by determining the difference between the nominal cut (300 MeV/c) and a higher minimum momentum threshold of 350 MeV/c. The average systematic arising from the minimum momentum was found to be 10%. In the case of comparing all three targets in the experimental data, a higher minimum momentum threshold was used (500 MeV/c) due to the minimum momentum thresholds of the different targets. The systematic uncertainty associated with the minimum momentum cut of 500 MeV/c was studied by determining the difference between the nominal (500 MeV/c) cut and a lower (450 MeV/c) cut. For the 500 MeV/c minimum momentum threshold, the average systematic uncertainty was found to be 7%.

- **Flux normalisation**

In the analysis, we normalise the photon flux to the GiBUU prediction of the cross-section for quasi-free pion production (extracted from $^{12}\text{C}(\gamma, p)X$) in the photon energy range $600 - 700$ MeV. As discussed in Sec. 8.4, the expected 10% accuracy with which GiBUU describes the experimental data is a systematic in this normalisation. We also add a 1.8% systematic from the normalisation procedure, which comes from varying the integrated region as discussed in Sec. 8.4. To determine the visible cross-sections from the experimental data, it was essential to ensure the flux shape was understood and had no dependence on the trigger conditions. This was done by analysing the discrepancies between the "in-time" and "out-of-time" photon distributions. A systematic of 8.3% was determined as the systematic in the flux shape, bringing the total systematic when added in quadrature to 13.1%.

- **Acceptance Differences**

The acceptance systematic uncertainty was investigated by studying the change in the ratio of detected protons between the simulated and experimental data for each of the six sectors in CLAS. This provides us with an acceptance systematic uncertainty for each proton multiplicity as it is the average deviation of the ratio of detected protons in each sector in CLAS*, which would have no deviation if the acceptance was uniform. We first calculate the ratio of 1p events detected in the experimental data to the simulated data, in each sector, and determine the average ratio, $\overline{N_{\text{GSIM}}/N_{\text{Exp}}}$. Then, the deviation of the ratio in each sector from this average ratio is determined and an average deviation is determined, $\sigma_{\text{deviation}}$. Finally, the acceptance systematic uncertainty is presented as a percentage by dividing $\sigma_{\text{deviation}}$ by the average ratio between the six sectors:

*It also provides an efficiency systematic uncertainty as we have assumed the efficiencies are identical.

$$\sigma_{\text{acceptance}} = \frac{\sigma_{\text{deviation}}}{\frac{N_{\text{GSIM}}}{N_{\text{Exp}}}}. \tag{8.6}$$

Figure 8.42 presents the acceptance systematic uncertainty as a function of photon energy for all 1p reactions, showing that the acceptance systematic uncertainty does not vary substantially with photon energy (which we expect). The average acceptance systematic uncertainty was determined to be 5.7%, from the μ + RMS value. This acceptance systematic uncertainty is applied to all observables identical to the normalisation and flux systematic uncertainties. Higher-order protons suffer from a decrease in statistics, hence applying this method to higher-order protons would overestimate the systematic uncertainty by incorporating statistical effects. However, each proton detected in a given event has a 5.7% acceptance systematic uncertainty. Therefore, the total acceptance systematic uncertainty is then added in quadrature for each proton detected. For example, for 3 protons knocked out the total acceptance systematic uncertainty is $\sqrt{3 \times 5.7^2} = 9.9\%$.

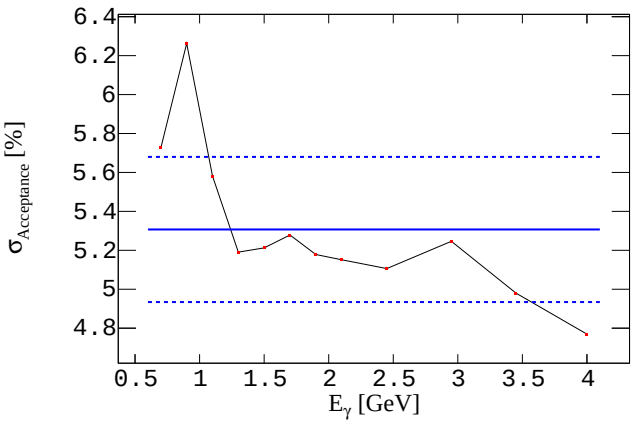

Figure 8.42: Acceptance systematic uncertainty, expressed as a percentage, as a function of photon energy for all 1 proton knockout reactions. The solid blue line presents the average percentage systematic uncertainty and the dashed blue lines present the average percentage systematic uncertainty ± the RMS value.

- **Target Nuclei Normalisation**

An additional systematic error associated with the difference between the three targets is attributed to the target position systematic error. We can estimate that the determination of the number of target nuclei has an upper-limit systematic error of 1% for the measurements of the thicknesses and densities of each respective target. An additional systematic for the discrepancy between the three targets is determined as the target with the largest difference from the average of the three targets. The average systematic arising from the difference in the three target nuclei was found to be 2%.

8.8 Total Uncertainty

The total uncertainty associated with the missing mass distributions is determined by taking the square of the sum of all uncertainties in quadrature, namely:

$$\sigma_{\text{tot}} = \sqrt{(\sigma_{\text{stat}})^2 + (\sigma_{\text{sys}})^2 + (\sigma_{\text{acceptance}})^2 + (\sigma_{\text{scaling}})^2 + (\sigma_{\text{flux}})^2}, \tag{8.7}$$

where σ_{tot} is the total uncertainty, σ_{stat} is the statistical uncertainty, σ_{sys} is the total systematic uncertainty from varying the analysis cuts applied to select the protons, $\sigma_{\text{acceptance}}$ is the systematic due to the acceptance (and efficiency) differences between experiment and simulation, σ_{scaling} is the systematic due to scaling the experimental data to an absolute cross section scale and σ_{flux} is the systematic arising from the flux shape.

8.9 Photoinduced Many-Proton Knockout Results

We first present results from our study of photoinduced many-proton knockout, obtained from analysis of archive CLAS data. We first give an overview of the plots that are presented and subsequently provide a discussion of the results in the following sections.

8.9.1 Overview of Results Presented

The visible cross sections as a function of shifted missing mass are shown in Figs. 8.43-8.60 for 2p, 3p, 4p knockout. As well as the total visible cross sections, distributions for each final state are also shown with differing cuts on the recoil system viz. $p_{\perp}^{\text{miss}} \leq 0.2$ GeV/c, $0.6 \leq \cos(\theta_{\text{Recoil}}) \leq 0.6$ (see captions), which are primarily designed to emphasize the direct knockout yield as discussed in Sec. 8.5. For these plots, the data from all targets has a 500 MeV/c momentum threshold to remove data where the CLAS acceptance changes rapidly (mainly for the larger butanol target - as discussed in Subsec. 8.2.8). Our estimated systematic errors (Sec. 8.7) are also shown on each plot as a function of missing mass. The turquoise band shows the full systematic error, including the estimated systematic from the minimum proton momentum threshold. As this latter error is derived from the agreement between GiBUU and the data (and is therefore a combined systematic of the data and the GiBUUU modelling), we also present (purple error band) the systematic without this contribution. This latter estimate more accurately reflects the systematic uncertainty in the data alone, without the large model-dependent errors from the GiBUU modelling.

As high multiplicity data typically involves lower momenta final state protons (particularly when the reaction is associated with a high missing mass) the yields are reduced significantly when using the large 500 MeV/c momentum cut (this choice of cut is largely driven by the higher proton momentum threshold for the data from the butanol target).

In Figs. 8.61-8.78 we therefore also show the results for 4p, 5p and 6p knockout with the minimum threshold reduced to 300 MeV/c (for these plots the GiBUU simulation similarly uses this reduced proton momentum threshold).

Although this will leave discrepancies between the targets due to the differing experimental thresholds for each target (most visible at large missing mass, see Subsec. 8.5.4), it still gives useful information on the quality of the GiBUU description of high multiplicity knockout. In Figs. 8.79 and 8.80 we show the missing mass distributions for 1p knockout from the carbon target and the simulated data.

8.9.2 Total Visible Cross-Sections for Many-Proton Knockout

The 2p missing mass distributions with no cuts on the reconstructed recoiling system are presented in Figs. 8.43 and 8.44. The distributions show strength near the $m_{\mathrm{miss}}^{\mathrm{shift}} \sim 0$ regions although as the photon energy increases most strength is at high $m_{\mathrm{miss}}^{\mathrm{shift}}$. GiBUU gives a reasonable general description of the shape and magnitude (within the systematic errors) up to photon energies around 1.8 GeV. At higher photon energies it overpredicts the low $m_{\mathrm{miss}}^{\mathrm{shift}}$ strength and underpredicts the peak observed at higher $m_{\mathrm{miss}}^{\mathrm{shift}}$. This higher peak could be attributable to the missing 3π processes in GiBUU, which would be a sizeable contribution at higher photon energies. However, it could arise from other missing processes or poor modelling of 2π production. These new data will help to guide improvements in the model.

The corresponding 3p distributions, shown in Figs. 8.45 and 8.46, show similar features. GiBUU gives a general description of the shape and magnitude (within the systematic errors) up to photon energies around 1.8 GeV. At higher photon energies it underpredicts the large peak of strength at higher $m_{\mathrm{miss}}^{\mathrm{shift}}$. The latter may be due to the modelling as discussed above. The same comments hold for the corresponding 4p distributions presented in Figs. 8.47 and 8.48.

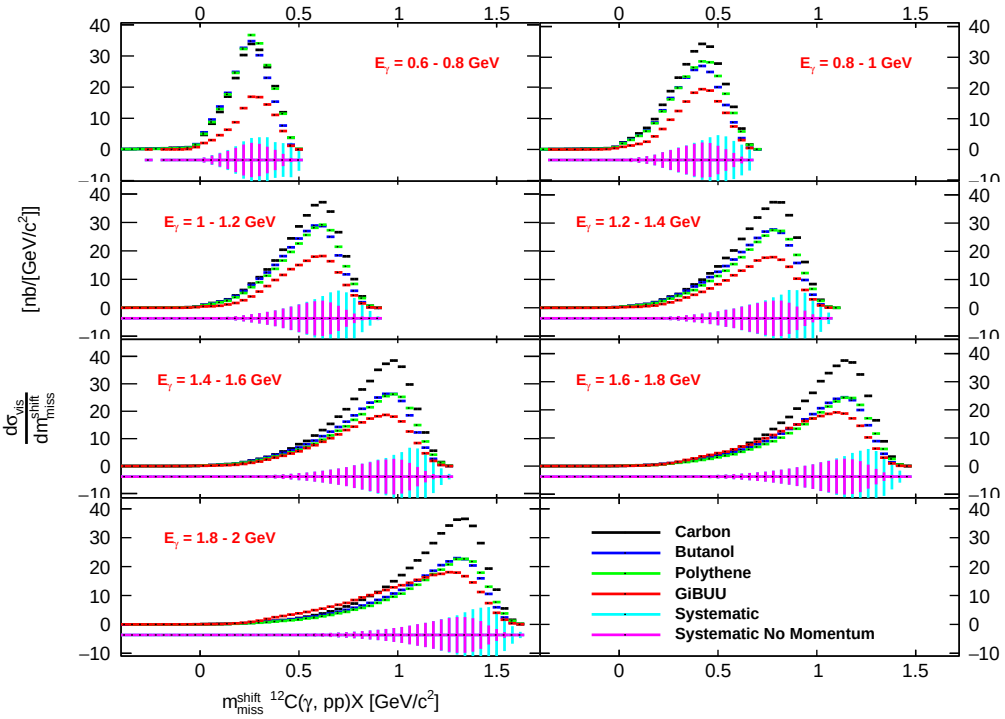

Figure 8.43: The shifted missing mass of the reaction $^{12}\mathrm{C}(\gamma, p_1 p_2)X$ for low/medium energy bins of E_γ. The systematics are presented as a band.

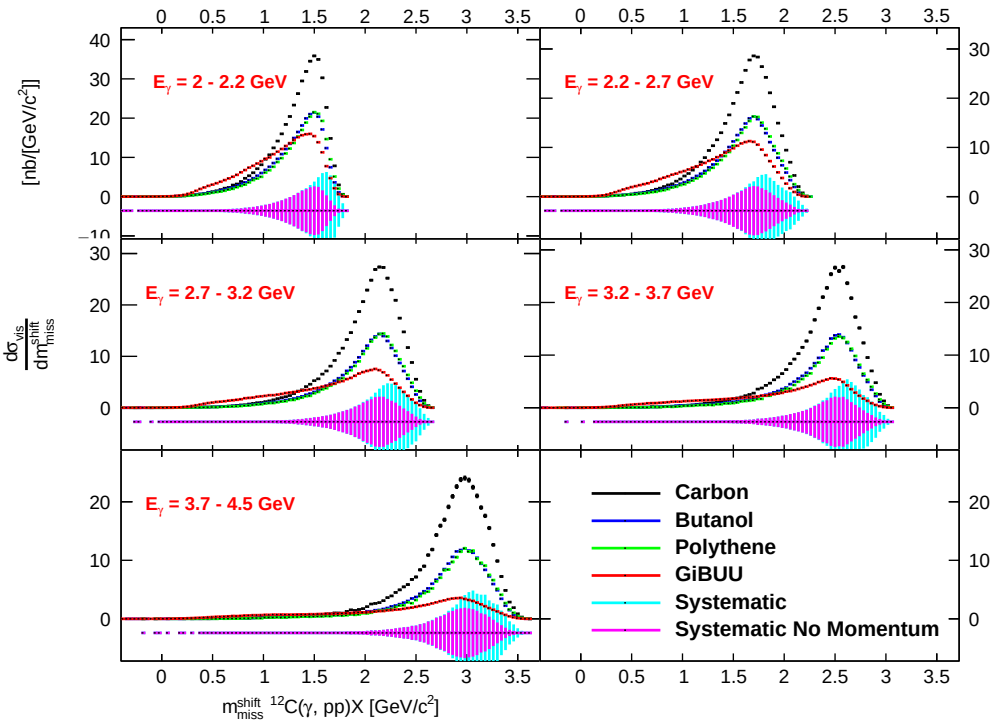

Figure 8.44: The missing mass of the reaction $^{12}\mathrm{C}(\gamma, p_1 p_2)X$ for high energy bins of E_γ. The systematics are presented as a band.

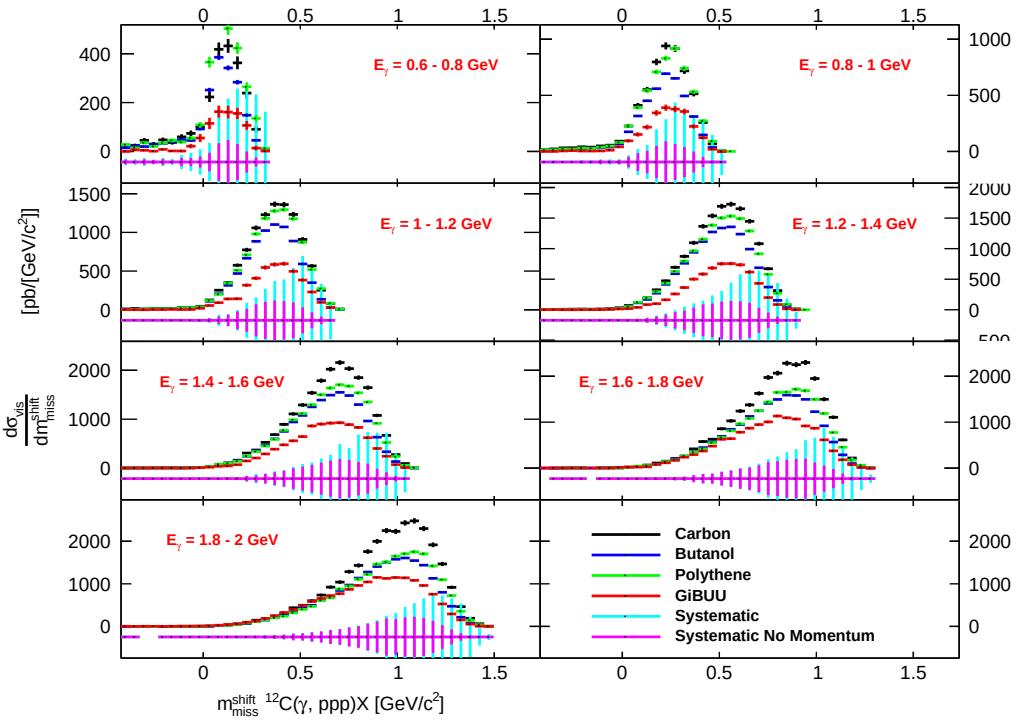

Figure 8.45: The shifted missing mass of the reaction $^{12}\mathrm{C}(\gamma, p_1p_2p_3)X$ for low/medium energy bins of E_γ. The systematics are presented as a band.

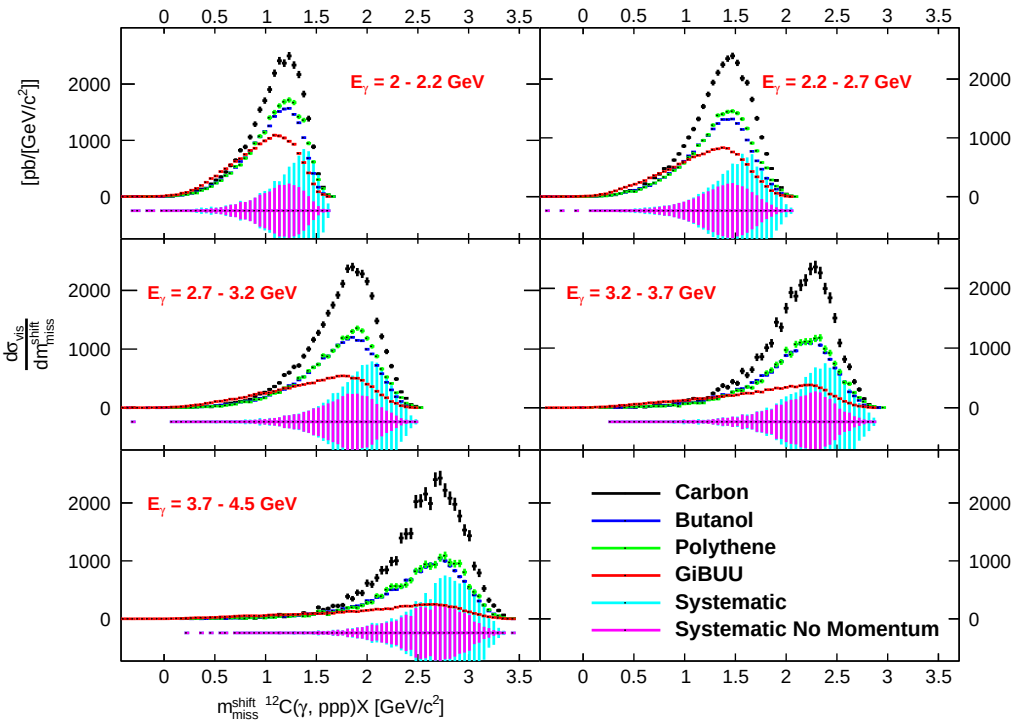

Figure 8.46: The missing mass of the reaction $^{12}\mathrm{C}(\gamma, p_1p_2p_3)X$ for high energy bins of E_γ. The systematics are presented as a band.

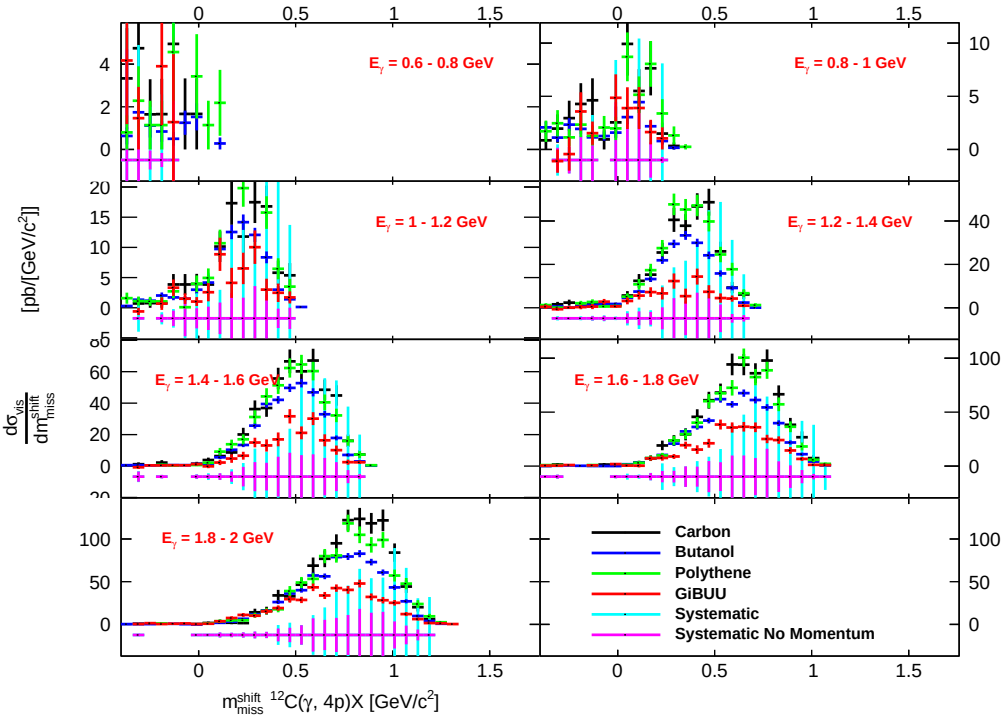

Figure 8.47: The shifted missing mass of the reaction $^{12}\mathrm{C}(\gamma, p_1p_2p_3p_4)X$ for low/medium energy bins of E_γ. The systematics are presented as a band.

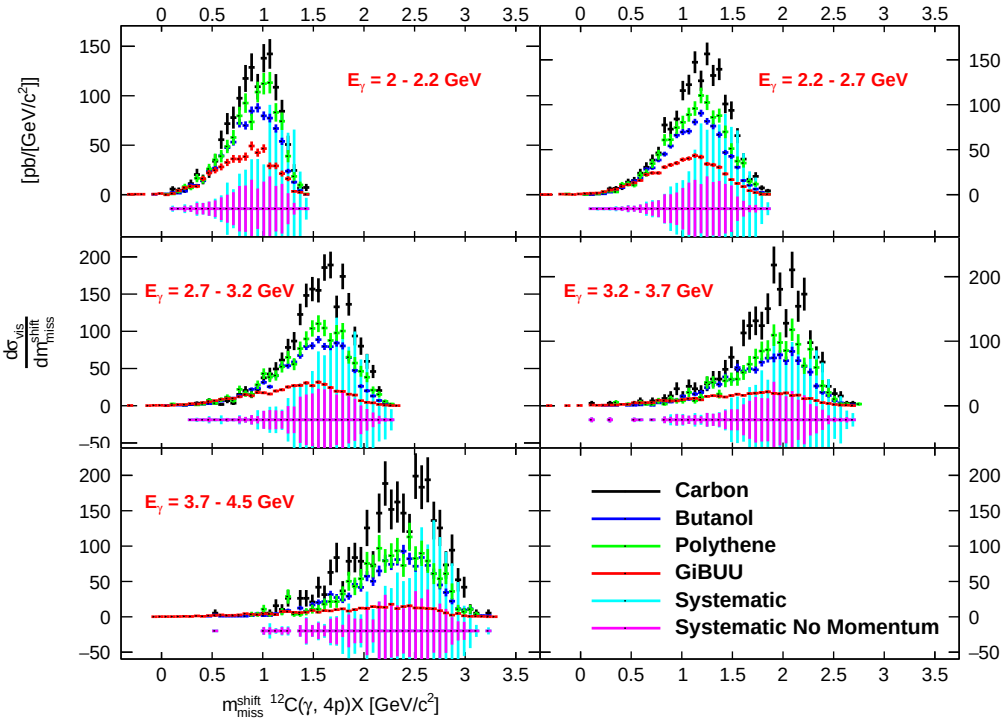

Figure 8.48: The missing mass of the reaction $^{12}\mathrm{C}(\gamma, p_1p_2p_3p_4)X$ for high energy bins of E_γ. The systematics are presented as a band.

8.9.3 Many-Proton Knockout with Restrictions on $p_{\perp}^{\mathrm{miss}} < 0.2$ GeV/c

It was discussed and shown in Sec. 8.5 that additional restrictions applied to the residual recoiling system enhance the direct knockout signal. The corresponding plots for 2p, 3p and 4p with the $p_{\perp}^{\mathrm{miss}} < 0.2$ GeV/c cut, are presented in Figs. 8.49, 8.50, 8.51, 8.52, 8.53 and 8.54. For 2p this cut produces a far more pronounced structure in the region near zero missing mass (associated mainly with the direct knockout processes) and changes the relative strength and shape of the structures at higher mass. At low photon energies, the distinct shape of this low mass region (as well as the general shape of the distribution for all missing mass) is reasonably reproduced by GiBUU. At higher photon energies the agreement deteriorates significantly. Above 3.7 GeV there is evidence of a small bump around a missing mass of 1 GeV/c^2 not evident in the GiBUU predictions, which may be a source of future work. For 3p the $p_{\perp}^{\mathrm{miss}}$ cut reveals similar "bump" structures at low missing mass, hinting at signatures for direct knockout contributions. For 4p the statistics are poorer, but similar general comments hold as for the other knockout channels.

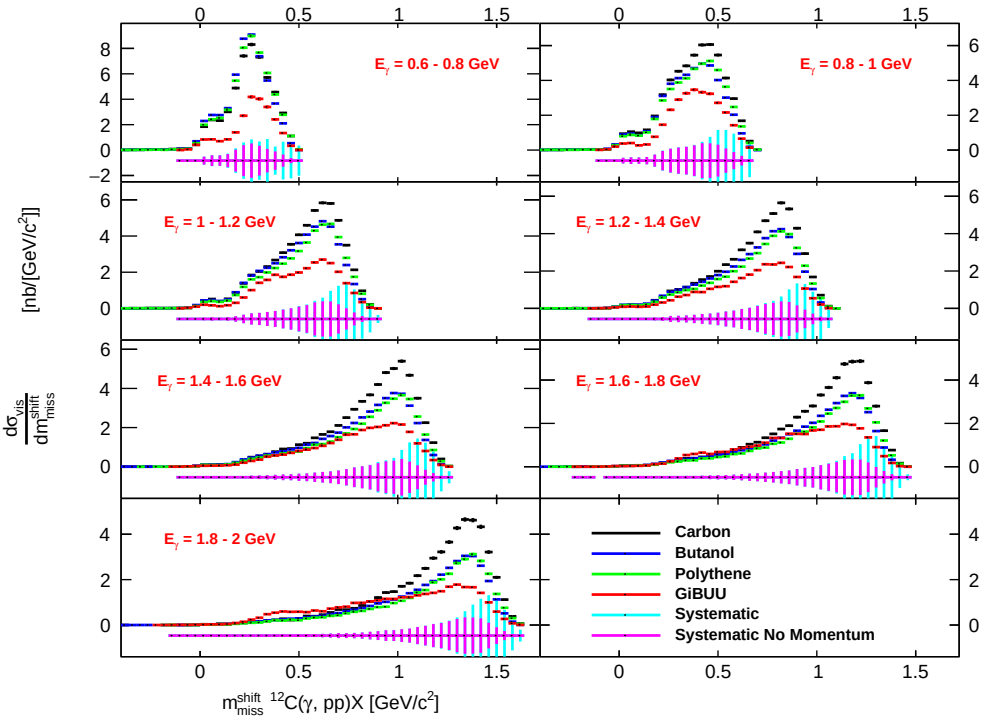

Figure 8.49: The shifted missing mass of the reaction $^{12}\mathrm{C}(\gamma, p_1 p_2)X$ with an additional cut on $p_{\perp}^{\mathrm{miss}} < 0.2$ GeV/c for low/medium energy bins of E_{γ}. The systematics are presented as a band.

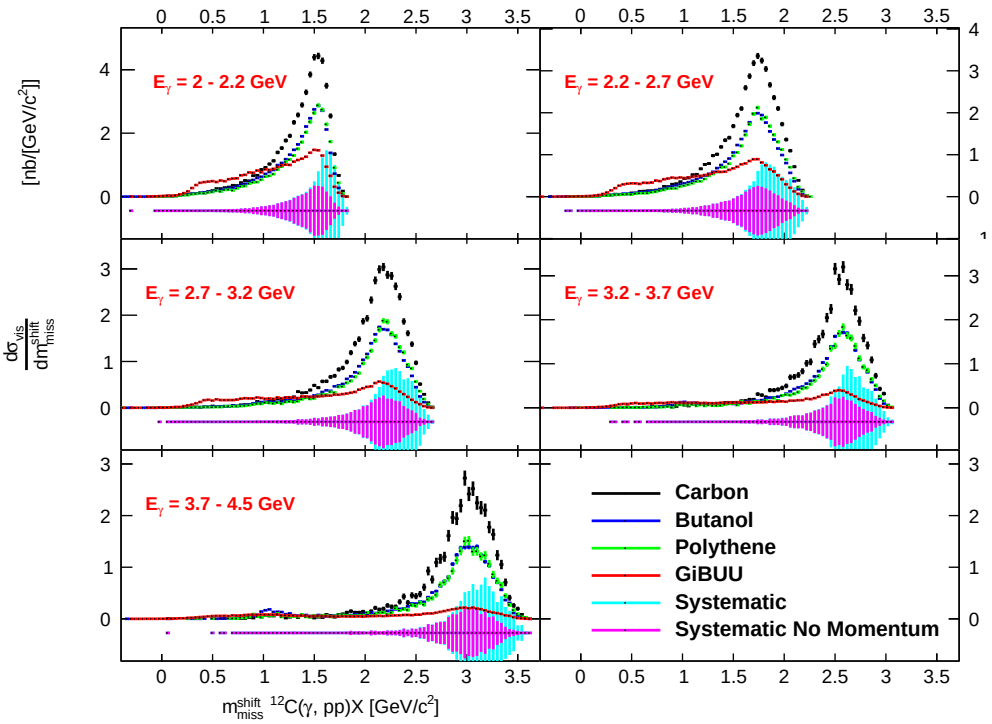

Figure 8.50: The missing mass of the reaction $^{12}\mathrm{C}(\gamma, p_1 p_2)X$ with an additional cut on $p_\perp^{\mathrm{miss}} < 0.2$ GeV/c for high energy bins of E_γ. The systematics are presented as a band.

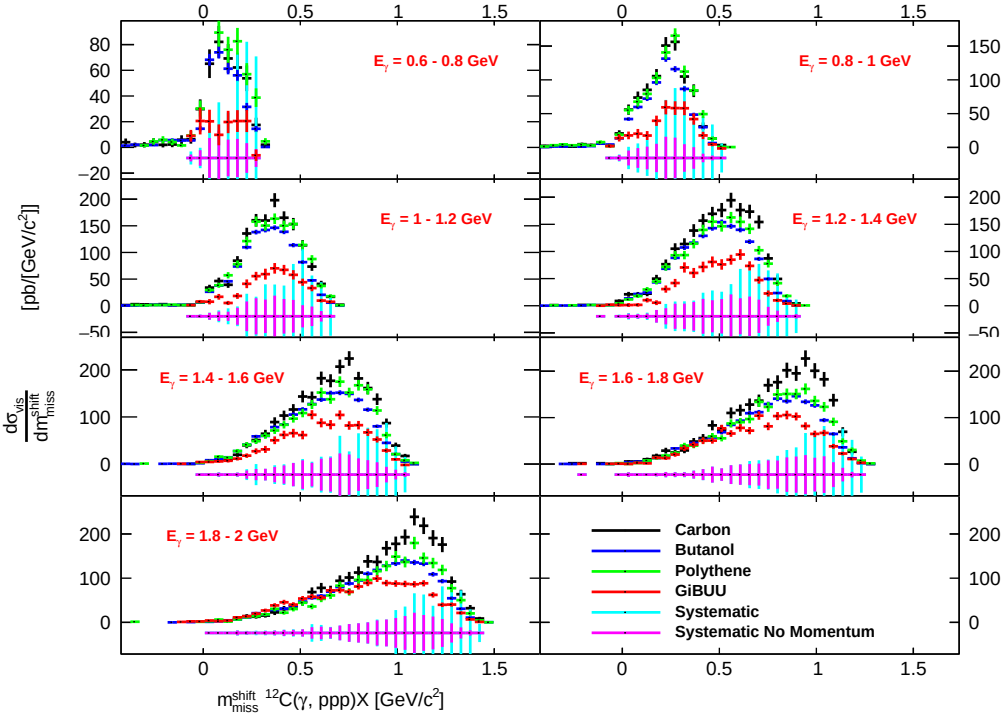

Figure 8.51: The shifted missing mass of the reaction $^{12}\mathrm{C}(\gamma, p_1 p_2 p_3)X$ with an additional cut on $p_\perp^{\mathrm{miss}} < 0.2$ GeV/c for low/medium energy bins of E_γ. The systematics are presented as a band.

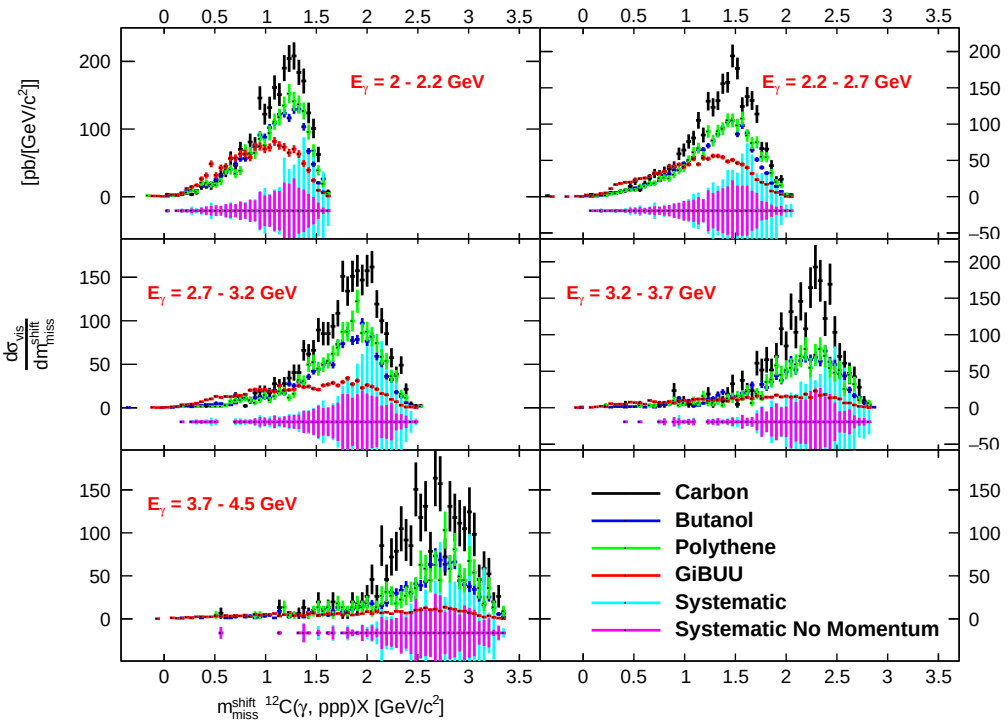

Figure 8.52: The missing mass of the reaction $^{12}\mathrm{C}(\gamma, p_1p_2p_3)X$ with an additional cut on $p_\perp^{\mathrm{miss}} < 0.2$ GeV/c for high energy bins of E_γ. The systematics are presented as a band.

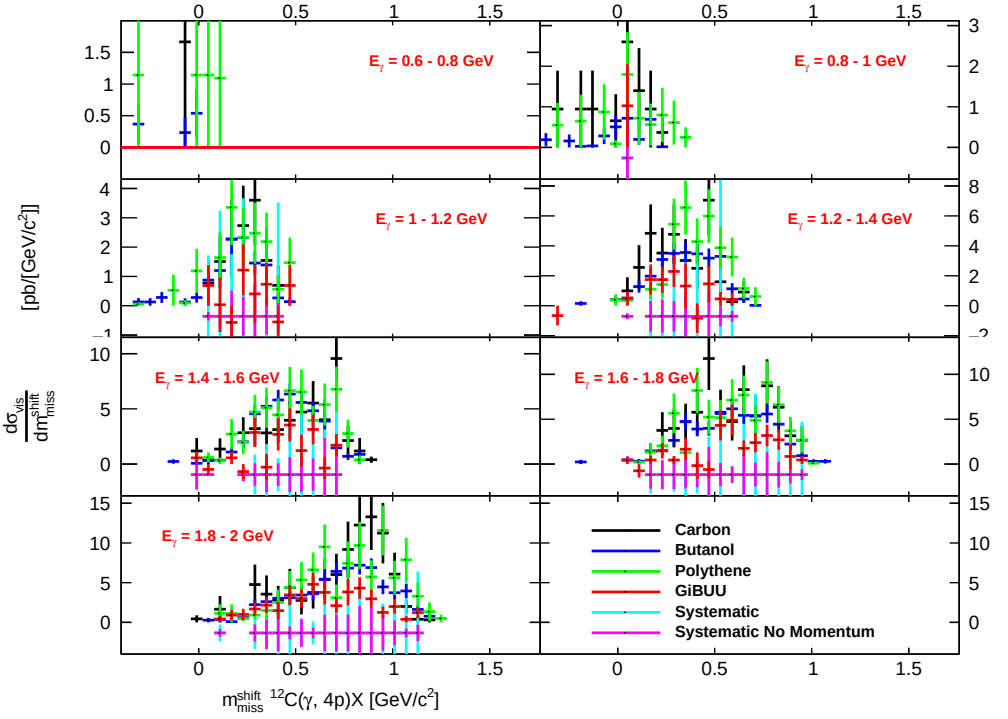

Figure 8.53: The shifted missing mass of the reaction $^{12}\mathrm{C}(\gamma, p_1p_2p_3p_4)X$ with an additional cut on $p_\perp^{\mathrm{miss}} < 0.2$ GeV/c for low/medium energy bins of E_γ. The systematics are presented as a band.

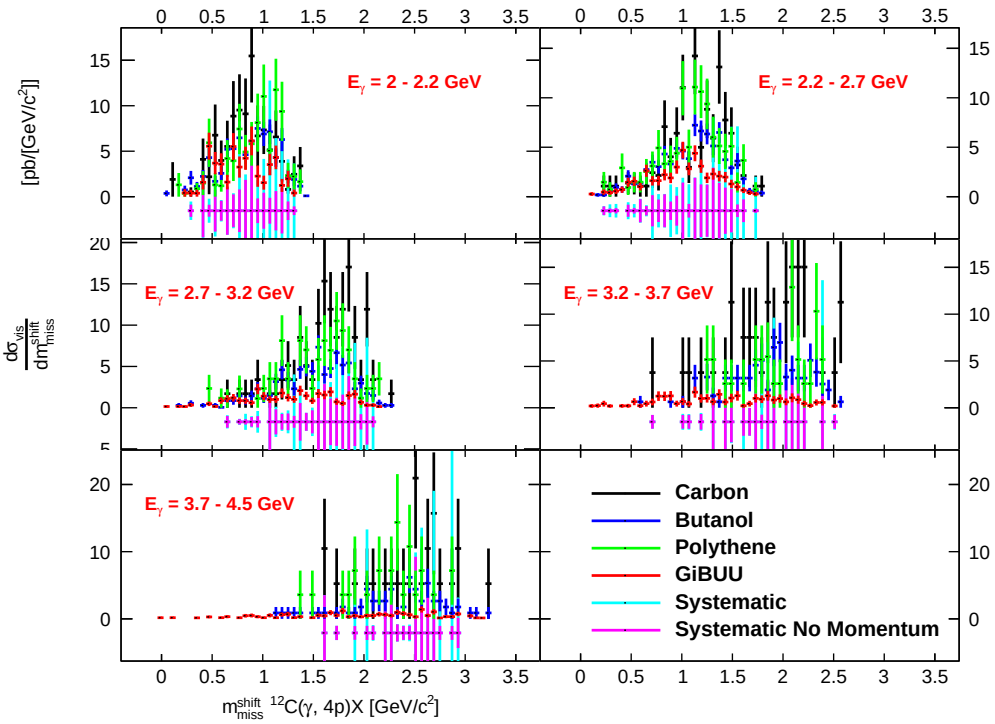

Figure 8.54: The missing mass of the reaction $^{12}\mathrm{C}(\gamma, p_1p_2p_3p_4)X$ with an additional cut on $p_\perp^{\mathrm{miss}} < 0.2$ GeV/c for high energy bins of E_γ. The systematic errors are presented as a band as detailed in the text.

8.9.4 Many-Proton Knockout with Restrictions on $p_\perp^{\mathrm{miss}}$ and Polar Angle of Recoiling System

The missing mass distributions with $p_\perp^{\mathrm{miss}} < 0.2$ GeV/c and -0.6 $< \cos\theta_{\mathrm{Recoil}} <$ 0.6 cuts applied are presented in Figs. 8.55, 8.56, 8.57, 8.58, 8.59 and 8.60. For 2p this combination of cuts produces a resolved direct knockout peak at low missing masses. The different shapes of the missing mass distributions are in good agreement with the data, up to around 2 GeV photon energy, and the magnitude is reasonably well reproduced in all except the lowest photon energy bin. For the higher photon energies, there are indications that the higher missing mass structure around 1 GeV/c^2 is underpredicted. For 3p the cuts reveal a resolved direct knockout peak at low missing mass. For the higher photon energies, the statistical accuracy is poor - although GiBUU is on scale with the measured strength and agrees with the shape as it is resolved by the data. The same holds for the 4p data.

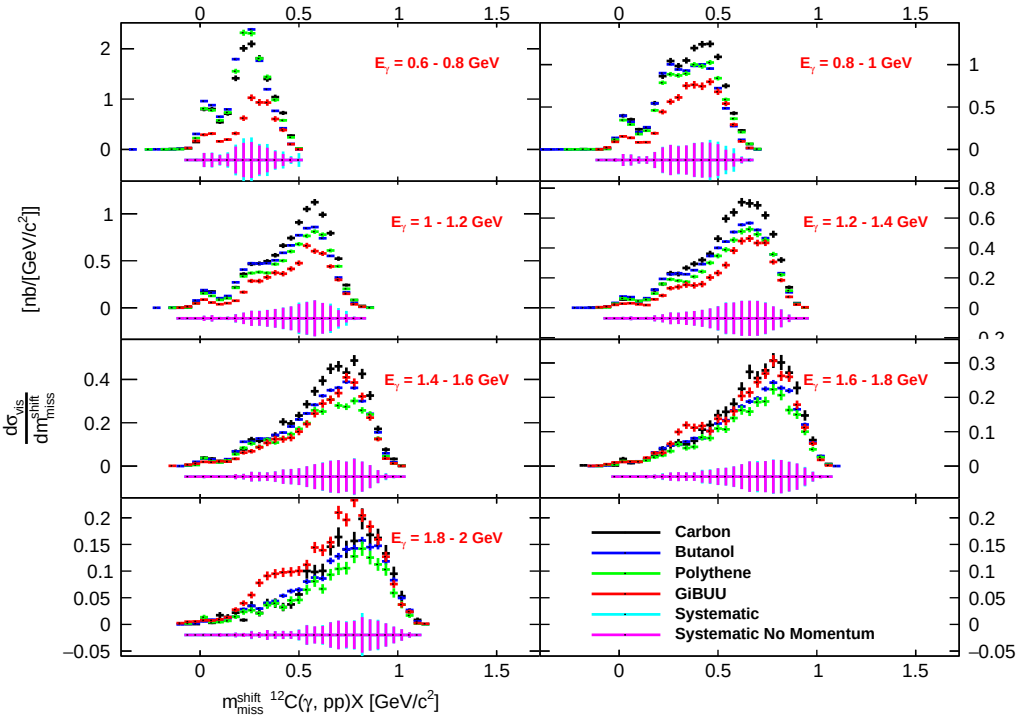

Figure 8.55: The shifted missing mass of the reaction $^{12}\mathrm{C}(\gamma, p_1 p_2)X$ with an additional cut on $p_\perp^{\mathrm{miss}} < 0.2$ GeV/c and -0.6 $< \cos\theta_{\mathrm{Recoil}} <$ 0.6 for low/medium energy bins of E_γ. The systematics are presented as a band.

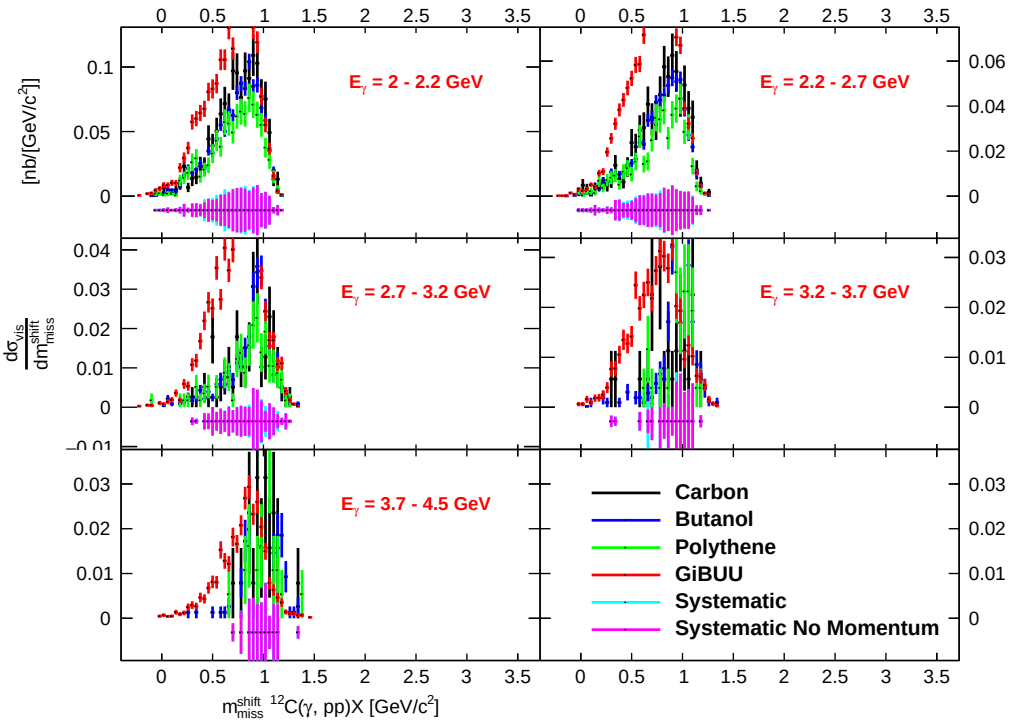

Figure 8.56: The missing mass of the reaction $^{12}\mathrm{C}(\gamma, p_1 p_2)X$ with an additional cut on $p_\perp^{\mathrm{miss}} < 0.2$ GeV/c and -0.6 $< \cos\theta_{\mathrm{Recoil}} <$ 0.6 for high energy bins of E_γ. The systematics are presented as a band.

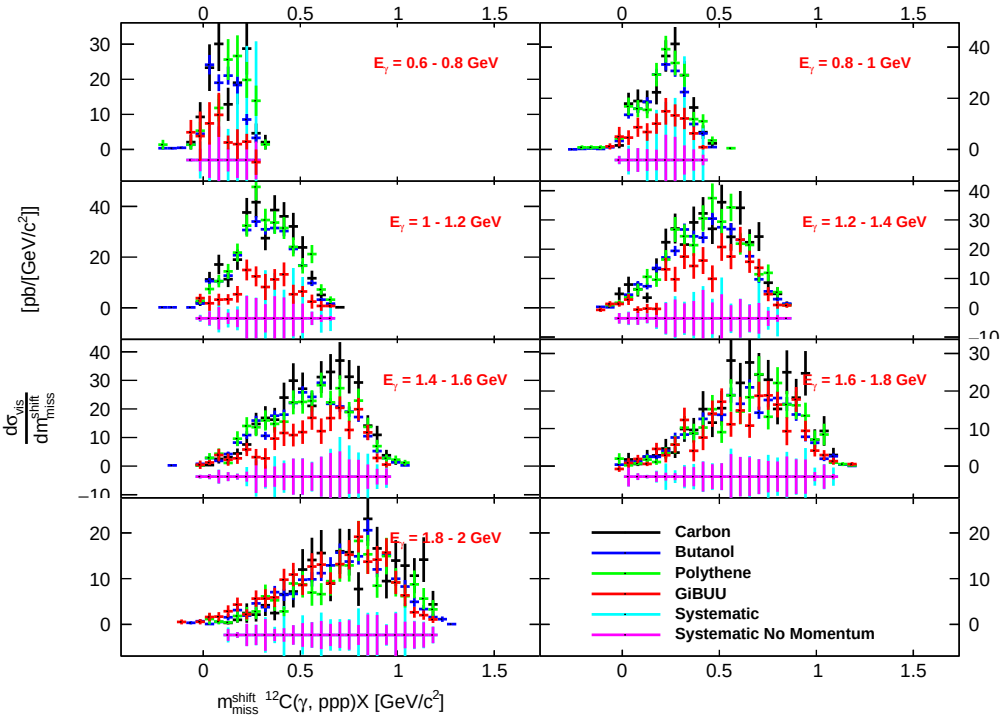

Figure 8.57: The shifted missing mass of the reaction $^{12}\mathrm{C}(\gamma, p_1p_2p_3)X$ with an additional cut on $p_\perp^{\mathrm{miss}} < 0.2$ GeV/c and -0.6 $< \cos\theta_{\mathrm{Recoil}} <$ 0.6 for low/medium energy bins of E_γ. The systematics are presented as a band.

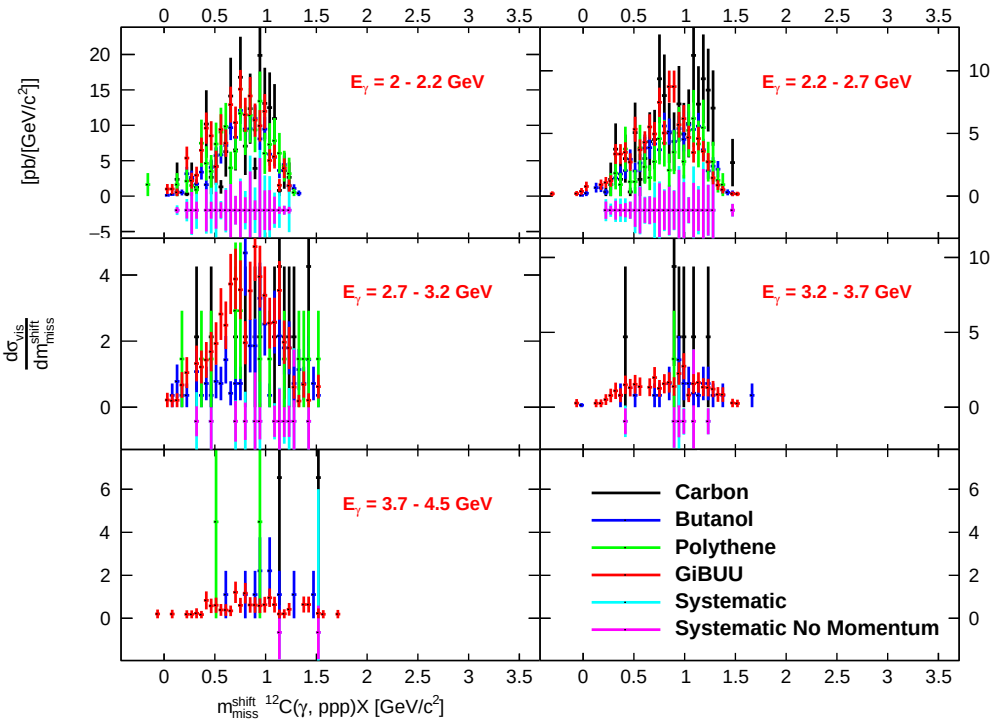

Figure 8.58: The missing mass of the reaction $^{12}\mathrm{C}(\gamma, p_1p_2p_3)X$ with an additional cut on $p_\perp^{\mathrm{miss}} < 0.2$ GeV/c and -0.6 $< \cos\theta_{\mathrm{Recoil}} <$ 0.6 for high energy bins of E_γ. The systematics are presented as a band.

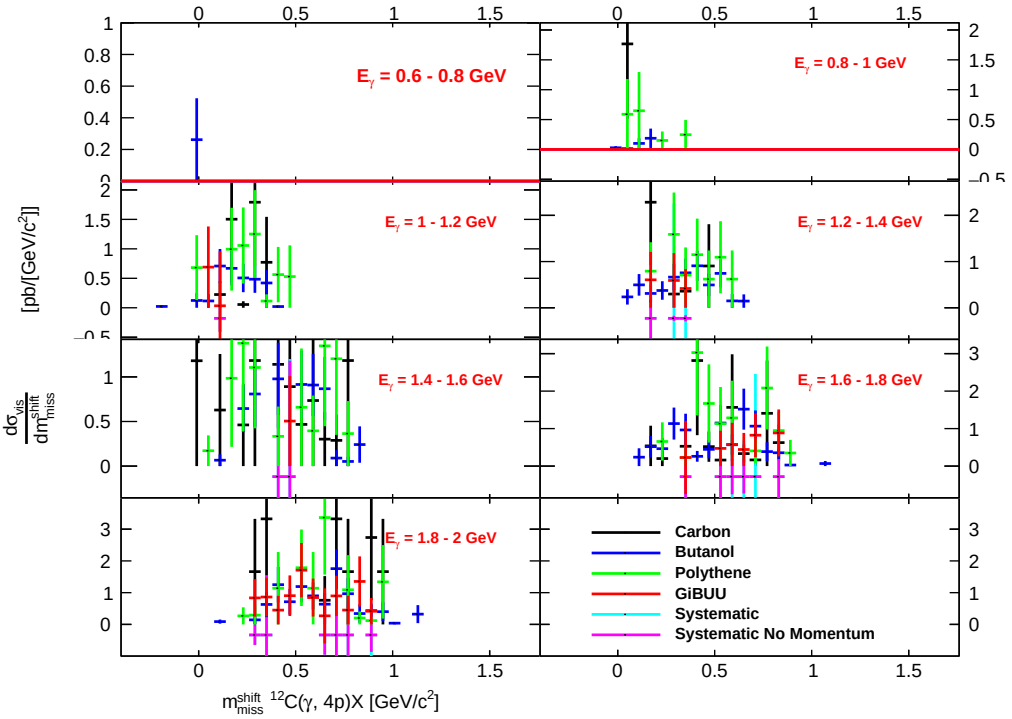

Figure 8.59: The shifted missing mass of the reaction $^{12}\mathrm{C}(\gamma, p_1p_2p_3p_4)X$ with an additional cut on $p_\perp^{\mathrm{miss}} < 0.2$ GeV/c and -0.6 $< \cos\theta_{\mathrm{Recoil}} <$ 0.6 for low/medium energy bins of E_γ. The systematics are presented as a band.

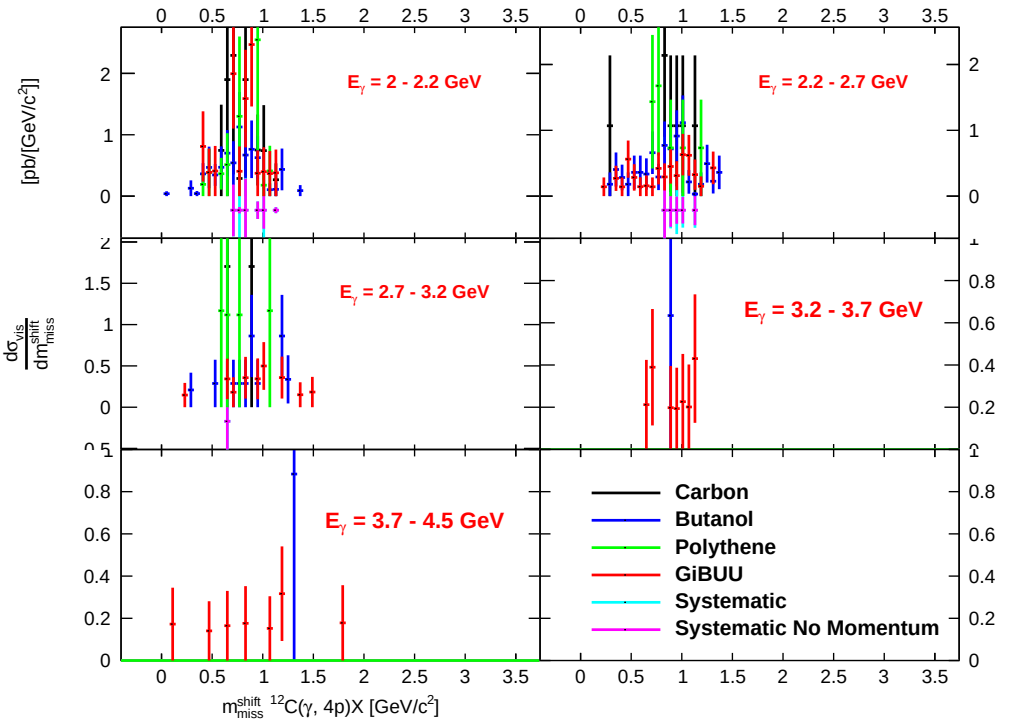

Figure 8.60: The missing mass of the reaction $^{12}\mathrm{C}(\gamma, p_1p_2p_3p_4)X$ with an additional cut on $p_\perp^{\mathrm{miss}} < 0.2$ GeV/c and -0.6 $< \cos\theta_{\mathrm{Recoil}} <$ 0.6 for high energy bins of E_γ. The systematics are presented as a band.

8.9.5 Many-Proton Knockout with Reduced Proton Momentum Threshold

As discussed in Subsec. 8.9.1, to assess the accuracy of GiBUU in modelling high multiplicity knockout reactions, such as 4p, 5p and 6p, we also present data and model predictions with a lowered minimum momentum threshold. As the different minimum momentum thresholds from each target will impact the visible yield (and cross section), we do not expect detailed agreement between the targets where low momentum protons are detected (corresponding typically to higher missing mass). The low missing mass region, where direct knockouts reside, typically involves higher energy protons and will be less affected by momentum thresholds from the different targets. The polythene target (having the lowest experimental threshold) would be expected to be the closest to the GiBUU simulated data. carbon and butanol have similar (higher) minimum momentum thresholds.

The missing mass distributions for all three targets in the g9a experiment and gsim data are presented in Figs. 8.61, 8.62, 8.63, 8.64, 8.65 and 8.66 for 4p, 5p and 6p knockout, respectively, with a minimum momentum threshold of 300 MeV/c and no additional cuts on the residual system. The data from the different targets are similar at low missing mass, but the polythene target shows larger strengths at higher missing mass (expected from its lower proton momentum threshold). The lower threshold allows statistically well-resolved measures of the 4p cross-section. For the lower photon energy bins strength exists at masses close to zero and may reflect direct knockout contributions. At higher photon energies the strength is mainly at higher missing mass. GiBUU gives general agreement in the shape and magnitude up to around 2.2 GeV photon energy. Beyond this, it significantly underestimates the strength, which is mainly occurring at higher missing mass. Similar features are observed for the 5p and 6p data (although more limited by statistics).

Similar plots to those shown in this section, with a restriction on the residual system of $p_{\perp}^{\mathrm{miss}} < 0.2$ GeV/c, are presented in Figs. 8.67, 8.68, 8.69, 8.70, 8.71 and 8.72 for 4, 5 and 6 proton knockout reactions, respectively, with a minimum momentum threshold of 300 MeV/c.

The corresponding missing mass plots with restriction on the residual system of $p_{\perp}^{\mathrm{miss}} <$ 0.2 GeV/c and -0.6 $< \cos\theta_{\mathrm{Recoil}} <$ 0.6, are presented in Figs. 8.73, 8.74, 8.75, 8.76, 8.77 and 8.78 for 4p, 5p and 6p knockout reactions, respectively, with a minimum momentum threshold of 300 MeV/c.

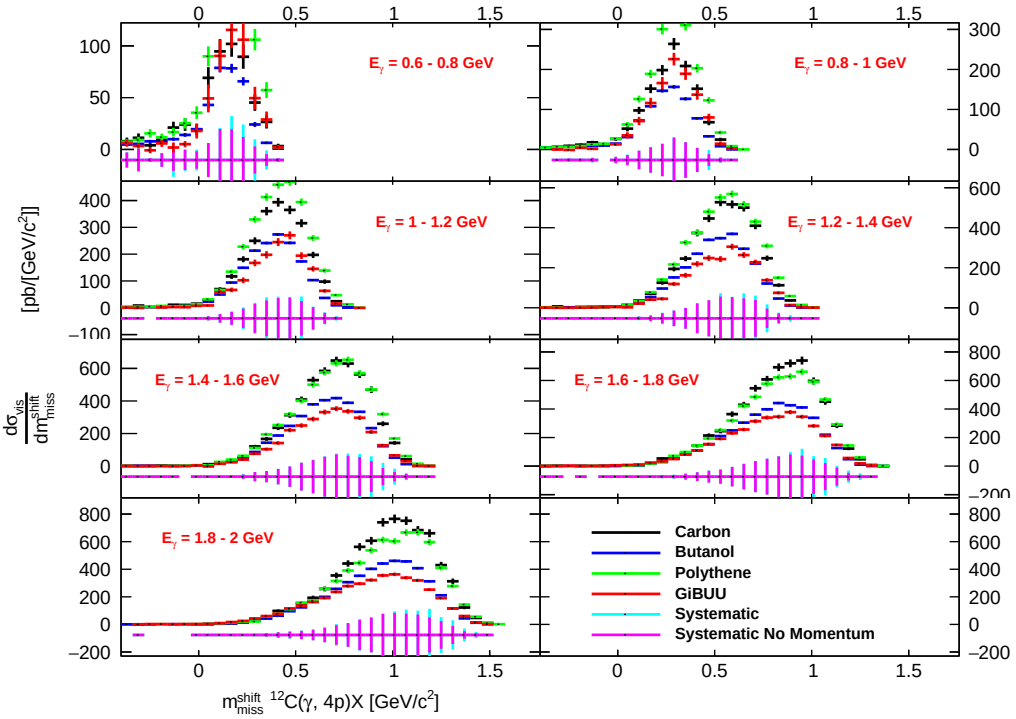

Figure 8.61: The shifted missing mass of the reaction $^{12}\mathrm{C}(\gamma, 4p)X$ for low/medium energy bins of E_γ. The systematics are presented as a band.

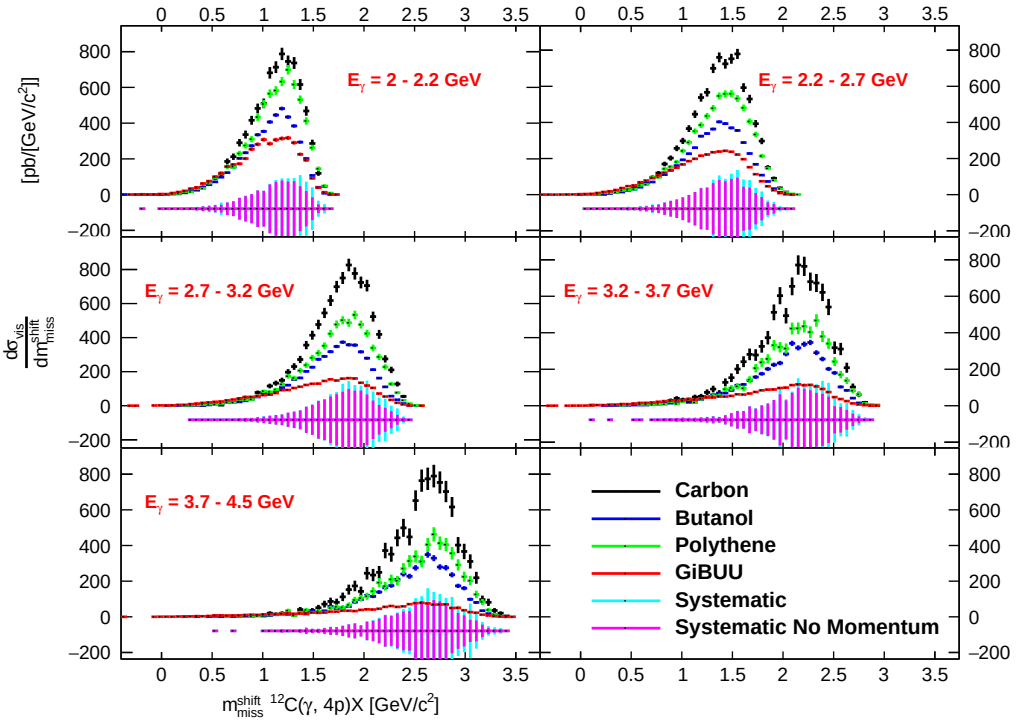

Figure 8.62: The missing mass of the reaction $^{12}\mathrm{C}(\gamma, 4p)X$ for high energy bins of E_γ. The systematics are presented as a band.

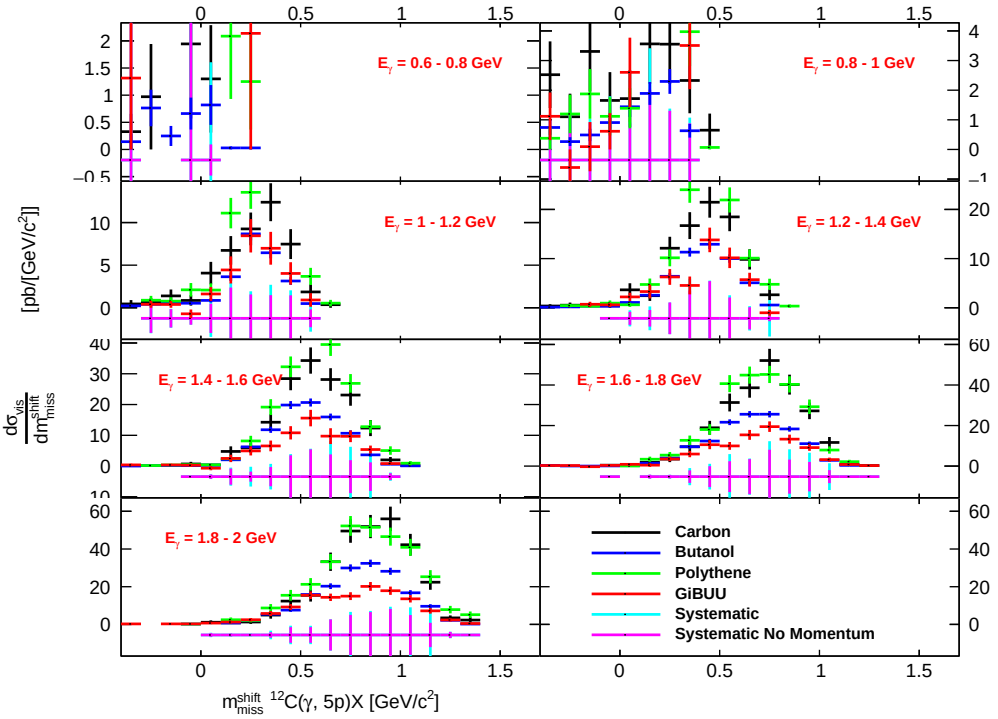

Figure 8.63: The shifted missing mass of the reaction $^{12}\mathrm{C}(\gamma, 5p)X$ for low/medium energy bins of E_γ. The systematics are presented as a band.

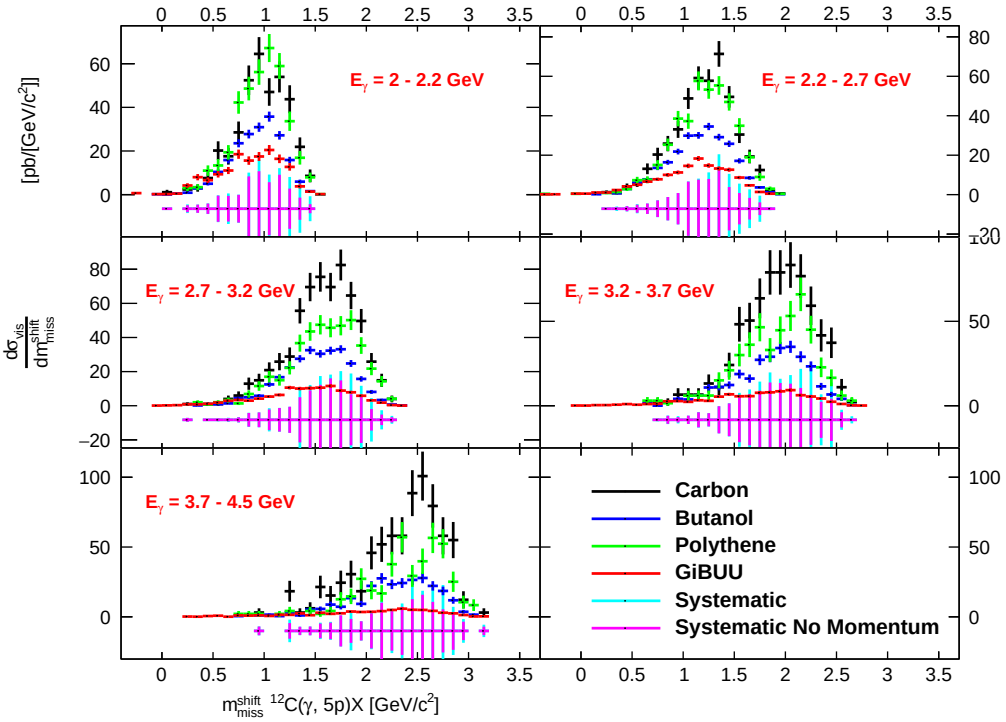

Figure 8.64: The missing mass of the reaction $^{12}\mathrm{C}(\gamma, 5p)X$ for high energy bins of E_γ. The systematics are presented as a band.

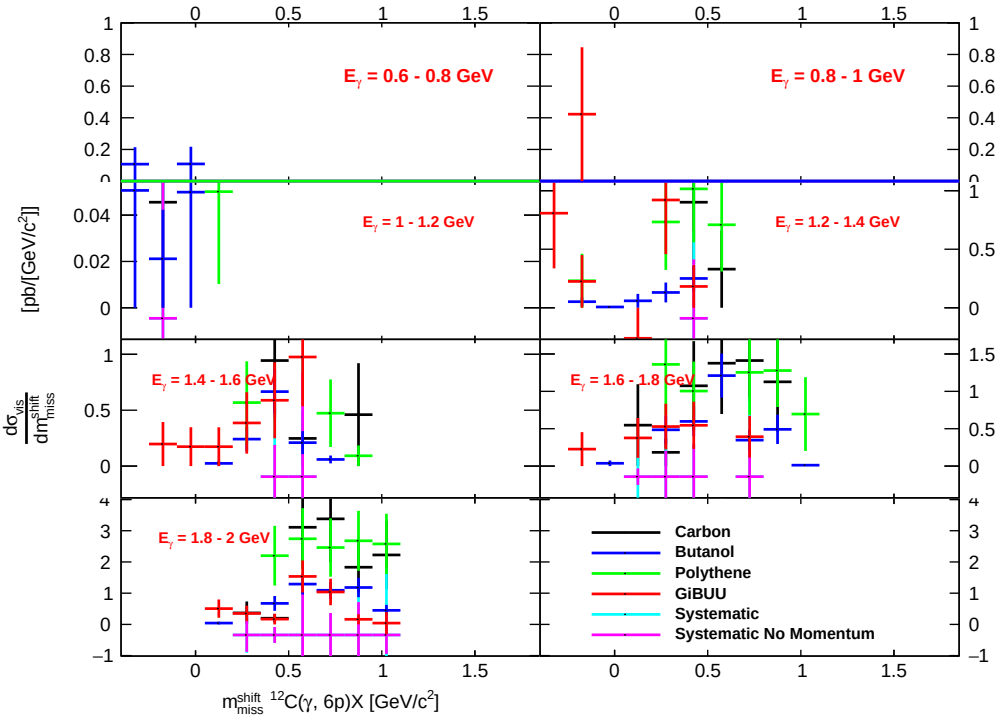

Figure 8.65: The shifted missing mass of the reaction $^{12}\mathrm{C}(\gamma, 6p)X$ for low/medium energy bins of E_γ. The systematics are presented as a band.

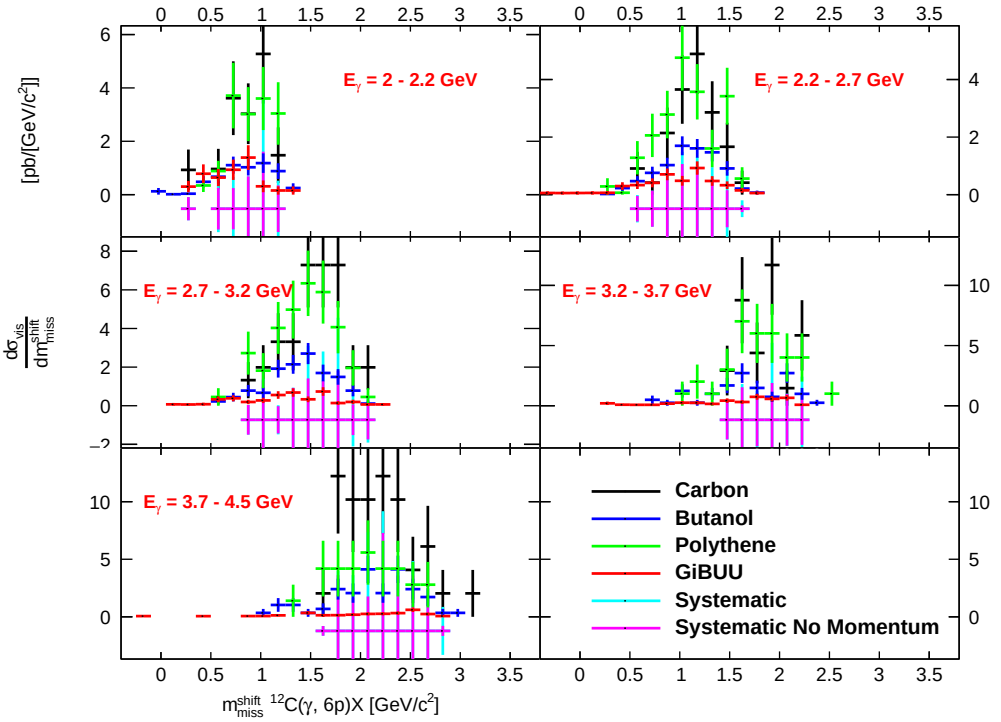

Figure 8.66: The missing mass of the reaction $^{12}\mathrm{C}(\gamma, 6p)X$ for high energy bins of E_γ. The systematics are presented as a band.

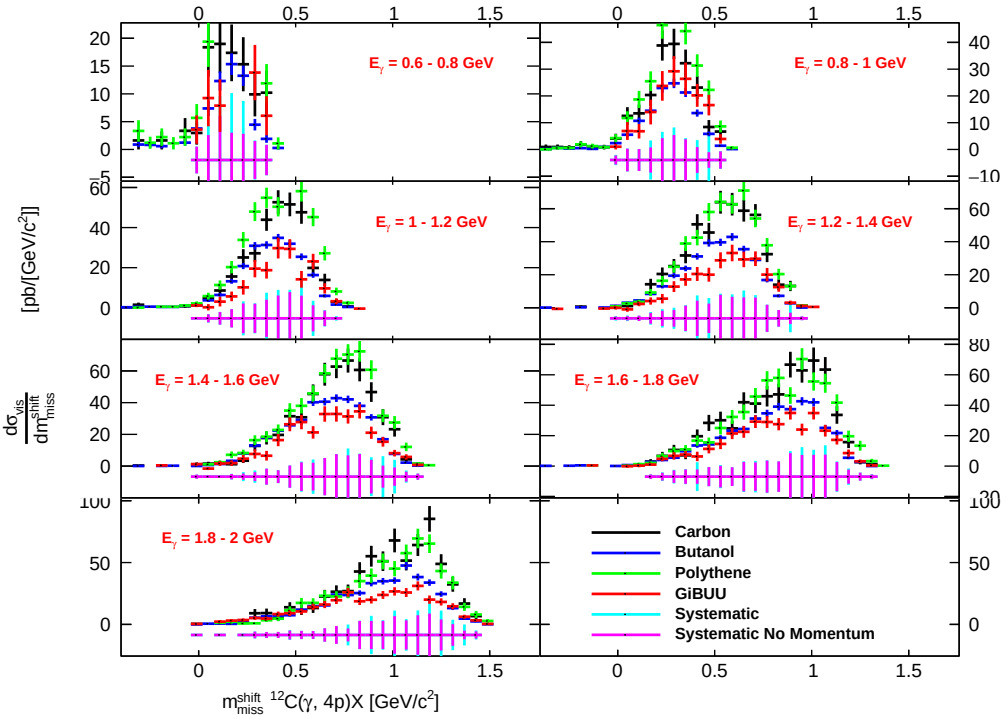

Figure 8.67: The shifted missing mass of the reaction $^{12}\mathrm{C}(\gamma, 4p)X$ with an additional cut on $p_{\perp}^{\mathrm{miss}} < 0.2$ GeV/c for low/medium energy bins of E_{γ}. The systematics are presented as a band.

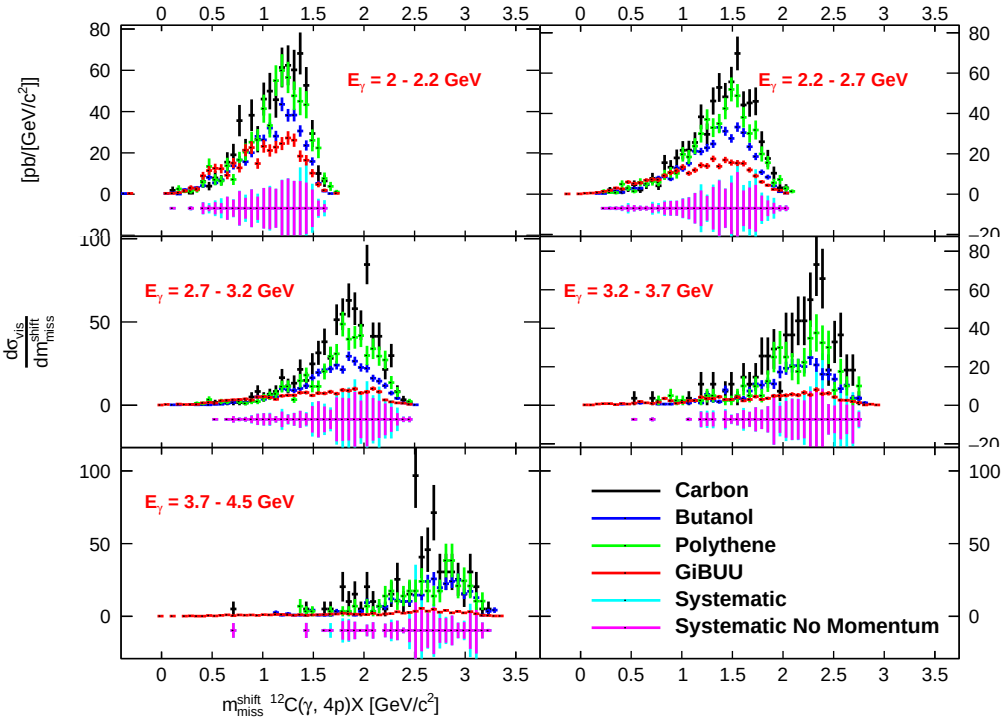

Figure 8.68: The missing mass of the reaction $^{12}\mathrm{C}(\gamma, 4p)X$ with an additional cut on $p_{\perp}^{\mathrm{miss}} < 0.2$ GeV/c for high energy bins of E_{γ}. The systematics are presented as a band.

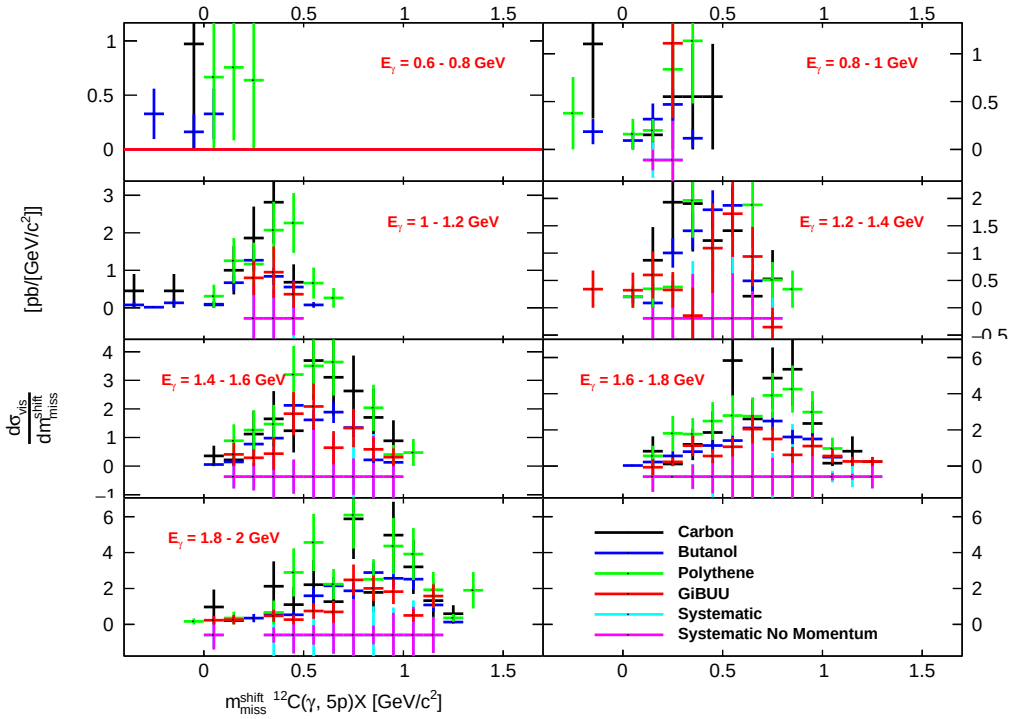

Figure 8.69: The shifted missing mass of the reaction $^{12}\mathrm{C}(\gamma, 5p)X$ with an additional cut on $p_{\perp}^{\mathrm{miss}} < 0.2$ GeV/c for low/medium energy bins of E_{γ}. The systematics are presented as a band.

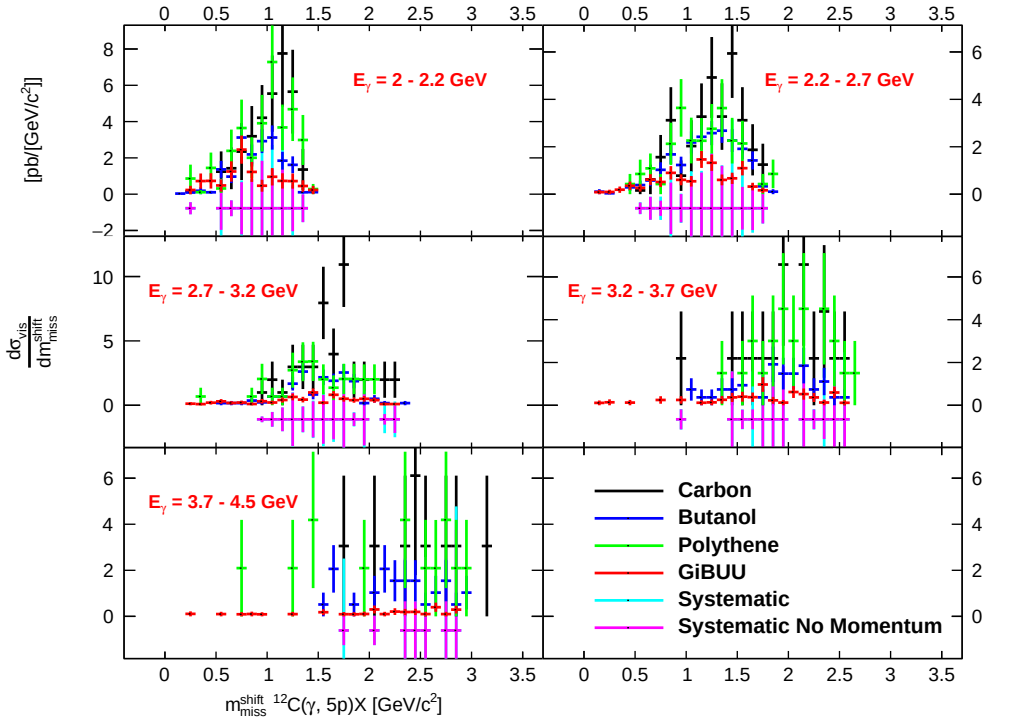

Figure 8.70: The missing mass of the reaction $^{12}\mathrm{C}(\gamma, 5p)X$ with an additional cut on $p_{\perp}^{\mathrm{miss}} < 0.2$ GeV/c for high energy bins of E_{γ}. The systematics are presented as a band.

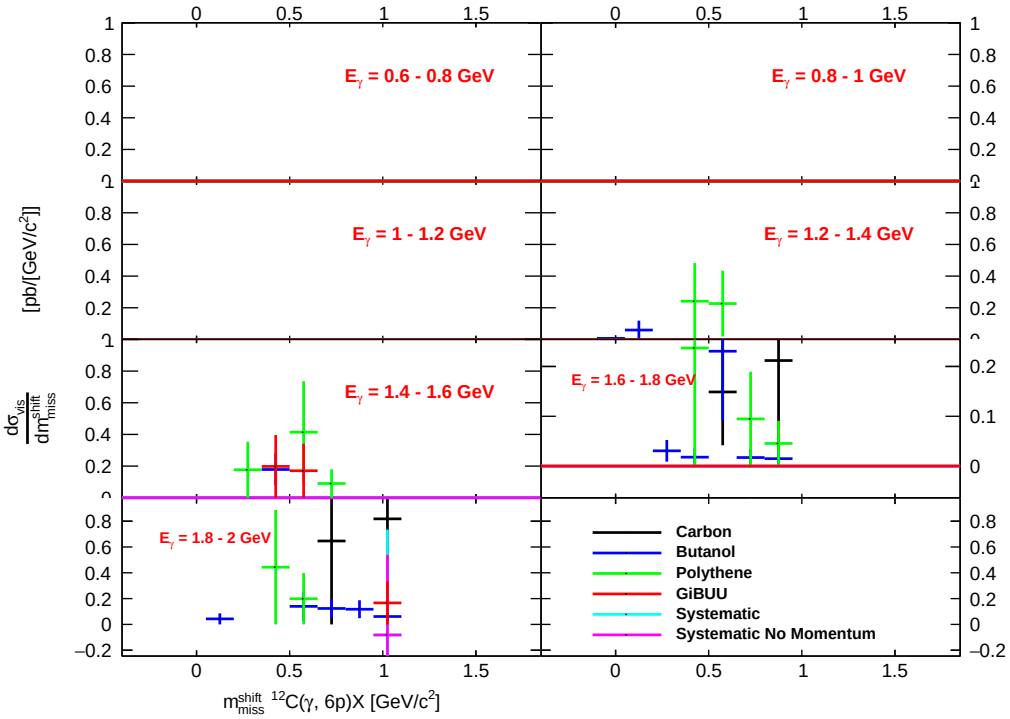

Figure 8.71: The shifted missing mass of the reaction $^{12}\mathrm{C}(\gamma, 6p)X$ with an additional cut on $p_{\perp}^{\mathrm{miss}} < 0.2$ GeV/c for low/medium energy bins of E_{γ}. The systematics are presented as a band.

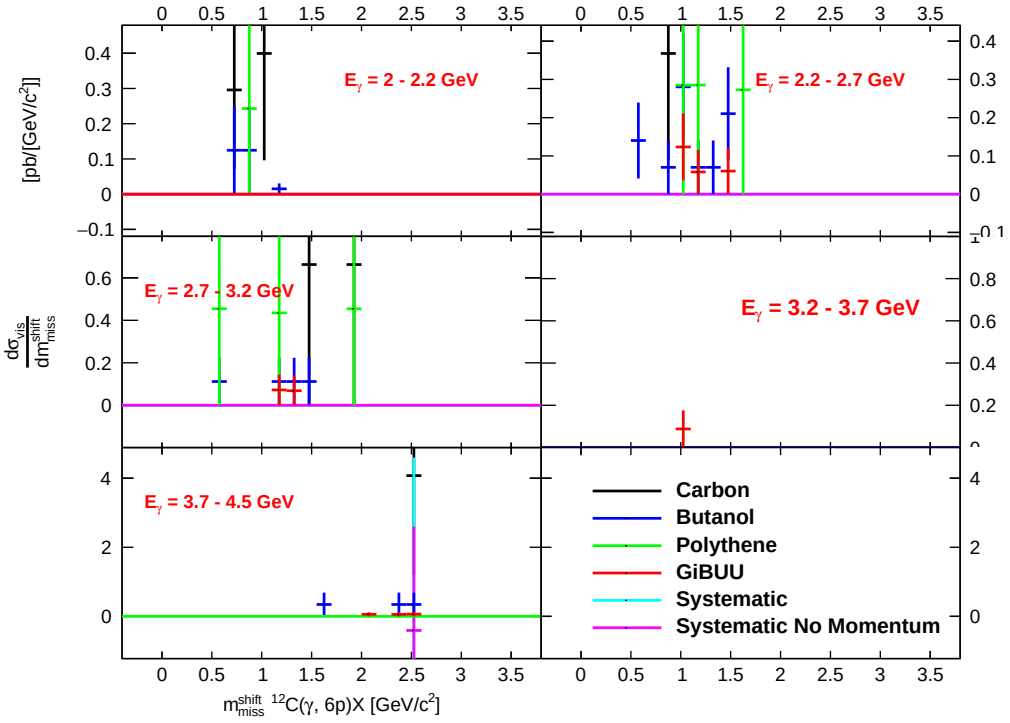

Figure 8.72: The missing mass of the reaction $^{12}\mathrm{C}(\gamma, 6p)X$ with an additional cut on $p_{\perp}^{\mathrm{miss}} < 0.2$ GeV/c for high energy bins of E_{γ}. The systematics are presented as a band.

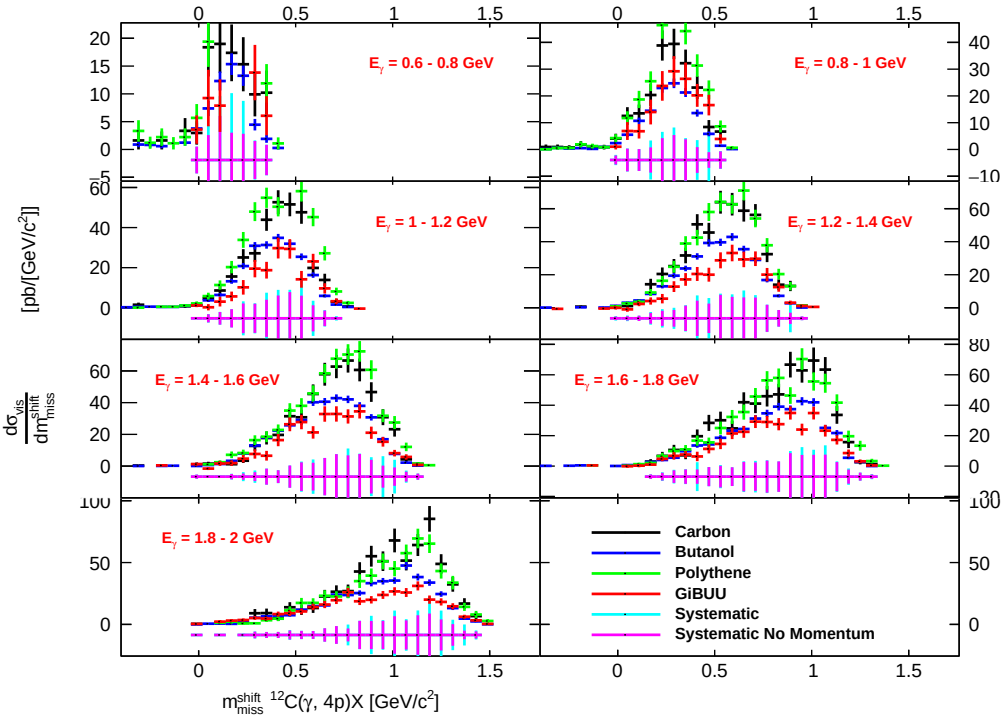

Figure 8.73: The shifted missing mass of the reaction $^{12}\mathrm{C}(\gamma, 4p)X$ with an additional cut on $p_{\perp}^{\mathrm{miss}} < 0.2$ GeV/c and -0.6 $< \cos\theta_{\mathrm{Recoil}} <$ 0.6 for low/medium energy bins of E_{γ}. The systematics are presented as a band.

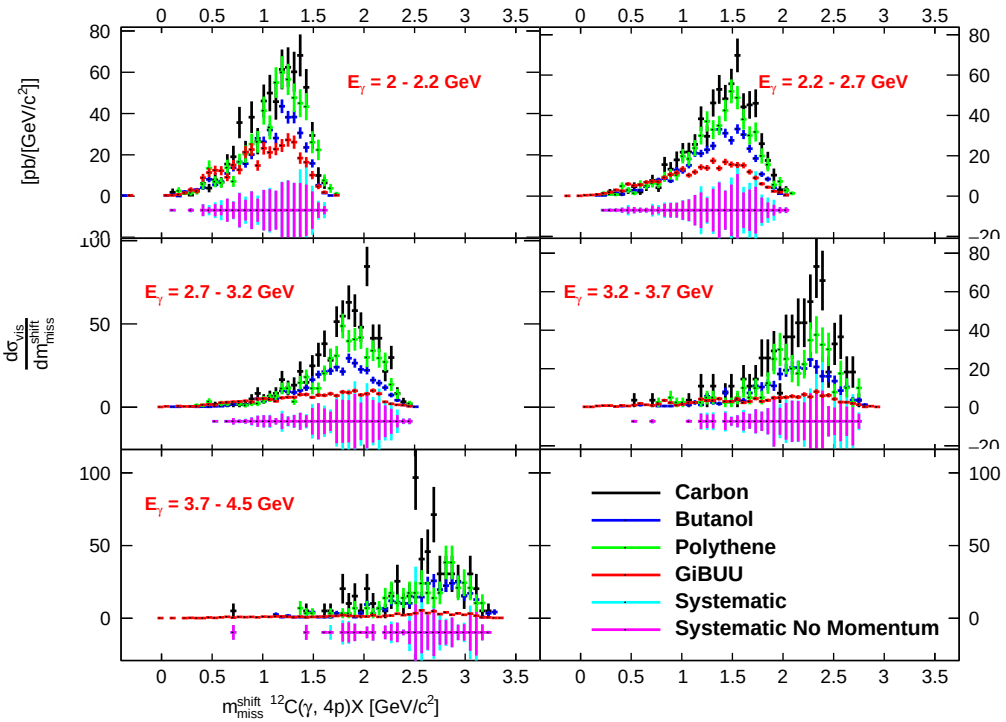

Figure 8.74: The missing mass of the reaction $^{12}\mathrm{C}(\gamma, 4p)X$ with an additional cut on $p_{\perp}^{\mathrm{miss}} < 0.2$ GeV/c and -0.6 $< \cos\theta_{\mathrm{Recoil}} <$ 0.6 for high energy bins of E_{γ}. The systematics are presented as a band.

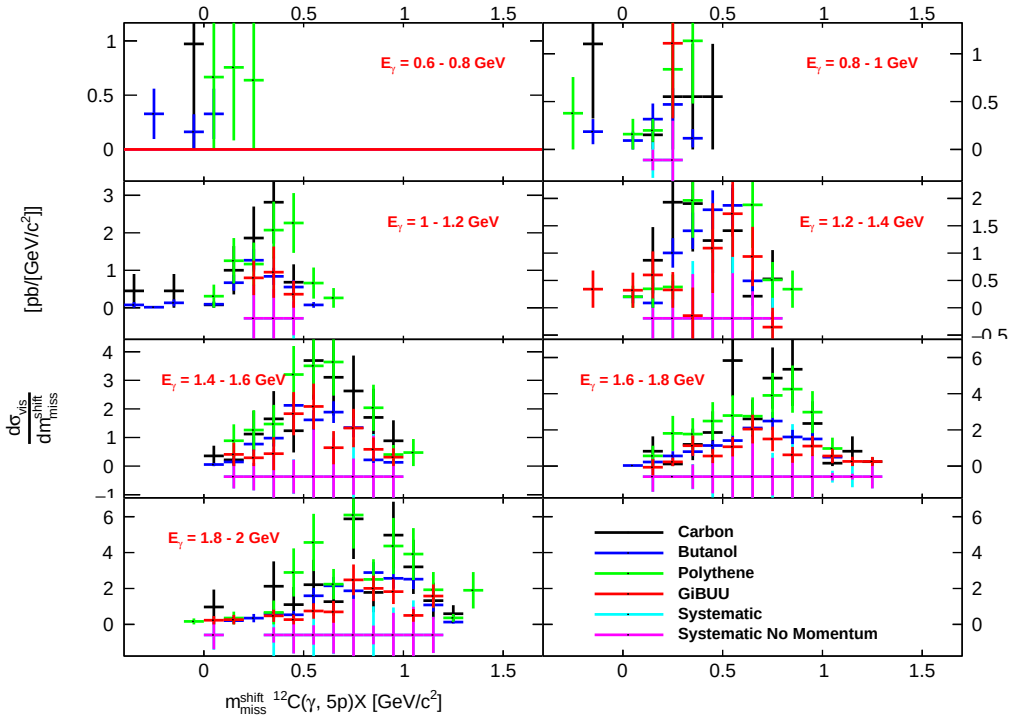

Figure 8.75: The shifted missing mass of the reaction $^{12}\mathrm{C}(\gamma, 5p)X$ with an additional cut on $p_{\perp}^{\mathrm{miss}} < 0.2$ GeV/c and -0.6 $< \cos\theta_{\mathrm{Recoil}} <$ 0.6 for low/medium energy bins of E_{γ}. The systematics are presented as a band.

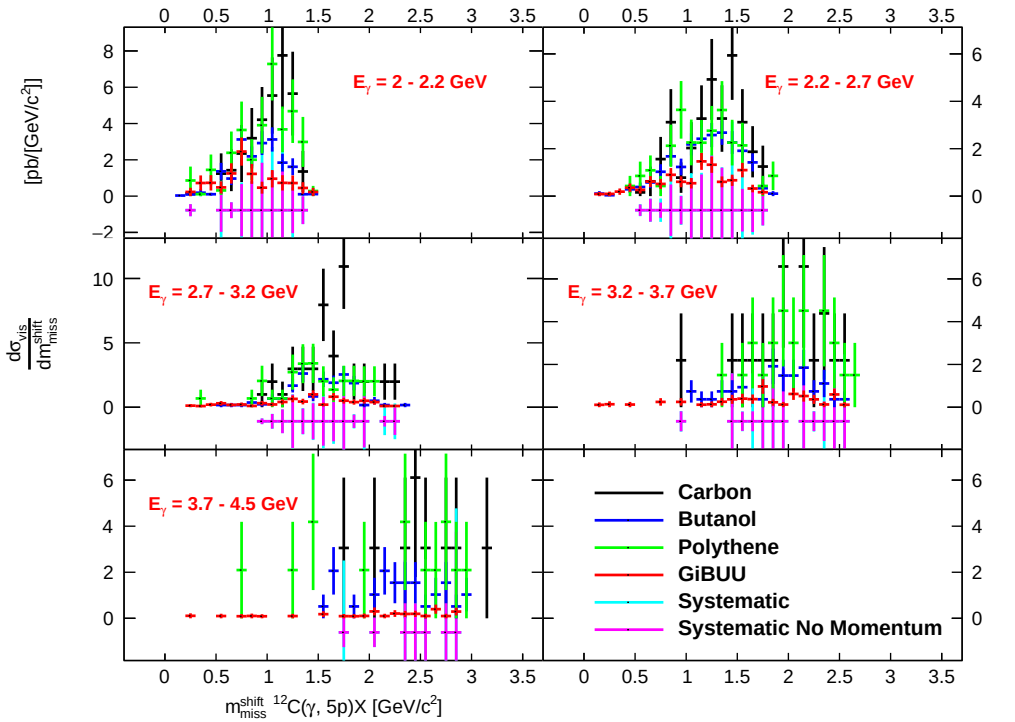

Figure 8.76: The missing mass of the reaction $^{12}\mathrm{C}(\gamma, 5p)X$ with an additional cut on $p_{\perp}^{\mathrm{miss}} < 0.2$ GeV/c and -0.6 $< \cos\theta_{\mathrm{Recoil}} <$ 0.6 for high energy bins of E_{γ}. The systematics are presented as a band.

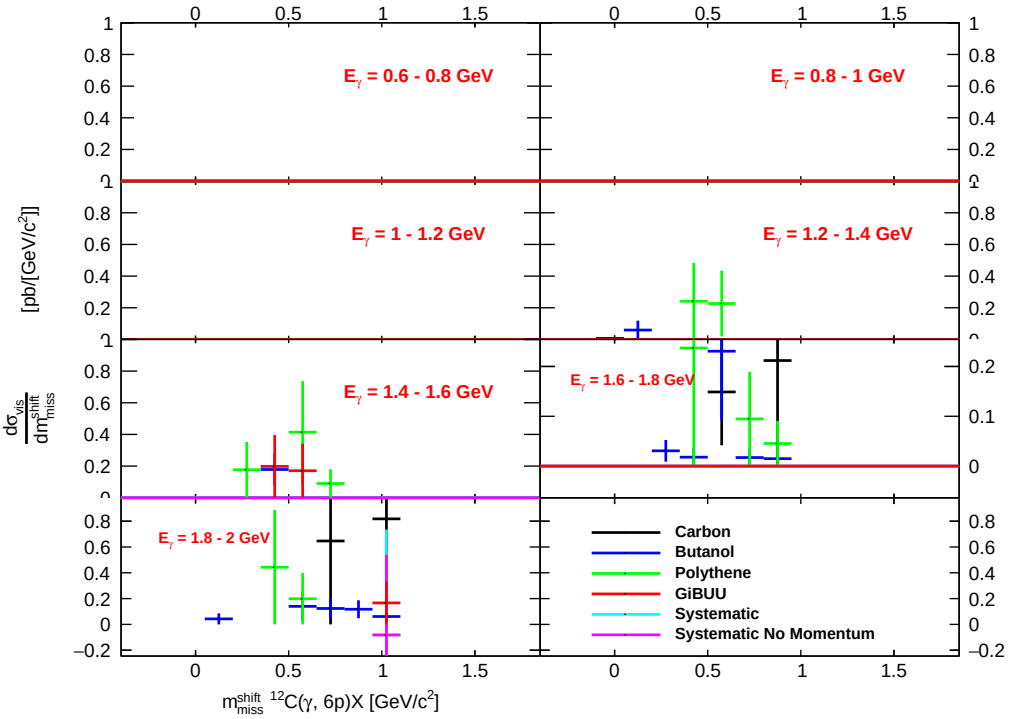

Figure 8.77: The shifted missing mass of the reaction $^{12}\mathrm{C}(\gamma, 6p)X$ with an additional cut on $p_{\perp}^{\mathrm{miss}} < 0.2$ GeV/c and -0.6 $< \cos\theta_{\mathrm{Recoil}} <$ 0.6 for low/medium energy bins of E_{γ}. The systematics are presented as a band.

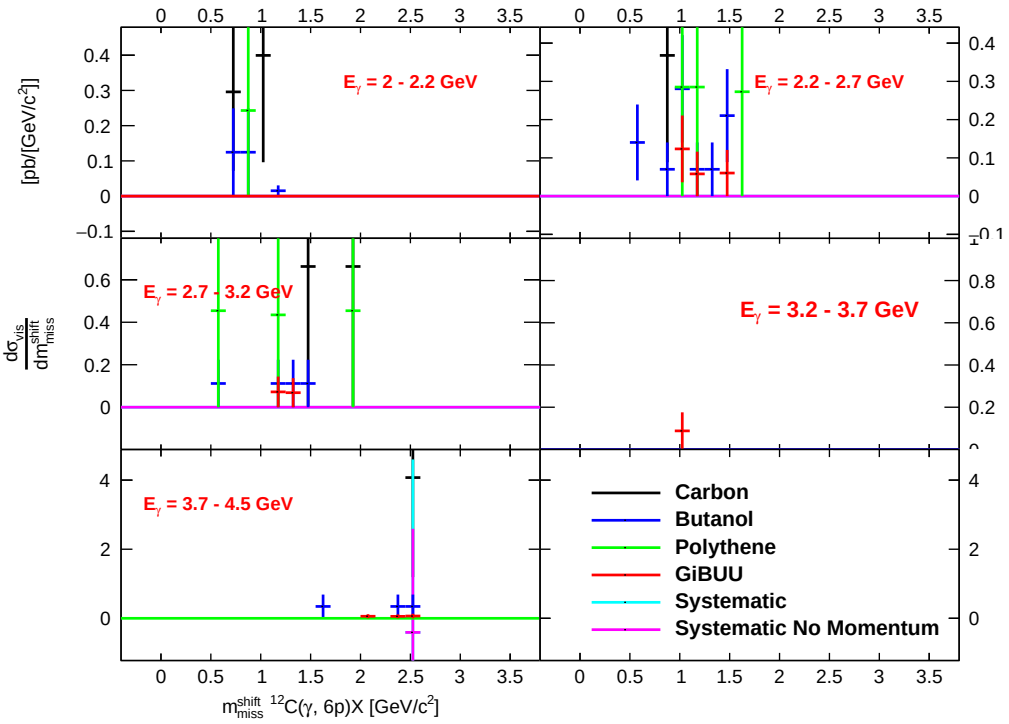

Figure 8.78: The missing mass of the reaction $^{12}\mathrm{C}(\gamma, 6p)X$ with an additional cut on $p_{\perp}^{\mathrm{miss}} < 0.2$ GeV/c and -0.6 $< \cos\theta_{\mathrm{Recoil}} <$ 0.6 for high energy bins of E_{γ}. The systematics are presented as a band.

Evidence for a structure near missing mass of zero, perhaps attributable to 4p direct knockout reactions, is indicated from these data. Weak indications from 5p are also evident (only seen when the data is combined and rebinned). The $6p$ knockout data lacks much statistical definition with these cuts, hence no strong conclusions can be drawn.

8.9.6 Single-Proton Knockout and In-Medium Meson Production

The $^{12}\mathrm{C}(\gamma, p)X$ reaction, provides sensitivity to in-medium meson photoproduction processes from the detected nucleon. In calculating the missing mass (X) we assume the photon interacted with a stationary proton in the nucleus (i.e. the reconstructed missing mass will be smeared by Fermi motion).

Figures 8.79 and 8.80 show missing mass distribution comparisons between the experimental and simulated data, for $^{12}\mathrm{C}(\gamma, p)X$ reactions. For low photon energies, the shape of the distribution is reasonably well described for positive missing masses (note that the small narrow bump in the experimental data at the pion mass is from the small ice (hydrogen) contamination on the downstream surface of the target and should be neglected in the comparison). From Fig. 8.25 these regions, which are dominated by 1π and 2π production, indicate a reasonable theoretical description of these processes. However, even at these low photon energies the tail of events at negative missing mass squared is not well described. From Fig. 8.25, the yield in this region has significant contributions from resonance production and the data here could help to inform and improve the model. Note that negative missing mass implies the role of off-shell objects (e.g. virtual pion exchanges where the proton is involved in 2N or 3N processes) and/or final state interactions which distort the reconstruction of the recoiling system.

For higher photon energies above 2 GeV, the yields are predicted to be dominated by resonance production (see Fig. 8.26). However, the data show much larger strength at higher missing mass and exhibit rather different distributions. The strong peak near the pion mass predicted by GiBUU is not strongly evidenced in the experimental data. This may indicate that reactions seeded by initial pion production are overestimated in GiBUU or FSI processes for the nucleon are strongly underestimated. For higher missing mass regions above 1 $(\mathrm{GeV/c^2})^2$ significant excess strength and structures are evident in the data. At least in part, this could be attributed to the lack of any description of 3π production in the GiBUU model, whose threshold opens up at photon energies of 1.5 GeV. This lack of description of 3π production (and inaccuracies in the modelling of 1π and 2π) are a likely cause of the underpredictions at high missing mass observed also in the 2p, 3p, 4p, 5p and 6p data at high photon energies.

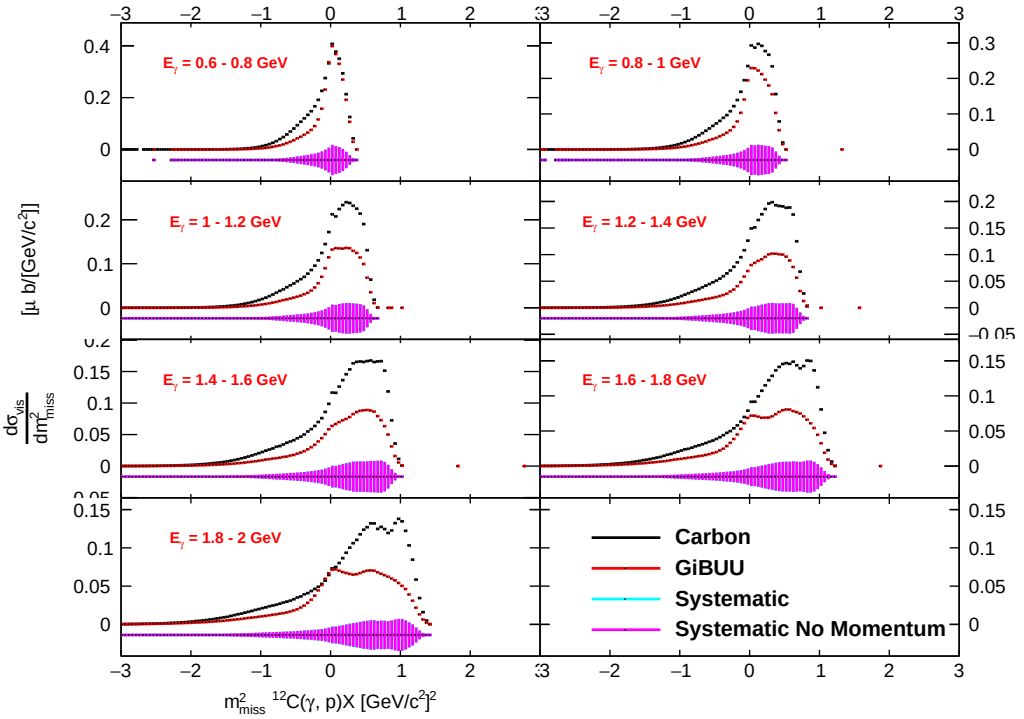

Figure 8.79: The missing mass squared of the $^{12}\mathrm{C}(\gamma, p)X$ reaction for low/medium energy bins of E_γ, where both data sets have been normalised to an absolute cross-section scale.

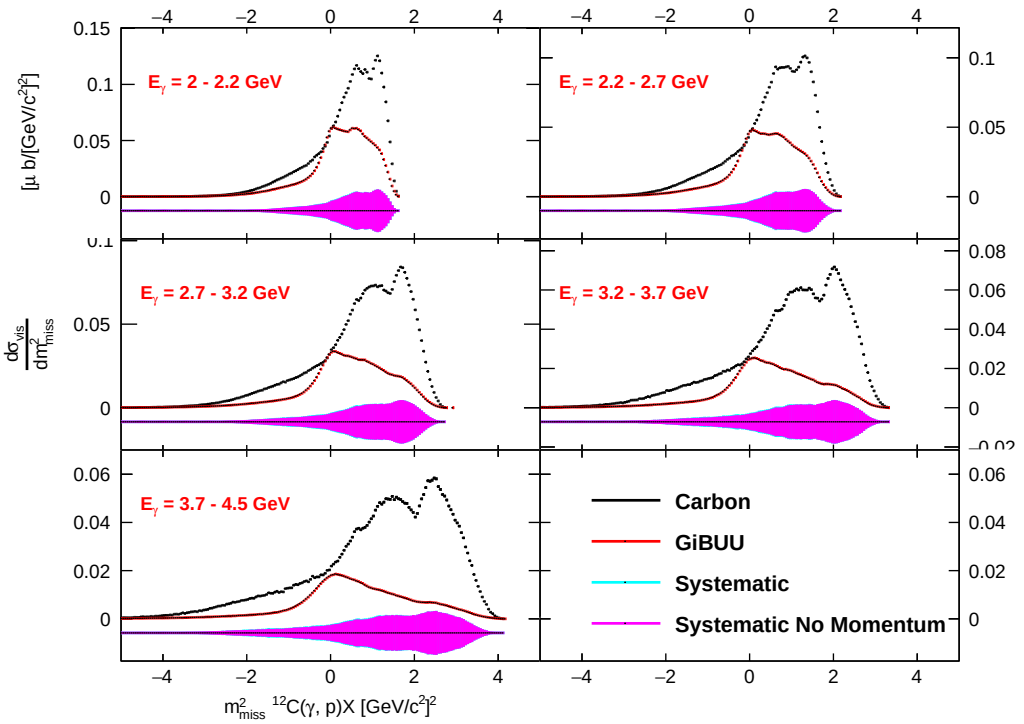

Figure 8.80: The missing mass squared of the $^{12}\mathrm{C}(\gamma, p)X$ reaction for high energy bins of E_γ, where both data sets have been normalised to an absolute cross-section scale.

8.9.7 Conclusion

In conclusion, the GiBUU model has been shown to provide a generally good account of the previously unexplored many-proton knockout processes (2p, 3p, 4p, 5p), with a statistically limited yet informative comparison to the 6p many-proton knockout reactions, for 0.6 GeV $\leq E_\gamma \leq$ 2.0 GeV, albeit with indications of discrepancies in describing the detailed shape of the missing mass distributions. For $E_\gamma >$ 2.0 GeV, the description of the missing mass distributions for all knockout channels deteriorates. This may be because in this energy regime, the modelling is more exposed to missing processes (e.g. 3π), and poor modelling (overprediction) of the single π production. The discrepancies between theory and data highlighted in this work may give information to constrain future developments of the theory. However, even before this, many proton knockout predictions in this region can still be informed (and roughly benchmarked in terms of the expected cross sections) by the studies done here. The observation of direct 2p, 3p, 4p and (weakly) 5p knockout reactions is observed. Cuts on the transverse momentum and polar angle of the recoiling system showed clear enhancement of the contribution of direct processes, with the resulting bump or peak structures also evidenced in GiBUU, owing to a reasonable description of the residual system and predicted direct knockout strength by GiBUU.

The work shows for the first time that direct photoinduced knockout processes exist at these high energies. This is the first time that direct 2p or 3p knockout has been evidenced above $\sim$ 300 MeV in photonuclear reactions on heavy nuclei. Future work will use such data to constrain the treatment of resonances in GiBUU and other many-body theories, as well as assess the role of 2N, 3N, ..., and SRC mechanisms, and whether such data can constrain their nature.

The work also benchmarks the quality of the GiBUU predictions for photoinduced many-proton knockout processes. This will allow the GiBUU model to be used in predictions for a spallation source (see Subsec. 8.9.8), with systematic uncertainties benchmarked to the present experimental measurement. It is clear that such processes are modelled with accuracy at a level such that GiBUU predictions for photon spallation can be considered reasonably accurate.

8.9.8 A First Scoping of the Potential for Photon-Based Spallation Sources

The benchmarking of the theoretical description of the many-proton knockout processes in ^{12}C provides greater confidence when using the model to predict the scenarios for heavier nuclei. In this section, we scope the use of such processes as the basis of a spallation source for heavier nuclear targets, through the (now) benchmarked GiBUU model, Such spallation processes from heavy nuclei have the potential to reach areas of the nuclear

chart not possible from current facilities.

For example with a lead target, if 4 protons are knocked out, the produced nuclides are already at the limit of current knowledge. Such nuclei below lead are predicted to have significant lifetimes (order seconds) offering the possibility for study (e.g. beta half-lives) if they can be removed and implanted. For example, ^{204}Pt has a lifetime of $\approx$ 10 s. Reaching further below lead has the potential to access key nuclides on the path of the r-process, below ^{208}Pb. However, for heavier nuclei there are swathes of neutron-rich nuclei not yet observed in the laboratory - see Fig. 8.1, which shows the currently observed nuclides and the large regions of empty space between the current knowledge and the predicted neutron drip lines.

The most comprehensive data is on the proton-rich side of stability - due to the current production mechanisms used to produce them (e.g. collision of ions which preferentially populates proton-rich nuclei due to $N/Z > 1$ for anything but the lightest ions). This shortfall in the neutron-rich region, and its physics impacts, is well highlighted, for example, see recent results from ISOLDE at CERN [103]. Modern, and future, techniques such as fragmentation and isotope separation are targeted to produce low-intensity beams of neutron-rich nuclei below ^{208}Pb (which is of particular importance due to the path of the r-process through these nuclei and their pivotal contribution to nucleosynthesis as the "waiting point"). Current proposals for techniques, which could feasibly produce significant yields, e.g. multi-nucleon transfer, look promising, but are hindered by the technological developments required to manipulate the reaction products for spectroscopy purposes [104, 105].

Clearly, the production of such nuclei through many-proton knockout will have small cross-sections. However, the frontiers of intensity for photon beams are undergoing a revolution with next-generation compact photon source (CPS) technologies [94]. A factor of $> 10^6$ more photons per second than available in this analysis will be reached.

In this section, we show the total GiBUU predictions for the cross sections to produce different final state nuclei. This is obtained for heavy (lead and uranium) targets. The cross sections presented are without the inclusion of the acceptance for detecting the final state protons in a detector system, which would not be necessary for a spallation source. As the results in the previous sections show, GiBUU underpredicts the yields by up to a factor of 3 at the higher photon energies, so this should be taken into account. However such factors do not significantly influence the general conclusions on the properties of a future spallation source.

The GiBUU cross sections for the production of final state nuclei as a function of A and Z are shown for a range of incident photon energies in Figs. 8.81 and 8.82. The produced nuclei show a symmetric distribution around $N = Z$, as might be expected from reactions induced by the (uncharged) photon and the similar cross-sections for initial interactions

with neutrons and protons in the nucleus. It is clear that such photon-induced processes have cross sections to produce neutron-rich nuclei up to ∼14 protons south of ^{208}Pb, well beyond the current limits of observation in a laboratory.

We also present GiBUU predictions for ^{238}U where different regions of final state nuclei can be accessed Figs. 8.83 and 8.84. The use of a heavier target also populates the key unknown nuclei below lead.

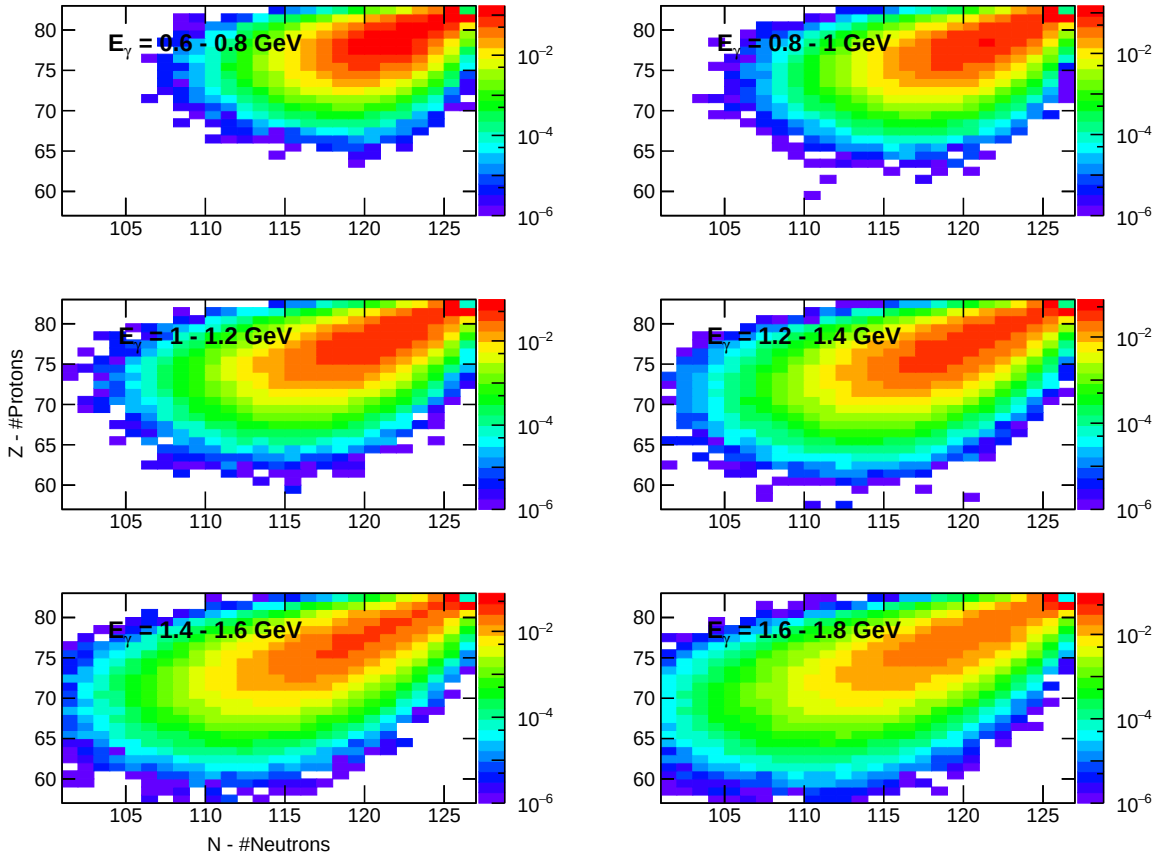

Figure 8.81: Raw GiBUU distributions showing the number of protons knocked out, #Protons, subtracted from the total number of protons in the target nucleus, Z, as a function of the number of neutrons knocked out, #Neutrons, subtracted from the total number of neutrons in the target nucleus, N, for ^{208}Pb for low/medium E_γ energy bins. Events with protons and/or neutrons that have undergone charge exchange have been removed. The z scale presents the cross-section in units of μb, with a log scale applied.

The GiBUU model works on a weights-based basis, implemented onto a phase space generator for the final state particles. The nuclides presented in the plots were derived from 5 million incident photons, which sets the lower limit on reaction cross sections to produce an event. Running with a larger sample would reveal cross sections for the production of even more exotic nuclides than displayed i.e. the boundaries of the predictions presented are due to statistics rather than a lack of processes to reach beyond this apparent boundary.

The nuclear chart distributions show the true potential of this study. It is possible to

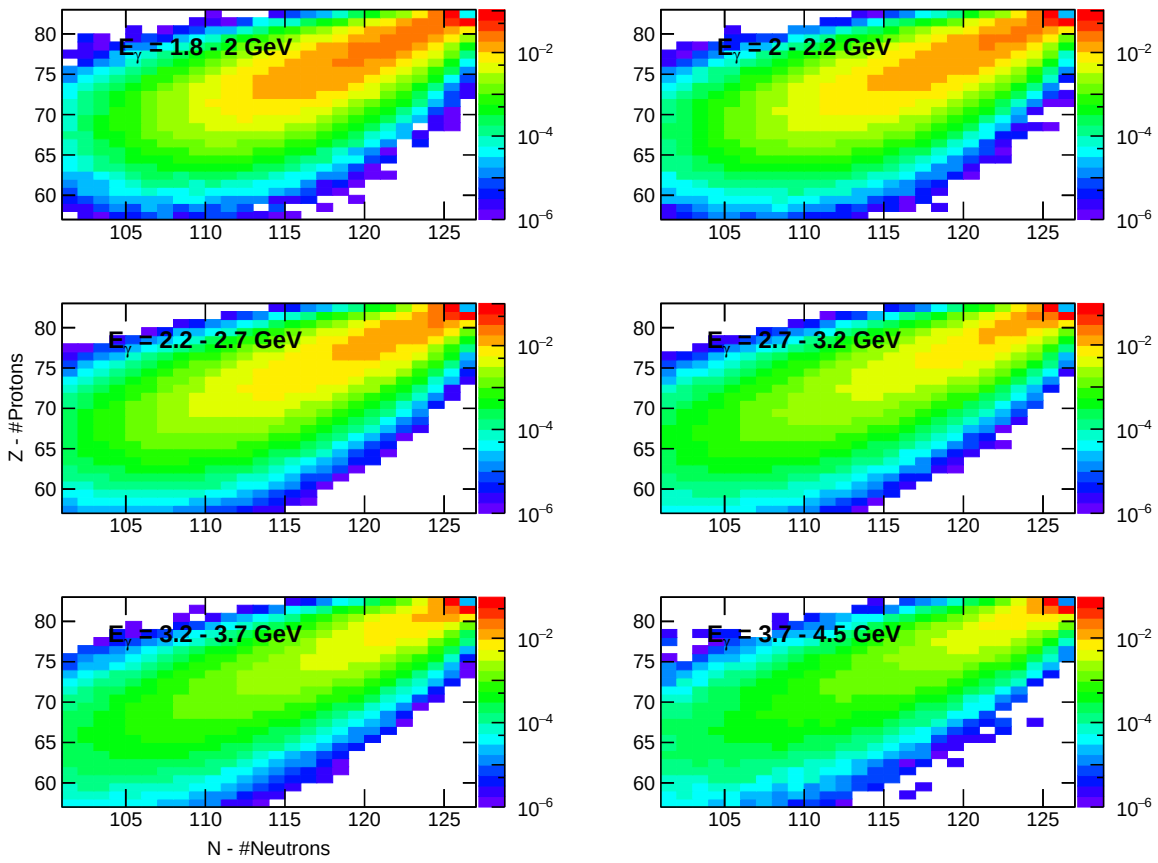

Figure 8.82: As for Fig. 8.81, now with high energy photons impinged on ^{208}Pb.

access a completely uncharted territory of the nuclear chart using real photon beams as a spallation source. With the demonstrated underestimation of high multiplicities in GiBUU, shown in Subsec. 8.9.5, the reach would be enhanced further. This work could lay the foundations for future endeavours, focusing on using real photon beams as a spallation source to further our understanding of the nuclear chart.

As a first assessment of the production rates/hour for these exotic neutron-rich nuclei, we take a 1 mm-thick ^{208}Pb and ^{238}U and the expected CPS photon flux of 1×10^{12} photons/s taken from Ref. [94]. Using Eq. (8.3), we can deduce the number densities of lead and uranium. Then we can determine the rate/hour from the product:

$$\text{Rate/hour} = \Phi_\gamma \times N \times \sigma_i \times (3600\text{s/h})\,. \tag{8.8}$$

where Φ_γ is the CPS photon flux, N is the number density of the target and σ_i is the cross section for the reaction, for example $^{208}\text{Pb}(\gamma, 3p)X$. Figure 8.85 presents the typical production rates/hour for exotic nuclei produced in 1 mm-thick targets of ^{208}Pb and ^{238}U. The figure clearly illustrates the remarkable potential to produce a large number of exotic nuclei, and given the half-lives of these nuclei would be considerably larger than the half-lives for light exotic nuclei (as shown in Ref. [106] for nuclides such as ^{200}Os and ^{202}Ir,

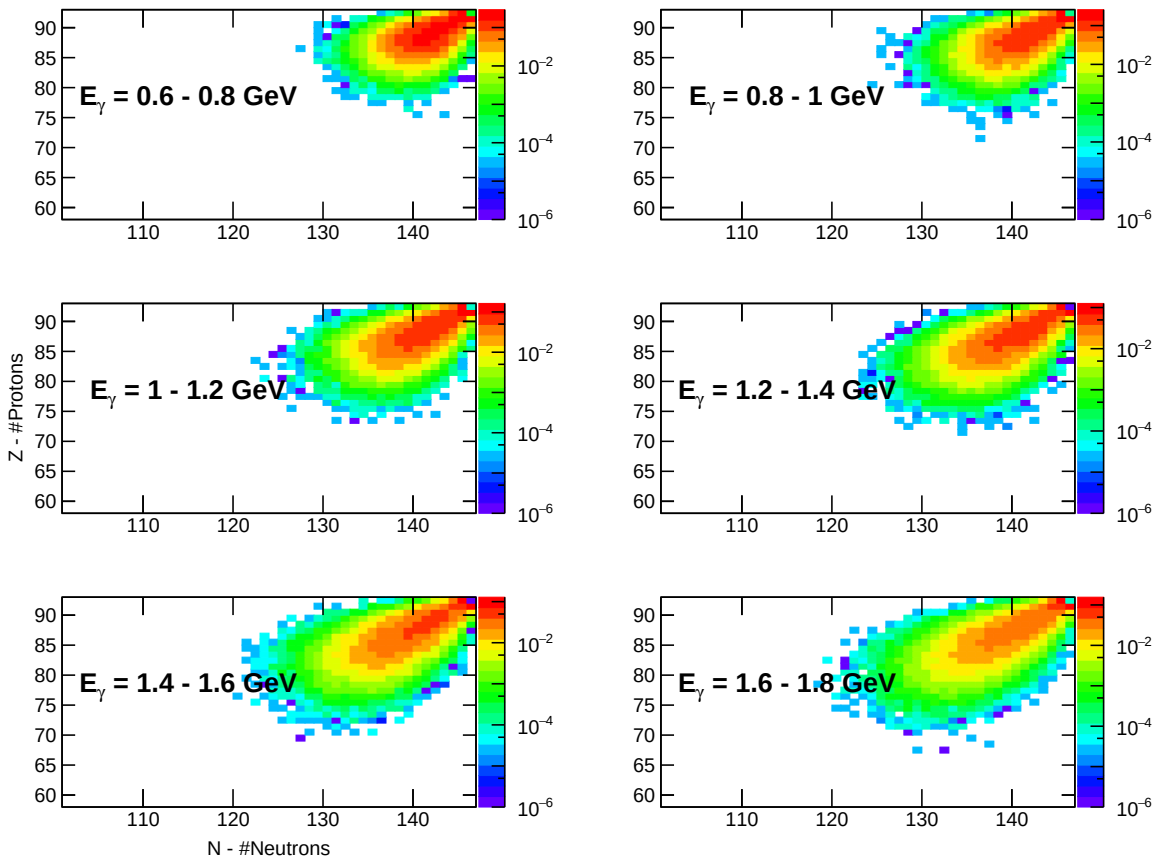

Figure 8.83: As for Fig. 8.81, now with high energy photons impinged on ^{238}U.

which have half-lives of seconds), future work to establish methods to extract and study the nuclei is a crucial next step.

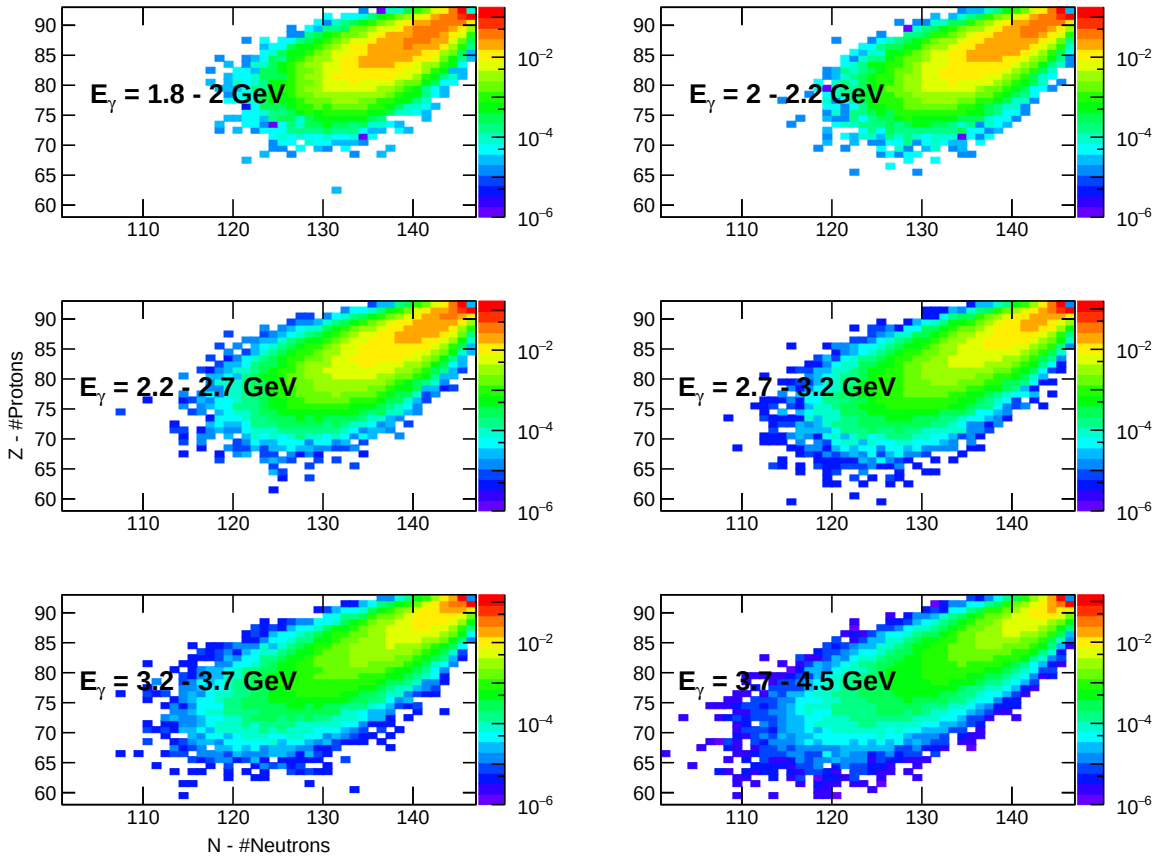

Figure 8.84: As for Fig. 8.81, now with low/medium energy photons impinged on ^{238}U.

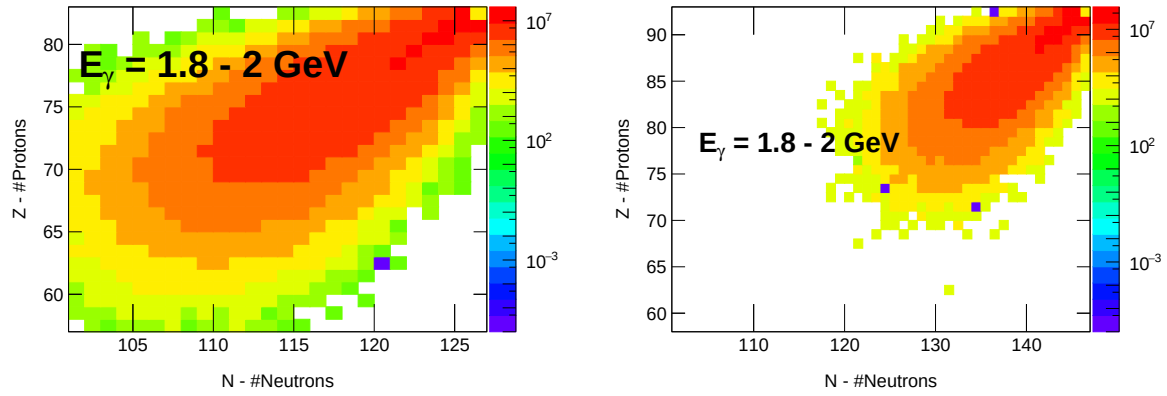

Figure 8.85: The raw GiBUU nuclear chart distributions for the photon energies $E_\gamma = 1.8 - 2.0$ GeV impinged on ^{208}Pb (left) and ^{238}U (right) targets at a rate of 1×10^{12} photons/s. The z-axis has been converted to a rate/hour, illustrating the typical production rate of the exotic isotopes produced.

Chapter 9

Results from the e4ν CLAS12 Analysis

"If I have seen further it is by standing on the shoulders of Giants."

- Isaac Newton

This chapter presents our results from electron scattering reactions from nuclear targets (^{2}D, ^{12}C and ^{40}Ar), for electron beam energies 2, 4 and 6 GeV, with comparisons to GENIE and GiBUU. Final states of $A(e,e'p)X$, $A(e,e'p\pi^-)X$, $A(e,e'p\pi^+)X$, $A(e,e'p\pi^0)X$, $A(e,e'p\pi^+\pi^-)X$ and $A(e,e'pp)X$ reactions are presented and the quality of the reconstruction of the (known) incident electron beam energy from the various final states is presented.

The section is structured as follows. Firstly, a brief introduction outlines the motivation for the measurements, which are crucial not only for nuclear theory but also for the efficacy of neutrino beam reconstruction in neutrino experiments. Following this the particle selection methods for identifying the scattered electrons and final state protons, pions and kaons in CLAS12 are described, for both the experimental and simulated data. Following this, the normalisation procedure to place the experimental data and GiBUU and GENIE on a common scale is presented. Subsequently, we present a discussion of the restrictions we impose on the recoiling system and their effectiveness in suppressing backgrounds. The full statistical and systematic uncertainties in the measurements are then discussed. Finally, the results for the different electron scattering reactions, for the various targets and beam energies, are presented. The implications of the results and their impact on future neutrino oscillation experiments are briefly discussed.

9.1 Introduction

Next-generation neutrino facilities, such as DUNE (Deep Underground Neutrino Experiment), require precise modelling of neutrino event generators to determine the initial neutrino flux and incident beam energy. GENIE, a state-of-the-art neutrino event generator, along with other theoretical models, fails to accurately describe the nuclear interactions which drive the observed interactions in neutrino-nuclei collisions. Without precise modelling of fundamental in-medium nuclear reaction processes, the neutrino oscillation parameters extracted from neutrino experiments will have large systematic uncertainties. As discussed in Sec. 2.4, the theoretical models are used to deconvolute the neutrino flux from the measured events and subsequently determine the initial beam energy, typically referred to as the true energy. Poor modelling of the fundamental processes results in large biases when reconstructing the initial neutrino beam energies.

Approximately 20 trillion trillion solar neutrinos—neutrinos that emerge from fusion reactions in the Sun, particularly from β-decays in the proton-proton (pp) chains as the Sun burns hydrogen and converts it into helium—pass through the Earth each day. For example, the first step of the pp chain is $p + p \rightarrow^2 \mathrm{D} + e^+ + \nu_e + 0.42$ MeV, where two protons (hydrogen nuclei) fuse to produce a deuteron (^{2}D), which contains one proton and one neutron inside its nucleus, releasing a positron (e^+) and an electron neutrino (ν_e) to conserve quantum numbers. Additionally, a small amount of energy is released due to the binding energy of the newly formed deuteron. The overall reaction can be summarised as $4p + 2e^- \rightarrow^4 \mathrm{He} + 2\nu_e$, releasing a total energy of approximately 26 MeV. It is difficult to constrain the models for neutrino experiments given that weak interactions are suppressed in relation to electromagnetic interactions. Additionally, the neutrino oscillation observables, such as the probability of neutrino flavour α oscillating to neutrino flavour β, presented in Eq. (2.8) for the two-flavour case, depends on the true energy and the oscillation parameters themselves. Since we do not know the beam, or the oscillation parameters, reconstructing the initial beam with a high level of accuracy is necessary for an accurate extraction of the oscillation parameters.

The accelerator at Fermilab will accelerate protons to energies of up to 120 GeV and direct them at a graphite target to produce mesons. These mesons are then focused using magnetic horns and directed into a long vacuum pipe, where they decay and produce an intense neutrino flux, with most neutrinos having energies between 1 and 10 GeV. This neutrino beam will first encounter a near detector situated about 574 meters from the neutrino source, which will be used to characterize the neutrino flavour and flux at that location. The neutrinos will then travel approximately 1,300 kilometres underground to the Sanford Underground Research Facility, where they will interact with large liquid argon time projection chambers in the far detector [107]. The detection of particles at the far detector will be compared to measurements from the near detector. These comparisons are crucial for accurately reconstructing the far detector flux with minimal

systematic uncertainty. This is particularly important because a significant portion of the current uncertainty stems from an incomplete understanding of nuclear physics, making accurate flux reconstruction essential for extracting neutrino oscillation parameters with low systematic uncertainty. Fortunately, neutrinos belong to the lepton family of particles, which also include electrons. Since there is a wealth of data available on electrons with known initial beam energies, and as discussed in Chap. 2, the two particle species exhibit similar nuclear physics, this data can help reduce uncertainties in neutrino measurements.

At the Thomas Jefferson National Laboratory (JLab), we use mono-energetic, high-luminosity electron beams, with precise knowledge of the beam energies to study electron scattering events. Knowing the initial beam energy allows us to constrain the theoretical models, as a direct benchmark of the predicted cross sections can be made. Moreover, we can use our precise knowledge of the beam energy to test the simulating power of various theoretical models. Using the wide range of beam energies available to us (2.1, 4.0 and 6.0 GeV), we can study various fundamental interactions, including how well the models capture these key physics aspects. Importantly, these models have never been benchmarked against real data for the beam energies and targets available to us in the RGM experiment, and the beam energies available directly overlap with the kinematical range relevant to DUNE ($1 - 10$ GeV). The liquid argon target will be of particular interest, given the time projection chambers at DUNE are filled with liquid argon.

As discussed previously, we can use the electron scattering data available at JLab to benchmark the models for use with neutrino scattering data. Using Eq. (2.11) we can test if the models can reconstruct the initial electron beam by detecting all product particles of the reactions observed, which is the method adopted at neutrino oscillation facilities. We present the first benchmark from the new high-luminosity CLAS12 RGM experiment, for many-body reactions involving multi-proton knockout and multi-pion channels. Such reactions are important for benchmarking the models, particularly for the denser nuclear mediums such as argon, which have a larger probability for multi-nucleon knockout. Multi-nucleon knockout channels can arise from many fundamental processes, as discussed in Sec. 2.2, such as pion reabsorption, 2N and 3N forces, MECs and SRCs, to name a few. These reactions contribute significantly to the background observed in electron- and neutrino-nuclei interactions, hence their importance for benchmarking the models. A comparison of the quasielastic scattering reaction will be provided, given its importance to the neutrino community (it is analogous to CC neutrino reactions).

9.2 Particle Identification

Similarly to the previous analysis, standard CLAS12 software was used to translate detector information into physical information for the particles. This information is then stored in HIPO files, which is the standard framework used for analysing CLAS12 data.

The criteria for this analysis follows a semi-exclusive event selection, where the scattered electron and charged hadrons are included, or excluded, with certainty. Neutral particles are ignored in this analysis. The particle identification for this analysis is dependent on the particle species and detector systems involved in the reconstruction of the particles. We start with the scattered electron, which is also the trigger particle for our events, that is detected in the Forward Detector (FD) only. Afterwards, we discuss the particle identification used to determine the charged hadrons in the FD and Central Detector (CD) separately.

9.2.1 Particle Status Cut

A particle that registers a hit in a given detector will be assigned a value, called particle status, which is not unique to the particle. The status represents the detector topology and is the sum of a set of numbers associated with detector hits. The particle status is determined by Eq. (9.1), given by:

$$\begin{aligned} status =& 1000 \times \mathrm{FT} + 2000 \times \mathrm{FD} + 4000 \times \mathrm{CD} + 8000 \times \mathrm{BAND} \\ &+ 100 \times N_{\mathrm{scint}} + 10 \times N_{\mathrm{cal}} + 1 \times N_{\mathrm{cher}}, \end{aligned} \tag{9.1}$$

where FT is the Forward Tagger, FD is the Forward Detector, CD is the Central Detector, BAND is the Backwards Angle Neutron Detector, N_{scint} is the number of scintillator counters hit, N_{cal} is the number of calorimeter counters hit and N_{cher} is the number of Cherenkov counters hit.

Table 9.1 details how the variables in Eq. (9.1) are assigned their values and Fig. 9.1 presents the particle status for the trigger particle (left) and for all other charged hadrons (right) in the final state, for both the experimental (top) and simulated (bottom) data. The CLAS12 detector has a wide kinematic range suitable for detecting many particles, therefore the electron is restricted to the forward detector. If a particle was a part of

Number of scintillator hits	N_{scint}
Number of calorimeter hits	N_{cal}
Number of Cherenkov hits	N_{cher}
FT subsystem	$FT = 1$ if used, else 0
FD subsystem	$FD = 1$ if used, else 0
CD subsystem	$CD = 1$ if used, else 0

Table 9.1: Details of the CLAS12 Event Builder status assignment algorithm to determine if a particle is in the FD or CD, where Eq. (9.1) determines the assignment value.

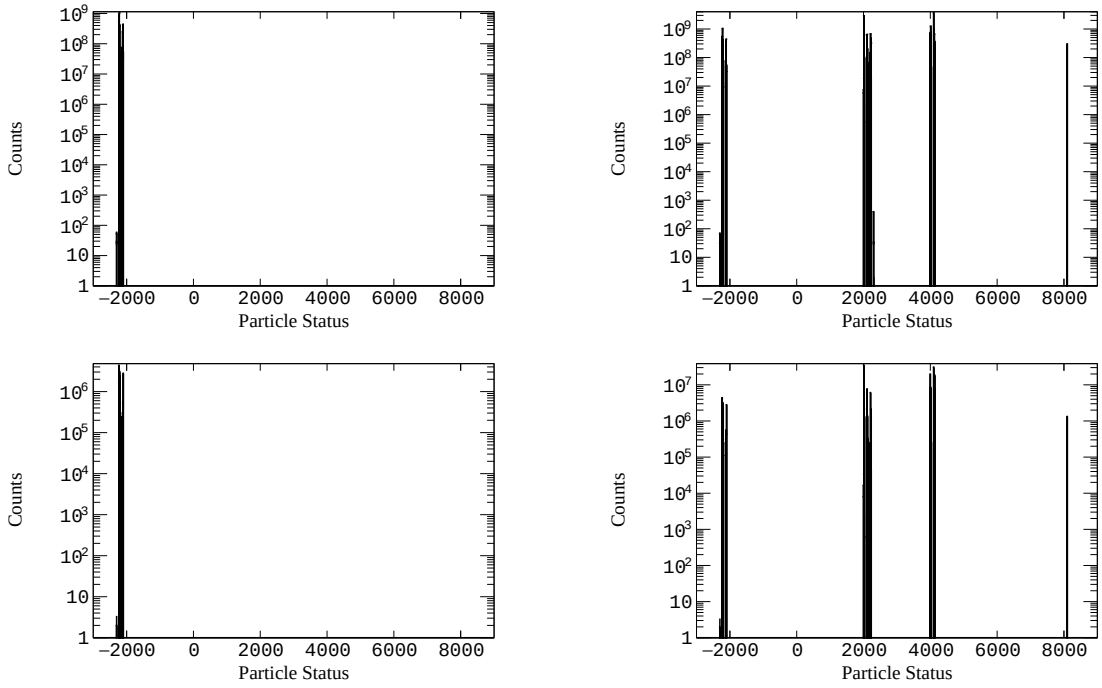

Figure 9.1: The particle status of all trigger particles (left) and all particles (right) for a 6 GeV electron beam impinged on a ^{12}C target. The top line presents the experimental data and the bottom line presents the GENIE data (generated using the G18 tune) passed through GEMC.

the trigger for the event, then it is assigned a negative status. Using the aforementioned rules, we, therefore, restrict the electron to having a status from $(-4000, -2000]$. This means that the electron trigger cannot be in the central detector or forward tagger and must register hits in the forward detector. Additionally, the electron trigger must register a hit in the scintillator counters, calorimeter counters and Cherkenov counters.

9.2.2 Electron Identification

The reconstruction software in CLAS12 assigns a PID value to each detected particle in the event, which is based on different criteria. For detected hadrons, it determines the PID based on the measured velocity and momentum of the particle matching the theoretically expected values for the velocity for each value of momentum. Since the trigger particle, which initiates the reaction in CLAS12, is assumed to have the speed of light, different criteria are required for assigning the PID value of the trigger particle. Table 9.2 summarises the electron identification cuts imposed when selecting a PID of 11 in the event builder.

Figure 9.2 presents the number of photoelectrons, N_{Phe}, produced in the HTCC (left) and the sum of the energies deposited in the inner and outer layers of the EC as a function of the energy deposited in the PCAL (right). The production of Cherenkov light depends on the velocity of the particle, and since electrons are lighter and move faster than pions they

Cut	Limits
Event Builder PID	11
Charge	-1
HTCC N_{Phe}	$N_{\mathrm{Phe}} > 2$
Energy deposited in PCAL	$E_{\mathrm{PCAL}} > 60$ MeV
Detector Signatures	Hit in HTCC, FTOF, ECAL

Table 9.2: Summary of the cuts applied to the trigger particle to determine good scattered electron candidates.

are more likely to emit Cherenkov light and produce more photoelectrons. It is sufficient to separate electrons and pions up to the momentum threshold of 4.9 GeV by requiring that $N_{\mathrm{Phe}} > 2$.

Contrariwise to electrons, pions are minimum ionising particles that deposit a lower and constant energy shower into the EC. A clear separation between the pion signature and electron signature can be seen from the right plot in Fig. 9.2, where the cut $E_{\mathrm{PCAL}} > 60$ MeV removes a large fraction of pion trigger events. It is clear that the simulation produces a larger sample of pion triggers, thereby indicating an issue with the modelling at these higher energies. This is not an issue for the forthcoming analysis, as it is clear the first set of cuts, presented in Fig. 9.2, are effective at removing a large proportion ($> 90\%$) of the pion sample. To ensure the trigger particle is a good-quality electron, we apply additional cuts to those applied in the event builder, which are described in more detail below.

Electromagnetic Calorimeter Fiducial Cuts

Electron identification near the edges of the calorimeter can be problematic due to energy "leaks" removing some of the deposited energy. This effect is illustrated in Fig. 9.3 as the Sampling Fraction (SF) of electrons near the edge of the calorimeter (0 cm) drops. Cutting electrons which deposit their energy near the edge of the detector in the V and W coordinate plane at V $\geq$ 14 cm and W $\geq$ 14 cm. The third coordinate, U, is restricted implicitly after applying the triangular cut on the edges of the V and W coordinate, hence we do not apply any cuts on the U coordinate. The effect that restricting the V and W coordinates has on the U coordinate is presented in Fig. 9.4. Both the experimental and simulated data are shown in each figure.

Electromagnetic Calorimeter Sampling Fraction Cut

Sampling fraction cuts are applied to compliment the PCAL energy threshold cut and further remove negative pion trigger particles. The sampling fraction is given as the ratio

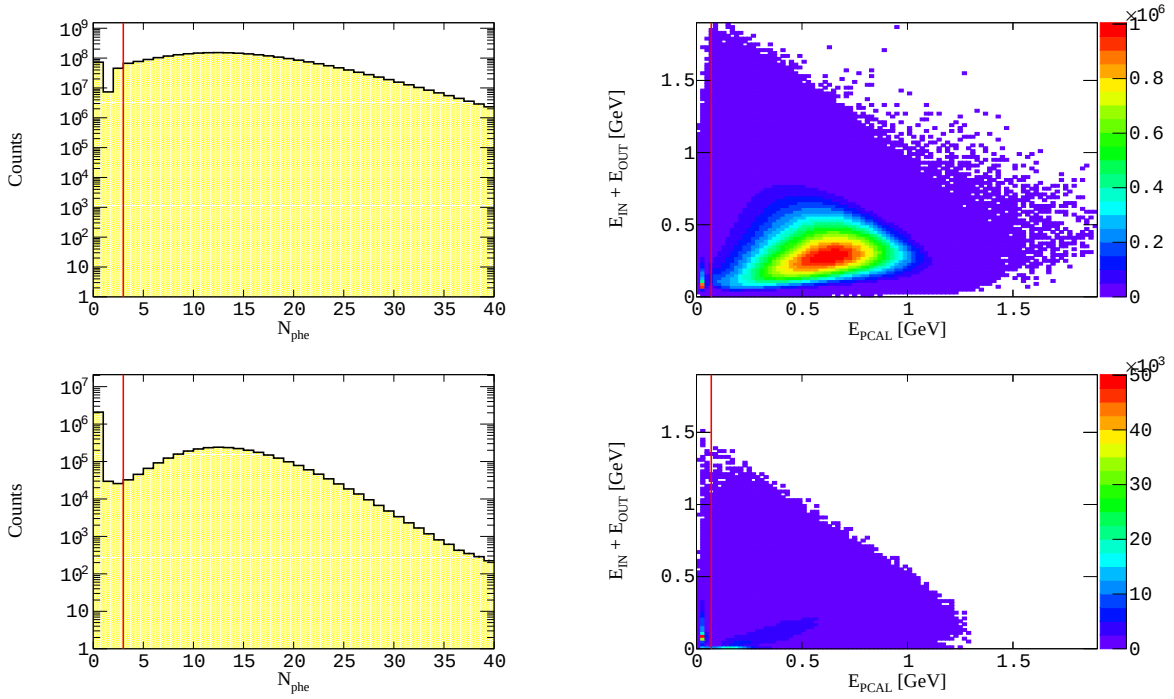

Figure 9.2: The left distribution presents the number of photoelectrons produced by the trigger particle (with a log scale applied), while the distribution on the right presents the sum of the energies deposited in the inner and outer layers of the EC as a function of the energy deposited in the PCAL. These cuts are applied when selecting a PID of 11 in the event builder. The top line presents the experimental data and the bottom line presents the simulated data for 6 GeV electron beams impinged on a ^{12}C target.

of the sum of the energy deposited in all three layers of the ECAL by a particle to the momentum of the particle, and is defined by the following equation:

$$\mathrm{SF} = \frac{E_{\mathrm{PCAL}} + E_{\mathrm{IN}} + E_{\mathrm{OUT}}}{p}, \tag{9.2}$$

where E_{PCAL}, E_{IN} and E_{OUT} are the energy deposited in the PCAL, ECIN and ECOUT, respectively, and p is the momentum of the particle. Electron candidates will produce a sampling fraction of around 0.25 which is momentum dependent. Conversely, pions deposit a constant SF that is independent of momentum. The cut applied to the SF is determined by fitting a Gaussian to a limited range of the SF (0.18, 0.28) in slices of momentum and extracting the $\mu \pm 3\sigma$. The $\mu \pm 3\sigma$ is then fitted with a polynomial of order 4, which constructs the limits of the sampling fraction cut. This procedure is done for each target and each beam energy for individual sectors as the cut is sector dependent. The cuts do not vary much between the different targets as it is largely target-independent. Figures 9.5 and 9.6 present the sampling fraction as a function of the momentum for each of the six sectors in the FD, for the experimental and simulated data, respectively, with 6 GeV electron beams impinged on ^{12}C targets. Example fits for determining the cut positions are presented in Fig. 9.7 for two separate momentum slices. The parameters of

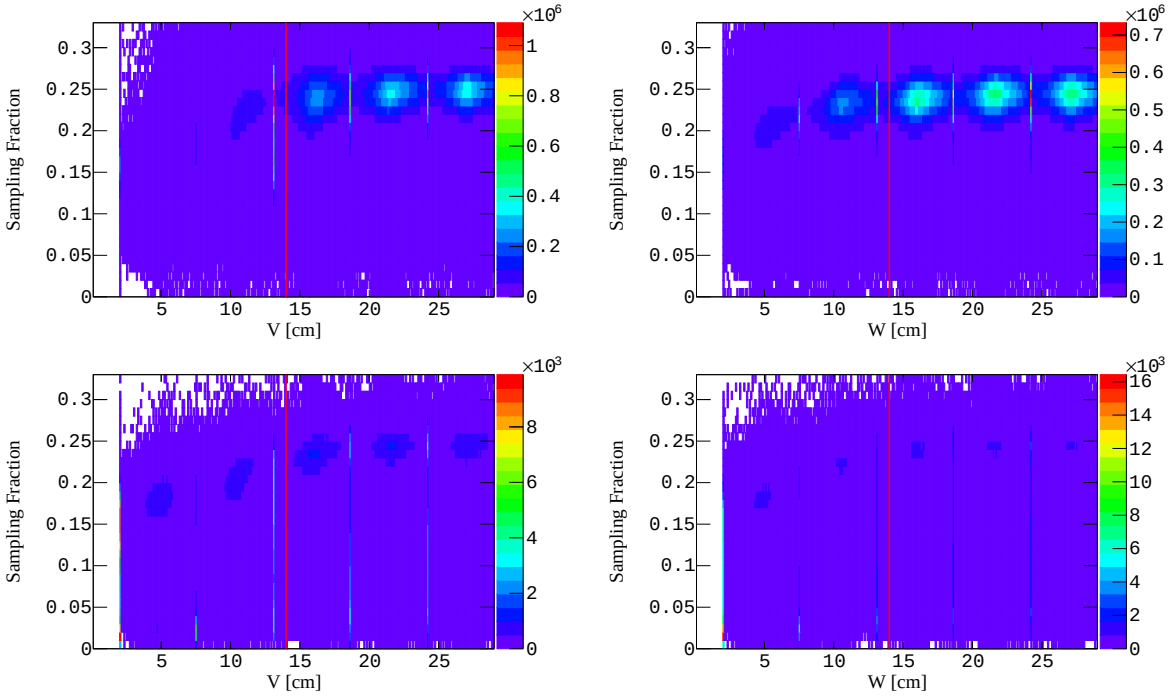

Figure 9.3: The SF as a function of the PCAL V and W coordinate distances to the edge of the detector for 6 GeV data. The red lines indicate the position of our cuts. The top distributions present the experimental data, while the bottom distributions present the simulated data.

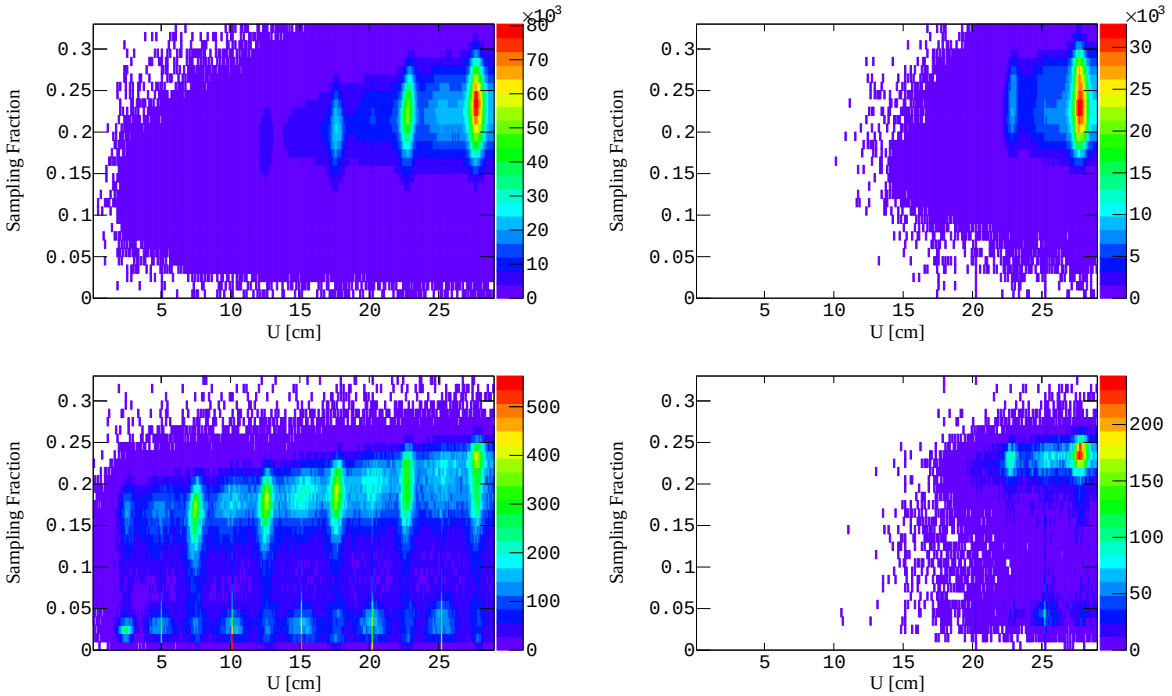

Figure 9.4: The SF as a function of the PCAL U coordinate distance to the edge of the detector before (left) and after (right) applying triangular fiducial cuts on the V and W coordinates for 6 GeV data. The top distributions present the experimental data, while the bottom distributions present the simulated data.

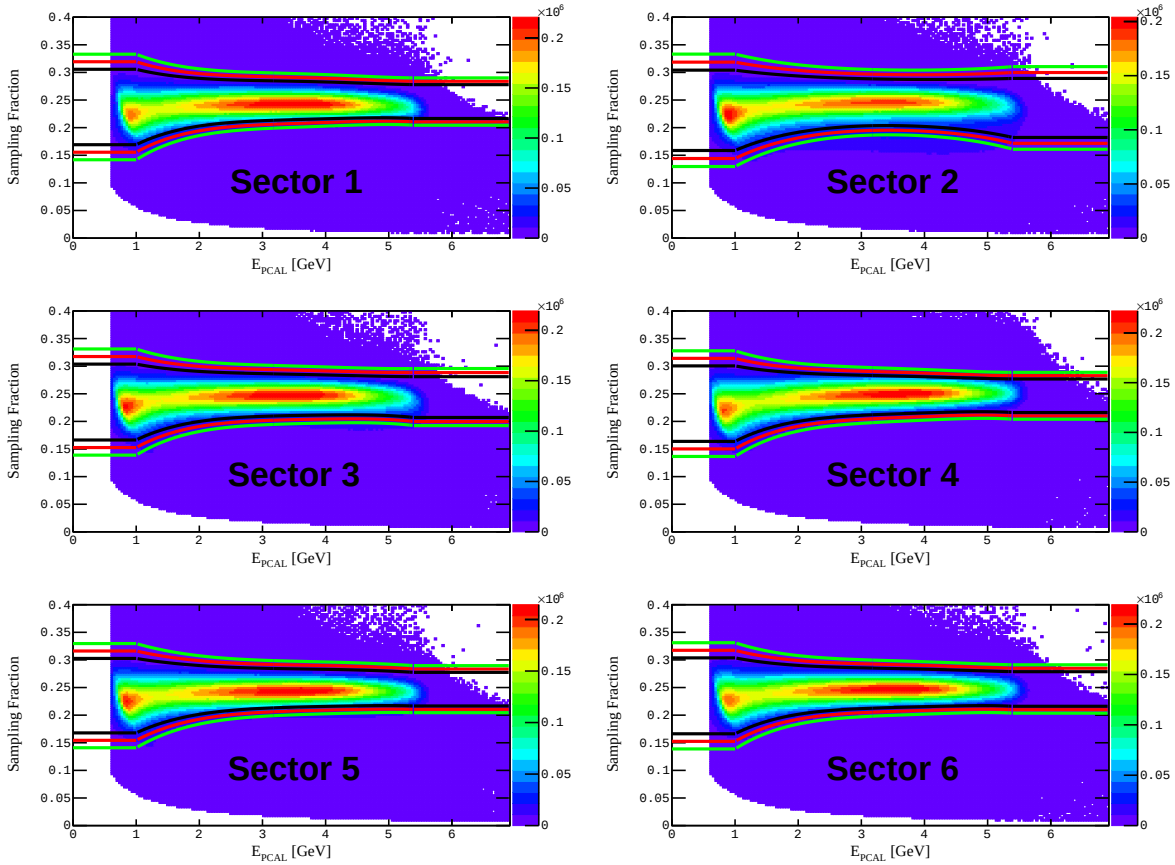

Figure 9.5: The sampling fraction as a function of momentum for all six sectors of the FD for 6 GeV electron beams impinged on a ^{12}C target.

the fits used are shown in App. B.

Electron Drift Chamber Fiducial Cuts

Effects near the edge of the DC wires can produce poor reconstruction of tracks that travel close to the edge of the DC wires. A cut is placed on the distance of the electrons to the edge of the DC wires in all three regions of the DC. χ^2/NDF provides information on the quality of the track, where lower values result in greater track reconstruction quality. The average χ^2/NDF as a function of the distance to the edge of the DC wires is presented for all three regions in Figs. 9.8 (experimental data) and 9.9 (simulated data), where the average χ^2/NDF represents the average value of the distance to the edge, in each bin. The red lines indicate the position of the cuts used for the electrons, and we require a hit in all three layers of the DC, which is commensurate with the cut employed. The cuts employed have a minimal dependence on the beam energy and a negligible dependence on the target. Therefore, for all experimental data (every beam energy setting) we cut on 4.0 cm, 3.5 cm and 9.5 cm for DC regions 1, 2 and 3, respectively. For the simulated data, we cut on 1.5 cm, 4.0 cm and 7.0 cm for DC regions 1, 2 and 3, respectively.

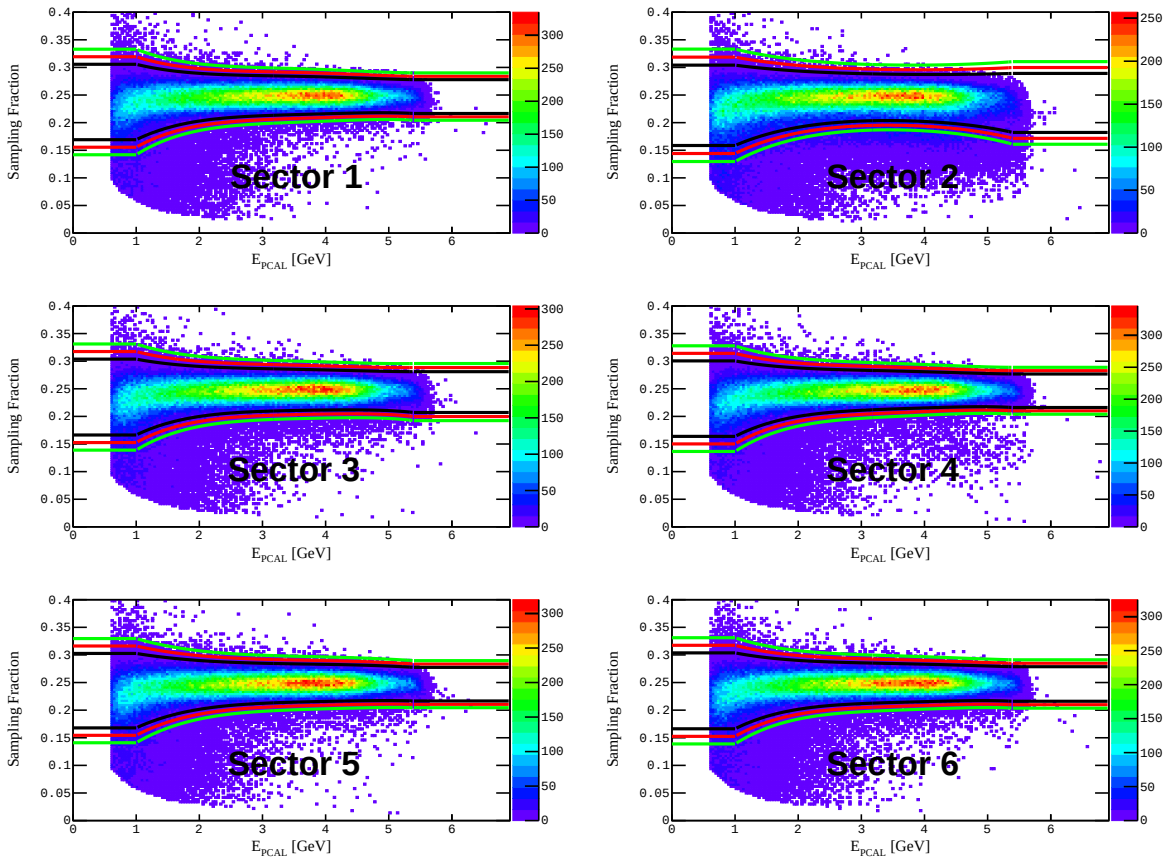

Figure 9.6: As for Fig. 9.5, but now for simulated data.

Electron Reaction Vertex

The RGM experiment utilised several different targets from single- to multi-solid foil targets, including liquid targets of varying thicknesses (see Tab. 4.2), with each target owning a unique geometry and construction. To ensure that only physical events that emerge from the target are selected, we impose cuts on the z-vertex position of the scattered electrons (shown in Tab. 9.4). Electrons which interact down the beamline with

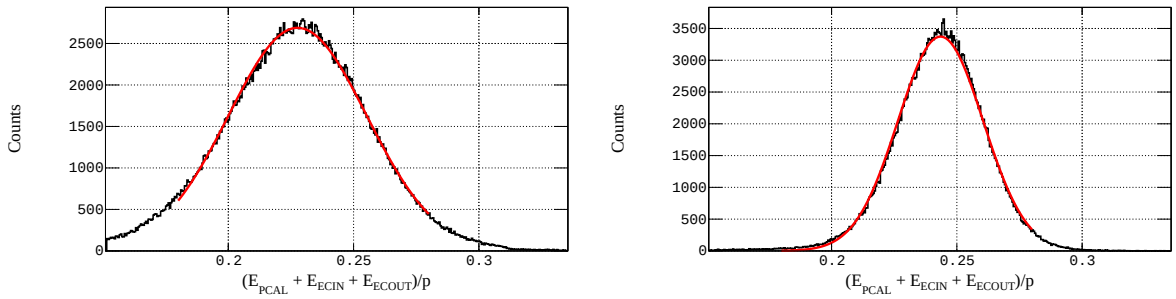

Figure 9.7: Example fits of SF for different momentum slices; $1.115 - 1.120$ GeV/c (left) and $3.455 - 3.460$ GeV/c (right). The distributions were fitted using a Gaussian function in a limited range of SF = (0.18, 0.28). The distributions are for the experimental data for 6 GeV electron beams impinged on a ^{12}C target.

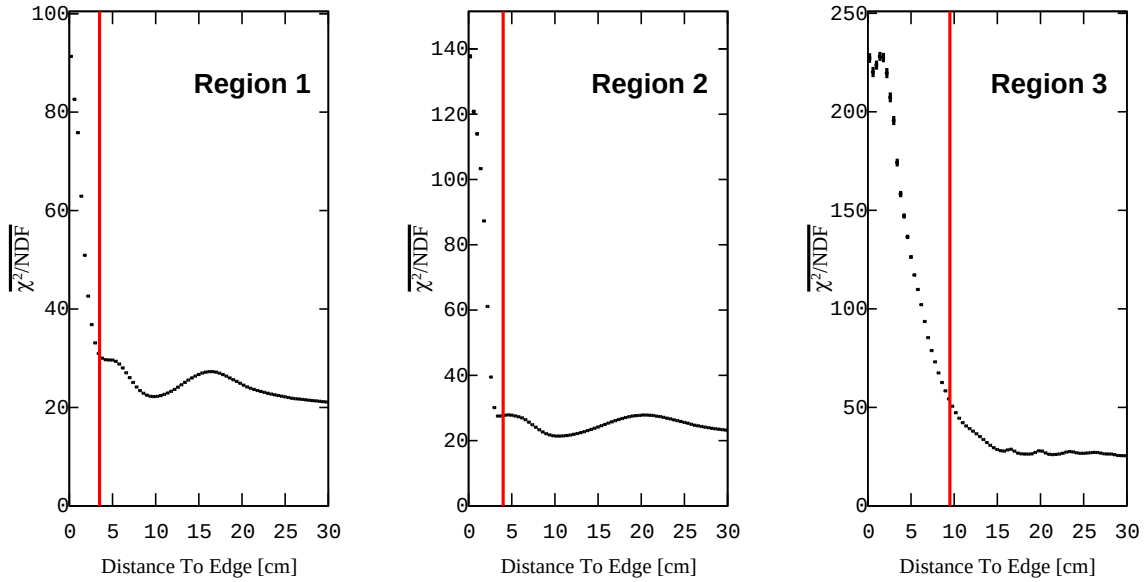

Figure 9.8: The average χ^2/NDF as a function of the distance to the edge of the DC wires for region 1 (left) region 2 (middle) and region 3 (right). The data are for 6 GeV electron beams impinged on ^{12}C targets and the red lines indicate the position of the cuts employed.

other materials can appear as features (small bumps) on the vertex distributions, which are removed with the vertex cuts. The vertex must also be accurately modelled in the GEMC simulation. The vertices in GEMC are shifted by -3 cm to align the targets with the CLAS12 reference frame (this shift is automatically applied), hence they are reconstructed to different positions (shown in Tab. 9.3) that correspond to the experimental positions.

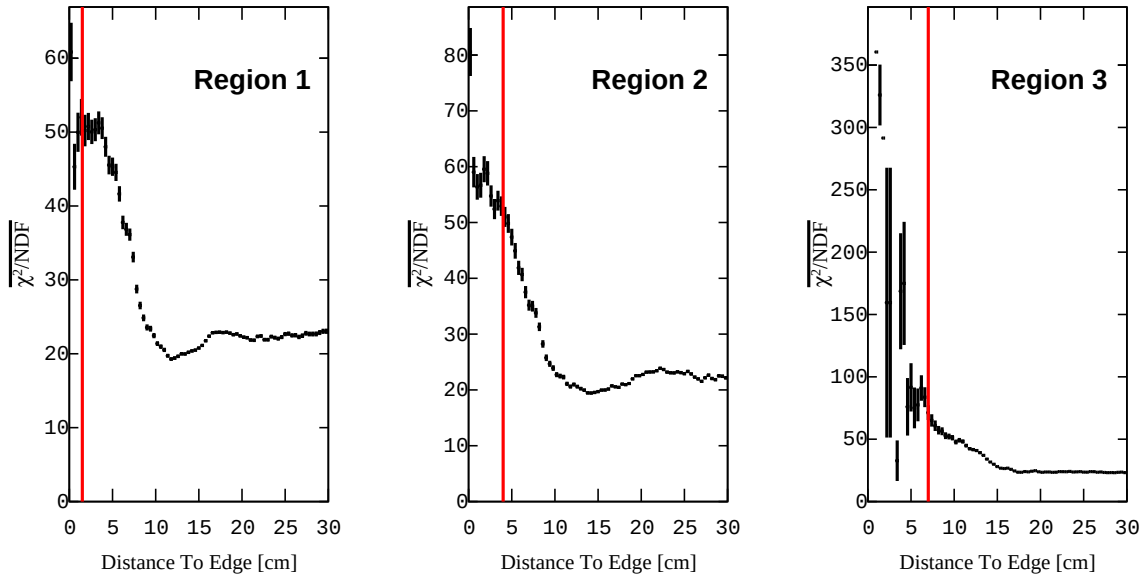

Figure 9.9: As for Fig. 9.8, but for simulated data.

Target	z-vertex cut (cm)	Notes
^{1}H, ^{2}D, ^{4}He	0	Liquid cell; vertices extend -2.5 cm to 2.5 cm
^{12}C, ^{120}Sn	-1.875, -0.625, 0.625, 1.875	4-foil targets
^{40}Ca, ^{48}Ca	0	Single target (neglecting 0.5 cm Target thickness)
^{40}Ar	-2.5	Neglecting target thickness
^{12}C, ^{120}Sn	2.5	1-foil targets

Table 9.3: Target positions and notes for the GEMC simulation.

	z-vertex cut (cm)	
Target	**Experimental Data**	**Simulated data**
^{2}D	$-7.0 < z < 2.2$	$-7.00 < z < 1.00$
^{12}C (4-foil)	$-6.6 < z < 2.6$	$-6.33 < z < 0.44$
^{12}C (1-foil)	$-3.85 < z < 0.1$	$-1.96 < z < 1.06$
^{40}Ar	$-7.29 < z < -3.03$	$-7.00 < z < -3.88$

Table 9.4: Vertex cuts applied to the experimental and simulated data for the scattered electron.

The left distribution in Fig. 9.10 shows the electron vertex distribution of the ^{12}C 4-foil target for 6 GeV electron beams, while the right distribution presents the ϕ component of the scattered electron as a function of the z-vertex for the same data. The simulated data is also shown on the bottom line. The distribution on the right, for both the experimental (top) and simulated (bottom) data, shows that the vertex does not change with ϕ, or, in other words, it shows there is little sector dependence on the reconstructed electron vertex. The electron vertex between one sector and another deviates by less than the resolution of the FD (about 0.7 cm). The 4-foils cannot be separated in the reconstructed vertex for the experimental data, due to the vertex resolution of the FD. Contrariwise, in the simulation we see clearly the 4 foils, which indicates our vertex resolution is greater in the simulated data than the experimental data. For single-foil solid targets, the z-vertex distribution is fitted with a Gaussian in a limited range (depending on thicknesses) and the vertex cuts are determined by the $\mu \pm 3\sigma$ position. The Full Width Half Maximum (FWHM) of the z-position is determined for liquid and multi-foil targets, and the vertex cuts are given by the position of the FWHM $\pm$ 3σ, where the standard deviation is that determined by the single-foil target, as it is determined purely from tracking resolution compared to the negligible target thickness. ^{40}Ar has a negligible target thickness, hence we adopt the same method employed to single foil targets for ^{40}Ar. The same method is employed for the simulated data.

The liquid ^{40}Ar target posed significant challenges for the construction of its full geometry in the GEMC simulation. The liquid cell was specially designed to house the liquid argon with different dimensions (0.5 cm thickness) to the standard 5 cm-thick liquid target cells used in other experiments and for the ^{1}H, ^{2}D and ^{4}He targets in RGM. The liquid argon target was treated as a solid single-foil target (given its negligible target thickness in

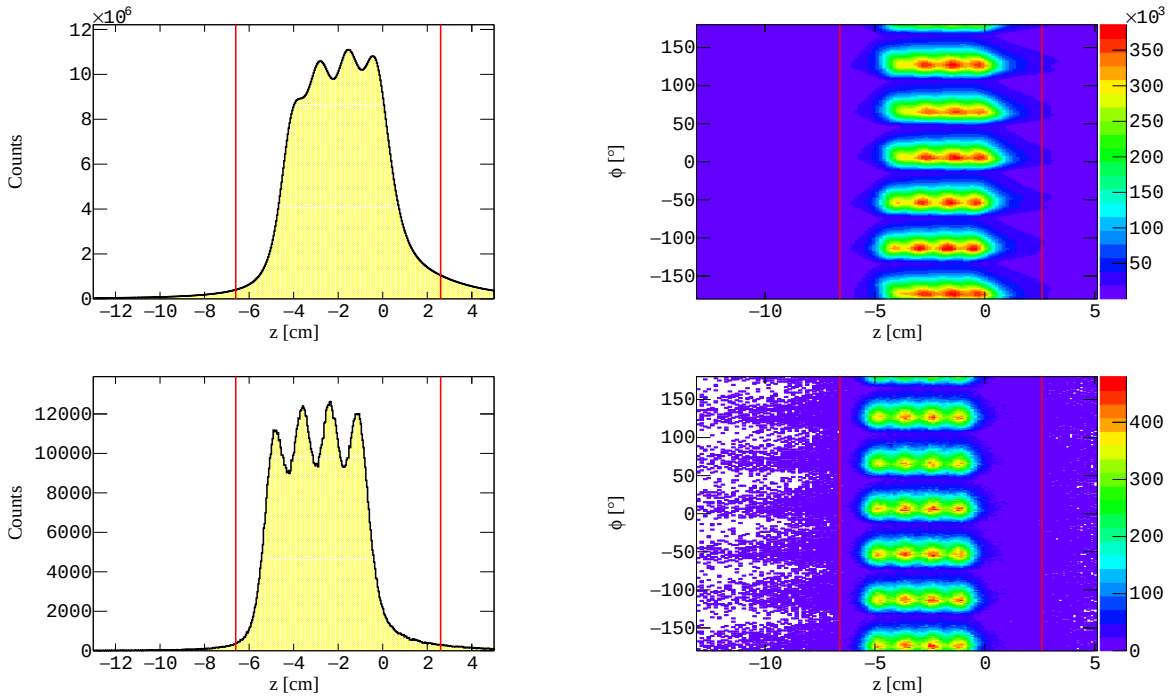

Figure 9.10: The reconstructed z-vertex (left) for scattered electrons with initial energy of 6 GeV impinged on ^{12}C 4-foil targets. The red lines indicate the position of the cuts employed. The right distribution presents the ϕ component of the scattered electron as a function of the z-vertex, showing little sector dependence on the vertex reconstruction. The top line presents the experimental data, while the bottom line presents the simulated data.

comparison to the detector resolution) that was placed further downstream to the position of the liquid target cell (centred at -5.5 cm) during the experiment. It was especially important to place the liquid argon target cell in its nominal position as targets situated at different positions will have different angular and momentum acceptances. The energy loss corrections for this target will be different between the GEMC and RGM data, though this will mostly affect particles at or near the threshold, meaning that the simulation will provide a reasonable reproduction of the argon target. Systematic uncertainties related to the use of a solid target over the liquid-cell target will be estimated. This approach was used as full GEMC implementation of the Argon target is not currently available from the CLAS collaboration.

The electron $x - y$ vertex distribution is presented in Fig. 9.11 for the experimental (left) and simulated (right) data, which shows the distribution is dominated by detector resolution. This is expected since the beam spot (the position the beam hits the target) was a few hundred μm and was well monitored to maintain a constant position, even when changing targets and beam energies. The 6-sector structure of the FD is clearly visible in both data sets. No cuts are applied to the $x - y$ distribution in this analysis.

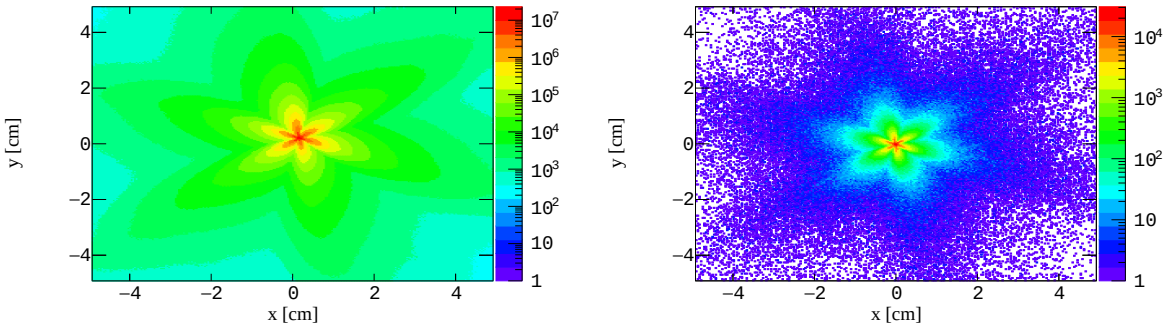

Figure 9.11: The reconstructed y-vertex as a function of the reconstructed x-vertex for scattered electrons with initial energy of 6 GeV impinged on ^{12}C 4-foil targets. The distributions are for experimental (left) and simulated (right) data.

9.2.3 Hadron Identification - Forward Detector

The FD requires a rather simple particle identification criteria as particle identification in the FD detector is very good. This is consistent with its distance from the target (providing good time of flight resolution) and the size of the detector, allowing for a good separation of charged particle species. The FD is capable of reliably detecting protons, pions and kaons of both charges (though due to acceptance negative kaons have extremely low statistics for 2 GeV data) in the momentum ranges appropriate for the RGM data. The cuts imposed are presented below. Particles detected in the FD should have a status = (2000, 3999), hence this requirement is imposed to determine FD particles.

Drift Chamber Fiducial Cuts

The DC fiducial cuts imposed on the scattered electrons are also imposed on all charged tracks in the FD. We require that each charged track registers a hit in all three regions of the DC and that the tracks do not sway too close to the edge of the wires. Figure 9.12 present the average χ^2/NDF as a function of the distance to the edge of the DC in all three regions for both positive (top) and negative (bottom) hadrons. Similarly to the electron case, the cut has little to no dependence on the target, beam energy and hadron species. The cuts imposed for the experimental data are 4.0 cm, 3.5 cm and 7.5 cm for DC regions 1, 2 and 3, respectively. For the simulated data the cuts applied to DC regions 1, 2 and 3 are 2.5 cm, 1.5 cm and 3.5 cm, respectively.

Particle Identification Cuts

As previously mentioned, the particle identification in the FD is excellent for particles with momenta from $0.4 - 4$ GeV/c. The left distribution in Fig. 9.14 presents the velocity as a function of the momentum for positively charged pions, kaons and protons after selecting their respective particle identification numbers (e.g. 2212 for protons) in the event builder, and the right distribution presents the same variables after cutting on the

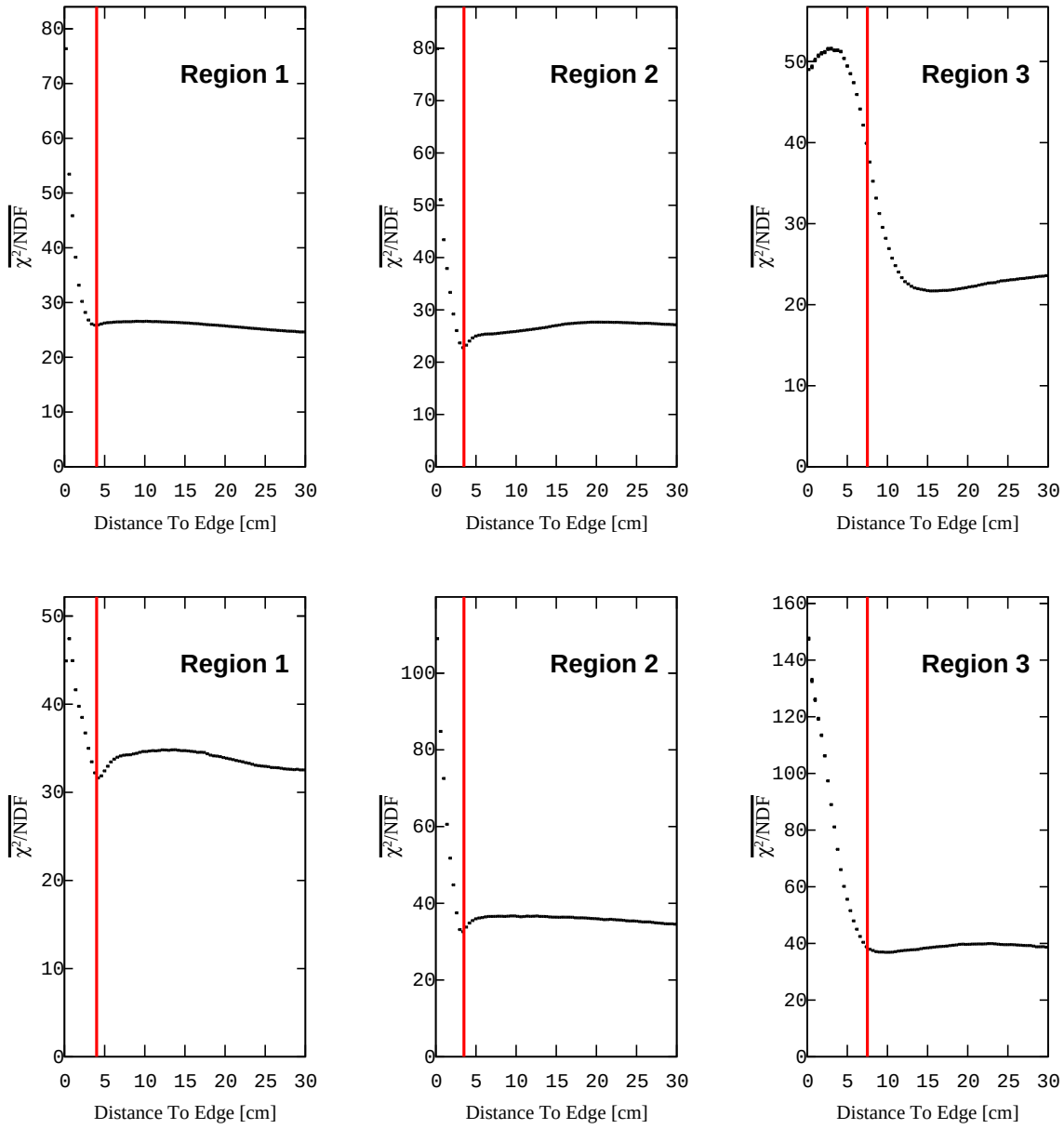

Figure 9.12: The average χ^2/NDF as a function of the distance to the edge of the DC wires for region 1 (left) region 2 (middle) and region 3 (right). The data are for 6 GeV electron beams impinged on ^{12}C targets and the red lines indicate the position of the cuts employed. The top distributions are for positive hadrons, while the bottom distributions are for negative hadrons.

$\mu \pm 3\sigma$ of a Gaussian fit to the χ^2 distribution of the particles. The χ^2 distribution provides the quality of the fit of a track, i.e. it determines how confident we are the particle species assigned to the track is the true particle species. The χ^2 distribution for protons is presented in Fig. 9.15, where the red lines indicate the position of the cuts applied to the particle. The two distributions illustrate that the simple cuts imposed are effective at removing badly reconstructed particles in the FD. The distribution for the simulated data is also presented.

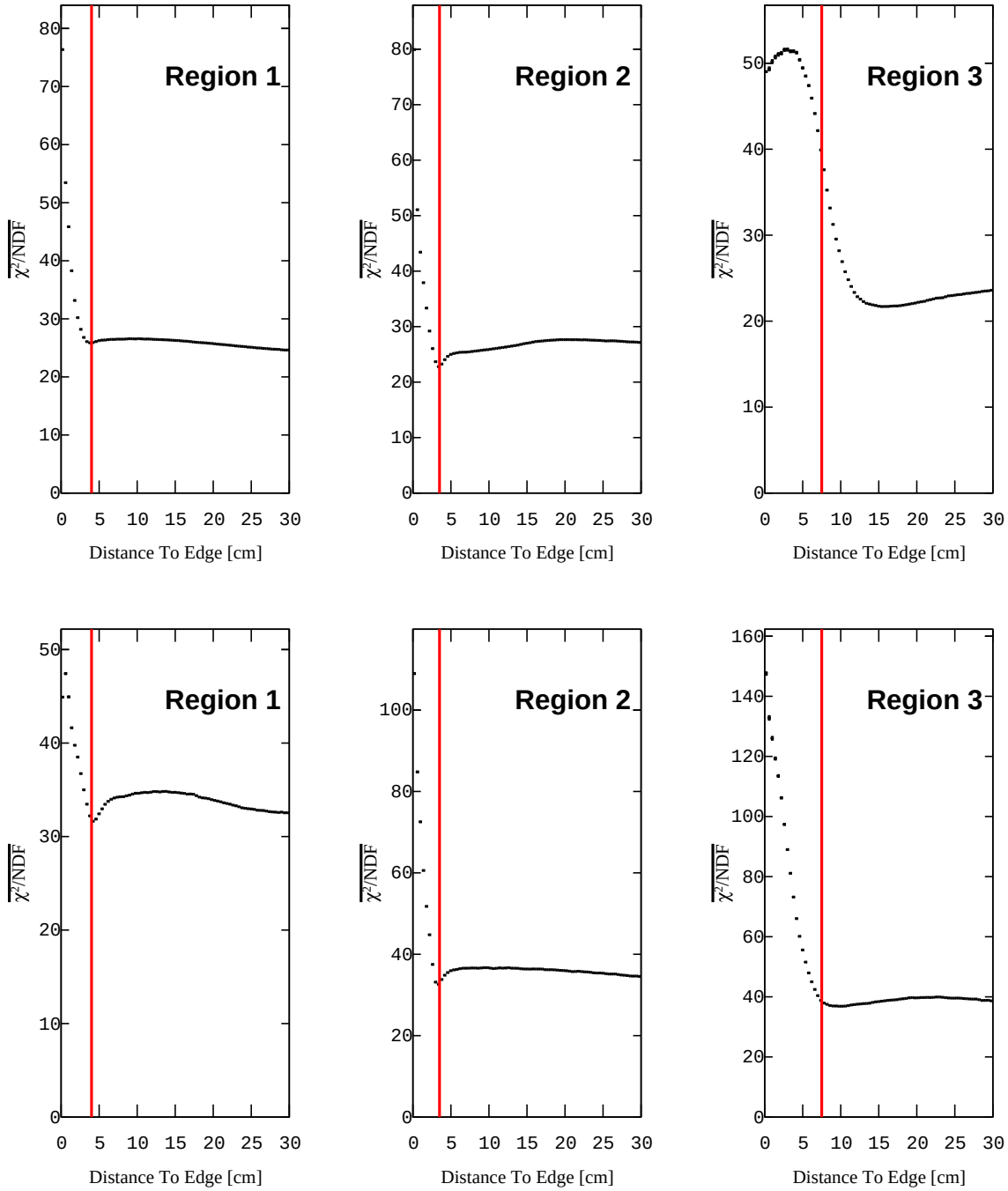

Figure 9.13: As for Fig. 9.12, but now for the simulated data.

Reaction Vertex

The vertex position of the hadrons must also be restricted since the vertex resolution for hadrons is different from the scattered electron. There is also a small dependence on the central position and width of the reconstructed z-vertex depending on the charge of the hadrons. Therefore, we apply separate z-vertex cuts to the charges of the hadrons detected in the FD. The method for determining the position of the cuts is identical to that used for the scattered electron vertex. Figure 9.16 presents the reconstructed z-vertex for both

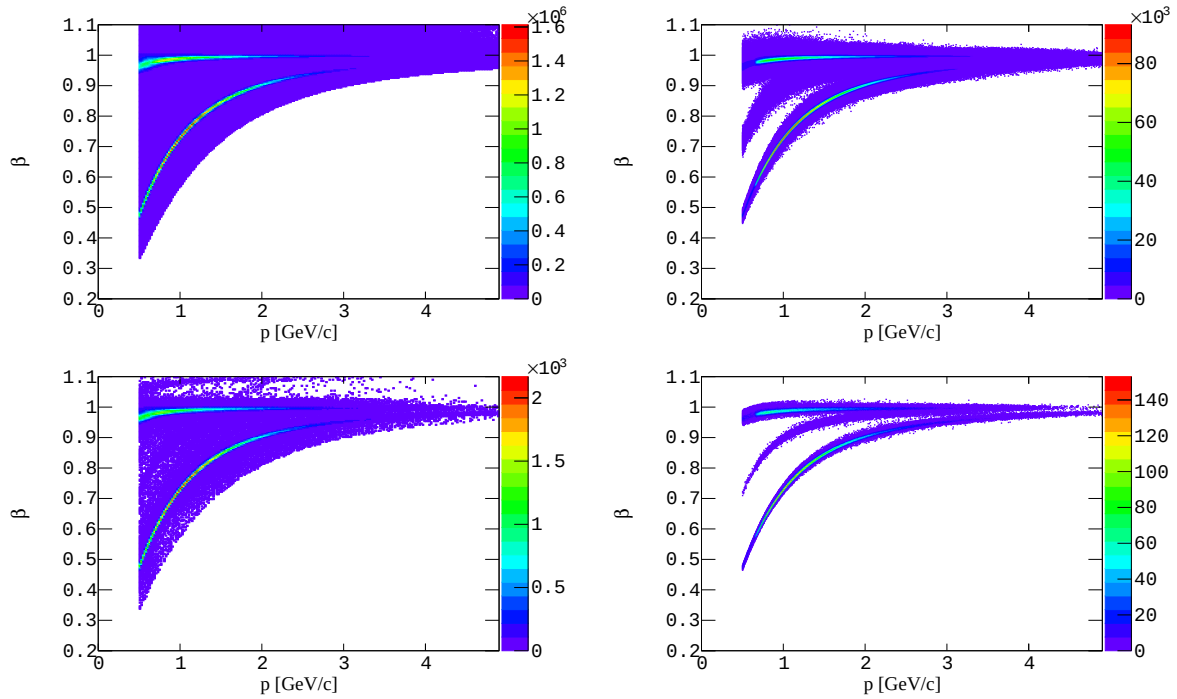

Figure 9.14: The velocity of positively charged tracks as a function of their momentum before (left) and after (right) χ^2 PID cuts. The data are for 6 GeV electron beams impinged on ^{12}C targets. The top distributions are for the experimental data and the bottom distributions are for the simulated data.

positively (left) and negatively (right) charged hadrons in the FD. The distributions for the simulated data are also shown.

Additional cuts are placed on the vertex distance between the scattered electron and the charged hadrons, Δz, which also has charge dependence. Figure 9.17 presents the Δz distribution between the scattered electron and positively (left) and negatively (right) charged hadrons. The red lines indicate the positions of the cuts imposed on the Δz distribution, which are determined from the $\mu \pm 3\sigma$ position of a fitted Gaussian. The Δz distributions for the simulated data are also presented.

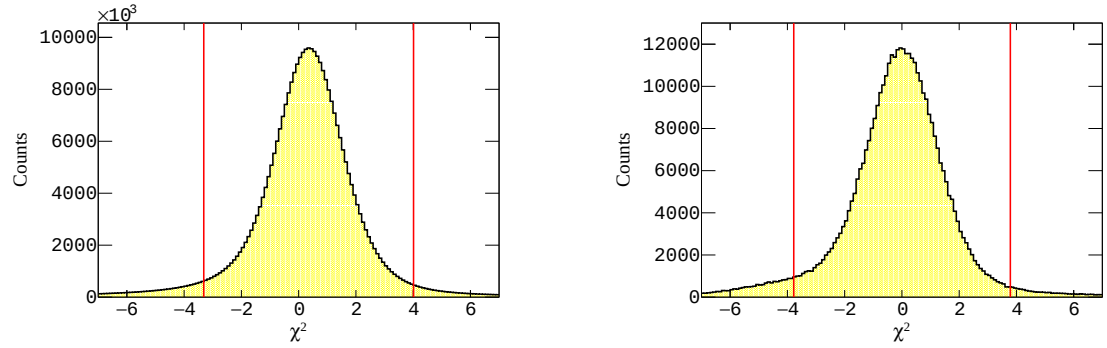

Figure 9.15: The χ^2 PID fit of protons for the experimental (left) and simulated (right) data, with 6 GeV electron beams impinged on ^{12}C targets. The red lines indicate the position of the cuts employed.

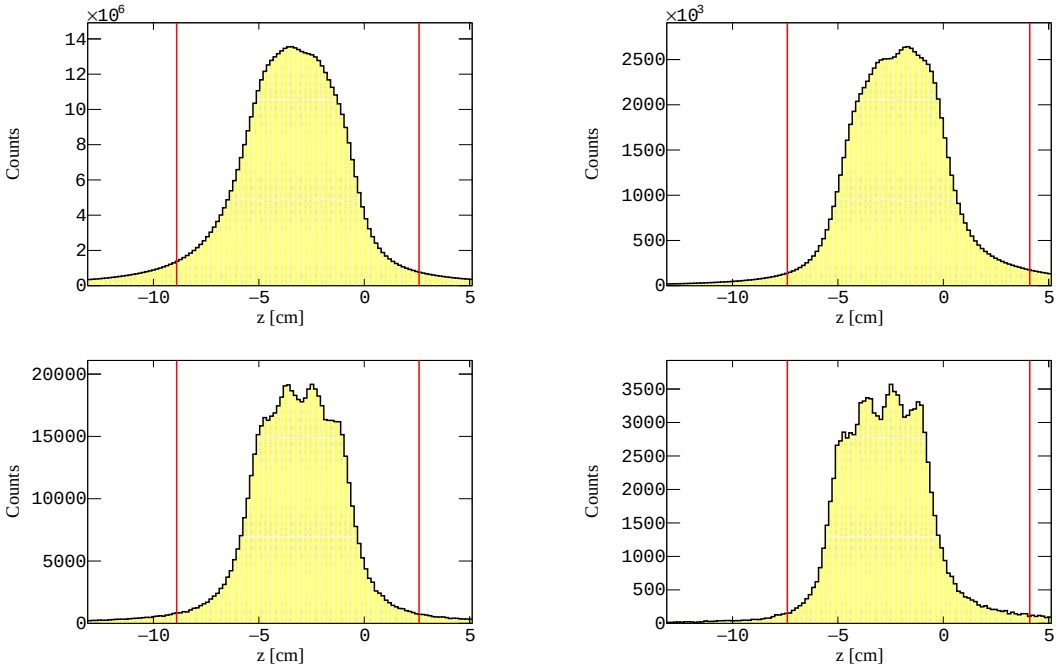

Figure 9.16: The reconstructed z-vertex for positively (left) and negatively (right) charged hadrons in the FD for 6 GeV electron beams impinged on ^{12}C 4-foil target. The red lines indicate the position of the cuts employed. The top two distributions are for the experimental data, while the bottom two distributions are for the simulated data.

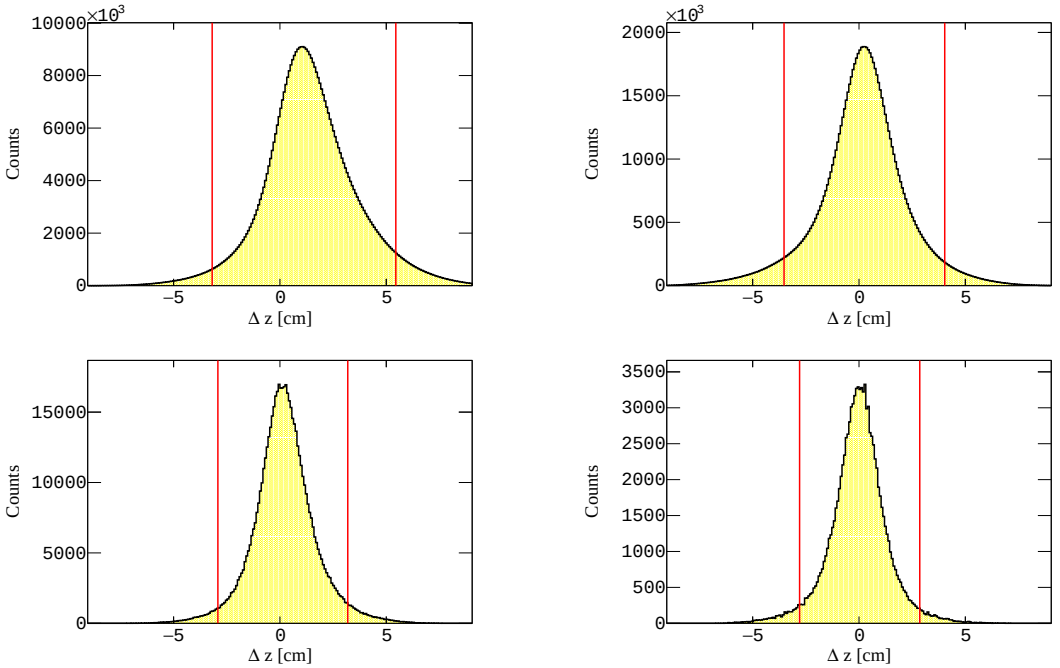

Figure 9.17: The difference between the reconstructed z-vertex of the scattered electron and positively (left) and negatively (right) charged hadrons in the FD for electron beams with energy 6 GeV impinged on ^{12}C 4-foil targets. The red lines indicate the position of the cuts employed. The top two distributions are for the experimental data, while the bottom two distributions are for the simulated data.

9.2.4 Hadron Identification - Central Detector

The central detector provides a significantly worse resolution for detecting particle time-of-flight due to the distance of the detector from the target position, although the CD does provide excellent vertex position resolution. The cuts applied to the hadrons detected in the CD are presented in this subsection.

Micromegas Vertex Tracker Fiducial Cuts

As we have previously discussed, the CD is composed of multiple layers including the Silicon Vertex Tracker (SVT), which has 6 layers and 3 regions. There are physical gaps between the regions and tracking near the edges of these physical gaps is poor. The hit information is saved for the first and last layer of the Micromegas Vertex Tracker (MVT), for which we remove any particles that have a hit < 0.5 cm from the edge of either layer. This cut is imposed because the size of the MVT clusters is $0.25 - 0.5$ cm. The distance to the edge of the first (left) and last (right) layer of the MVT is shown in Fig. 9.18

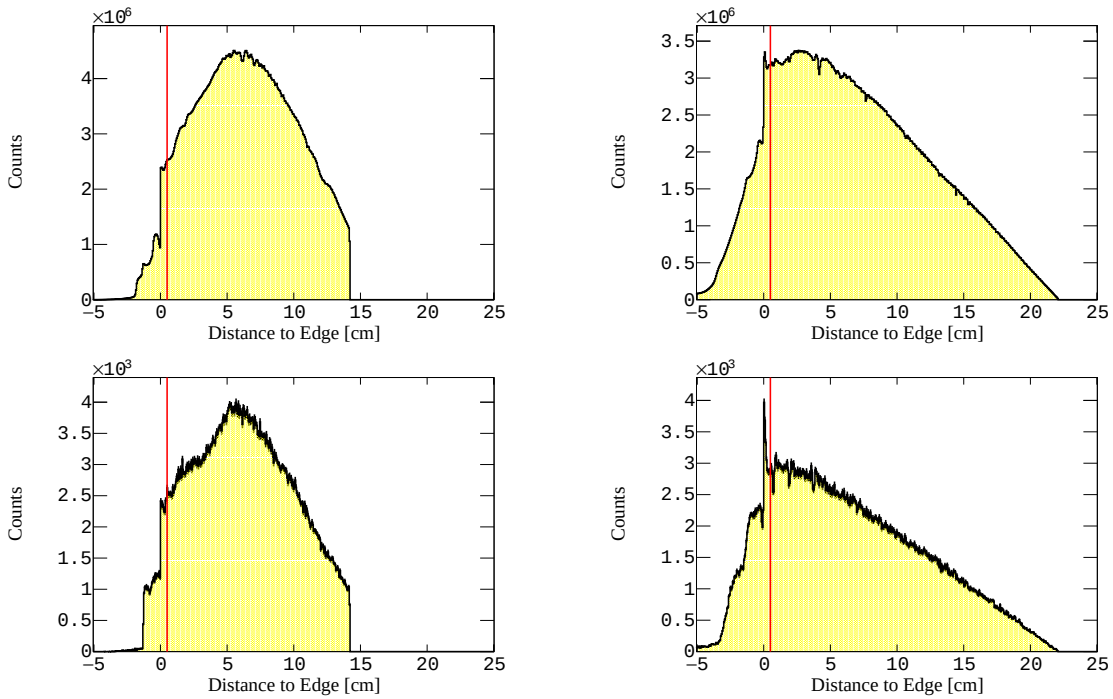

Figure 9.18: The distance to the edge of the first (left) and last (right) layer of the MVT for all charged hadrons with 6 GeV electron beams impinged on a ^{12}C 4-foil target. The red lines indicate the position of the cuts employed. The top line presents the experimental data and the bottom line presents the simulated data.

The hit information of the particles can also be used to determine the azimuthal component, ϕ (in cylindrical coordinates), of the particles at the first and last layer of the MVT. The ϕ component determines which sector the particles are in. If the ϕ component of the particle corresponds to two different sectors, the particle is removed from further analysis as particles cannot cross the physical gaps between the three sectors in the CD and be

reliably tracked and reconstructed. The effect of applying these two MVT restrictions on the ϕ component of reconstructed particles in the CD is illustrated in Fig. 9.19. The figure presents the transverse momentum component, $p_\perp$, of protons as a function of their ϕ component. As for the FD, the ϕ component resembles the different sectors of the CD. Three clear gaps, resembling the physical barriers between the three sectors of the CD, can be seen.

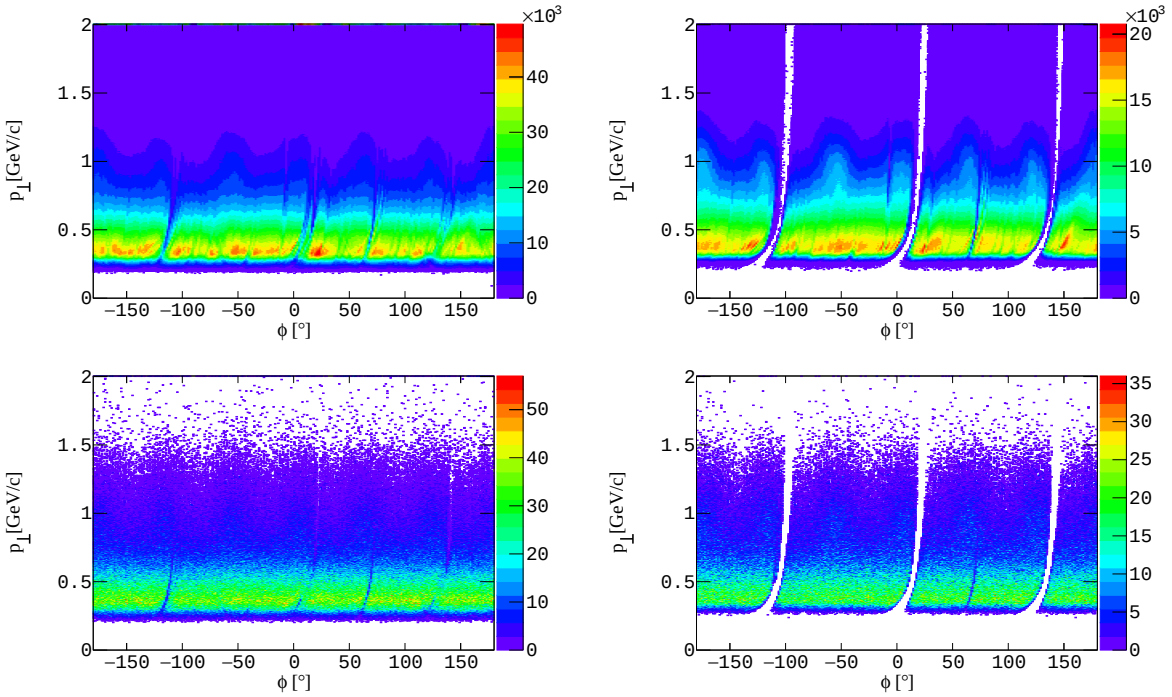

Figure 9.19: The transverse momentum of protons in the CD as a function of their ϕ component before (left) and after (right) applying the MVT restrictions for 6 GeV electron beams impinged on ^{12}C 4-foil targets. The red lines indicate the position of the cuts employed. The top line corresponds to the experimental data, while the bottom line corresponds to the simulated data.

Time-of-Flight Cuts

The distance of the CD from the target position is significantly shorter than the FD, which hinders our charged particle identification. Kaons cannot be detected in the CD, the resolution is too poor. Protons and pions will be determined through the time-of-flight cuts, Δ_{TOF}, which are defined by Eq. (6.13). The difference in the expected time-of-flight and the measured time-of-flight for a proton is shown in the left distribution in Fig. 9.20 for all positively charged tracks. The red lines indicate the nominal position of the cuts which are determined by fitting a polynomial (of order 4) to the $\mu \pm 3\sigma$ of a Gaussian fitted in a limited range of Δ_{TOF} (-0.2, 0.2) ns in slices of momentum. The black and green lines present the tighter ($\mu \pm 2.5\sigma$) and looser ($\mu \pm 3.5\sigma$) positions, respectively. The systematic uncertainty associated with each Δ_{TOF} cut is determined by varying the cut position between the three lines. Δ_{TOF} is mostly momentum-independent and deteriorates

near the momentum threshold. The middle distribution in Fig. 9.20 presents the same distribution but for the expected Δ_{TOF} of positive pions for positive tracks that do not survive the proton cuts. Positive tracks that do not survive the proton or π^+ cuts are not assigned a PID and are removed from further analysis. The right distribution in the same figure presents the expected Δ_{TOF} for negatively charged pions for all negative tracks. Any negative tracks that do not survive the π^- cuts are removed from further analysis. The Δ_{TOF} distributions for the simulated data are also presented in Fig. 9.20.

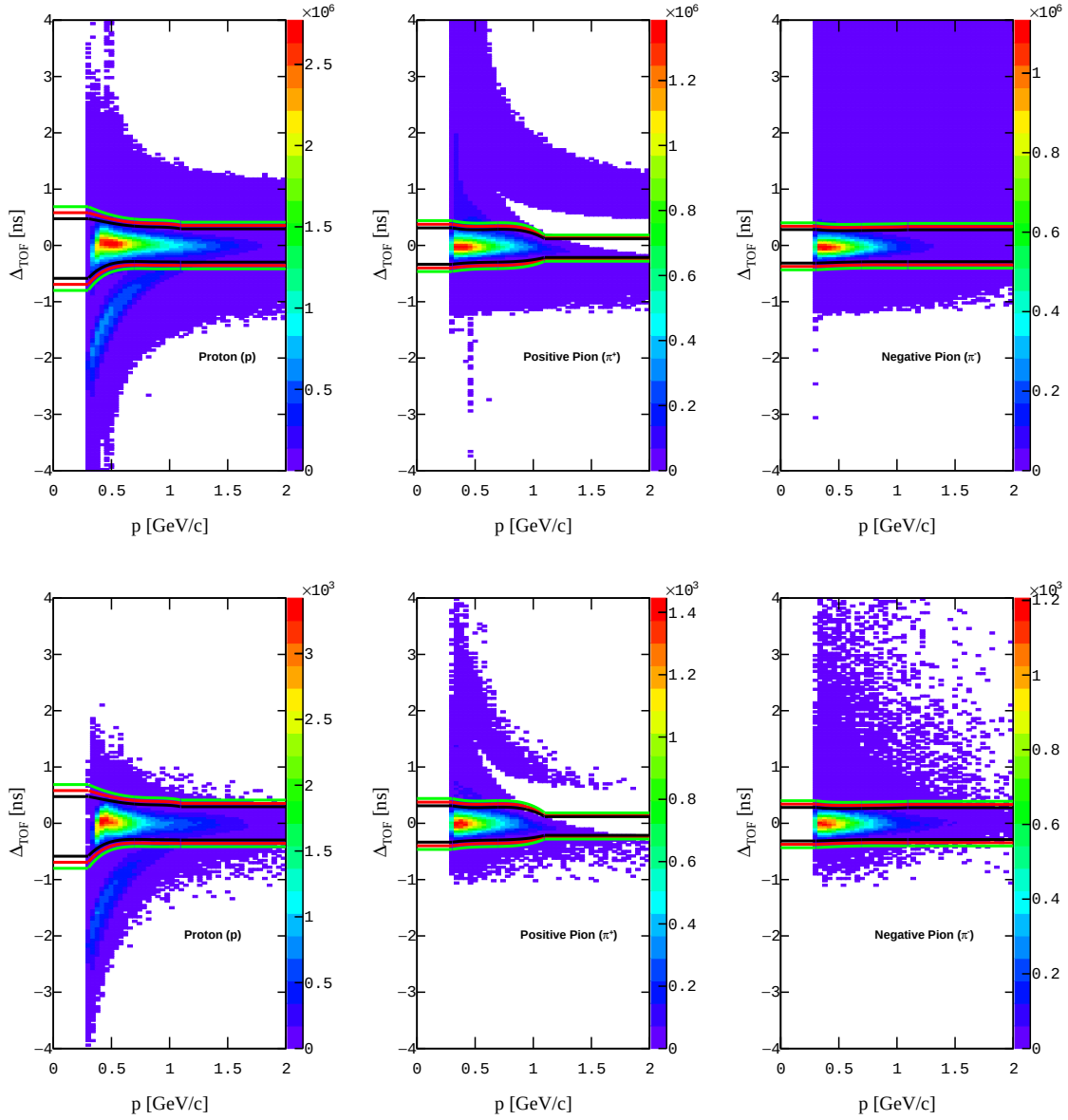

Figure 9.20: The expected Δ_{TOF} for protons (left) for all positively charged tracks in the CD and for positive pions (middle) for all positive tracks that do not survive the proton cuts. The right distribution presents the expected Δ_{TOF} for negative pions for all negatively charged tracks. The red lines indicate the position of the cuts. The cuts are determined by fitting a polynomial to the $\mu \pm 3\sigma$ of a Gaussian fitted in a limited range of Δ_{TOF} in slices of momentum. The experimental data is presented in the top line and the simulated data is presented in the bottom line.

Reaction Vertex

Similarly to the FD particles, we need to cut on the vertex position of particles in the CD. The resolution of the CD is excellent, even distinguishing the individual foils in multi-foil target configurations. Likewise to the FD, we apply separate z-vertex cuts to the charges of the hadrons detected in the CD. The method for determining the position of the cuts is identical to that used for the electron vertex. Figure 9.21 presents the reconstructed z-vertex for both positively (left) and negatively (right) charged hadrons in the CD.

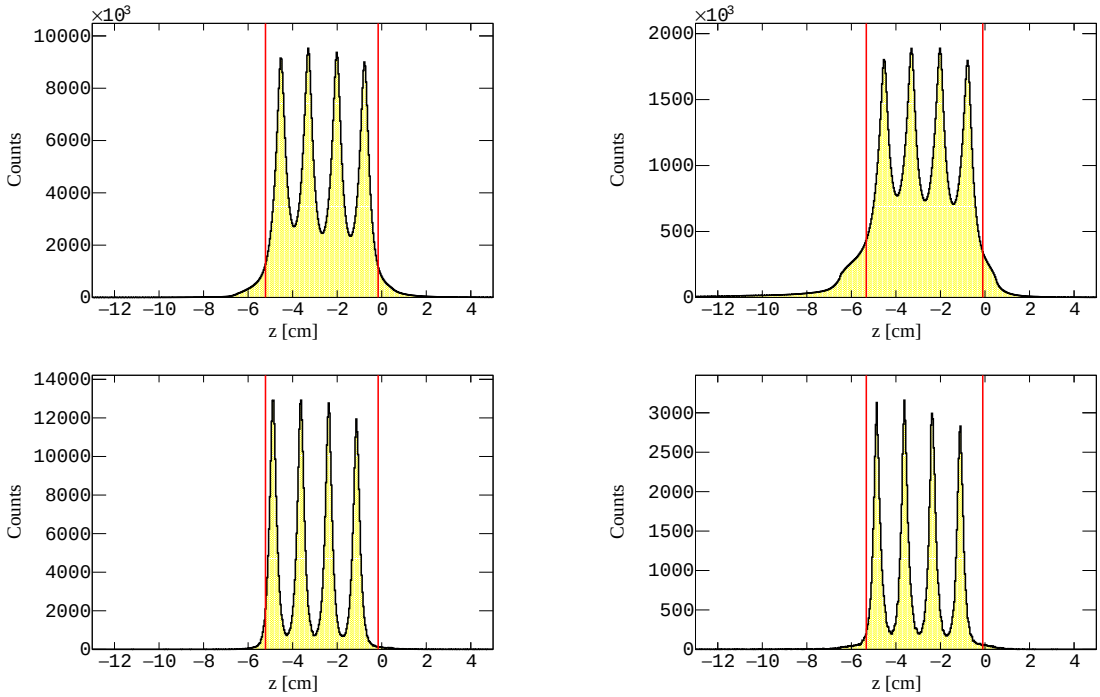

Figure 9.21: The reconstructed z-vertex for positively (left) and negatively (right) charged hadrons in the CD for electron beams with energy 6 GeV impinged on ^{12}C 4-foil targets. The red lines indicate the position of the cuts employed. The top line presents the experimental data, while the bottom line presents the simulated data.

Cuts are also placed on the Δz distribution between the scattered electron and charged hadrons in the CD, which also has charge dependence. Figure 9.22 presents the Δz distribution between the scattered electron and positively (left) and negatively (right) charged hadrons in the CD. The red lines indicate the positions of the cuts determined as previously described. The distributions for the simulated data are also shown.

9.2.5 Minimum Momentum Threshold

Similarly to the analysis presented in Chap. 8, below a particular value of momentum the reconstruction of particles is unreliable. The CD and FD have different momentum thresholds, given the aforementioned differences between the two detectors. Different momentum thresholds will also be applied to the scattered electron and hadrons, including different minimum momentum thresholds for the scattered electron depending on the

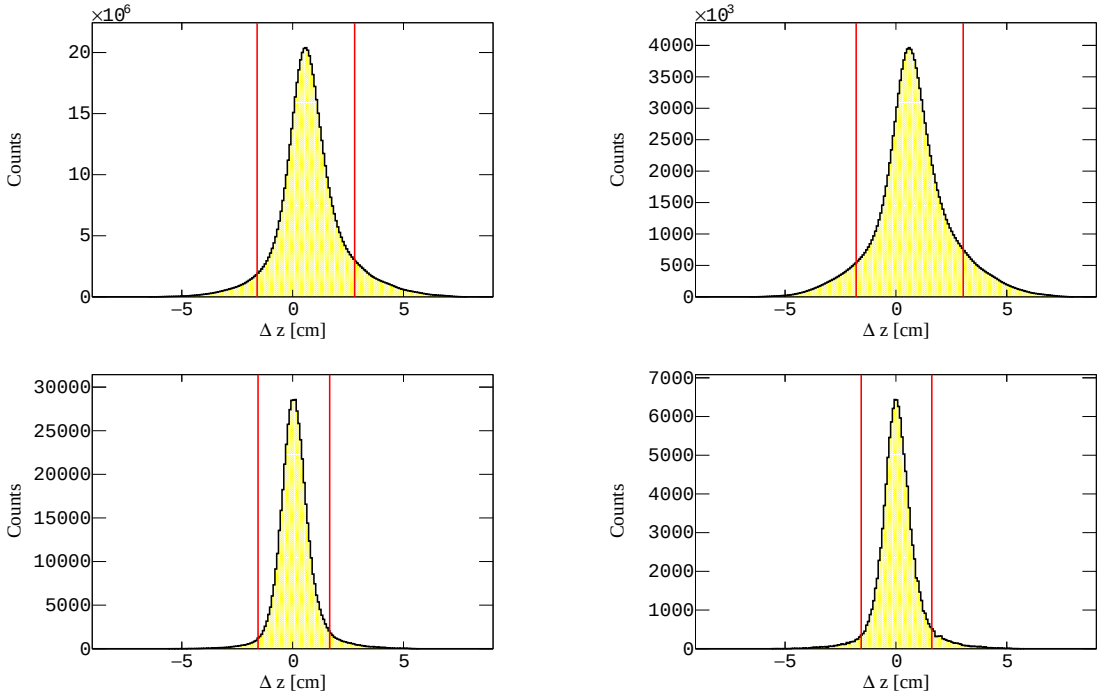

Figure 9.22: The difference between the reconstructed z-vertex of the scattered electron and positively (left) and negatively (right) charged hadrons in the CD for electron beams with energy 6 GeV impinged on ^{12}C 4-foil targets. The red lines indicate the position of the cuts employed. The top line presents the experimental data, while the bottom line presents the simulated data.

beam energy. For all hadrons in the CD, we apply a uniform 300 MeV/c cut for all electron beam energy settings. A larger uniform minimum momentum threshold of 500 MeV/c is applied to the hadrons in the FD, also independent of the beam energy setting used. These different minimum momentum thresholds are attributed to the difference in the lengths between the two detectors and the target position. If the beam energy is 2.1 GeV, then a minimum momentum threshold of 500 MeV/c is applied to the scattered electron. However, if the beam energy is larger than this (4.0 and 6.0 GeV) then a higher threshold of 600 MeV/c is employed for the scattered electron.

9.3 Cross-Section Normalisation

The crux of our analysis is to provide a comparison of experimentally observed electron scattering reactions to those predicted by two theoretical models. A common scale for the data is a one-dimensional visible cross section, $\frac{d\sigma^{\text{vis}}}{dE_{\text{Rec}}}$. Each data set has a different method for putting the data onto an absolute scale which we will discuss in the coming section.

Determining Experimental Cross-Sections

During the RGM experiment, the Faraday cup collected the total charge accumulated throughout each run period. Therefore, along with knowing the total aerial density and thickness of the targets used, we can determine the luminosity. The total time period of each run is used to determine an integrated luminosity (fb^{-1}). The integrated luminosity for each target and beam energy is provided in Tab. 4.3. The relationship between the reaction yield, the integrated luminosity and the cross-section is given by:

$$N = \sigma \times \int Ldt, \tag{9.3}$$

where N is the reaction yield, σ is the reaction cross section and $\int Ldt$ is the integrated luminosity. Therefore, the ratio of the reaction yield to the integrated luminosity provides the reaction cross-section in fb.

Determining GiBUU Cross-Sections

GiBUU provides a weight on an event-by-event basis. The weight is the cross-section per nucleon of the reaction generated. To determine the total reaction cross-section in GiBUU, we must follow the procedure in Sec. 3.1. We must sum over all weights (not just the pure number of events measured) and multiply this weight by the nucleon mass, A, to obtain the total reaction cross-section for the target nucleus rather than the cross-section per nucleon, using Eq. (3.5). The units of each weight is 10^{-33} cm^2 for electrons.

Determining GENIE Cross-Sections

The GENIE model generates events without a weight and provides a total cross-section of all reactions for the primary electron beam energy of interest. This is illustrated in Fig. 3.3. After determining the total cross-section for the beam energy used, we can determine the reaction cross-section in GENIE using Eq. (3.6). The units of σ_{tot} for GENIE is typically expressed in μb (10^{-30} cm^2).

With the methodology presented in this section, the data and all simulated distribution samples are put on an absolute cross-section scale where direct comparisons of the re-

constructed electron beam energy and missing mass can be made. We present the final results as one-dimensional cross-sections, as presented in the recent publication [27].

9.4 Kinematic Observables for e4ν Analysis

Neutrino oscillation experiments, including but not limited to DUNE, do not know the individual incident neutrino beam energy for each reaction. Although when measuring electron-nucleus reactions this information is available - for compatibility with neutrino analysis methods we cannot use this measured observable in the analysis. The observables used in the data analysis are described below, all relying only on the target nucleus and the final state particles.

9.4.1 Particle Multiplicity

The charged particle detection in CLAS12 is excellent, therefore we impose strict conditions on the multiplicities of charged particles depending on the reaction of interest. For example, if we are studying $A(e, e'p\pi^+\pi^-)X$ reactions then we would impose that $N_p = 1$, $N_{\pi^+} = 1$, $N_{\pi^-} = 1$, $N_{K^+} = 0$ and $N_{K^-} = 0$, where we discard any event with a different charged particle topology. It is important to note that, as previously stated, the kaons can only be detected in the FD, hence the condition for kaons is applied only for the FD. Neutral particles in the FD have a lower efficiency and neutrals in the CD are not well understood. For these reasons, we only include neutral selection criteria if we are studying reactions involving neutral pions, otherwise, we ignore the number of neutral particles detected in an event.

9.4.2 Missing Transverse Momentum

Since the incident electron beam (neutrino beam in oscillation experiments) travels in the z-plane, we can use the particles detected to determine the missing transverse momentum, which should be low for direct processes. The missing transverse momentum is calculated using Eq. (7.11) and Fig. 9.23 presents the $p_\perp^{\text{miss}}$ distributions for $^{12}\text{C}(e, e'p)X$, $^{12}\text{C}(e, e'p\pi^-)X$, $^{12}\text{C}(e, e'p\pi^+\pi^-)X$ and $^{12}\text{C}(e, e'pp)X$ reactions with a primary electron beam energy of 6 GeV.

It is clear from the previous distributions that restricting $p_\perp^{\text{miss}} < 0.2$ GeV/c amplifies our direct process signal and nullifies the background. Direct proton knockout processes have a slightly modified cut of $p_\perp^{\text{miss}} < \sqrt{n} \times 0.2$ GeV/c, where n is the number of protons detected, which is justified by Fig. 9.23 that shows the $p_\perp^{\text{miss}} < 0.2$ GeV/c cut is too restrictive on the statistics. To help further illustrate the power of the $p_\perp^{\text{miss}}$ cut, Fig. 9.24 presents the missing transverse momentum as a function of the reconstructed beam energy, for primary electron beams of 6 GeV, for the same four reactions presented throughout

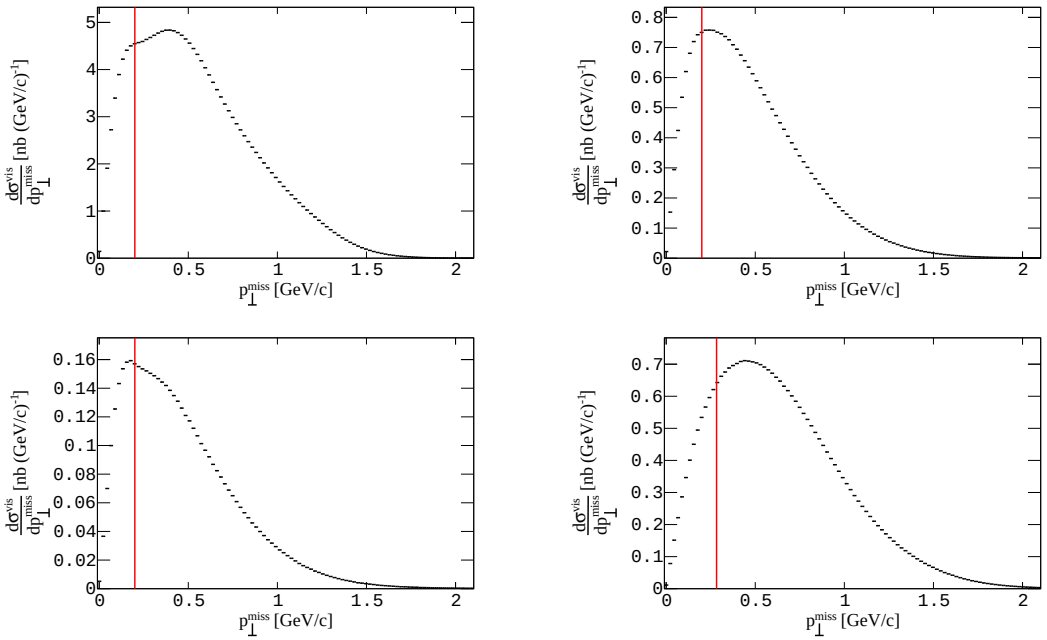

Figure 9.23: The missing transverse momentum for 6 GeV electron beams impinged on a ^{12}C target for $^{12}\mathrm{C}(e,e'p)X$ (top left), $^{12}\mathrm{C}(e,e'p\pi^-)X$ (top right), $^{12}\mathrm{C}(e,e'p\pi^+\pi^-)X$ (bottom left) and $^{12}\mathrm{C}(e,e'pp)X$ (bottom right). The red lines indicate the position of the cut imposed for the reaction.

this subsection.

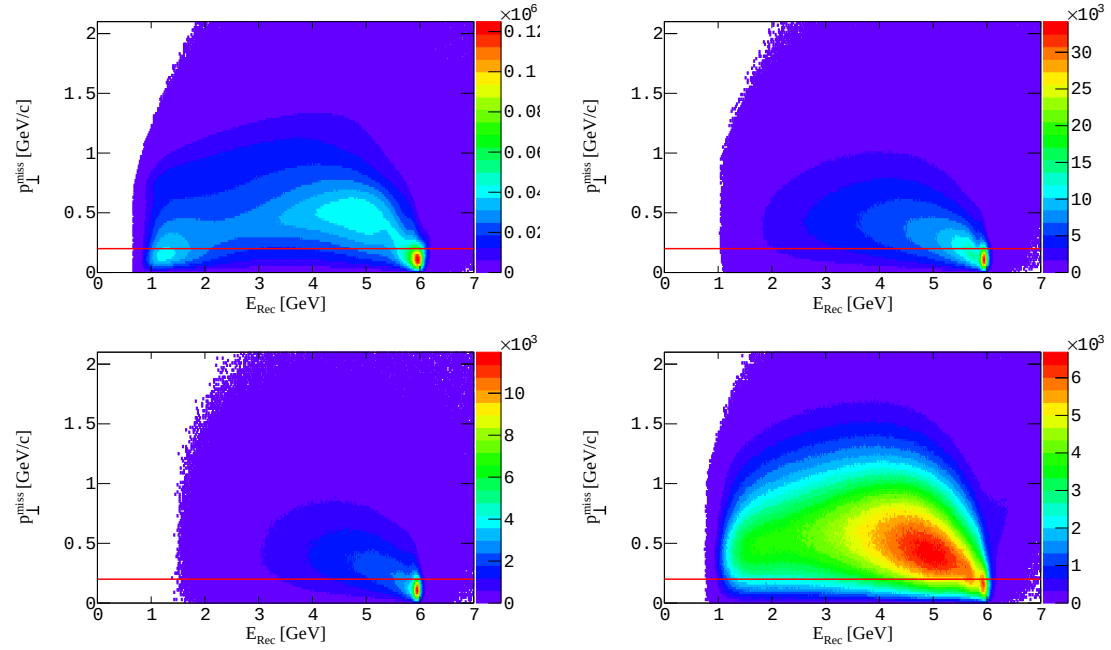

Figure 9.24: The missing transverse momentum as a function of the reconstructed electron beam energy for incident electron beams of energy 6 GeV impinged on a ^{12}C target for $^{12}\mathrm{C}(e,e'p)X$ (top left), $^{12}\mathrm{C}(e,e'p\pi^-)X$ (top right), $^{12}\mathrm{C}(e,e'p\pi^+\pi^-)X$ (bottom left) and $^{12}\mathrm{C}(e,e'pp)X$ (bottom right). The red lines indicate the position of the cut imposed for the reaction.

9.4.3 Invariant Mass Selection

The invariant mass of the product particles can be used to infer the physics processes responsible for the final state reactions observed. The invariant mass is calculated using Eq. (7.4) and the invariant mass of the $p+\pi^-$, $\pi^+ + \pi^-$, $\pi^+ + \pi^- + \pi^0$ and $K^+ + K^-$ for the reactions $^{12}\mathrm{C}(e, e'p\pi^-)X$, $^{12}\mathrm{C}(e, e'p\pi^+\pi^-)X$, $^{12}\mathrm{C}(e, e'pK^+K^-)X$ and $^{12}\mathrm{C}(e, e'p\pi^+\pi^-\pi^0)X$ is shown in Fig. 9.25 for electron beam energies of 6 GeV. In addition, Fig. 9.26 present the beam energy reconstruction as a function of the invariant mass for the aforementioned reactions. It demonstrates a strong correlation between the expected resonances and the reconstruction of the correct beam energy.

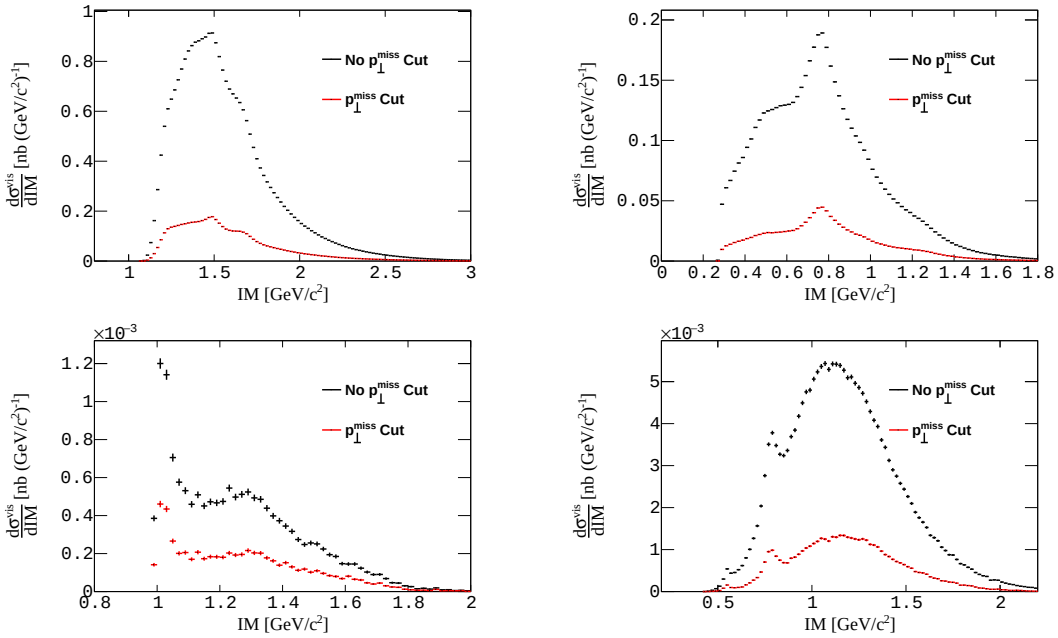

Figure 9.25: The invariant mass for 6 GeV electron beams impinged on a ^{12}C target for $p + \pi^-$, $\pi^+ + \pi^-$, $\pi^+ + \pi^- + \pi^0$ and $K^+ + K^-$ for the reactions $^{12}\mathrm{C}(e, e'p\pi^-)X$ (top left), $^{12}\mathrm{C}(e, e'p\pi^+\pi^-)X$ (top right), $^{12}\mathrm{C}(e, e'pK^+K^-)X$ (bottom left) and $^{12}\mathrm{C}(e, e'p\pi^+\pi^-\pi^0)X$ (bottom right) with (red line) and without (black line) a $p_\perp^{\mathrm{miss}}$ cut applied.

The neutral pions are reconstructed from pairs of photons that are detected in the FD. The combinatorics of photon multiplicities greater than 2 complicates the selection of neutral pions, therefore we restrict the photon multiplicity in the FD to $N_\gamma^{\mathrm{FD}} = 2$. The invariant mass of two photons detected in the FD is presented in Fig. 9.27, where the distribution is fitted with a Gaussian function in a limited range of invariant mass (0.11, 0.16) GeV/c^2 and the cuts are given by the $\mu \pm 3\sigma$ of the fitted Gaussian. The cut window represents the range of invariant mass deemed acceptable for neutral pion reconstruction. Once the neutral pion is selected it is given its nominal mass, which is the same procedure for all other particles in the event builder.

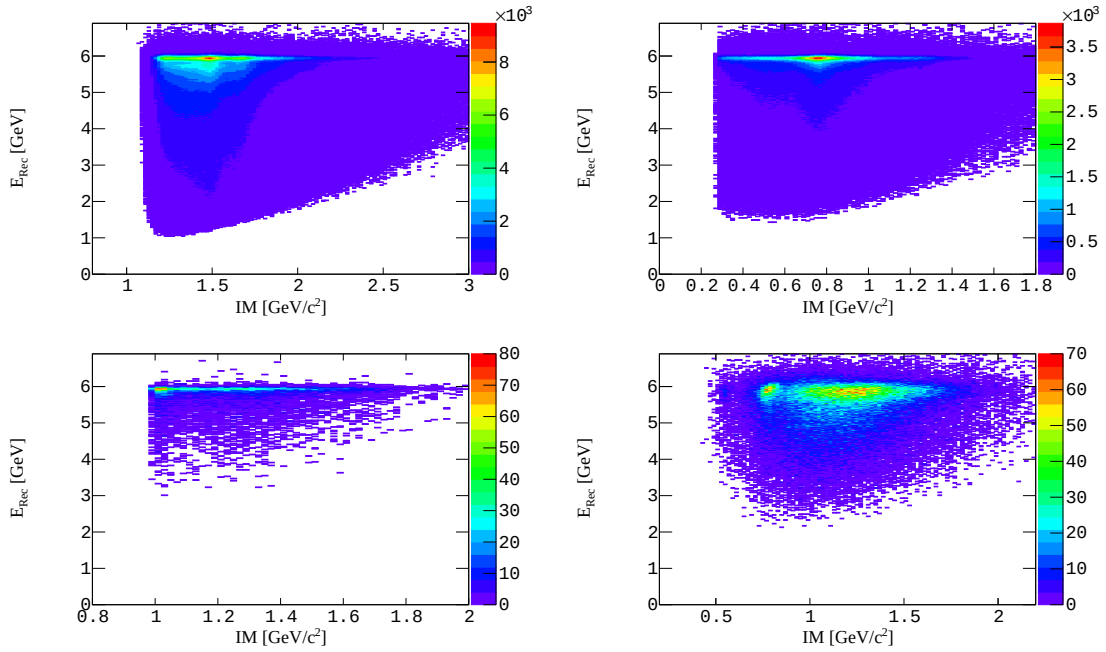

Figure 9.26: The electron beam energy reconstruction as a function of the invariant mass for 6 GeV electron beams impinged on a ^{12}C target for $p + \pi^-$, $\pi^+ + \pi^-$, $\pi^+ + \pi^- + \pi^0$ and $K^+ + K^-$ for the reactions $^{12}\mathrm{C}(e, e'p\pi^-)X$ (top left), $^{12}\mathrm{C}(e, e'p\pi^+\pi^-)X$ (top right), $^{12}\mathrm{C}(e, e'pK^+K^-)X$ (bottom left) and $^{12}\mathrm{C}(e, e'p\pi^+\pi^-\pi^0)X$ (bottom right).

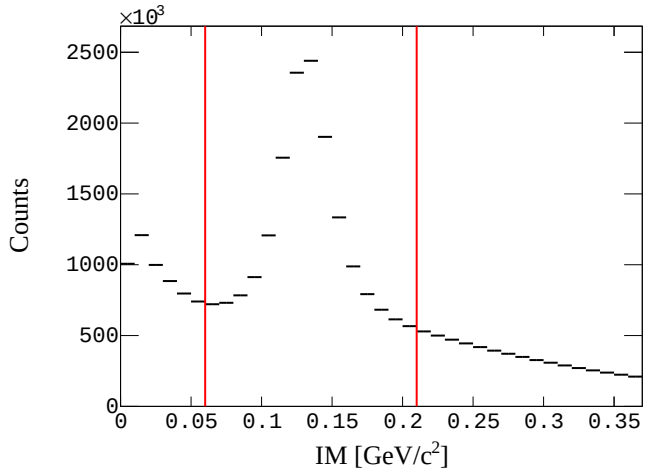

Figure 9.27: The invariant mass of two photons, γ_1 and γ_2, for 6 GeV electron beam impinged on a ^{12}C target. The red lines indicate the position of the cut imposed for the reaction and they are given by the $\mu \pm 3\sigma$ position of a Gaussian fitted in a limited range of invariant mass (0.11, 0.16) GeV/c^2.

9.5 Systematic Studies - Electron Beam Energy Reconstruction Distributions

The systematic uncertainties are determined with a similar methodology to the analysis presented in Chap. 8. The difference in this analysis is that the systematic uncertainty is determined on a bin-by-bin basis in reconstructed electron beam energy, given that the

final results are presented as a one-dimensional cross section ($d\sigma^{\text{vis}}/dE_{\text{Rec}}$). The estimated systematic errors are summarised in Tab. 8.4 for the reconstructed electron beam energy. Likewise, to the previous analyses presented in this thesis, some of the systematic uncertainties are independent of E_{Rec}. Systematic errors derived from varying the position of analysis cuts, are derived from studying the difference in agreement between the reconstructed electron beam energy from the experimental data and GEMC data, $E_{\text{Rec}}^{\text{sim}} - E_{\text{Rec}}^{\text{exp}}$. The difference in changing the cut from the nominal position to a tighter/looser position is given by $\Delta\frac{d\sigma^{\text{vis}}}{dE_{\text{Rec}}} = \left(E_{\text{Rec}}^{\text{sim}} - E_{\text{Rec}}^{\text{exp}}\right)_{\text{nom}} - \left(E_{\text{Rec}}^{\text{sim}} - E_{\text{Rec}}^{\text{exp}}\right)'$, where $\left(E_{\text{Rec}}^{\text{sim}} - E_{\text{Rec}}^{\text{exp}}\right)_{\text{nom}}$ and $\left(E_{\text{Rec}}^{\text{sim}} - E_{\text{Rec}}^{\text{exp}}\right)'$ is the difference in reconstructed energy between the two data sets for the nominal and tighter/looser cuts, respectively. The systematic errors are studied for all distributions of E_{Rec} (different reactions) and each electron beam energy setting. The largest difference between the nominal and tighter, or looser, cut is taken as the upper estimate for the systematic uncertainty in each bin of E_{Rec}.

- **Sampling Fraction Cut**

The systematic error arising from the sampling fraction cut was determined by varying the SF cut between the $\mu \pm 3\sigma$ and $\mu \pm 2.5/3.5\sigma$ positions. The systematic uncertainty arising from the SF cuts for $^{12}\text{C}(e, e'p)X$ reactions, with electron beam energies of 6 GeV and comparisons to the GENIE model with the G18 tune applied, are presented in Fig. 9.28. The average systematic error arising from the SF cut is 2%. The large percentage systematic errors at reconstructed beam energies greater than the true beam energy is not unexpected as these are unphysical, background events. It is also not unexpected to have large percentage uncertainties around the edge of acceptance at very low reconstructed beam energies, particularly for cuts which are momentum-dependent.

- **Electron DC Fiducial Cuts**

The systematic uncertainty arising from the DC fiducial cuts for the electron was determined by comparing the results of $\frac{d\sigma^{\text{vis}}}{dE_{\text{Rec}}}$ with and without the cuts applied. The average systematic arising from the DC fiducial cuts for the electron is 5%.

- **Electron Reaction Vertex**

The systematic error arising from the Reaction vertex position of the electron was determined by varying the cut between the $\mu \pm 3\sigma$ and $\mu \pm 2.5/3.5\sigma$ positions. The average systematic arising from the reaction vertex cut is $< 1\%$.

- **Hadron Reaction Vertex**

The systematic error arising from the Reaction vertex position of the hadrons was determined by varying the cut between the $\mu \pm 3\sigma$ and $\mu \pm 2.5/3.5\sigma$ positions for particles in both the FD and CD separately. This was done as they both have differing position resolutions. The average systematic arising from the reaction vertex cut in the FD and CD is $< 1\%$ and 2%, respectively.

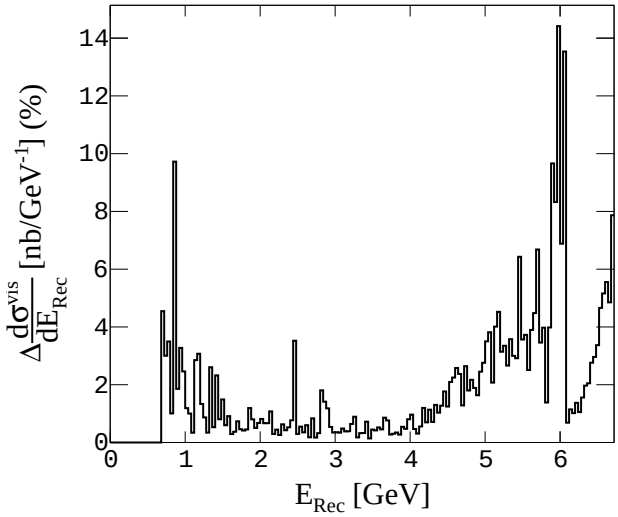

Figure 9.28: The systematic uncertainty, expressed as a percentage, as a function of the reconstructed electron beam energy for the SF cuts. The data is for $^{12}\mathrm{C}(e,e'p)X$ reactions with electron beams of 6 GeV, where the systematic errors are determined from comparisons to the GENIE model with the G18 tune applied.

- **Hadron Δz Reaction Vertex**

The systematic uncertainty in the Δz cut was determined from an identical method to the z cut. The average systematic arising from the Δz cut in the FD and CD is 1% and 4%, respectively. The larger systematic uncertainty in the CD can be attributed to applying a cut that mixes the resolutions of the electrons in FD and the hadrons in the CD.

- **Hadron DC Fiducial Cuts**

The systematic uncertainty arising from the DC fiducial cuts for the hadrons was determined by using the same method as for the electrons. The average systematic uncertainty arising from the DC fiducial cuts for the hadrons is $< 1\%$.

- **MVT Fiducial Cuts**

The systematic error in the MVT fiducial cut was studied by comparing the results of $\frac{d\sigma^{\mathrm{vis}}}{dE_{\mathrm{Rec}}}$ with and without the cut applied. The average systematic error arising from the MVT fiducial cuts is 5%.

- **FD Particle Identification Cuts (χ^2)**

The systematic error in varying the χ^2 cut from its nominal to a tighter/looser cut was studied by comparing the results of $\frac{d\sigma^{\mathrm{vis}}}{dE_{\mathrm{Rec}}}$ between the nominal and tighter/looser cuts. The average systematic error arising from the PID cuts in the FD is 1%.

- **CD Particle Identification Cuts (Δ_{TOF})**

The systematic error in varying the Δ_{TOF} cut from its nominal to a tighter/looser cut was

studied by comparing the results of $\frac{d\sigma^{\text{vis}}}{dE_{\text{Rec}}}$ between the nominal and tighter/looser cuts for the proton, positive pion and negative pion. The average systematic error in the Δ_{TOF} cut is 3% for protons, $< 1\%$ for positive pions and $< 1\%$ for negative pions. The lower systematic uncertainty for the pions is expected given that the negative pions are the only negative particle species detectable in the CD, and that the positive pions are determined sequentially after removing the proton sample, thereby reducing the background.

- **Minimum Momentum Threshold**

The systematic uncertainty associated with applying the minimum momentum threshold was determined by varying the momentum threshold from its nominal value to a looser threshold. The average systematic error arising from the momentum threshold was found to be 7%.

9.6 Results

The results for benchmarking the theoretical models for the various targets and beam energies are presented as visible cross sections as a function of the reconstructed electron beam energy. Results showcasing the performance of the theoretical models, with and without the cuts discussed in Sec. 9.4 applied, are presented. The systematic uncertainty from comparisons to each model is also presented in each plot, appearing as bands to present the systematic uncertainty, while the error bars on each data point represent the statistical uncertainty.

9.6.1 2 GeV Results

Starting with the lowest beam energy, each target of interest operated at this beam energy (2 GeV). The GiBUU model is not compared to data for the deuterium target as it is not well modelled by its nuclear matter approximations. In each figure in the results presented here, the black lines represent the data while the red, green and blue lines represent the GiBUU model, and the GENIE model with the G18 and SuSAv2 tunes applied, respectively. The systematic uncertainty arising from comparisons with each model is presented with the same colours. Figs. 9.29 to 9.46 present the reactions $A(e,e'p)X$, $A(e,e'p\pi^-)X$, $A(e,e'p\pi^+)X$, $A(e,e'p\pi^0)X$, $A(e,e'p\pi^+\pi^-)X$ and $A(e,e'pp)X$, respectively, with 2 GeV electrons impinged on various targets. A cut on the missing transverse momentum ($p_\perp^{\text{miss}} < 0.2$ GeV/c) is applied, in which we present the results with and without this cut applied. The neutral pions are determined through the methods discussed in Sec. 9.4.3.

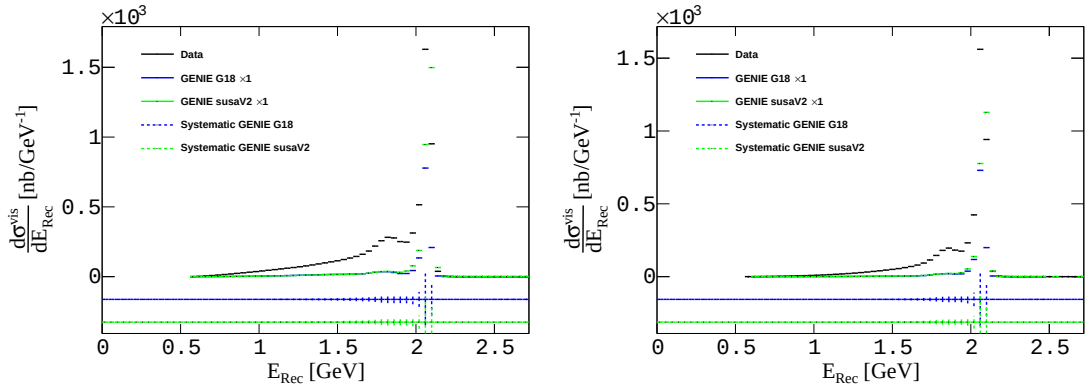

Figure 9.29: The comparisons of $^{2}\mathrm{D}(e,e'p)X$ reactions, with GENIE SuSAv2 (green) and G18 (blue), for 2 GeV electron beams without (left) and with (right) an additional cut on $p_{\perp}^{\mathrm{miss}} < 200$ MeV/c. The experimental data is presented as the black line.

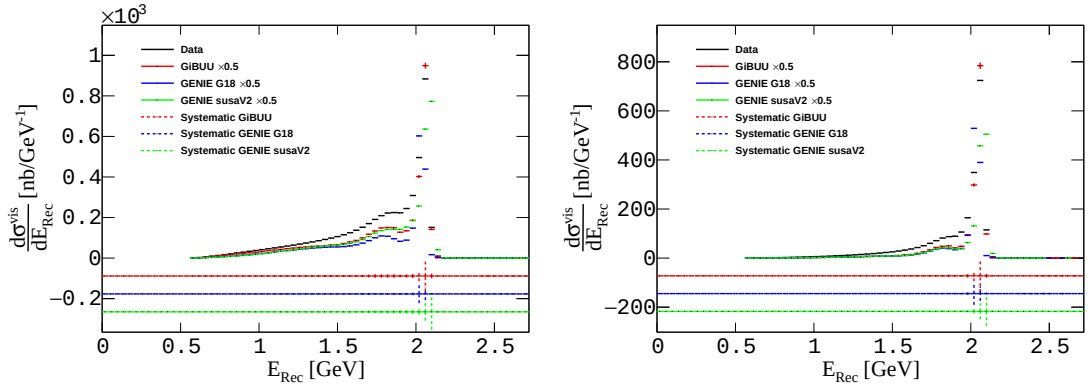

Figure 9.30: The comparisons of $^{12}\mathrm{C}(e,e'p)X$ reactions, with GENIE SuSAv2 (green), G18 (blue) and GiBUU (red), for 2 GeV electron beams without (left) and with (right) an additional cut on $p_{\perp}^{\mathrm{miss}} < 200$ MeV/c. The experimental data is presented as the black line.

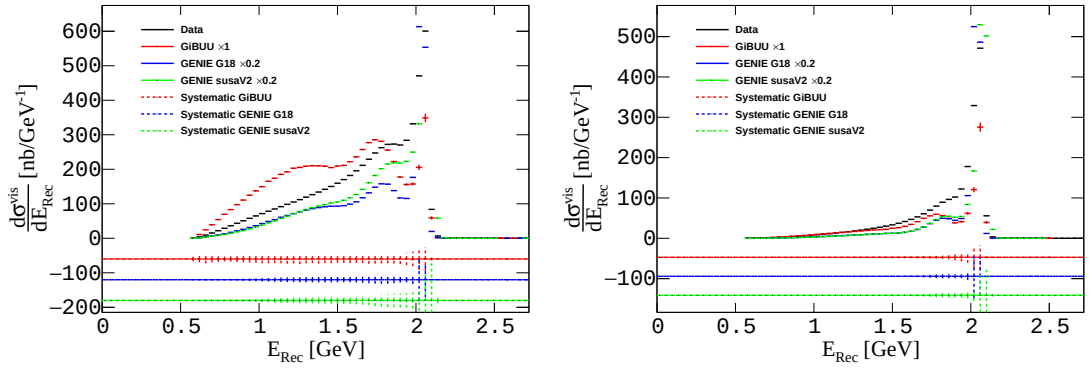

Figure 9.31: The comparisons of $^{40}\mathrm{Ar}(e,e'p)X$ reactions, with GENIE SuSAv2 (green), G18 (blue) and GiBUU (red), for 2 GeV electron beams without (left) and with (right) an additional cut on $p_{\perp}^{\mathrm{miss}} < 200$ MeV/c. The experimental data is presented as the black line.

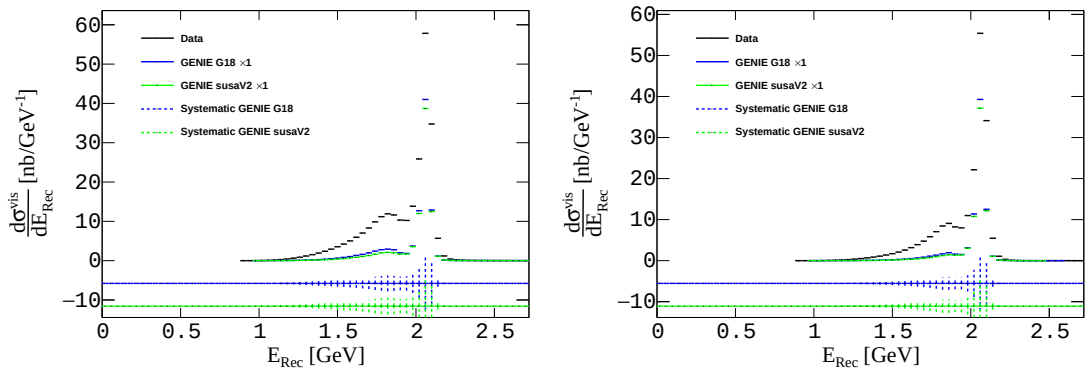

Figure 9.32: The comparisons of $^{2}\mathrm{D}(e,e'p\pi^{-})X$ reactions, with GENIE SuSAv2 (green) and G18 (blue), for 2 GeV electron beams without (left) and with (right) an additional cut on $p_{\perp}^{\mathrm{miss}} < 200$ MeV/c. The experimental data is presented as the black line.

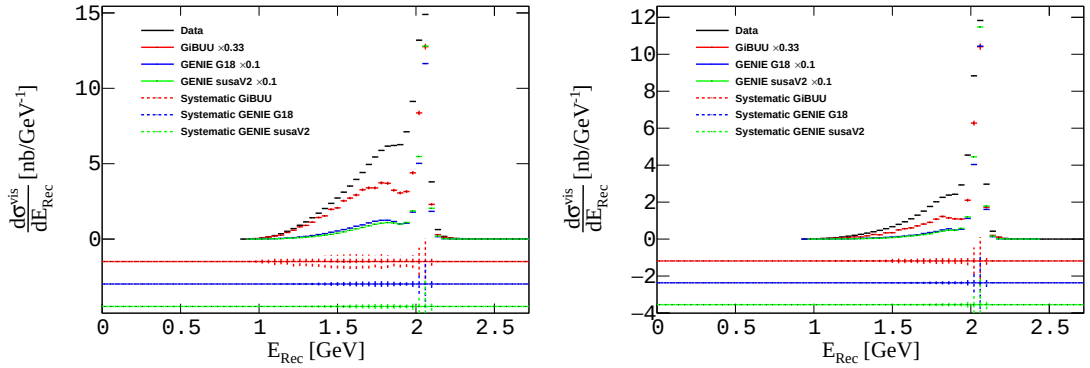

Figure 9.33: The comparisons of $^{12}\mathrm{C}(e,e'p\pi^{-})X$ reactions, with GENIE SuSAv2 (green), G18 (blue) and GiBUU (red), for 2 GeV electron beams without (left) and with (right) an additional cut on $p_{\perp}^{\mathrm{miss}} < 200$ MeV/c. The experimental data is presented as the black line.

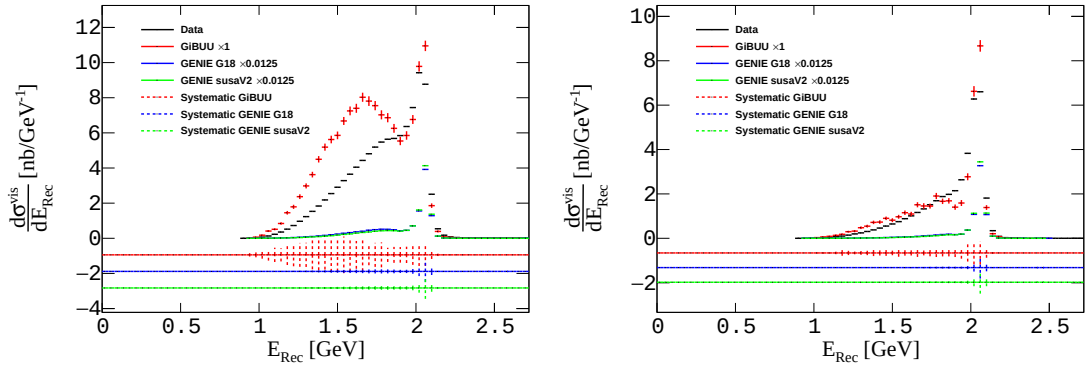

Figure 9.34: The comparisons of $^{40}\mathrm{Ar}(e,e'p\pi^{-})X$ reactions, with GENIE SuSAv2 (green), G18 (blue) and GiBUU (red), for 2 GeV electron beams without (left) and with (right) an additional cut on $p_{\perp}^{\mathrm{miss}} < 200$ MeV/c. The experimental data is presented as the black line.

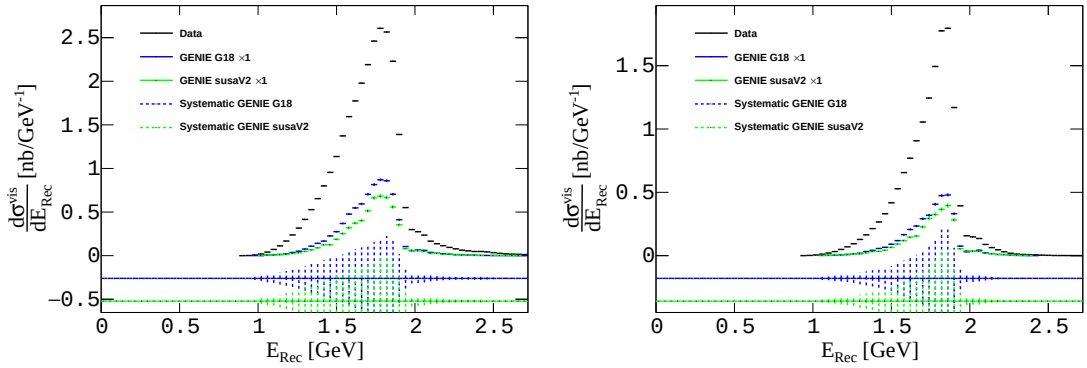

Figure 9.35: The comparisons of $^{2}\mathrm{D}(e,e'p\pi^{+})X$ reactions, with GENIE SuSAv2 (green) and G18 (blue), for 2 GeV electron beams without (left) and with (right) an additional cut on $p_{\perp}^{\mathrm{miss}} < 200$ MeV/c. The experimental data is presented as the black line.

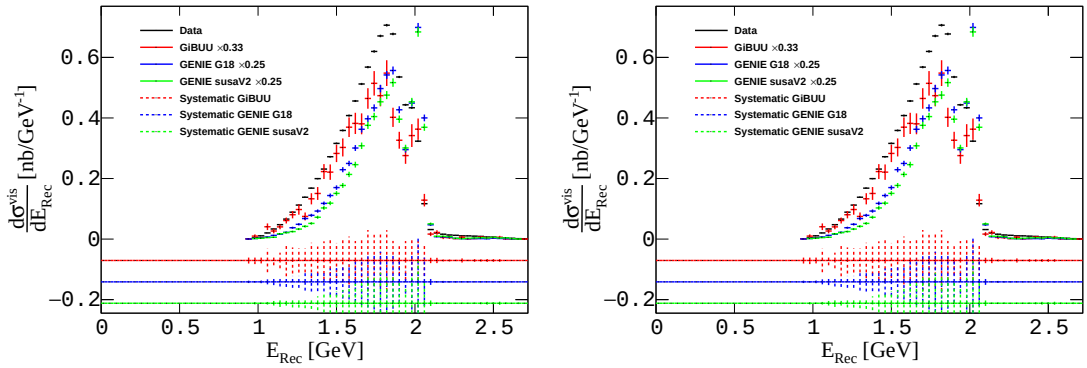

Figure 9.36: The comparisons of $^{12}\mathrm{C}(e,e'p\pi^{+})X$ reactions, with GENIE SuSAv2 (green), G18 (blue) and GiBUU (red), for 2 GeV electron beams without (left) and with (right) an additional cut on $p_{\perp}^{\mathrm{miss}} < 200$ MeV/c. The experimental data is presented as the black line.

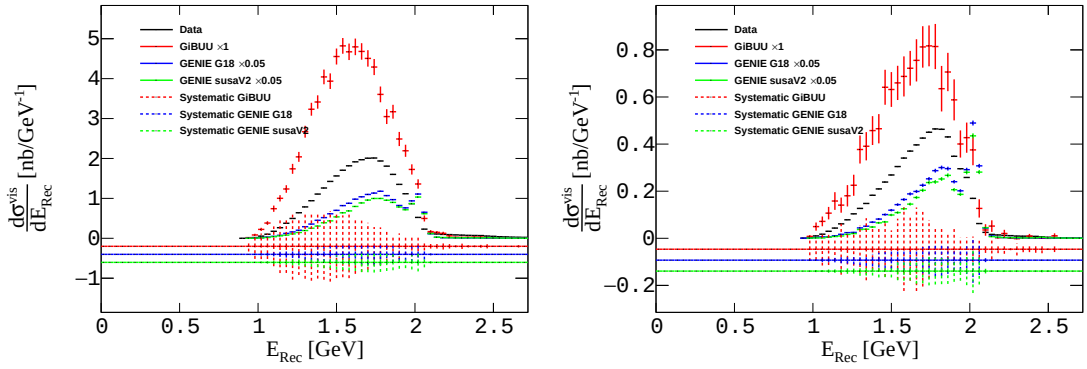

Figure 9.37: The comparisons of $^{40}\mathrm{Ar}(e,e'p\pi^{+})X$ reactions, with GENIE SuSAv2 (green), G18 (blue) and GiBUU (red), for 2 GeV electron beams without (left) and with (right) an additional cut on $p_{\perp}^{\mathrm{miss}} < 200$ MeV/c. The experimental data is presented as the black line.

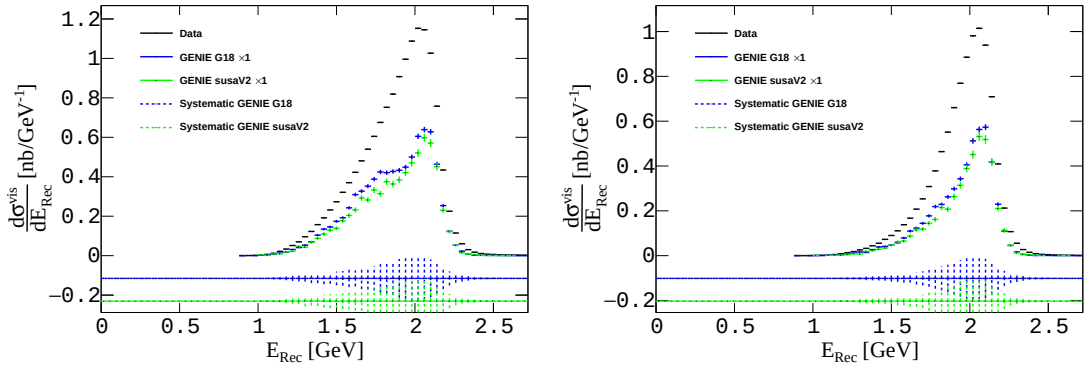

Figure 9.38: The comparisons of $^{2}\mathrm{D}(e,e'p\pi^{0})X$ reactions, with GENIE SuSAv2 (green) and G18 (blue), for 2 GeV electron beams without (left) and with (right) an additional cut on $p_{\perp}^{\mathrm{miss}} < 200$ MeV/c. The experimental data is presented as the black line.

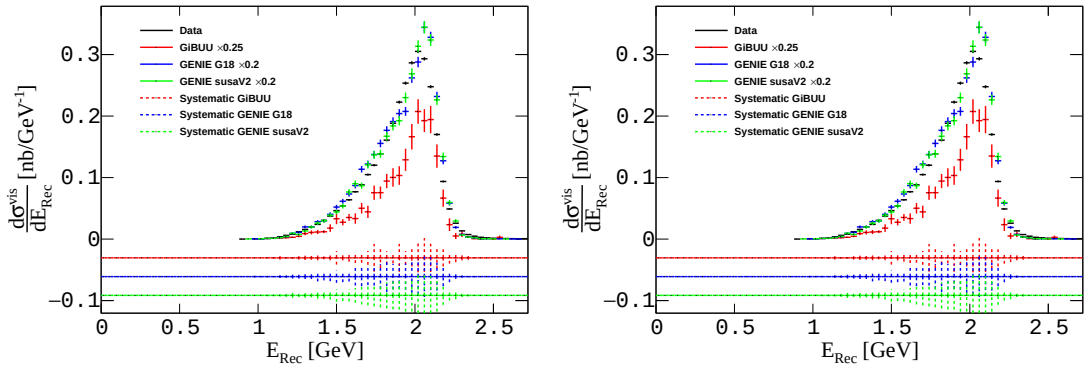

Figure 9.39: The comparisons of $^{12}\mathrm{C}(e,e'p\pi^{0})X$ reactions, with GENIE SuSAv2 (green), G18 (blue) and GiBUU (red), for 2 GeV electron beams without (left) and with (right) an additional cut on $p_{\perp}^{\mathrm{miss}} < 200$ MeV/c. The experimental data is presented as the black line.

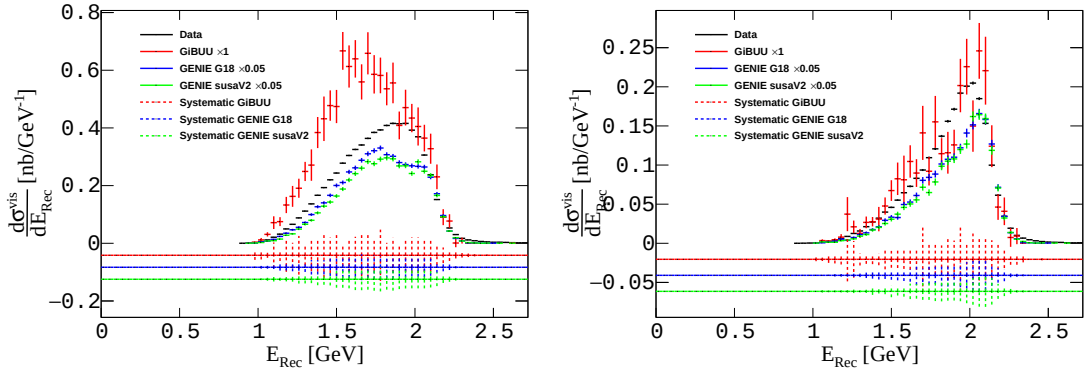

Figure 9.40: The comparisons of $^{40}\mathrm{Ar}(e,e'p\pi^{0})X$ reactions, with GENIE SuSAv2 (green), G18 (blue) and GiBUU (red), for 2 GeV electron beams without (left) and with (right) an additional cut on $p_{\perp}^{\mathrm{miss}} < 200$ MeV/c. The experimental data is presented as the black line.

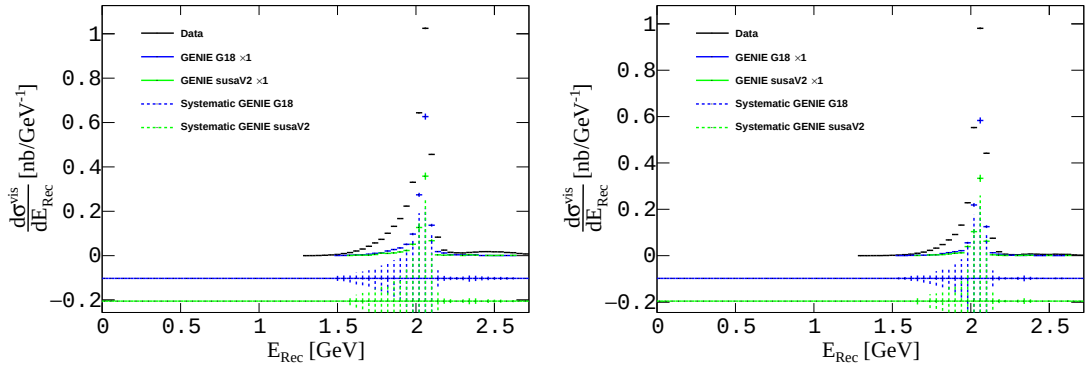

Figure 9.41: The comparisons of $^{2}\mathrm{D}(e,e'p\pi^{+}\pi^{-})X$ reactions, with GENIE SuSAv2 (green) and G18 (blue), for 2 GeV electron beams without (left) and with (right) an additional cut on $p_{\perp}^{\mathrm{miss}} < 200$ MeV/c. The experimental data is presented as the black line.

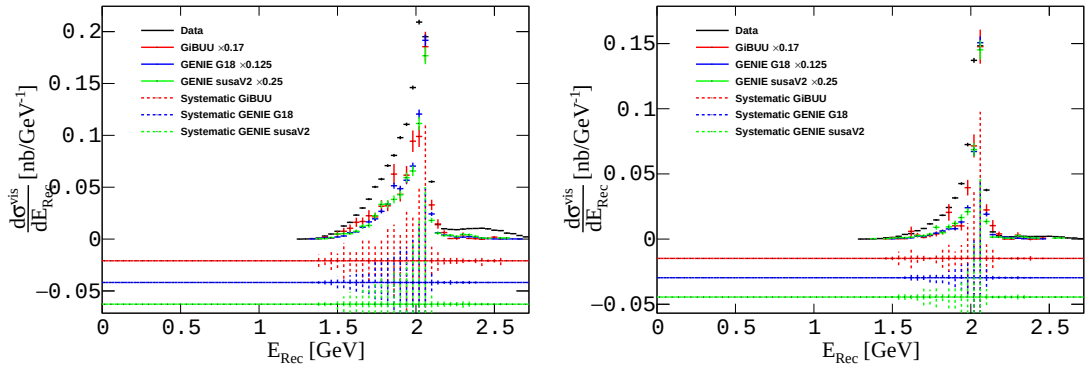

Figure 9.42: The comparisons of $^{12}\mathrm{C}(e,e'p\pi^{+}\pi^{-})X$ reactions, with GENIE SuSAv2 (green), G18 (blue) and GiBUU (red), for 2 GeV electron beams without (left) and with (right) an additional cut on $p_{\perp}^{\mathrm{miss}} < 200$ MeV/c. The experimental data is presented as the black line.

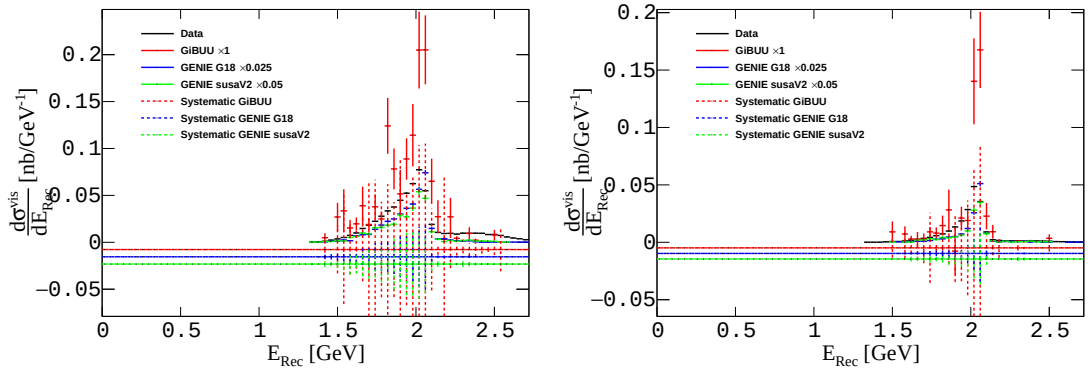

Figure 9.43: The comparisons of $^{40}\mathrm{Ar}(e,e'p\pi^{+}\pi^{-})X$ reactions, with GENIE SuSAv2 (green), G18 (blue) and GiBUU (red), for 2 GeV electron beams without (left) and with (right) an additional cut on $p_{\perp}^{\mathrm{miss}} < 200$ MeV/c. The experimental data is presented as the black line.

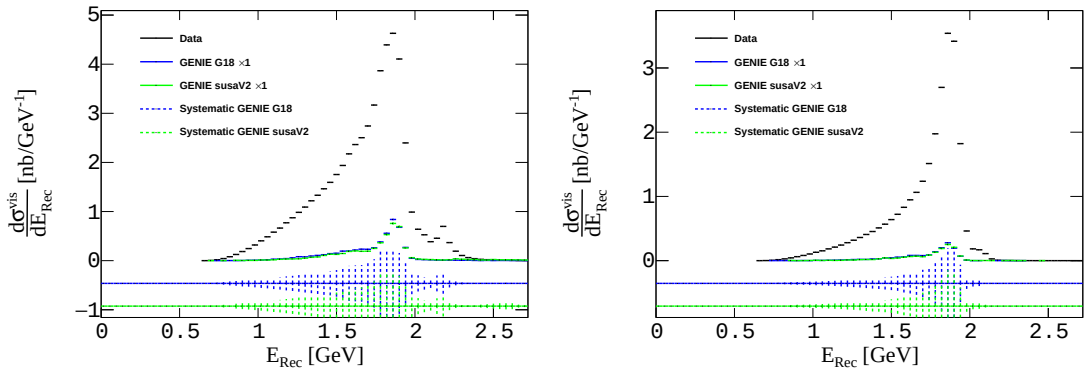

Figure 9.44: The comparisons of $^{2}\mathrm{D}(e,e'pp)X$ reactions, with GENIE SuSAv2 (green) and G18 (blue), for 2 GeV electron beams without (left) and with (right) an additional cut on $p_{\perp}^{\mathrm{miss}} < 200$ MeV/c. The experimental data is presented as the black line.

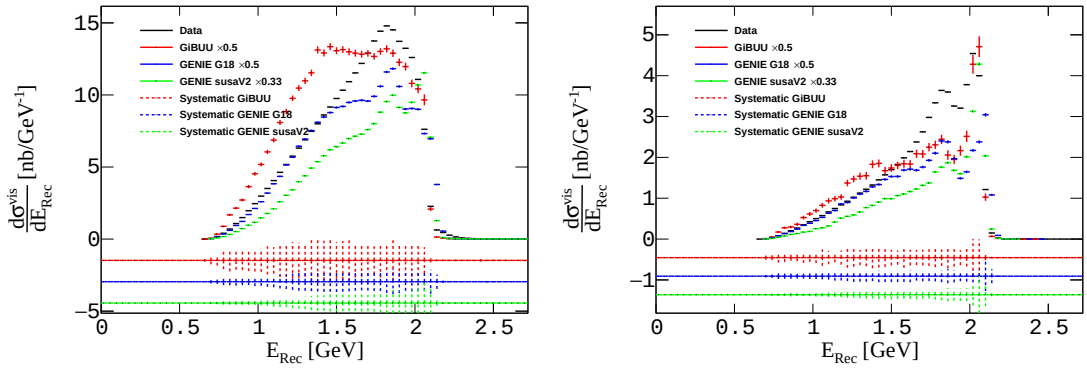

Figure 9.45: The comparisons of $^{12}\mathrm{C}(e,e'pp)X$ reactions, with GENIE SuSAv2 (green), G18 (blue) and GiBUU (red), for 2 GeV electron beams without (left) and with (right) an additional cut on $p_{\perp}^{\mathrm{miss}} < 200$ MeV/c. The experimental data is presented as the black line.

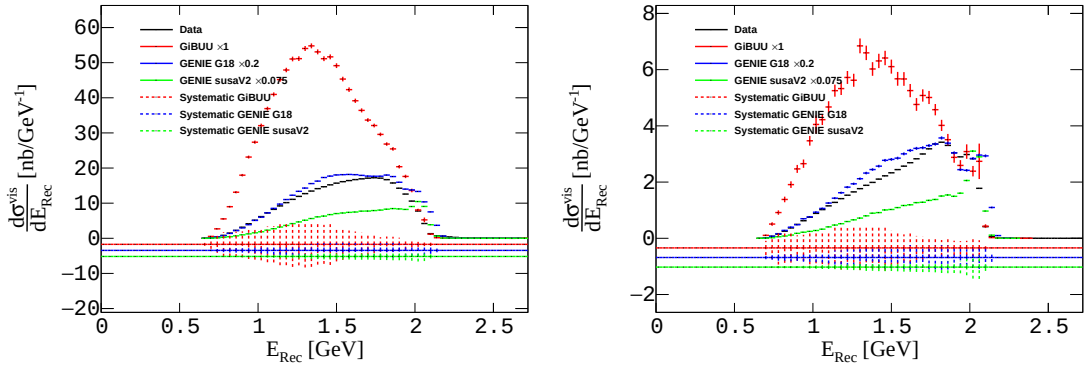

Figure 9.46: The comparisons of $^{40}\mathrm{Ar}(e,e'pp)X$ reactions, with GENIE SuSAv2 (green), G18 (blue) and GiBUU (red), for 2 GeV electron beams without (left) and with (right) an additional cut on $p_{\perp}^{\mathrm{miss}} < 200$ MeV/c. The experimental data is presented as the black line.

The results are surprising as they indicate that even the simplest of reactions are poorly constrained by GENIE and GiBUU, despite the relatively clean environment due to the modest beam energy used and the relatively light target nuclei. The previous publication presented in Subsec. 3.3.2 had similar conclusions, hence there is a consistency between our results and the results previously published. However, higher-order configurations are yet to be tested and we provide the first comparisons of such reactions. Simple reactions involving a single meson (pion) knockout alongside the ejected proton are poorly constrained, particularly by GENIE for ^{40}Ar. The modelling of GENIE becomes progressively worse with increasing nuclear mass, whereas GiBUU tends to overpredict ^{12}C cross sections and more accurately model the heavier ^{40}Ar target cross sections. Another observation, regarding the background observed in the models, is that the second peak seen in quasielastic reactions for ^{2}D presented in Fig. 9.29 is present in the data and models. This peak corresponds to the resonance production mechanisms, where the scattered electron and proton are detected, but the π^0 emerging from the resonance mechanism was not detected. Contrariwise, for higher mass targets this is not seen in the data, but the models both predict this second peak to be strong and clear, which is typically associated with resonances or a missing pion. In heavier targets, the resonances are typically broader and washed out due to effects discussed in Chap. 2. Therefore, we expect the distributions observed in the experimental data, which indicates a tuning of the in-medium modifications are required in both models.

An additional observation is that both GENIE and GiBUU capture the fact a direct 2p knockout reaction is not possible from ^{2}D. The ^{2}D nucleus contains a single proton and a single neutron, therefore, for this reaction to occur, the neutron must have undergone charge exchange after a resonance excitation (e.g., $n \rightarrow \Delta \rightarrow p + \pi^-$), where the two protons were detected, but the π^- went undetected.

9.6.2 4 GeV Results

Moving on to another beam energy that was covered in the previous results (4 GeV). The Deuterium target was not utilised at this beam energy, therefore we present results for the ^{12}C and ^{40}Ar targets only. The data are presented as for the 2 GeV case. Figs. 9.47 to 9.58 present the reactions $A(e,e'p)X$, $A(e,e'p\pi^-)X$, $A(e,e'p\pi^+)X$, $A(e,e'p\pi^0)X$, $A(e,e'p\pi^+\pi^-)X$ and $A(e,e'pp)X$, respectively, with 4 GeV electrons impinged on the ^{12}C and ^{40}Ar targets. A cut on the missing transverse momentum, $p_\perp^{\text{miss}} < 0.2$ GeV/c is applied, in which we present the results with and without this cut applied.

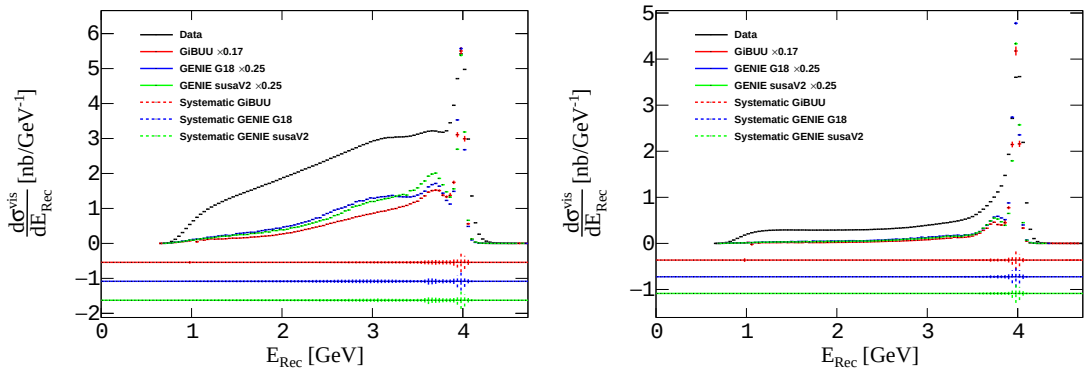

Figure 9.47: The comparisons of $^{12}\mathrm{C}(e,e'p)X$ reactions, with GENIE SuSAv2 (green), G18 (blue) and GiBUU (red), for 4 GeV electron beams without (left) and with (right) an additional cut on $p_{\perp}^{\mathrm{miss}} < 200$ MeV/c. The experimental data is presented as the black line.

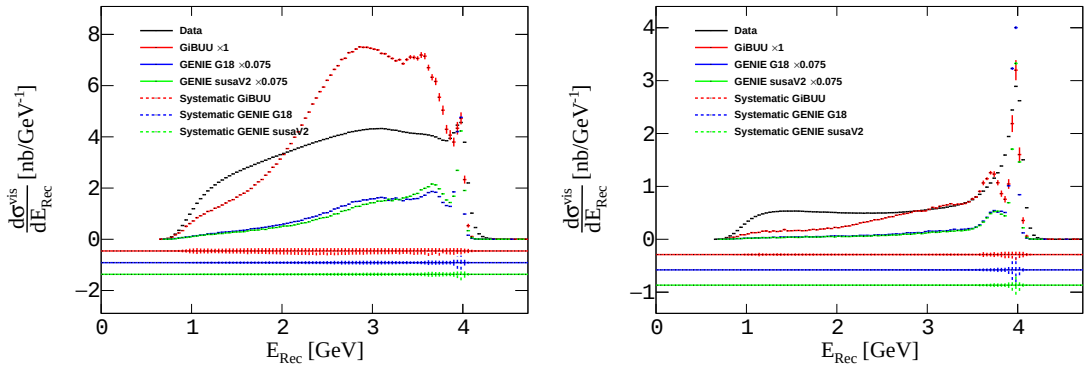

Figure 9.48: The comparisons of $^{40}\mathrm{Ar}(e,e'p)X$ reactions, with GENIE SuSAv2 (green), G18 (blue) and GiBUU (red), for 4 GeV electron beams without (left) and with (right) an additional cut on $p_{\perp}^{\mathrm{miss}} < 200$ MeV/c. The experimental data is presented as the black line.

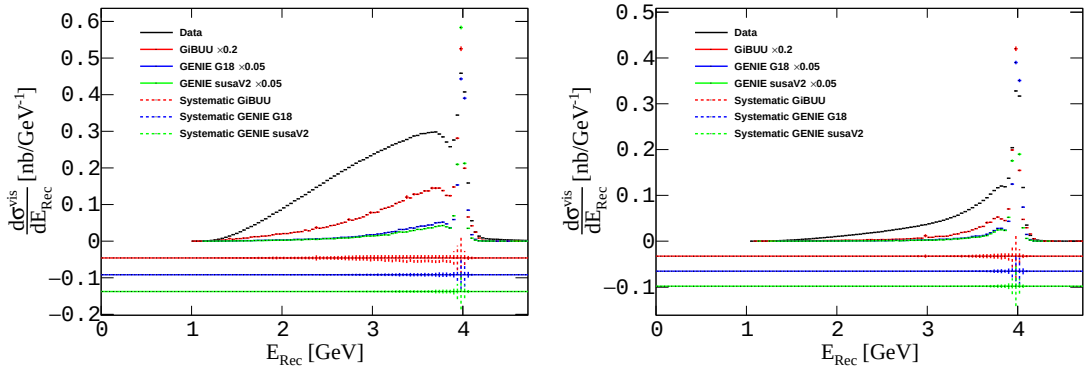

Figure 9.49: The comparisons of $^{12}\mathrm{C}(e,e'p\pi^{-})X$ reactions, with GENIE SuSAv2 (green), G18 (blue) and GiBUU (red), for 4 GeV electron beams without (left) and with (right) an additional cut on $p_{\perp}^{\mathrm{miss}} < 200$ MeV/c. The experimental data is presented as the black line.

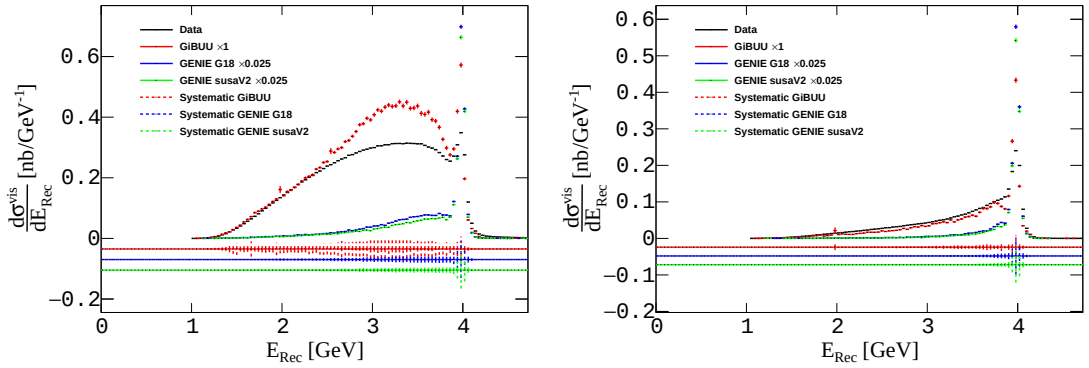

Figure 9.50: The comparisons of $^{40}\mathrm{Ar}(e,e'p\pi^-)X$ reactions, with GENIE SuSAv2 (green), G18 (blue) and GiBUU (red), for 4 GeV electron beams without (left) and with (right) an additional cut on $p_\perp^{\mathrm{miss}} < 200$ MeV/c. The experimental data is presented as the black line.

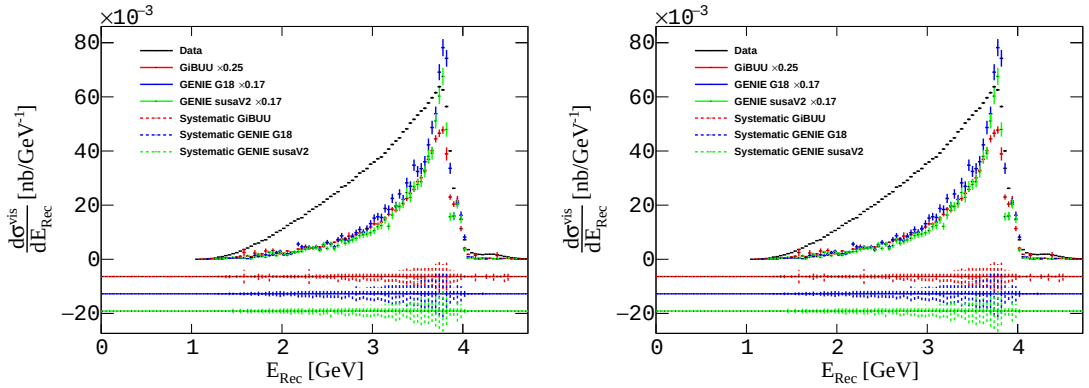

Figure 9.51: The comparisons of $^{12}\mathrm{C}(e,e'p\pi^+)X$ reactions, with GENIE SuSAv2 (green), G18 (blue) and GiBUU (red), for 4 GeV electron beams without (left) and with (right) an additional cut on $p_\perp^{\mathrm{miss}} < 200$ MeV/c. The experimental data is presented as the black line.

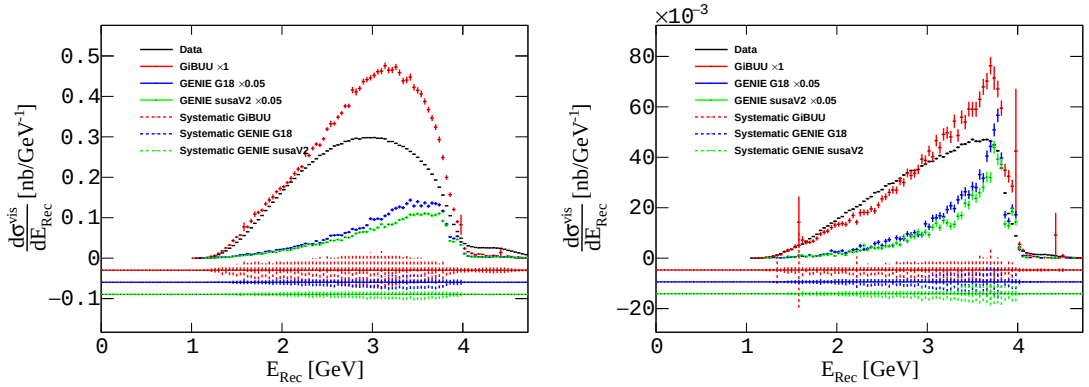

Figure 9.52: The comparisons of $^{40}\mathrm{Ar}(e,e'p\pi^+)X$ reactions, with GENIE SuSAv2 (green), G18 (blue) and GiBUU (red), for 4 GeV electron beams without (left) and with (right) an additional cut on $p_\perp^{\mathrm{miss}} < 200$ MeV/c. The experimental data is presented as the black line.

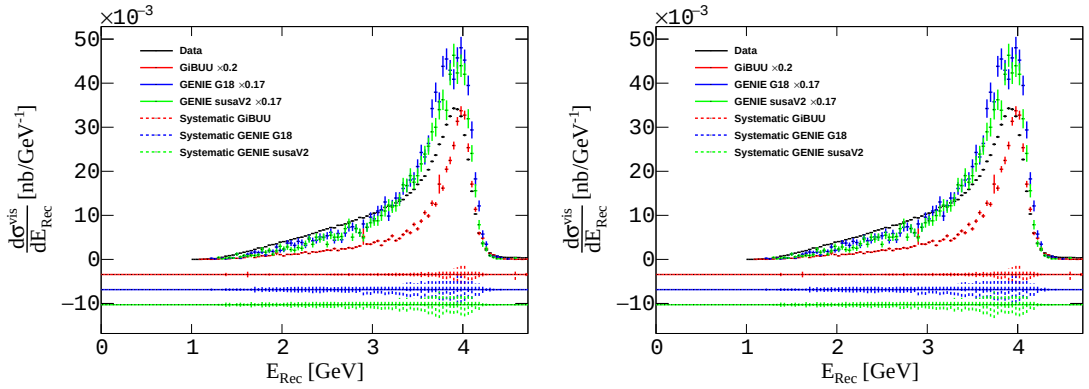

Figure 9.53: The comparisons of $^{12}\mathrm{C}(e,e'p\pi^0)X$ reactions, with GENIE SuSAv2 (green), G18 (blue) and GiBUU (red), for 4 GeV electron beams without (left) and with (right) an additional cut on $p_\perp^{\mathrm{miss}} < 200$ MeV/c. The experimental data is presented as the black line.

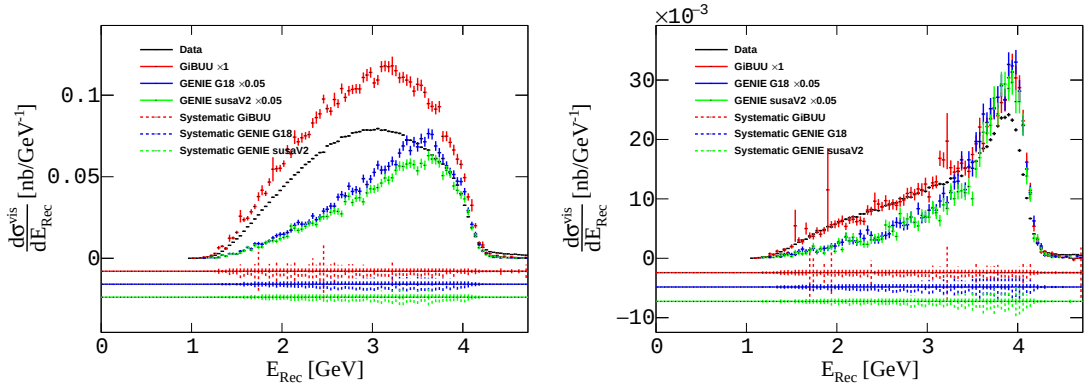

Figure 9.54: The comparisons of $^{40}\mathrm{Ar}(e,e'p\pi^0)X$ reactions, with GENIE SuSAv2 (green), G18 (blue) and GiBUU (red), for 4 GeV electron beams without (left) and with (right) an additional cut on $p_\perp^{\mathrm{miss}} < 200$ MeV/c. The experimental data is presented as the black line.

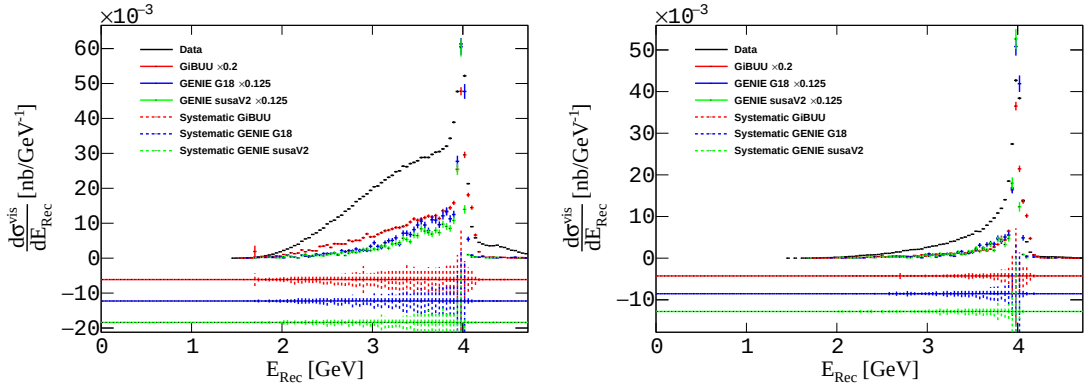

Figure 9.55: The comparisons of $^{12}\mathrm{C}(e,e'p\pi^+\pi^-)X$ reactions, with GENIE SuSAv2 (green), G18 (blue) and GiBUU (red), for 4 GeV electron beams without (left) and with (right) an additional cut on $p_\perp^{\mathrm{miss}} < 200$ MeV/c. The experimental data is presented as the black line.

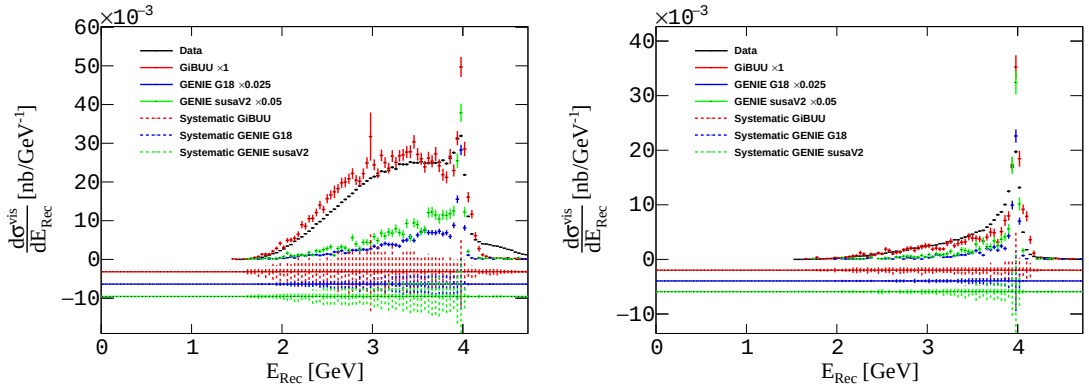

Figure 9.56: The comparisons of $^{40}\mathrm{Ar}(e,e'p\pi^+\pi^-)X$ reactions, with GENIE SuSAv2 (green), G18 (blue) and GiBUU (red), for 4 GeV electron beams without (left) and with (right) an additional cut on $p_\perp^{\mathrm{miss}} < 200$ MeV/c. The experimental data is presented as the black line.

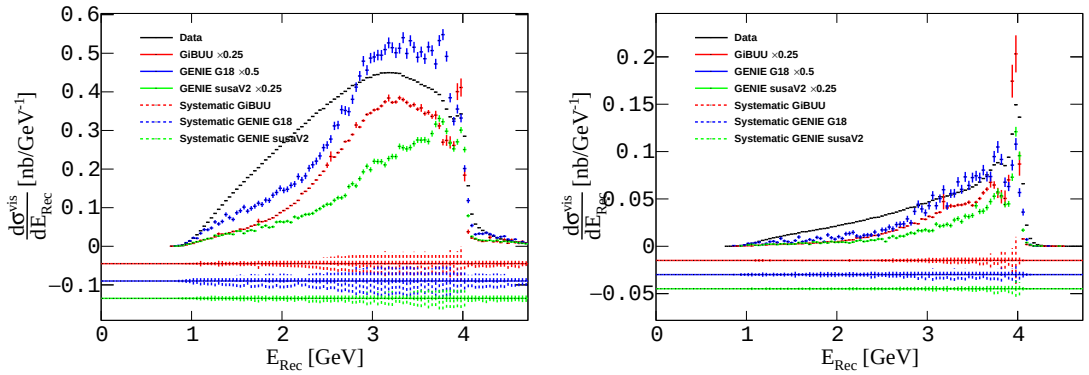

Figure 9.57: The comparisons of $^{12}\mathrm{C}(e,e'pp)X$ reactions, with GENIE SuSAv2 (green), G18 (blue) and GiBUU (red), for 4 GeV electron beams without (left) and with (right) an additional cut on $p_\perp^{\mathrm{miss}} < 200$ MeV/c. The experimental data is presented as the black line.

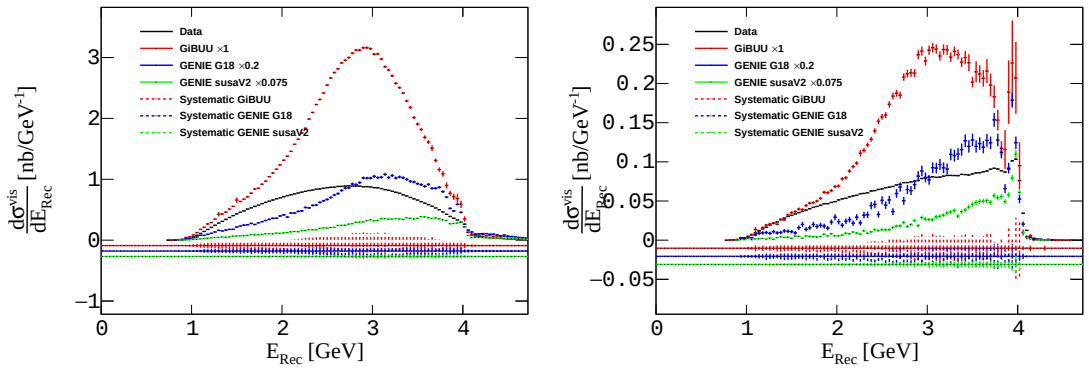

Figure 9.58: The comparisons of $^{40}\mathrm{Ar}(e,e'pp)X$ reactions, with GENIE SuSAv2 (green), G18 (blue) and GiBUU (red), for 4 GeV electron beams without (left) and with (right) an additional cut on $p_\perp^{\mathrm{miss}} < 200$ MeV/c. The experimental data is presented as the black line.

Comparisons with the GENIE model reveal large discrepancies between the data and the model, especially for reactions involving one or more pions in the final state. The model poorly reflects the experimental data for ^{40}Ar, which indicates a large tuning of the model is required. As previously stated, ^{40}Ar will be crucial for next-generation facilities like DUNE. Therefore, if GENIE is to be used for extracting the oscillation parameters, the nuclear physics must be re-modelled. On the other hand, GiBUU, while overpredicting the results for many reactions from ^{12}C targets, accurately models the reactions observed from $^{4}0Ar$ targets. Future studies will need to clarify the reliability of these results, given that a full-scale simulation of the target must be conducted, although the results are a good indication of how well GiBUU models ^{40}Ar reactions. The general shape of the data is reproduced by both models for ^{12}C, but for ^{40}Ar the secondary peaks, forming about 300 MeV below the true beam energy, do not replicate the broadness observed in the experimental data. This could reflect inaccuracies in the model.

9.6.3 6 GeV Results

The final beam energy presented is the highest (6 GeV), and enters a new kinematical region not previously explored for this work, which overlaps with a large area of the DUNE kinematics. The Argon target is not presented at this beam energy, therefore we present results for the ^{2}D and ^{12}C targets only. The data are presented as for the 2 GeV case. Figs. 9.59 to 9.70 present the reactions $A(e,e'p)X$, $A(e,e'p\pi^-)X$, $A(e,e'p\pi^+)X$, $A(e,e'p\pi^0)X$, $A(e,e'p\pi^+\pi^-)X$ and $A(e,e'pp)X$, respectively, with 6 GeV electrons impinged on the ^{12}C and ^{40}Ar targets. A cut on the missing transverse momentum, $p_\perp^{\text{miss}} < 0.2$ GeV/c is applied, in which we present the results with and without this cut applied.

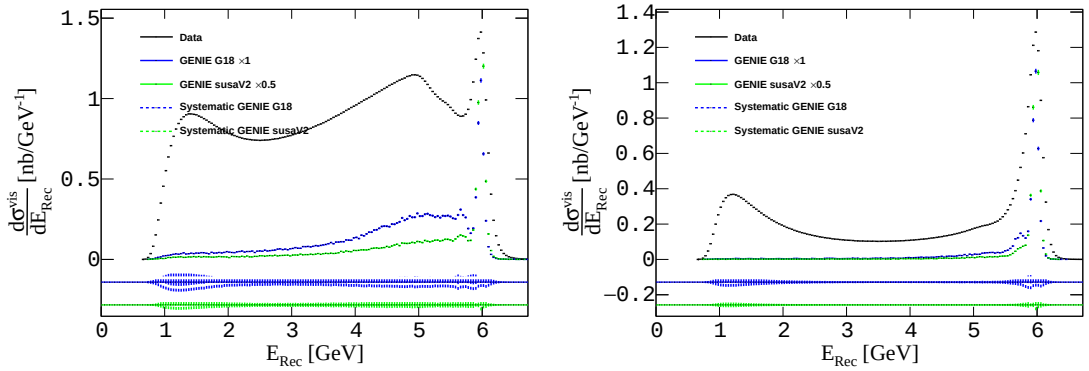

Figure 9.59: The comparisons of ^{2}D$(e,e'p)X$ reactions, with GENIE SuSAv2 (green) and G18 (blue), for 6 GeV electron beams without (left) and with (right) an additional cut on $p_\perp^{\text{miss}} < 200$ MeV/c. The experimental data is presented as the black line.

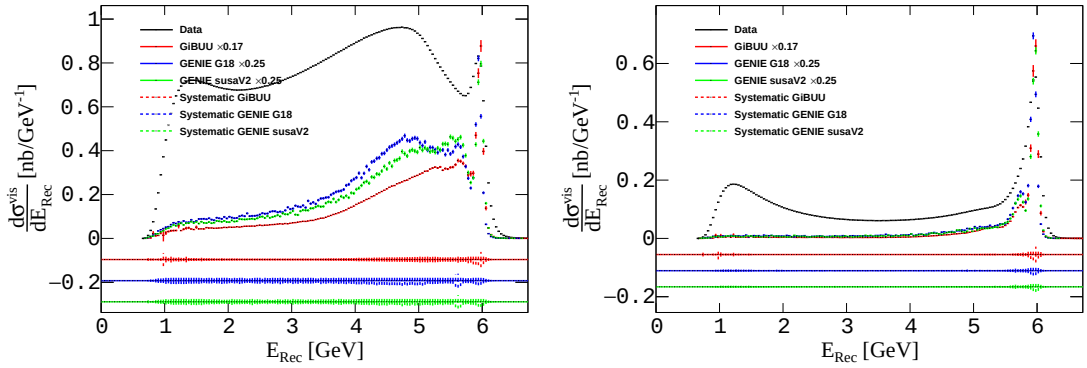

Figure 9.60: The comparisons of ^{12}C$(e,e'p)X$ reactions, with GENIE SuSAv2 (green), G18 (blue) and GiBUU (red), for 6 GeV electron beams without (left) and with (right) an additional cut on $p_{\perp}^{\text{miss}} < 200$ MeV/c. The experimental data is presented as the black line.

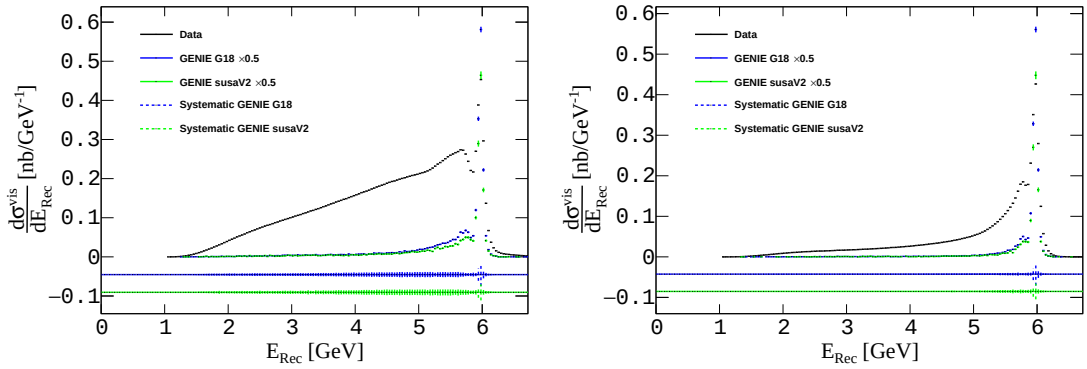

Figure 9.61: The comparisons of ^{2}D$(e,e'p\pi^{-})X$ reactions, with GENIE SuSAv2 (green) and G18 (blue), for 6 GeV electron beams without (left) and with (right) an additional cut on $p_{\perp}^{\text{miss}} < 200$ MeV/c. The experimental data is presented as the black line.

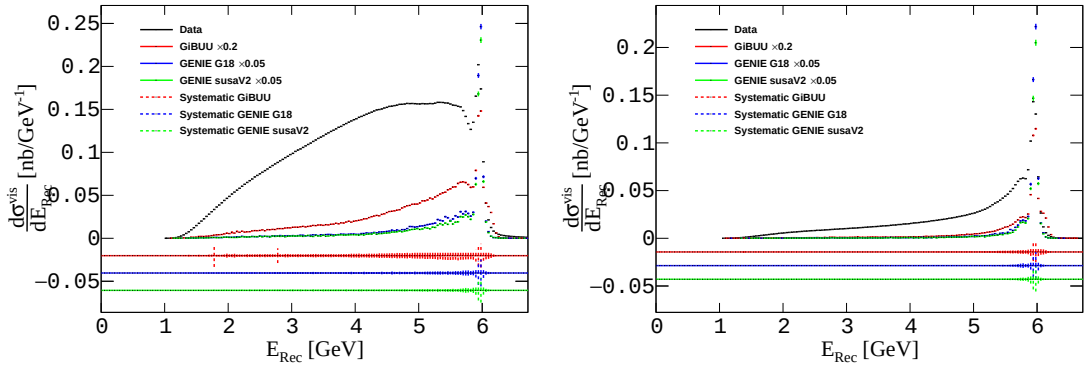

Figure 9.62: The comparisons of ^{12}C$(e,e'p\pi^{-})X$ reactions, with GENIE SuSAv2 (green), G18 (blue) and GiBUU (red), for 6 GeV electron beams without (left) and with (right) an additional cut on $p_{\perp}^{\text{miss}} < 200$ MeV/c. The experimental data is presented as the black line.

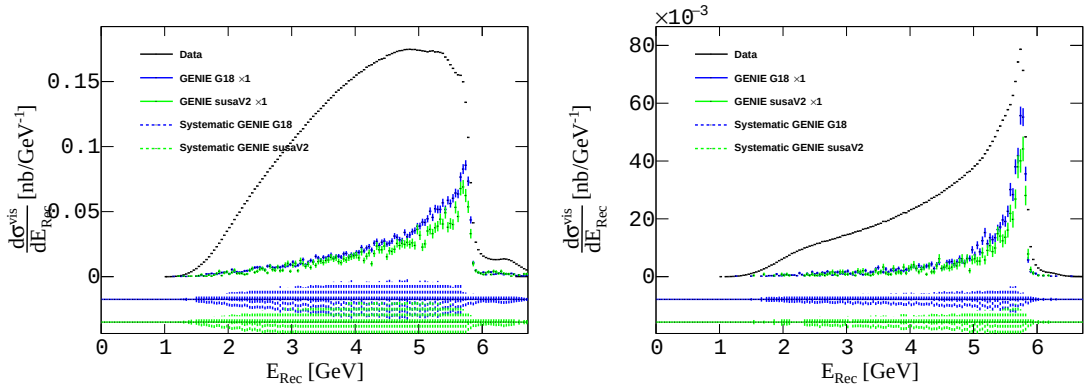

Figure 9.63: The comparisons of ^{2}D$(e,e'p\pi^+)X$ reactions, with GENIE SuSAv2 (green) and G18 (blue), for 6 GeV electron beams without (left) and with (right) an additional cut on $p_\perp^{\text{miss}} < 200$ MeV/c. The experimental data is presented as the black line.

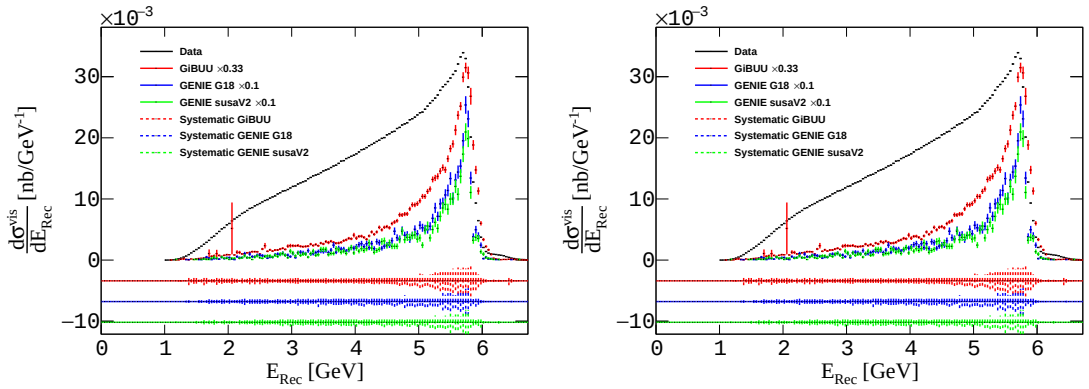

Figure 9.64: The comparisons of ^{12}C$(e,e'p\pi^+)X$ reactions, with GENIE SuSAv2 (green), G18 (blue) and GiBUU (red), for 6 GeV electron beams without (left) and with (right) an additional cut on $p_\perp^{\text{miss}} < 200$ MeV/c. The experimental data is presented as the black line.

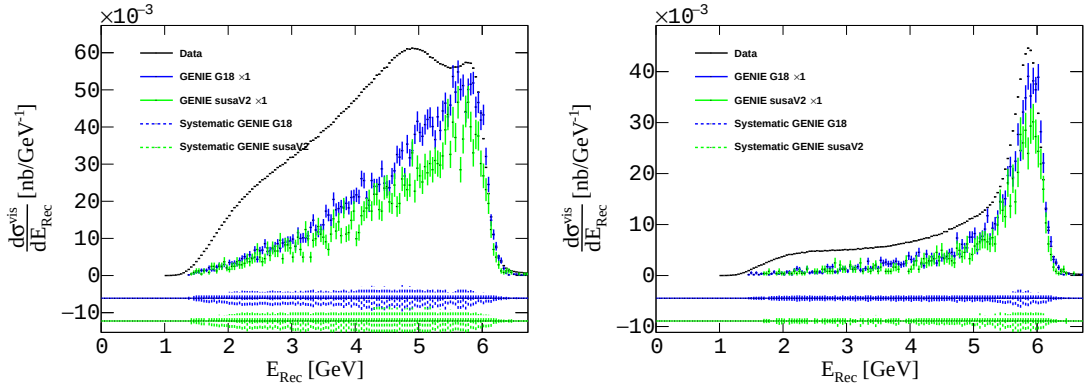

Figure 9.65: The comparisons of ^{2}D$(e,e'p\pi^0)X$ reactions, with GENIE SuSAv2 (green) and G18 (blue), for 6 GeV electron beams without (left) and with (right) an additional cut on $p_\perp^{\text{miss}} < 200$ MeV/c. The experimental data is presented as the black line.

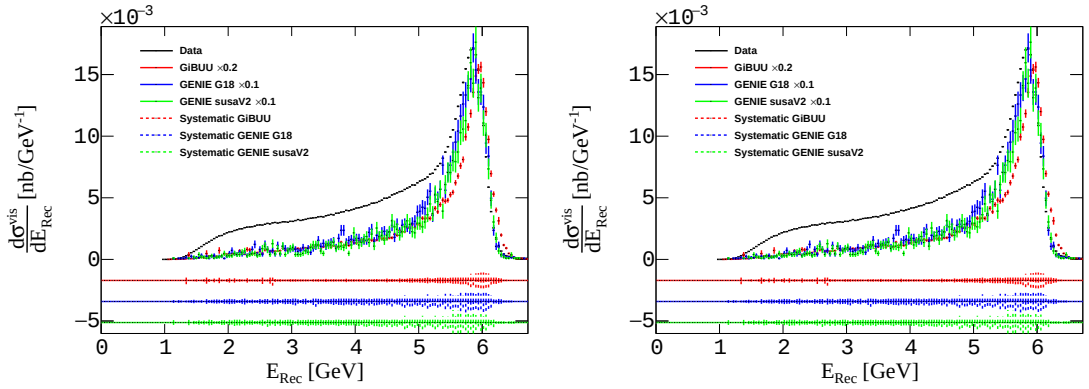

Figure 9.66: The comparisons of $^{12}\mathrm{C}(e,e'p\pi^0)X$ reactions, with GENIE SuSAv2 (green), G18 (blue) and GiBUU (red), for 6 GeV electron beams without (left) and with (right) an additional cut on $p_\perp^{\mathrm{miss}} < 200$ MeV/c. The experimental data is presented as the black line.

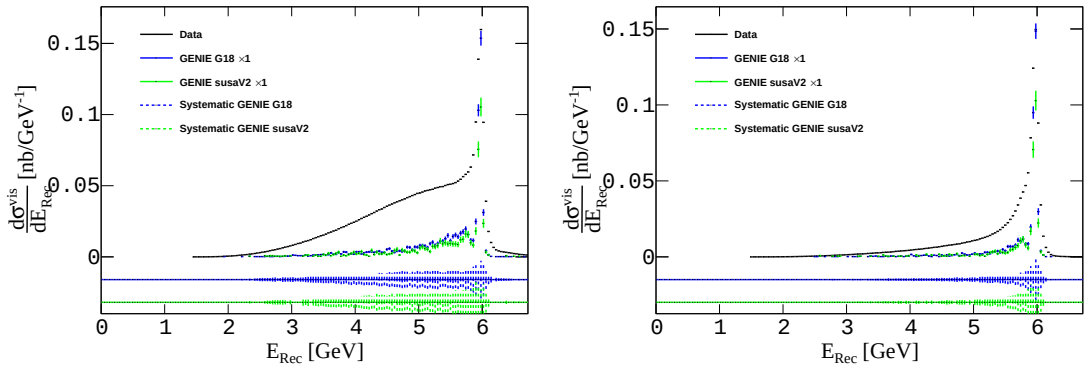

Figure 9.67: The comparisons of $^{2}\mathrm{D}(e,e'p\pi^+\pi^-)X$ reactions, with GENIE SuSAv2 (green) and G18 (blue), for 6 GeV electron beams without (left) and with (right) an additional cut on $p_\perp^{\mathrm{miss}} < 200$ MeV/c. The experimental data is presented as the black line.

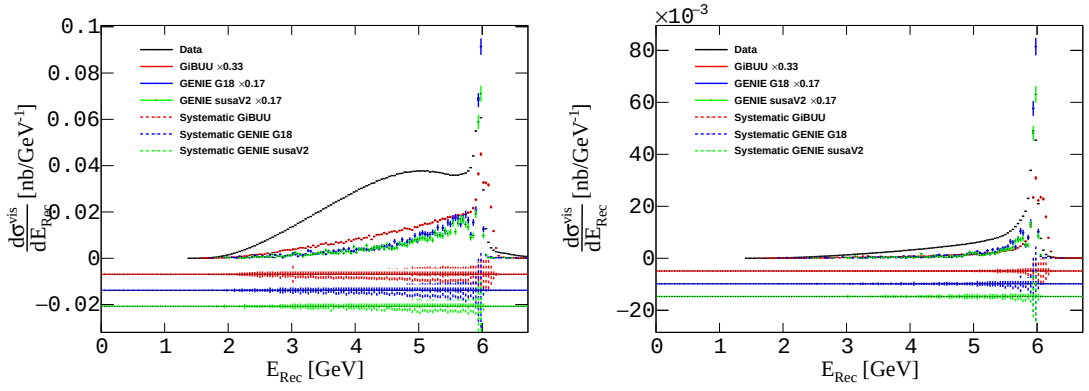

Figure 9.68: The comparisons of $^{12}\mathrm{C}(e,e'p\pi^+\pi^-)X$ reactions, with GENIE SuSAv2 (green), G18 (blue) and GiBUU (red), for 6 GeV electron beams without (left) and with (right) an additional cut on $p_\perp^{\mathrm{miss}} < 200$ MeV/c. The experimental data is presented as the black line.

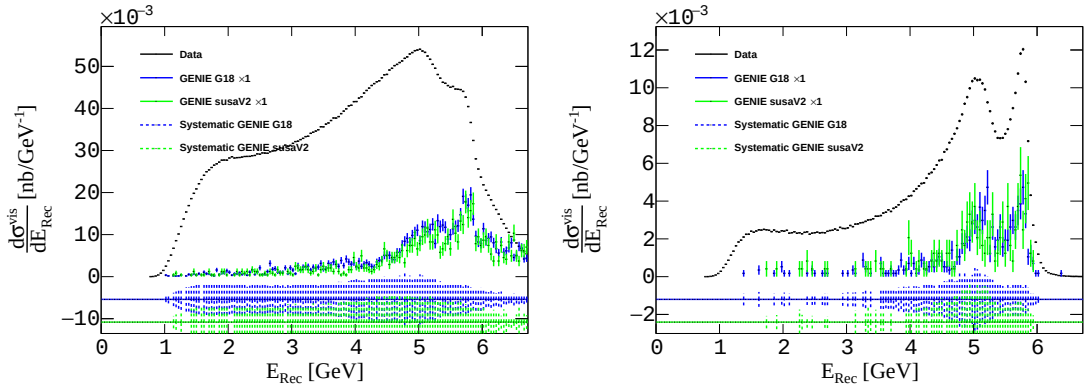

Figure 9.69: The comparisons of ^{2}D$(e,e'pp)X$ reactions, with GENIE SuSAv2 (green) and G18 (blue), for 6 GeV electron beams without (left) and with (right) an additional cut on $p_\perp^{\text{miss}} < 200$ MeV/c. The experimental data is presented as the black line.

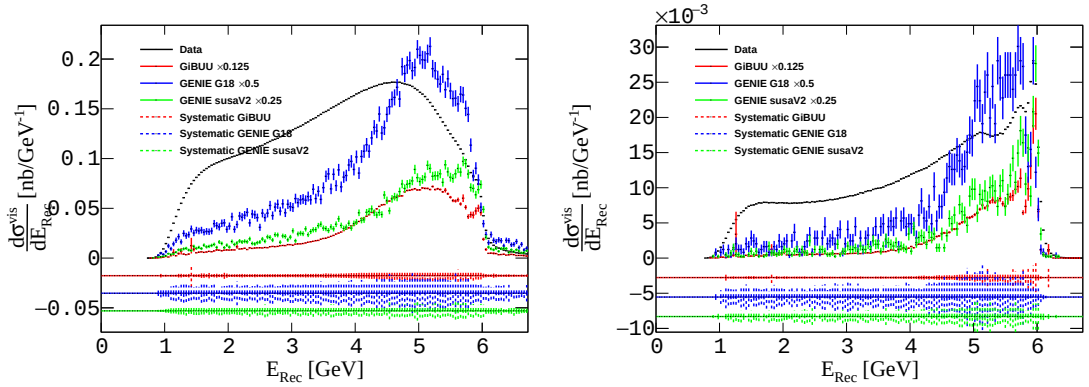

Figure 9.70: The comparisons of ^{12}C$(e,e'pp)X$ reactions, with GENIE SuSAv2 (green), G18 (blue) and GiBUU (red), for 6 GeV electron beams without (left) and with (right) an additional cut on $p_\perp^{\text{miss}} < 200$ MeV/c. The experimental data is presented as the black line.

At this beam energy, the GENIE model predicts the cross sections for ^{2}D reactions with good accuracy when reconstructing the true beam energy. However, events that reconstruct to lower beam energies, typically attributed to events with missing particles, which are influenced by many-body processes, do not replicate the experimental data. Both GiBUU and GENIE provide a poor modelling of the experimental data for all reactions seen for ^{12}C targets. The backgrounds are typically understated (in comparison to the predicted true beam energy peaks), while the peaks for events which reconstruct to the true beam energy are overstated by a few factors (typically by a factor of 5 or 6). These results indicate a modest overhaul for electron scattering cross sections is required at this beam energy, though future comparisons to ^{40}Ar will reveal if this overhaul is required for light nuclei only.

9.6.4 Conclusion

In conclusion, the GENIE model performs well for the lightest target (^{2}D), while GiBUU performs exceptionally well for the heaviest target (^{40}Ar) across all electron beam energies used with these targets. However, both models exhibit poor modelling of all reactions studied using ^{12}C targets, regardless of the electron beam energy setting. Reactions involving pions in the final state are generally modelled worse than those without pions ($A(e,e'p)X$ and $A(e,e'pp)X$). This study highlights the need to constrain electron-nuclei interactions, including neutrino-nuclei interactions, in future developments of theoretical models. Despite these limitations, the models successfully predict such reactions and replicate many general shapes observed in the data. In many cases, if the overall normalisation of the cross sections were adjusted, and additional processes, such as the missing 3π production in GiBUU, were included in the models, they could potentially give better agreement with the data. A significant observation in the results here is that reactions with pions in the final state generally produce cleaner distributions for the reconstructed electron beam energy. The background in such reactions is minimised and the peak of interest is sharper. This could be important for next-generation acceptance-based neutrino beam facilities, such as DUNE, which may wish to seek such reaction channels for determining their neutrino oscillation parameters. Given the importance of ^{40}Ar for next-generation neutrino facilities, based on the current results, GiBUU appears to be more suitable for future neutrino oscillation experiments, offering a significant reduction in the systematic uncertainties associated with the extracted oscillation parameters.

Chapter 10

Summary and Outlook

"Wherever you go, there you are."

- Jon Kabat-Zinn

In this chapter, the conclusions of the two major analyses presented in this thesis are brought together into one overarching summary and outlook. The implications of the results, in the context of the theoretical models, are discussed. The impact of the results on future spallation and neutrino oscillation facilities and experiments is contextualised.

10.1 Summary

This thesis presents an extensive new body of data on photo and electro-induced hadron knockout from nuclear targets obtained with the CLAS and CLAS12 detector systems at Jefferson Lab in the USA. The measurements challenge our understanding of the fundamental many-body nuclear theory. Predictions from the leading theoretical models are compared directly to the measured visible cross-sections for a range of final states and target nuclei. The work is not only of crucial importance for developing next-generation nuclear theory for such reactions but also directly impacts systematic errors in next-generation neutrino facilities such as DUNE. The results also benchmark the capabilities for a possible future photon-induced spallation source.

The first analysis presents data on photoinduced many-proton knockout from nuclei (multiplicity one to six) using real photon beams. The data is compared to one of the leading nuclear reaction theories (GiBUU), with its predictions passed through the acceptance of the detector system. The cross sections for photon energy bins in the range 600 MeV to 4500 MeV were obtained as a function of the reconstructed missing mass of the recoiling system. The GiBUU model gave a broad description of the cross-section and its shape as a function of missing mass up to photon energies of 2 GeV for all processes up to 6p knockout. At higher energies, missing processes in the model such as 3π production

are evidenced in the data and worsen the comparison. Such effects are most clearly evidenced in the one-proton knockout data and the new results will offer the possibility to improve the modelling of resonance production and propagation, including FSI effects, in the nuclear medium.

Searches for evidence of direct knockout were carried out using restrictions on the reconstructed recoiling system. Restricting the transverse momenta of the recoiling system to those expected from direct reactions (i.e. within the region of the Fermi momentum of the struck nucleons) revealed a peak close to zero missing mass for 2p, 3p and 4p knockout. Further cuts to remove background processes through restrictions on the polar angle of the recoiling system enhanced the peaks further. Analysis of the events in the GiBUU simulation showed that these resolved peaks at low missing mass are associated with direct processes. The work presents the first clear evidence of direct proton knockout from a heavy nucleus for any photon energy above 0.3 GeV. This newly resolved process offers new opportunities to constrain the properties of nucleon resonance in the medium (e.g. which contribute through $N^* - N \rightarrow NN$) as well as the possibility to gain increased sensitivity to short-range correlations and three-body forces.

A first assessment of using real photon beams as a spallation source to access neutron-rich nuclei was explored using the simulating power of the newly benchmarked GiBUU for many proton knockout processes. The potential for this method is promising, as GiBUU predicts that a swathe of unobserved exotic nuclei, currently out of reach, are accessible with significant production rates using next-generation intense CPS photon beams on thin ($<$ a few mm thick) ^{208}Pb or ^{238}U targets.

A second analysis presented in the thesis was an analysis of electron scattering on a range of nuclei using the CLAS12 detector at JLab. The analysis aims to challenge and benchmark two state-of-the-art theory models with the newly collected, high-statistics data from the RGM experiment, and provide a comprehensive comparison between the theory models. The analysis is part of the e4ν initiative at JLab and provides the first data at higher beam energies compatible with the neutrino energies of future facilities such as DUNE. Many different reactions, for different targets (^{2}D, ^{12}C and ^{40}Ar) and beam energy configurations (2, 4 and 6 GeV), were compared. The reaction $A(e, e'p)X$, which was published in the previous e4ν analysis shown in Subsec. 3.3.2, had similar conclusions to the previous results on ^{12}C. Further targets (^{2}D and ^{40}Ar) were shown, which produced different conclusions from that of the carbon target, indicating discrepancies in the model predictions. Additional reactions, such as $A(e, e'pp)X$, $A(e, e'p\pi^-)X$, $A(e, e'p\pi^+)X$ and $A(e, e'p\pi^0)X$, were presented, including $A(e, e'p)$ and $A(e, e'p\pi^+\pi^-)$. In almost all cases for the ^{2}D target, the predicted GENIE cross sections were on a comparable scale, with some reactions presenting a good reproduction of the experimental data. It should be noted that the shape of the background is not well reproduced, as such backgrounds are influenced by the modelling of processes that induce many-body knockout processes. A discussion

of the fundamental reaction mechanisms in electron-nucleus interactions was discussed in Subsec. 2.2. An underpredicted background would imply that fundamental mechanisms, such as multi-pion-induced knockouts, are poorly modelled and require improvement.

In the case of ^{12}C and ^{40}Ar targets, the GENIE model, for both the G18 and suSAv2 tunes, vastly overpredicts the cross-section strength, particularly for ^{40}Ar. All reactions have a poorly modelled background and an overpredicted reaction strength for the direct knockout peak. GiBUU produced more promising results for the two targets, even capturing the cross-section for the ^{40}Ar target for some reactions involving 4 GeV electron beams. However, there is still an underprediction for the background in GiBUU for both the ^{12}C and ^{40}Ar targets, with an overprediction in the direct knockout strength for ^{12}C.

As previously stated, the ^{40}Ar target posed significant challenges in its modelling. Alternative methods were used in the absence of a detailed simulation of this target, specifically, we used the approximation of a single-foil target geometry with its vertex position displaced to the position of the argon target. For this reason, the systematic errors determined for the argon target may require additional contributions. This is the source of future work, where a full simulation of the ^{40}Ar target geometry will be implemented once the simulated target configuration is available. However, the results determined for the different targets are not unexpected. GiBUU is a statistical model, which works best for medium to heavy nuclei, whereas GENIE works well for lighter nuclei. Therefore, the overprediction from GENIE for targets heavier than ^{2}D and the accuracy of the GiBUU model may be anticipated to some extent. In any case, the results indicate that a substantial tuning of the models is required for these targets, at each electron beam energy studied in this work.

10.2 Outlook

The work from the two analyses is crucial for next-generation neutrino oscillation facilities. DUNE will use liquid argon time projection chambers for the identification of neutrino-nuclei interactions. The neutrinos are products of particle interactions from proton-graphite interactions, in which mesons produced in the particle interactions decay to release muon neutrinos (ν_μ). The models that we have benchmarked against the experimental data are widely used in neutrino oscillation experiments. However, given the inadequacies of modelling reactions from ^{40}Ar by GENIE and GiBUU, a tuning of these models is required. Extraction of the oscillation parameters with the models in their current state would lead to large biases and systematic uncertainties in the reconstruction of the initial neutrino energy. Ultimately, this would lead to large systematic uncertainties associated with the extracted neutrino oscillation parameters.

The studies on both photo- and electro-induced many-body knockout reactions are particularly important for constraining many-body processes. Multi-proton knockout reactions

would be expected to be a prominent background in neutrino-nuclei interactions, especially if the nuclear target is heavy (such as ^{40}Ar). Pion production is a key initial seed reaction in attaining these multi-nucleon knockout channels, hence benchmarking pion channels is important for controlling the background. Resonance production, which typically induces further nucleon knockout through pion production, is an important seed reaction for which the models need to be benchmarked. GiBUU and GENIE do not have all resonances implemented, therefore the strength of dominant and non-dominant resonances must be tested, particularly in the nuclear medium where resonances are usually broader and more difficult to measure.

Future work for the many-proton knockout should seek an experiment dedicated to the research of many-body interactions. Additional nuclear targets should be used, to measure the direct strength of the reactions we have measured in heavier nuclei. Future work for the electron scattering analysis should seek to quantify the full systematic uncertainties and provide further comparisons of additional reactions. Reactions involving kaons and resonance production are furthermore of high priority, given their importance for neutrino physics.

> *"When I was sixteen, I won a great victory. I felt in that moment I would live to be a hundred. Now I know I shall not see thirty. None of us know our end, really, or what hand will guide us there. A king may move a man, a father may claim a son, but that man can also move himself, and only then does that man truly begin his own game. Remember that howsoever you are played or by whom, your soul is in your keeping alone, even though those who presume to play you be kings or men of power. When you stand before God, you cannot say, 'But I was told by others to do thus,' or that virtue was not convenient at the time. This will not suffice. Remember that."*
>
> - King Baldwin IV, Kingdom of Heaven (2005)

Bibliography

[1] Particle Data Group. Review of particle physics. *Progress of Theoretical and Experimental Physics*, 2020(8):1–2093, August 2020.

[2] J. Allday. Quarks, leptons and the big bang. *Routledge, 2nd Edition, ISBN 978-0-7503-0806-9*, 2001.

[3] Chelsea Gohd. What is Dark Energy? Inside our accelerating, expanding Universe `https://science.nasa.gov/universe/`.

[4] Finches&quarks. Quarks.jpg [explanation of quarks in relation to matter in general], Oct 2016.

[5] E. Rutherford. Lxxix. the scattering of α and β particles by matter and the structure of the atom. *The London, Edinburgh, and Dublin Philosophical Magazine and Journal of Science*, 21(125):669–688, 1911.

[6] James Chadwick. The existence of a neutron. *Proceedings of the Royal Society of London. Series A, Containing Papers of a Mathematical and Physical Character*, 136(830):692–708, 1932.

[7] Baishan Hu, Weiguang Jiang, Takayuki Miyagi, et al. Ab initio predictions link the neutron skin of 208pb to nuclear forces. *Nature Physics*, 18(10):1196–1200, August 2022.

[8] A. Ekström, C. Forssén, G. Hagen, et al. What is ab initio in nuclear theory? *Frontiers in Physics*, 11, 2023.

[9] Maria Goeppert Mayer. On closed shells in nuclei. ii. *Phys. Rev.*, 75:1969–1970, Jun 1949.

[10] S. Frullani and J. Mougey. Single Particle Properties of Nuclei Through (e, e' p) Reactions. *Adv. Nucl. Phys.*, 14:1–283, 1984.

[11] Matthew Duer, O. Hen, E. Piasetzky, et al. Probing high-momentum protons and neutrons in neutron-rich nuclei. *Nature*, 560:617–621, 08 2018.

[12] B. Schmookler. Modified structure of protons and neutrons in correlated pairs. *Nature*, 566(7744):354–358, February 2019.

[13] A. Schmidt, J.R. Pybus, R. Weiss, et al. Probing the core of the strong nuclear interaction. *Nature*, 578(7796):540–544, February 2020.

[14] Roman Pasechnik and Michal Šumbera. Different faces of confinement. *Universe*, 7(9), 2021.

[15] Richard W. Haymaker. Confinement studies in lattice qcd. *Physics Reports*, 315(1):153–173, 1999.

[16] A. Einstein. Über einen die erzeugung und verwandlung des lichtes betreffenden heuristischen gesichtspunkt (on a heuristic viewpoint concerning the production and transformation of light). *Annalen der Physik*, 322(6):132–148, 1905.

[17] Louis De Broglie. *Recherches sur la théorie des quanta (Research on the Theory of Quanta).* PhD thesis, Migration-université en cours d'affectation, 1924.

[18] Beck, Reinhard and Thoma, Ulrike. Spectroscopy of baryon resonances. *EPJ Web Conf.*, 134:02001, 2017.

[19] A. Starostin et al. Measurement of $3pi^0$ photoproduction on the proton from threshold to 1.4 GeV. 1 2011.

[20] N. Zachariou, D. Watts, J. McAndrew, et al. Double polarisation observable g for single pion photoproduction from the proton. *Physics Letters B*, 817:136304, 04 2021.

[21] P. Roy, S. Park, V. Crede, et al. First measurements of the double-polarization observables f, p, and h in ω photoproduction off transversely polarized protons in the N^* resonance region. *Phys. Rev. Lett.*, 122:162301, Apr 2019.

[22] Daniel Watts. *A Survey of Photonuclear Reactions on 12C.* University of Glasgow (United Kingdom), 1997.

[23] N. Bianchi, V. Muccifora, and E. De Sanctis. Total hadronic photoabsorption cross section on nuclei in the nucleon resonance region. *Phys. Rev. C*, 54:1688–1699, Oct 1996.

[24] J. J. Thomson. Xl. cathode rays. *The London, Edinburgh, and Dublin Philosophical Magazine and Journal of Science*, 44(269):293–316, 1897.

[25] M. Khachatryan. Validation of neutrino energy estimation using electron scattering data. *Ph.D. Thesis, Old Dominion University*, 2019.

[26] Clyde L Cowan Jr, Frederick Reines, FB Harrison, et al. Detection of the free neutrino: a confirmation. *Science*, 124(3212):103–104, 1956.

[27] M Khachatryan, L.B Weinstein, O Hen, et al. Electron-beam energy reconstruction for neutrino oscillation measurements. *Nature*, 599(7886):565–570, 2021.

[28] P. Coloma, P. Huber, C.-M. Jen, et al. Neutrino-nucleus interaction models and their impact on oscillation analyses. *Physical Review D*, 89(7), April 2014.

[29] K. Abe, R. Akutsu, A. Ali, et al. Constraint on the matter–antimatter symmetry-violating phase in neutrino oscillations. *Nature*, 580(7803):339–344, April 2020.

[30] L. Alvarez-Ruso, M. Sajjad Athar, M.B. Barbaro, et al. Nustec white paper: Status and challenges of neutrino–nucleus scattering. *Progress in Particle and Nuclear Physics*, 100:1–68, May 2018.

[31] K. Abe, R. Akutsu, A. Ali, et al. Search for *cp* violation in neutrino and antineutrino oscillations by the t2k experiment with 2.2×10^{21} protons on target. *Phys. Rev. Lett.*, 121:171802, Oct 2018.

[32] M. A. Acero, P. Adamson, and L. Aliaga. New constraints on oscillation parameters from ν_e appearance and ν_μ disappearance in the nova experiment. *Phys. Rev. D*, 98:032012, Aug 2018.

[33] A. M. Ankowski, P. Coloma, P. Huber, et al. Missing energy and the measurement of the *cp*-violating phase in neutrino oscillations. *Phys. Rev. D*, 92:091301, Nov 2015.

[34] L. Aliaga, M. Kordosky, T. Golan, et al. Neutrino flux predictions for the numi beam. *Phys. Rev. D*, 94:092005, Nov 2016.

[35] L. Haegel. T2k near detector constraints for oscillation results, 2017.

[36] Janus Weil and Ulrich Mosel. The gibuu transport model. *EPJ Web of Conferences*, 52:06007–, 06 2013.

[37] K. Gallmeister and U. Mosel. Transport-theoretical description of nuclear reactions. *Physics Reports*, 512(1):1–124, 2012. Transport-theoretical Description of Nuclear Reactions.

[38] Stefan Teis. Transporttheoretische beschreibung von relativistischen schwerionenkollisionen bei sis-energien. 1996.

[39] Markus Wagner, Alexei Larionov, and Ulrich Mosel. Kaon and pion production at cbm energies.

[40] M. Wagner, A. B. Larionov, and U. Mosel. Kaon and pion production in relativistic heavy-ion collisions. *Phys. Rev. C*, 71:034910, Mar 2005.

[41] Pythia website. Pythia website. `https://www.pythia.org/`, April 2024.

[42] GM Welke, M Prakash, TTS Kuo, S Das Gupta, and C Gale. Azimuthal distributions in heavy ion collisions and the nuclear equation of state. *Physical Review C*, 38(5):2101, 1988.

[43] Oliver Buss. Photon-and pion-induced reactions in a transport approach. *Other thesis*, 2008.

[44] GiBUU website. Gibuu. `https://gibuu.hepforge.org/`. First accessed: October 2020.

[45] E. Oset and L.L. Salcedo. Delta self-energy in nuclear matter. *Nuclear Physics A*, 468(3):631–652, 1987.

[46] J. S. O'Connell, W. R. Dodge, J. W. Lightbody, et al. Electron scattering in the excitation region of the delta resonance on nuclei with $a = 1\text{to}16$. *Phys. Rev. Lett.*, 53:1627–1629, Oct 1984.

[47] T. Leitner, O. Buss, L. Alvarez-Ruso, et al. Electron- and neutrino-nucleus scattering from the quasielastic to the resonance region. *Phys. Rev. C*, 79:034601, Mar 2009.

[48] C. Andreopoulos, A. Bell, D. Bhattacharya, et al. The genie neutrino monte carlo generator. *Nuclear Instruments and Methods in Physics Research Section A: Accelerators, Spectrometers, Detectors and Associated Equipment*, 614(1):87–104, 2010.

[49] Costas Andreopoulos, Christopher Barry, Steve Dytman, et al. The genie neutrino monte carlo generator: Physics and user manual, 2015.

[50] A. Bodek and J. L. Ritchie. Further studies of fermi-motion effects in lepton scattering from nuclear targets. *Phys. Rev. D*, 24:1400–1402, Sep 1981.

[51] A. Bodek and J. L. Ritchie. Further studies of fermi-motion effects in lepton scattering from nuclear targets. *Phys. Rev. D*, 24:1400–1402, Sep 1981.

[52] Omar Benhar, Nicola Farina, Hiroki Nakamura, Makoto Sakuda, and Ryoichi Seki. Electron-and neutrino-nucleus scattering in the impulse approximation regime. *Physical Review D—Particles, Fields, Gravitation, and Cosmology*, 72(5):053005, 2005.

[53] I.J. Douglas MacGregor. Short range nucleon correlations studied with electron and photon probes. *SciPost Phys. Proc.*, page 010, 2020.

[54] D. P. Watts et al. The C-12 (gamma, N N) reaction studied over a wide kinematic range. *Phys. Rev. C*, 62:014616, 2000.

[55] R.C. Carrasco, E. Oset, and L.L. Salcedo. Inclusive (gamma, pi) reactions in nuclei. *Nuclear Physics A*, 541(4):585–622, 1992.

[56] D. P. Watts et al. Three nucleon mechanisms in photoreactions. *Phys. Lett. B*, 553:25–30, 2003.

[57] Jefferson lab photos.

[58] Christoph W. Leemann, David R. Douglas, et al. The continuous electron beam accelerator facility: Cebaf at the jefferson laboratory. *Annual Review of Nuclear and Particle Science*, 51(1):413–450, 2001.

[59] J. Hansknecht and M. Poelker. Synchronous photoinjection using a frequency-doubled gain-switched fiber-coupled seed laser and eryb-doped fiber amplifier. *Phys. Rev. ST Accel. Beams*, 9:063501, Jun 2006.

[60] Jefferson Lab. Cebaf at 12 gev, 2024. Unpublished report.

[61] U. Timm. Coherent bremsstrahlung of electrons in crystals. *Fortschritte der Physik*, 17(12):765–808, 1969.

[62] D.I. Sober, Hall Crannell, Alberto Longhi, et al. The bremsstrahlung tagged photon beam in hall b at jlab. *Nuclear Instruments and Methods in Physics Research Section A: Accelerators, Spectrometers, Detectors and Associated Equipment*, 440(2):263–284, 2000.

[63] W.J. Briscoe et al. Nsf major research instrumentation.

[64] B.A. Mecking. Clas. *Nucl. Instrum. Meth.*, A503:513, 2003.

[65] S Taylor, S Ahmad, J Distelbrink, et al. The clas start counter. *Nuclear Instruments and Methods in Physics Research Section A: Accelerators, Spectrometers, Detectors and Associated Equipment*, 462(3):484–493, 2001.

[66] Y.G. Sharabian, M. Battaglieri, V.D. Burkert, et al. A new highly segmented start counter for the clas detector. *Nuclear Instruments and Methods in Physics Research Section A: Accelerators, Spectrometers, Detectors and Associated Equipment*, 556:246–258, 01 2006.

[67] M.D Mestayer, D.S Carman, B Asavapibhop, et al. The clas drift chamber system. *Nuclear Instruments and Methods in Physics Research Section A: Accelerators, Spectrometers, Detectors and Associated Equipment*, 449(1):81–111, 2000.

[68] G. Adams, V. Burkert, R. Carl, et al. The clas cherenkov detector. *Nuclear Instruments and Methods in Physics Research Section A: Accelerators, Spectrometers, Detectors and Associated Equipment*, 465(2):414–427, 2001.

[69] E.S. Smith, T. Carstens, J. Distelbrink, et al. The time-of-flight system for clas. *Nuclear Instruments and Methods in Physics Research Section A: Accelerators, Spectrometers, Detectors and Associated Equipment*, 432(2):265–298, 1999.

[70] M. Amarian, G. Asryan, K. Beard, et al. The clas forward electromagnetic calorimeter. *Nuclear Instruments and Methods in Physics Research Section A: Accelerators, Spectrometers, Detectors and Associated Equipment*, 460(2):239–265, 2001.

[71] C. Keith. Frost target. *Nucl. Instrum. Meth.*, A684:27, 2012.

[72] R. A. Arndt. Pion photoproduction from a polarized target. *CLAS Approved Experiment*, E03-105, 2006.

[73] V.D. Burkert, L. Elouadrhiri, K.P. Adhikari, et al. The clas12 spectrometer at jefferson laboratory. *Nuclear Instruments and Methods in Physics Research Section A: Accelerators, Spectrometers, Detectors and Associated Equipment*, 959:163419, 2020.

[74] Jefferson Lab CLAS12 Homepage. Jefferson lab. Accessed: October, 2020.

[75] M.D. Mestayer, K. Adhikari, R.P. Bennett, et al. The clas12 drift chamber system. *Nuclear Instruments and Methods in Physics Research Section A: Accelerators, Spectrometers, Detectors and Associated Equipment*, 959:163518, 2020.

[76] D.S. Carman, L. Clark, R. De Vita, et al. The clas12 forward time-of-flight system. *Nuclear Instruments and Methods in Physics Research Section A: Accelerators, Spectrometers, Detectors and Associated Equipment*, 960:163629, 2020.

[77] D.S. Carman, G. Asryan, V. Baturin, et al. The clas12 central time-of-flight system. *Nuclear Instruments and Methods in Physics Research Section A: Accelerators, Spectrometers, Detectors and Associated Equipment*, 960:163626, 2020.

[78] G. Asryan, Sh. Chandavar, T. Chetry, et al. The clas12 forward electromagnetic calorimeter. *Nuclear Instruments and Methods in Physics Research Section A: Accelerators, Spectrometers, Detectors and Associated Equipment*, 959:163425, 2020.

[79] Y.G. Sharabian et al. The clas12 high threshold cherenkov counter. *Nuclear Instruments and Methods in Physics Research Section A: Accelerators, Spectrometers, Detectors and Associated Equipment*, 968:163824, 2020.

[80] M. Ungaro, D. Anderson, G. Asryan, et al. The clas12 low threshold cherenkov detector. *Nuclear Instruments and Methods in Physics Research Section A: Accelerators, Spectrometers, Detectors and Associated Equipment*, 957:163420, 2020.

[81] A. Acker, D. Attié, S. Aune, et al. The clas12 forward tagger. *Nuclear Instruments and Methods in Physics Research Section A: Accelerators, Spectrometers, Detectors and Associated Equipment*, 959:163475, 2020.

[82] E.P. Segarra, F. Hauenstein, A. Schmidt, et al. The clas12 backward angle neutron detector (band). *Nuclear Instruments and Methods in Physics Research Section A: Accelerators, Spectrometers, Detectors and Associated Equipment*, 978:164356, 2020.

[83] P. Chatagnon, J. Bettane, M. Hoballah, et al. The clas12 central neutron detector. *Nuclear Instruments and Methods in Physics Research Section A: Accelerators, Spectrometers, Detectors and Associated Equipment*, 959:163441, 2020.

[84] R. Fair, N. Baltzell, R. Bachimanchi, et al. The clas12 superconducting magnets. *Nuclear Instruments and Methods in Physics Research Section A: Accelerators, Spectrometers, Detectors and Associated Equipment*, 962:163578, 2020.

[85] M.A. Antonioli, N. Baltzell, S. Boyarinov, et al. The clas12 silicon vertex tracker. *Nuclear Instruments and Methods in Physics Research Section A: Accelerators, Spectrometers, Detectors and Associated Equipment*, 962:163701, 2020.

[86] L. B. Weinstein. Drawings for rgm target cells, 2024. Private communication, March 2024.

[87] S. Boyarinov et al. The clas12 data acquisition system. *Nuclear Instruments and Methods in Physics Research Section A: Accelerators, Spectrometers, Detectors and Associated Equipment*, 966:163698, 2020.

[88] Elliott Wolin. GSIM - USer's Guide Version 1.1. `https://www.jlab.org/Hall-B/document/gsim/userguide.html`.

[89] MauriK Holtrop. Gsim information. `https://nuclear.unh.edu/~maurik/gsim_info.shtml`. First accessed: January 2021.

[90] Ken Livingston. ROOTBEER - a package for the analysis and conversion of CLAS BOS format data using ROOT. `http://nuclear.gla.ac.uk/~kl/rootbeer`.

[91] Maurizio Ungaro. The LUND format - GEMC `https://gemc.jlab.org/gemc/html/documentation/generator/lund.html`.

[92] Maurizio Ungaro. GEant 4 Monte Carlo - GEMC `https://gemc.jlab.org/gemc/html/index.html`.

[93] Marcin Białek. Cyclotron motion.jpg, November 2008.

[94] D. Day, P. Degtiarenko, and S. Dobbs . A conceptual design study of a compact photon source (cps) for jefferson lab. *Nuclear Instruments and Methods in Physics Research Section A: Accelerators, Spectrometers, Detectors and Associated Equipment*, 957:163429, 2020.

[95] T. Kajino and W. Aoki. Current status of r-process nucleosynthesis. *Progress in Particle and Nuclear Physics*, 107:109–166, July 2019.

[96] Jochen Erler and Noah Birge. The limits of the nuclear landscape. *Nature*, 486(7404):509–512, 2012.

[97] E. Pasyuk. Energy-loss corrections for charged particles in clas. *CLAS Note*, 2007:16, 2007.

[98] S. Strauch. Polarization observable $\mathbb{E}$ in $\vec{p}(\vec{\gamma}, \pi^+)n$ reaction. *CLAS Analysis Note*, 2014:101, 2014.

[99] Priyashree Roy and Zulkaida Akbar. Polarization Observables in (Vector-)Meson Photoproduction decaying to Multipion-Final States using the CLAS Polarized Frozen-Spin Target (FROST) and Polarized Photons. https://www.jlab.org/Hall-B/shifts/admin/paper_reviews/2018/AnalysisNote_2-8229355-2018-08-07-v4.pdf.

[100] Priyashree Roy. Measurement of polarization observables in vector meson photoproduction using a transversely-polarized frozen-spin target and polarized photons at clas, jefferson lab. *Ph.D. Thesis, Florida State University*, 2016.

[101] N. Zachariou. Determination of the azimuthal asymmetry of deuteron photodisintegration in the energy region $E_\gamma = 1.1 - 2.3$ GeV. *Ph.D. Thesis, George Washington University*, 2012.

[102] O. Lalakulich and U. Mosel. Gibuu and shallow inelastic scattering, 2013.

[103] L. Tang T., B. P. Kay, and C. R. Hoffman. First exploration of neutron shell structure below lead and beyond. *Physical Review Letters*, 124(6), feb 2020.

[104] Y. Hirayama, Y.X. Watanabe, and M. Mukai. Doughnut-shaped gas cell for kek isotope separation system. *Nuclear Instruments and Methods in Physics Research Section B: Beam Interactions with Materials and Atoms*, 412:11–18, 2017.

[105] G. Savard, M. Brodeur, J.A. Clark, et al. The $n = 126$ factory: A new facility to produce very heavy neutron-rich isotopes. *Nuclear Instruments and Methods in Physics Research Section B: Beam Interactions with Materials and Atoms*, 463:258–261, 2020.

[106] T. Kurtukian-Nieto, J. Benlliure, K.-H. Schmidt, et al. Recent progress in measuring β half-lives of nuclei approaching the r-process waiting point a = 195. *Nuclear Physics A*, 827(1):587c–589c, 2009. PANIC08.

[107] Andrea Falcone. Deep underground neutrino experiment: Dune. *Nuclear Instruments and Methods in Physics Research Section A: Accelerators, Spectrometers, Detectors and Associated Equipment*, 1041:167217, 2022.

Appendix A

Parameters For Many Proton Knockout Analysis Fit Functions

A.1 Delta Beta Fit Function Parameters

The following tables detail the fit functions, and their associated parameters, used in the specified momentum ranges for the momentum-dependent $\Delta\beta$ cuts used in the analysis.

Fit Function	$p_1 x + p_2$			
Momentum Range	$0.2 - 0.45\ GeV/c$			
Parameters	$\bar{x} + 3\sigma$	$\bar{x} - 3\sigma$	$\bar{x} + 2.5\sigma$	$\bar{x} - 2.5\sigma$
p_1	-0.00666601	0.00735476	-0.00549859	0.00618853
p_2	0.061224	-0.0626139	0.050907	-0.0523005

Table A.1: Fit parameters for the polynomial order 1 fit used for the momentum-dependent $\Delta\beta$ cuts applied to the experimental data in the momentum range $0.2 - 0.45\ GeV/c$ for proton 1.

Fit Function	$p_1x^7 + p_2x^6 + p_3x^5 + p_4x^4 + p_5x^3 + p_6x^2 + p_7x + p_8$			
Momentum Range	$0.45 - 1.9\ GeV/c$			
Parameters	$\bar{x} + 3\sigma$	$\bar{x} - 3\sigma$	$\bar{x} + 2.5\sigma$	$\bar{x} - 2.5\sigma$
p_1	0.00794168	0.0184964	0.00120887	0.0176346
p_2	-0.100898	-0.0601089	-0.0389575	-0.0632431
p_3	0.749302	-0.353724	0.472883	-0.263943
p_4	-1.63354	1.11762	-1.09554	0.894093
p_5	1.73155	-1.33618	1.17952	-1.08802
p_6	-0.977206	0.796572	-0.665948	0.653894
p_7	0.282395	-0.236386	0.191128	-0.194934
p_8	-0.0329111	0.0278542	-0.0220293	0.0230352

Table A.2: Fit parameters for the polynomial order 7 fit used for the momentum-dependent $\Delta\beta$ cuts applied to the experimental data in the momentum range $0.45 - 1.9\ GeV/c$ for proton 1.

Fit Function	$p_1x + p_2$			
Momentum Range	$0.35 - 0.75\ GeV/c$			
Parameters	$\bar{x} + 3\sigma$	$\bar{x} - 3\sigma$	$\bar{x} + 2.5\sigma$	$\bar{x} - 2.5\sigma$
p_1	-0.0052819	0.00553385	-0.00436123	0.00462523
p_2	0.043304	-0.0438472	0.0360085	-0.0365737

Table A.3: Fit parameters for the polynomial order 1 fit used for the momentum-dependent $\Delta\beta$ cuts applied to the simulated data in the momentum range $0.35 - 0.75\ GeV/c$ for proton 1.

Fit Function	$p_1x^7 + p_2x^6 + p_3x^5 + p_4x^4 + p_5x^3 + p_6x^2 + p_7x + p_8$			
Momentum Range	$0.75 - 2.5\ GeV/c$			
Parameters	$\bar{x} + 3\sigma$	$\bar{x} - 3\sigma$	$\bar{x} + 2.5\sigma$	$\bar{x} - 2.5\sigma$
p_1	-0.323354	0.257997	-0.270557	0.209465
p_2	1.58412	-1.26741	1.32482	-1.02959
p_3	-2.97311	2.34749	-2.48486	1.90416
p_4	3.02163	-2.36497	2.52272	-1.9166
p_5	-1.79531	1.39517	-1.49696	1.12989
p_6	0.623668	-0.481693	0.519273	-0.38989
p_7	-0.117419	0.0902053	-0.0976068	0.0729822
p_8	0.00925699	-0.00707895	0.00768154	-0.00572552

Table A.4: Fit parameters for the polynomial order 7 fit used for the momentum-dependent $\Delta\beta$ cuts applied to the simulated data in the momentum range $0.75-2.5\ GeV/c$ for proton 1.

Fit Function	$p_1x^2 + p_2x + p_3$			
Momentum Range	$0.2 - 0.33\ GeV/c$			
Parameters	$\bar{x} + 3\sigma$	$\bar{x} - 3\sigma$	$\bar{x} + 2.5\sigma$	$\bar{x} - 2.5\sigma$
p_1	0.241962	-0.0884745	0.214422	-0.0609367
p_2	-1.27037	0.381795	-1.13266	0.244106
p_3	1.97686	-0.658118	1.75724	-0.438522

Table A.5: Fit parameters for the polynomial order 1 fit used for the momentum-dependent $\Delta\beta$ cuts applied to the experimental data in the momentum range $0.2 - 0.33\ GeV/c$ for protons > 2.

Fit Function	$p_1x^7 + p_2x^6 + p_3x^5 + p_4x^4 + p_5x^3 + p_6x^2 + p_7x + p_8$			
Momentum Range	$0.33 - 1.2\ GeV/c$			
Parameters	$\bar{x} + 3\sigma$	$\bar{x} - 3\sigma$	$\bar{x} + 2.5\sigma$	$\bar{x} - 2.5\sigma$
p_1	-0.329902	0.244995	-0.281433	0.198912
p_2	3.75118	-2.76282	3.20224	-2.23994
p_3	-15.4265	11.1476	-13.1846	9.02305
p_4	33.3363	-23.8786	28.5026	-19.3276
p_5	-41.3239	29.4352	-35.3361	23.8405
p_6	29.5734	-20.9452	25.2904	-16.9781
p_7	-11.3627	7.99344	-9.71826	6.48502
p_8	1.81381	-1.26616	1.55158	-1.02815

Table A.6: Fit parameters for the polynomial order 7 fit used for the momentum-dependent $\Delta\beta$ cuts applied to the experimental data in the momentum range $0.33 - 1.2\ GeV/c$ for protons > 2.

Fit Function	$p_1x^2 + p_2x + p_3$	
Momentum Range	$0.2 - 0.33\ GeV/c$	
Parameters	$\bar{x} + 3\sigma$	$\bar{x} + 2.5\sigma$
p_1	0.112508	0.0998015
p_2	-0.482497	-0.438432
p_3	0.736029	0.669439

Table A.7: Fit parameters for the polynomial order 1 fit used for the momentum-dependent $\Delta\beta$ cuts applied to the simulated data in the momentum range $0.2-0.33\ GeV/c$ for protons > 2.

Fit Function	$p_1x^7 + p_2x^6 + p_3x^5 + p_4x^4 + p_5x^3 + p_6x^2 + p_7x + p_8$			
Momentum Range	$0.33 - 1.5\ GeV/c$ for positive $0.2 - 1.5\ GeV/c$ for negative			
Parameters	$\bar{x} + 3\sigma$	$\bar{x} - 3\sigma$	$\bar{x} + 2.5\sigma$	$\bar{x} - 2.5\sigma$
p_1	-0.083652	-0.0489715	-0.0844645	-0.0236739
p_2	0.950955	0.147209	0.922439	-0.0628946
p_3	-3.0581	-0.485583	-3.0046	0.41189
p_4	5.12919	0.838612	5.12414	-1.16809
p_5	-4.90012	-0.84538	-5.00105	1.70064
p_6	2.69281	0.49129	2.82121	-1.3491
p_7	-0.79445	-0.150282	-0.858482	0.555035
p_8	0.0975986	0.0185541	0.109297	-0.0925825

Table A.8: Fit parameters for the polynomial order 7 fit used for the momentum-dependent $\Delta\beta$ cuts applied to the simulated data in the specified momentum ranges for protons > 2.

A.2 Vertex Position Fit Function Parameters

The following table details the fit function, and its associated parameters, used to determine the target windows of the event vertex used in the analysis for the simulated data.

Fit Function	$p_1 e^{\frac{(x-p_2)^2}{2p_3}} + p_4 e^{\frac{(x-p_5)^2}{2p_6}} + p_7 x + p_8$
Parameters	Values
p_1	$7.86914e^5$
p_2	0.0170196
p_3	0.506275
p_4	$2.27275e^5$
p_5	0.077804
p_6	1.34579
p_7	$1.88743e^4$
p_8	-3.40556

Table A.9: Fit parameters for the double Gaussian + linear function used to determine the target windows for the simulated vertex.

A.3 Coincidence Time Fit Function Parameters

The following tables detail the fit functions, and their associated parameters, used in the specified momentum ranges for the momentum-dependent Δt cuts used in the analysis.

Fit Function	$p_1x^6 + p_2x^5 + p_3x^4 + p_4x^3 + p_5x^2 + p_6x + p_7$			
Momentum Range	$\frac{p_1+p_n}{2} = 0.3 - 1.35\ GeV/c$			
Parameters	$\bar{x} + 3\sigma$	$\bar{x} - 3\sigma$	$\bar{x} + 2.5\sigma$	$\bar{x} - 2.5\sigma$
p_1	38.2173	-27.6154	32.6986	-22.1016
p_2	-196.868	128.108	-169.498	100.791
p_3	482.203	-290.471	416.808	-225.299
p_4	-656.839	368.951	-569.595	282.15
p_5	510.842	-269.745	444.138	-203.501
p_6	-212.295	106.509	-184.934	79.3894
p_7	36.5212	-17.5998	31.8591	-12.9874

Table A.10: Fit parameters for the polynomial order 6 fit used for the momentum-dependent Δt cuts applied to the experimental data for the specified momentum range.

Fit Function	$p_1x^6 + p_2x^5 + p_3x^4 + p_4x^3 + p_5x^2 + p_6x + p_7$			
Momentum Range	$\frac{p_1+p_n}{2} = 0.3 - 1.55\ GeV/c$			
Parameters	$\bar{x} + 3\sigma$	$\bar{x} - 3\sigma$	$\bar{x} + 2.5\sigma$	$\bar{x} - 2.5\sigma$
p_1	23.0083	-22.7855	19.214	-18.9751
p_2	-100.289	99.9318	-83.7456	83.2779
p_3	223.638	-220.016	187.034	-183.105
p_4	-278.01	268.023	-232.993	222.572
p_5	196.658	-185.327	165.172	-153.51
p_6	-74.0958	68.2723	-62.3591	56.4046
p_7	11.5446	-10.4191	9.73315	-8.58679

Table A.11: Fit parameters for the polynomial order 6 fit used for the momentum-dependent Δt cuts applied to the simulated data for the specified momentum range.

Appendix B

Parameters For $e4\nu$ Analysis Fit Functions

B.1 Sampling Fraction Fit Function Parameters

The following tables detail the fit functions, and their associated parameters, used to determine the sampling fraction cuts in the simulated and experimental data.

Fit Function	$p_1x^4 + p_2x^3 + p_3x^2 + p_4x + p_5$				
Momentum Range	1.0 - 5.4 GeV/c				
Parameters	p_1	p_2	p_3	p_4	p_5
Sector 1	0.317198	-0.00121394	-0.00614205	0.00199881	-0.000194886
Sector 2	0.302146	0.0187661	-0.0122844	0.00287584	-0.000240434
Sector 3	0.316503	0.00662424	-0.0101086	0.00293118	-0.000266296
Sector 4	0.322494	-0.00698499	-0.000390492	0.000294787	-2.51236e-05
Sector 5	0.330529	-0.020929	0.00458072	-0.000464522	1.10593e-05
Sector 6	0.32548	-0.00924794	-0.00099323	0.000574305	-5.16358e-05

Table B.1: Fit parameters for the polynomial order 4 fit used for the momentum-dependent SF cuts applied to the experimental data in the momentum range 1.0 - 5.4 GeV/c. These parameters correspond to the $\mu + 3\sigma$ position.

Fit Function	$p_1x^4 + p_2x^3 + p_3x^2 + p_4x + p_5$				
Momentum Range	1.0 - 5.4 GeV/c				
Parameters	p_1	p_2	p_3	p_4	p_5
Sector 1	0.0589382	0.111026	-0.0356708	0.00535674	-0.000317973
Sector 2	0.0689158	0.0969521	-0.0327407	0.00534808	-0.000358565
Sector 3	0.0634225	0.114441	-0.0402893	0.00683405	-0.000479066
Sector 4	0.0446211	0.127947	-0.0434115	0.00712585	-0.000453877
Sector 5	0.0565128	0.12546	-0.0467842	0.0082382	-0.00055903
Sector 6	0.0614309	0.111341	-0.0363578	0.0056684	-0.000345757

Table B.2: Fit parameters for the polynomial order 4 fit used for the momentum-dependent SF cuts applied to the experimental data in the momentum range 1.0 - 5.4 GeV/c. These parameters correspond to the $\mu - 3\sigma$ position.

Fit Function	$p_1x^4 + p_2x^3 + p_3x^2 + p_4x + p_5$				
Momentum Range	1.0 - 5.4 GeV/c				
Parameters	p_1	p_2	p_3	p_4	p_5
Sector 1	0.379689	-0.0898302	0.0352967	-0.00621378	0.000398157
Sector 2	0.348518	-0.0400682	0.0117792	-0.00168895	0.000106001
Sector 3	0.365105	-0.070248	0.0270467	-0.0047711	0.000311884
Sector 4	0.360663	-0.0683643	0.026189	-0.00461757	0.000299586
Sector 5	0.353405	-0.0505795	0.0152197	-0.00196135	8.03422e-05
Sector 6	0.364296	-0.0679102	0.0249753	-0.00419115	0.00025758

Table B.3: Fit parameters for the polynomial order 4 fit used for the momentum-dependent SF cuts applied to the simulated data in the momentum range 1.0 - 5.4 GeV/c. These parameters correspond to the $\mu + 3\sigma$ position.

Fit Function	$p_1x^4 + p_2x^3 + p_3x^2 + p_4x + p_5$				
Momentum Range	1.0 - 5.4 GeV/c				
Parameters	p_1	p_2	p_3	p_4	p_5
Sector 1	0.0522216	0.151657	-0.0577706	0.0100424	-0.000655544
Sector 2	0.0623575	0.112914	-0.0363839	0.00560643	-0.000379143
Sector 3	0.0510367	0.149276	-0.0569949	0.00998301	-0.000667288
Sector 4	0.043866	0.155168	-0.0582973	0.0100936	-0.000659974
Sector 5	0.06192	0.131868	-0.046413	0.00750525	-0.000460852
Sector 6	0.0485343	0.151552	-0.0565807	0.00965769	-0.000620855

Table B.4: Fit parameters for the polynomial order 4 fit used for the momentum-dependent SF cuts applied to the simulated data in the momentum range 1.0 - 5.4 GeV/c. These parameters correspond to the $\mu - 3\sigma$ position.